INVESTIGATION OF WATER TRANSPORT PARAMETERS AND PROCESSES IN THE GAS DIFFUSION LAYER OF PEM FUEL CELLS

Joshua David Sole

Dissertation Submitted to the Faculty of

for the degree of:

DOCTOR OF PHILOSOPHY

in

Mechanical Engineering

Committee Members:

Michael W. Ellis, Chair

Scott W. Case

David A. Dillard

Douglas J. Nelson

Michael R. von Spakovsky

April 18, 2008

Blacksburg, Virginia, USA

Keywords: fuel cell, water transport, two phase flow, capillary pressure, relative permeability, GDL, gas diffusion layer, PEM, PEMFC

INVESTIGATION OF WATER TRANSPORT PARAMETERS AND PROCESSES IN THE GAS DIFFUSION LAYER OF PEM FUEL CELLS

Joshua David Sole

ABSTRACT

Constitutive relationships are developed to describe the water transport characteristics of the gas diffusion layer (GDL) of proton exchange membrane fuel cells (PEMFCs). Additionally, experimental fixtures and procedures for the determination of the constitutive relationships are presented. The water transport relationships are incorporated into analytical models that assess the impact of the water transport relations and that make PEMFC performance predictions. The predicted performance is then compared to experimental results.

The new constitutive relationships are significantly different than the currently popular relationships used in PEMFC modeling because they are derived from experiments on actual PEMFC gas diffusion layer materials. In prior work, properties of the GDL materials such as absolute permeability, liquid water relative permeability, porosity, and capillary behavior are often assumed or used as adjustment parameters in PEMFC models to simplify the model or to achieve good fits with polarization data. In this work, the constitutive relations are not assumed but are determined via newly developed experimental techniques.

The experimental fixtures and procedures were used to characterize common GDL materials including carbon papers and carbon cloths, and to investigate common treatments applied to these materials such as the bulk application of a hydrophobic polymer within the porous structure.

A one-dimensional model is developed to contrast results based on the new constitutive relations with results based on commonly used relationships from the PEMFC literature. The comparison reveals that water transport relationships can have a substantial impact on predicted GDL saturation, and consequently a significant impact on

cell performance. The discrepancy in saturation between cases can be nearly an order of magnitude. A two-dimensional model is also presented that includes the impact of the compressed GDL region under the shoulder of a bipolar plate. Results show that the compression due to the bipolar plate shoulder causes a significant increase in liquid saturation, and a significant reduction in oxygen concentration and current density for the paper GDL. In contrast, compression under the shoulder has a minimal impact on the cloth GDL. Experimental inputs to the 2-D model include: absolute permeability, liquid water relative permeability, the slope of the capillary pressure function with saturation, total porosity, GDL thickness, high frequency resistance, and appropriate Tafel parameters. Computational polarization curve results are compared to experimental polarization behavior and good agreement is achieved.

ACKNOWLEDGEMENTS

I'd like to thank all of my committee members for all that they have taught me during my course of study over the last five years. A special thanks to my committee chair, Dr. Mike Ellis, for his hands-on approach and patience while guiding me in my research endeavors. Thanks to Steve McCartney for his help with the SEM images included in this document. Finally, I'd like to thank my parents, brothers, sisters-in-law, nephews, and everyone else who has provided support in any way during my time at Virginia Tech.

DEDICATION

To Pap & Grandma, and Dad & Mom.

PREFACE

This work was completed at Virginia Polytechnic Institute and State University and was funded in part by Ecolectrix LLC, the National Science Foundation Integrative Graduate Education and Research Traineeship (NSF-IGERT) fellowship program, the United States Department of Energy Graduate Automotive Technology Education (GATE) program, and the Institute for Critical Technology and Applied Science (ICTAS) at Virginia Tech.

TABLE OF CONTENTS

LIST OF FIGURES

* Reproduced by permission of ECS – The Electrochemical Society

LIST OF TABLES

NOMENCLATURE

ENGLISH

$\%PTFE$	fraction of PTFE in bulk GDL structure by weight
A	frontal surface area
ASR_{2xGDL}	area specific resistance of two GDL layers
$ASR_{m,I}$	area specific resistance of the membrane and interfaces
c	gas species concentration
c^0	reference gas species concentration
c_p	specific heat of the gaseous mixture
$\mathbb{D}_{\alpha\beta}$	multicomponent Fick diffusivity
$\tilde{D}_{\alpha\beta}$	Maxwell-Stefan diffusivity
E_{cell}	terminal potential of the cell
E_{oc}	actual open circuit cell potential
$E_{oc,rev}$	reversible open circuit potential
F	Faraday's number
f_{HP}	heat partition factor
g	gravitational acceleration
HFR'	measured area specific high frequency resistance
j	average current density
j_e	local current density generated at the catalyst layer
j_0^0	reference exchange current density
K	absolute permeability
k_{carb}	thermal conductivity of the carbon phase
k_g	thermal conductivity of the gas phase
k_{LW}	thermal conductivity of the liquid water phase
$k_{r,g}$	relative permeability of the gas phase
$k_{r,LW}$	relative permeability of the liquid water phase
$k_{T.eff}$	effective local thermal conductivity

m_{dry}	mass of the dry GDL specimen
$m_{partial\text{-}S}$	mass of the partially saturated GDL specimen
m_{solid}	mass of the solid phase
M	molar mass of a species
$\dot{m}$	mass flow rate
N	number of layers
P_c	capillary pressure
$p_{sat}(T)$	temperature dependent saturation pressure of water
p	partial pressure of a species
R_u	universal gas constant
S	reduced liquid saturation
T	GDL thickness
T	temperature
T_{cell}	cell temperature
t_{mem}	membrane thickness
t_o	as-received GDL thickness
$\boldsymbol{u}$	velocity vector
u_{LW}	one-dimensional liquid water velocity
$\dot{V}_g$	volumetric flow rate of the gas phase
$\dot{V}_{LW}$	volumetric flow rate of the liquid water phase
VS_{cond}	volumetric source of condensation
VS_{evap}	volumetric source of evaporation
VS_{LW}^{net}	net volumetric rate of condensation
V_{solid}	volume of the solid phase
VS_T^{net}	net source of thermal energy
W_{solid}	weight of the solid phase
$W_{solid\ immersed\ in\ pentane}$	weight of the solid when immersed in pentane
y	mole fraction of a species

GREEK

α	alpha species
β	beta species
Δh_{fg}	enthalpy of vaporization for water
ΔP	pressure difference across a given length
ε	compressed porosity
ε_o	as-received porosity
$\eta_{act,C}$	cathode activation overpotential
η_{GDL}	GDL overpotential
$\eta_{m,i}$	overpotential of the membrane and interfaces
κ	effective permeability
μ	kinematic viscosity
ρ_{carbon}	density of the carbon phase in the GDL
$\rho_{pentane}$	density of pentane
ρ_{LW}	density of liquid water
ρ_{PTFE}	density of PTFE
$\boldsymbol{\sigma}_c$	GDL conductivity tensor
$\sigma_{GDL,x}$	through-plane GDL conductivity
$\sigma_{GDL,y}$	in-plane GDL conductivity
σ_i	effective ionic conductivity in the membrane
φ_c	local cathode GDL potential
φ_i	ionic potential in the membrane
$\varphi_{i,A}$	reference ionic potential at the anode-membrane interface
ψ_{cond}	condensation switch function
ψ_{evap1}	first evaporation switch function
ψ_{evap2}	second evaporation switch function
ω	mass fraction

SUBSCRIPTS

g	gaseous mixture
LW	liquid water
w	water (either phase)
wv	water vapor
O_2	diatomic oxygen species
N_2	diatomic nitrogen species
GFC	gas flow channel

1 INTRODUCTION

In recent years the interest and financial investment in alternative energy systems has increased dramatically. Political pressure for cleaner energy, economic pressure for more secure energy, and domestic pressure for greater energy independence, have all propelled the interest and investment in alternative energy systems. At the utility scale, much of the research and development has focused on methods for improving large scale power production, such as cleaner coal, and safer nuclear power plants. At smaller scales such as personal vehicle power, residential co-generation, and portable power, proton exchange membrane fuel cells (PEMFCs) have come to the foreground as one of the most promising energy system solutions.

The surge of interest in PEMFCs has fueled a tremendous increase in fuel cell research in the private sector, in academia, and in federally funded laboratories. Many scientists and engineers have spent the last decade working to understand the vast array of phenomena that govern the performance of PEMFC components and systems. Ideally, the process would go as follows: first a phenomenon is studied to a point where a good understanding has been established; second the new understanding of the phenomena is used to develop improved materials. Oftentimes, research does not follow this process due to the time pressure for improved product performance, and therefore, a trial and error approach is pursued for material development. Consequently, the trial and error tactic forces physical characterization and modeling of the governing physics to the background resulting in minimal analytical guidance for component design.

This dissertation focuses on the development of a fundamental understanding of the transport of species, particularly liquid water, within the gas diffusion layer of PEMFCs. For more than ten years, the transport of water within the PEMFC has been recognized as one of the key determinants of system performance. And yet, the understanding of liquid water transport and its effect on gas transfer in the gas diffusion layer (GDL) remains poorly understood with a heavy emphasis on unsubstantiated assumptions and descriptive rather than predictive analyses. This work seeks to address

many of these shortcomings through the development of a rigorous description of GDL transport phenomena that is grounded in experimentally verifiable material properties.

The first chapter of this work will provide a brief introduction to PEMFCs. The second chapter will focus on prior work related to mass transport in the GDL of PEMFCs with particular emphasis on water transport. Chapter 3 will present new experimental methods for determining GDL characteristics, while Chapter 4 will present the analytical framework in which the characteristics are applied to describe GDL transport processes. In the fifth chapter the results of the experiments are discussed, implemented in the analytical model, and used to make predictions which are then experimentally verified. Finally, conclusions will be drawn from the experimental and analytical results and will be presented in the sixth chapter.

1.1 PROTON EXCHANGE MEMBRANE FUEL CELL OPERATION

This section details the basic electrochemistry which occurs within proton exchange membrane fuel cells (PEMFCs), focusing exclusively on the electrodes and the membrane. The fuel cells of interest in this work are referred to as proton exchange membrane (PEM) fuel cells because the membrane separating the electrodes does just that, it permits the exchange of protons from the anode to the cathode due to its acidic nature.

At the anode, hydrogen is transported to the catalyst sites where it reacts to yield protons and electrons. Active catalyst sites must be in contact with the reactant gas, an electron conductor (typically carbon black) and a proton conductor (electrolyte) for the reaction to take place. The electrons produced travel into the electron conductor and through an external circuit which terminates at the cathode. The protons produced when the hydrogen molecules are split travel into the proton conductor, through the electrolyte membrane, and to an active catalyst site in the cathode catalyst layer. The anode reaction is presented in Eq. (1.1) below and in Figure 1.1.

$$2H_2 \rightarrow 4H^+ + 4e^- \qquad (1.1)$$

The reactive chemical species at the cathode of a PEM fuel cell is oxygen. At the cathode, diatomic oxygen is reduced on the catalyst surface where it combines with the electrons that have departed the anode and traveled the external circuit and with the protons which have departed the anode and traveled through the polymer electrolyte membrane. Diatomic oxygen molecules are required for this reaction at half the rate at which the diatomic hydrogen molecules are split into protons and electrons, and the resulting product is water. The cathode reaction is detailed in Eq. (1.2).

$$O_2 + 4H^+ + 4e^- \rightarrow 2H_2O \qquad (1.2)$$

Overall, PEM fuel cells yield the following reaction:

$$2H_2 + O_2 \rightarrow 2H_2O \qquad (1.3)$$

The electrode reactions and a schematic of the electrochemistry are summarized in Figure 1.1.

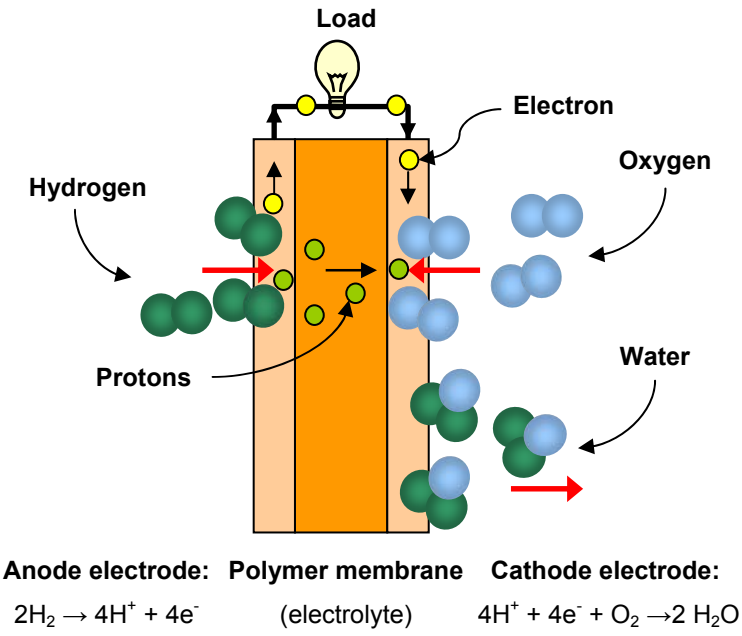

Figure 1.1 – Schematic of PEM fuel cell electrode reactions.

1.2 PEMFC COMPONENTS

There are relatively few components that make up a single PEMFC. Each of the following components - the polymer electrolyte membrane (PEM), the catalyst layers (CL), the gas diffusion layers (GDL), the collector plates, and the gas flow channels (GFC) are discussed briefly in this section.

Figure 1.2 illustrates the assembly of a single PEM fuel cell. Starting from the center and working outward, the polymer membrane separates the reactants in the PEMFC. The PEM is relatively impermeable to electrons, but an excellent conductor of protons, thus forcing electrons through the external circuit, while allowing the travel of protons to the cathode.

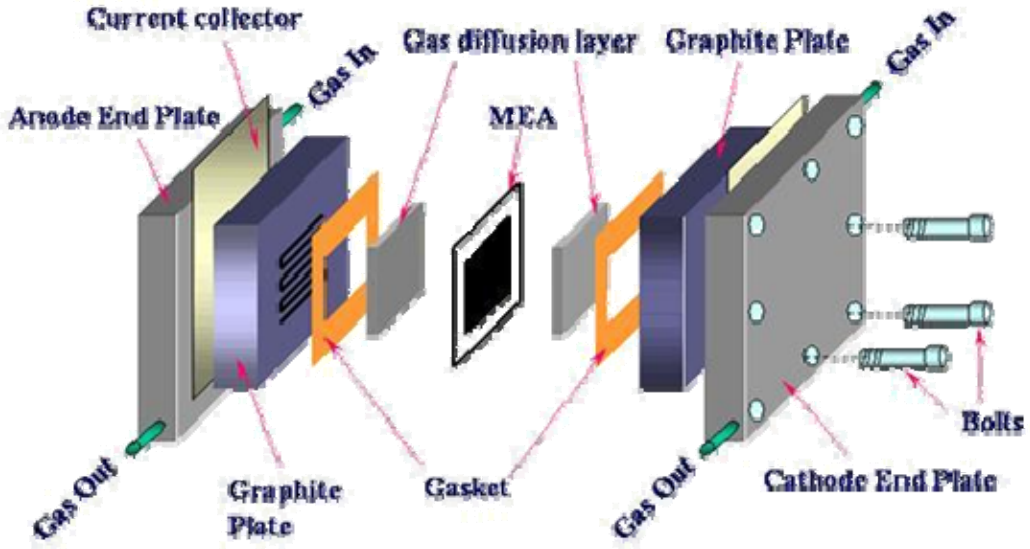

Figure 1.2 – Single PEM fuel cell components and assembly.

The catalyst layers used in PEMFCs are typically a mixture of platinum particles (dia.~1-7 nm) supported on carbon particles (dia.~30 nm), mixed in a ratio of approximately 2:1 with a proton conducting polymer electrolyte, typically Nafion® manufactured by DuPont. This mixture can be applied to the gas diffusion layer (to be discussed later) and then hot pressed to the membrane. Alternatively, the catalyst mixture can be applied directly to the membrane by a variety of methods such as, painting,

spraying, or hot pressing [2, 3]. In this work, the membrane with catalyst layers on each side is referred to as the membrane electrode assembly (MEA). In other works, MEA is sometimes used to mean the entirety of the membrane, catalyst layers, and gas diffusion layers.

The gas diffusion layer (GDL) in a PEMFC serves a variety of purposes. This layer must be porous to allow the hydrogen or oxygen to diffuse to the catalyst layers. Additionally, the GDL must be well suited to transport the water produced at the cathode reaction sites outward from the reaction sites to avoid electrode flooding. Flooding simply refers to the fact that if too much water surrounds the catalyst site, then it is more difficult for gases to diffuse to the catalyst site due to the presence of the water. The GDL must also be electrically conductive since the electrons produced at the anode must travel through the GDL to the external circuit and around to the cathode to complete the reaction. Resistance to corrosion is also an issue of concern since the GDL resides in a moist and acidic environment. Due to the requirements of permeability, electrical conductivity, and corrosion resistance, the GDL is typically constructed of flexible carbon fiber woven fabric, or stiff carbon fiber paper.

Another component required for PEMFCs are the collector plates. The collector plates are typically pressed against the gas diffusion layer to collect electrons from the anode GDL and transport them into the external circuit or to conduct electrons from the external circuit into the cathode GDL to complete the circuit.

The collector plates typically have a gas flow channel (GFC) machined or pressed into them to evenly distribute the reactant gas over the surface of the GDL. Common GFC designs include serpentine channel flow fields, interdigitated channel flow fields, and parallel channel flow fields, each of which has a particular set of benefits and drawbacks [4].

1.3 WATER TRANSPORT IN PEMFCS

Some components within PEMFCs need water to operate efficiently while others operate more effectively without water. The proton exchange membrane (PEM) is a

polymeric material whose conductivity has a strong dependence on water content [5]. Therefore, to improve the conductivity of such a material, it must have access to water. On the other hand, the gas diffusion layer (GDL) operates more effectively if there is no liquid water present because the liquid only serves as a blockage within the porous structure, therefore reducing the ability of the GDL to effectively distribute the reactant gases. The catalyst layer (CL) needs to be permeable so the reactants can diffuse to the reaction sites, yet also needs to effectively conduct protons in the electrolyte phase. It is therefore preferable for the CL to not be fully wetted or fully dry, but to have an intermediate level of water content.

The previous section discussed the chemical reactions at each electrode in PEMFCs. The cathode half-reaction is a source of water which must be transported out of the cell in some manner to avoid flooding of the cathode and its GDL. The generated water, along with all other water in the system can be transported via a variety of transport mechanisms. There are numerous processes by which water moves between and within the different components of PEMFCs. Some of the processes can enhance performance, while other can limit cell performance. Four main processes of water transport will be discussed in this section: vapor diffusion, electro-osmotic drag, back-diffusion, and pressure driven capillary flow.

Water vapor diffusion occurs through a gradient of water vapor concentration. Typically the inlet hydrogen is humidified to a level at or near a saturated condition to ensure that the water vapor concentration in the GFC is greater than the concentration near the anode catalyst layer. This gradient forces vapor diffusion from the GFC towards the PEM, therefore aiding in the maintenance of sufficient membrane hydration for good conductivity. The cathode gas is also typically humidified although it is not always necessary. If the cathode gas is excessively humidified it may discourage vapor diffusion of the product water from the catalyst layer to the gas channel. If the cathode gas is inadequately humidified it may allow the extraction of too much water from the cathode and encourage membrane dehydration. Obviously, there is a balance which must be achieved.

Electro-osmotic drag (EOD) is an interesting phenomenon that coincides with the proton exchange across the polymer membrane. As protons move across the PEM from

the anode electrode to the cathode electrode, they can "drag" water molecules along with them. This can result in an overly wet cathode and an overly dry anode. The potential for excess drying of the anode electrode is why the anode gases are typically fully humidified before entering the fuel cell stack.

Inevitably, the cathode is prone to having excess water due to the electrochemical generation of water, and due to the electro-osmotic drag which also increases water content. Anytime there is a gradient of water concentration (i.e. higher concentration at the cathode than at the anode) there is potential for water diffusion. In PEMFCs this is commonly referred to as back-diffusion because it counteracts the electro-osmotic drag. Although the diffusion of water through the membrane is important it is commonly outweighed by the EOD within the cell [5]. The net water flux from anode to cathode (EOD minus back-diffusion) can range from 0.1 water molecules per proton (at high current density), up to 0.6 water molecules per proton (at low current density) for common operating conditions [5].

Materials of all types are commonly classified based on their contact angle with water, θ_c, as hydrophilic (water will spread on the surface, (contact angle, $\theta_c<90°$)) or hydrophobic (water will bead on the surface, $\theta_c>90°$). The carbon fibers that typically comprise GDL materials can exhibit contact angles over a wide range ($80°<\theta_c<130°$) depending on surface oxidation and roughness. In PEMFC GDL materials it would be ideal if water would infiltrate the hydrophilic pores so that it could be removed via capillary forces at a rate in excess of the production rate at the cathode. Unfortunately, since GDL materials are only marginally hydrophilic if not hydrophobic, the capillary forces developed are extremely small and do not necessarily draw enough water in the desired direction toward the gas flow channel (GFC). Under these conditions, water pressure will increase slightly and may eventually fill all pore space in the GDL since nearly all of the pores exhibit similar wettability. If the entire GDL becomes filled with liquid water it becomes very difficult for reactants to reach the catalyst sites due to the flooding of the electrode.

In order to avoid electrode flooding it has become common practice for the GDL to be treated with a very hydrophobic polymer such as poly(tetrafluoroethylene) (PTFE, trade name Teflon® by DuPont). The contact angle of smooth PTFE is ~108° while PTFE

with high surface roughness can achieve nearly perfect non-wetting behavior exhibiting a contact angle of approximately 165° [6]. The bulk PTFE treatment of the GDL is thought to encourage a majority of pores to be free of liquid water to enable gas flow through the pores. Although these PTFE treated pores discourage liquid water, they are also sometimes filled due to increased levels of water generation. The increased level of water generation combined with the generally hydrophobic nature of the GDL can cause an increase in the pressure of the liquid water. Ideally, the increase in capillary pressure at high water production rates is sufficient to drive the flow of liquid water through the large hydrophobic pores while leaving the small hydrophobic pores open to gas transport.

1.4 RESEARCH OBJECTIVES

A fundamental, experimentally verified theory of water transport is crucial to understanding and improving PEM fuel cell operation. Significant work has been done to understand and model water transport in the PEM [5, 7-9]. Additionally, there have been numerous models developed for entire cells, and for the GDL as a standalone material. Unfortunately, all PEMFC models in the existing body of literature are based on assumptions regarding GDL water transport that are difficult to justify and difficult to experimentally verify.

Transport equations have been developed to model liquid water, and water vapor, within the porous GDL. Although the transport equations seem to address the proper phenomena, the constitutive equations generally assume a functional form that is difficult to justify and that has never been confirmed for the actual materials employed in the GDL of a PEMFC. In order to thoroughly understand water transport through the GDL, governing relationships which implement experimentally validated constitutive relationships must be utilized.

The objectives related to the experimental aspects of this work are as follows:

- Develop new experimental methods capable of determining the constitutive relationships that govern liquid water transport in the macroporous GDL region of PEMFCs
- Assess the impact that media structure (e.g., cloth or paper) has on the water transport relations.
- Assess the impact that a hydrophobic treatment has on the water transport relations.
- Assess the impact that GDL compression has on the water transport relations.

Although the primary focus of this work is experimental, an analytical framework is also necessary to demonstrate the effect of the experimentally developed constitutive equations and to compare them to existing models assumed in the PEMFC literature. Furthermore, the implementation of experimentally verified constitutive relations should reduce the need for parameter adjustment as is common in PEMFC models used to predict polarization performance. With these considerations in mind, the following is a list of the analytical objectives of this work:

- Develop a one-dimensional model of a cathode GDL cross-section for the purpose of qualitatively comparing the impact of constitutive water transport relations.
- Develop a 2-D cathode GDL model that does not require the use of any adjustment parameters, and instead relies on experimentally verified material properties and liquid water transport relations.
- Use the 2-D model to assess the impact that the compressed region under the bipolar plate shoulder can have on water transport and cell performance.
- Predict polarization performance for two PEMFCs utilizing fundamentally different GDL materials (carbon paper and carbon cloth) by only changing the experimentally determined properties and relations addressed in this work.

The primary goal of this work is to contribute significantly to the development of a comprehensive understanding of liquid transport and GDL performance by developing experimental methods that will, for the first time, measure the constitutive relations

necessary to describe liquid water transport in GDL material. Additionally, by eliminating a significant number of unknown or adjustable parameters from PEMFC models, this work will provide a substantial step forward along the path to PEMFC models being utilized as design tools for the fuel cell industry.

2 LITERATURE SURVEY

A variety of water transport models attempting to capture the effects of both liquid and vapor phase transport of water in proton exchange membrane fuel cells (PEMFCs) exist in the fuel cell literature. Many of these models include the entire structure of a single cell including the bipolar plates, the gas flow channels (GFCs), the gas diffusion layers (GDLs), the catalyst layers (CLs), and the polymer electrolyte membrane (PEM). Generally, however, simplifying assumptions and inadequate material characterization limit the effectiveness of these models as engineering design tools. The focus of this work is to improve the understanding of how water (in both liquid and vapor phases) exists and is transported within the GDL of a PEMFC. The following sections will outline the common methods used to model both water vapor and liquid water in the GDL of PEMFCs. Some of the reviewed literature was aimed exclusively at the modeling of water in the GDL [10-13] while much of it was aimed toward the modeling of the entire PEMFC [14-18]. In addition, general approaches to modeling transport processes in porous media are reviewed for their applicability to PEMFCs. Finally, some experimental techniques applied to porous media characterization are reviewed.

2.1 OVERVIEW OF GAS DIFFUSION LAYER TRANSPORT PROCESSES

Modeling of transport processes in the GDL of PEMFCs is difficult due to the presence of three phases. The solid phase is a matrix of solid material whose pore structure and surface properties influence how the fluid phases move through the solid matrix. The two fluid phases, liquid water and a gaseous mixture, are difficult to model due to the interaction between them and the exchange of mass between the phases due to evaporation and condensation. Furthermore, individual gases within the gaseous mixture are transported by diffusion within the porous structure.

Modeling of gas diffusion in an open volume is well established but complications arise when a solid matrix is introduced. Additionally, the modeling of gas diffusion is further complicated by the possibility of liquid water blocking a fraction of

the free space within the solid matrix. This water blockage is referred to as *saturation*. Common approaches for describing gas diffusion will be discussed in Section 2.2.

The movement of liquid water within the porous structure depends on the local liquid pressure, as well as the local gas pressure and the local characteristics of the solid matrix. The local pressure difference between phases is commonly termed *capillary pressure*. Transport of the liquid phase depends heavily on the gradient of capillary pressure. Modeling methods used for the transport of liquid water in the PEMFC literature will be discussed in Section 2.3.

Characterization of the exchange of water between the gaseous and liquid phases in the GDL requires an understanding of both equilibrium conditions and transport processes. Various approaches for describing this phenomenon are discussed further in Section 2.4.

Porosity and permeability are fundamental characteristics of porous media. Section 2.5 reviews some experimental techniques commonly used to determine porous media characteristics. Determining the porosity and permeability of porous media is vital to more advanced characterization.

The concepts of "saturation" and "capillary pressure" are essential to the understanding of diffusion, liquid transport, and exchange between phases. Thus, a discussion of transport in the GDL must begin with a discussion of these two key terms. The following sub-sections define these terms and discuss their implications for GDL transport.

2.1.1 Saturation in porous media

Within a flowing liquid and gas system there is a fluid phase which the solid phase attracts (wetting phase), and a fluid phase which the solid phase repels (non-wetting phase). This preference has to do with the surface tension of the fluids within the system, and the surface energy of the solid phase making up the porous matrix. For example, low surface tension fluids (e.g., n-pentane or n-hexane) tend to spread on nearly any solid material. In contrast, high surface tension fluids (e.g., water) will only spread

on high surface energy solids (e.g., aluminum), and will bead on low surface energy solids (e.g., Teflon®).

Of the available pore volume within the solid matrix, all of the volume is filled with either the wetting phase or the non-wetting phase. The fractional filling of the pore volume by a certain phase is referred to as saturation. Obviously, the definition is subject to some constraints. The sum of the wetting phase saturation and the non-wetting phase saturation must equal unity. Additionally, each type of saturation must be between zero and unity. These constraints are represented in equation form in Eq. (2.1)-(2.3).

$$(0 \le s_w \le 1) = \frac{pore\ volume\ filled\ with\ wetting\ phase}{total\ dry\ pore\ volume} \tag{2.1}$$

$$(0 \le s_{nw} \le 1) = \frac{pore\ volume\ filled\ with\ non\text{-}wetting\ phase}{total\ dry\ pore\ volume} \tag{2.2}$$

$$s_w + s_{nw} = 1 \tag{2.3}$$

Here s_w refers to the saturation of the wetting phase, and s_{nw} refers to the saturation of the non-wetting phase.

Recognizing that the sum of the phase saturations is always unity, it is often simpler to define the term saturation as referring to the phase of greater interest and thus simplify the terminology and nomenclature. In some textbooks [19] the convention is to measure the saturation of the wetting fluid within the porous media (especially for two liquid systems consisting of oil and water). Alternatively, in a system consisting of a liquid and a gas phase, such as the GDL in PEMFCs, the oil/water convention is typically broken and saturation refers to the saturation level of the liquid regardless of its wetting characteristics. This is the pattern which will be held to in this work; saturation will refer to liquid water saturation regardless of whether it is in the context of hydrophobic (water repelling) or hydrophilic (water wetting) media. In equation form this results in:

$$(0 \le s \le 1) = \frac{pore\ volume\ filled\ with\ liquid\ water}{total\ dry\ pore\ volume} \tag{2.4}$$

Local saturation within a porous matrix has been shown to be closely related to local capillary pressure [20] (to be discussed in more detail later). It is common for additional modifications to be made to saturation to improve the accuracy of given capillary pressure-saturation relationships [21]. The most common modification is the process of establishing a *reduced saturation (S)* which is effectively the *total saturation (s)* minus the *irreducible saturation (s_{ir})* which is also sometimes called an *immobile saturation*. The definition of the irreducible saturation is the saturation at which capillary pressure no longer affects saturation. When this point of irreducible saturation is reached it indicates that some of the fluid is still within the medium, but cannot be displaced, i.e. trapped fluid that is not in hydraulic communication with the bulk fluid. Therefore, the trapped fluid is also not at the same pressure as the bulk fluid, and is also not in thermodynamic equilibrium with the bulk [19]. The implication is that after initial saturation, complete desaturation is impossible, and a new reference point for saturation should be set which is the point at which the *reduced saturation* (*S*) is equal to zero rather than the point at which the *total saturation* (*s*) is equal to zero. Reduced saturation can be defined as follows:

$$S = \frac{s - s_{ir}}{1 - s_{ir}} \tag{2.5}$$

and;

$$(0 \le S \le 1) = \frac{pore\ volume\ filled\ with\ mobile\ liquid\ water}{total\ dry\ pore\ volume\ -\ volume\ of\ trapped\ liquid\ water} \tag{2.6}$$

Although this could prove to be an important characteristic in porous media in which significant portions of fluid can be trapped, it is less important in matrices composed mostly of flow pores. It is common practice in the PEMFC literature to either

ignore the irreducible saturation, or to define it as zero. Throughout the remainder of this chapter, the reduced saturation, S, will be the variable of interest even though many of the works discussed have defined $s_{ir} = 0$.

2.1.2 Capillary pressure in porous media

As previously mentioned, there is a relationship which exists between saturation and capillary pressure. Capillary pressure is defined as the pressure difference between fluid phases in a two-phase system. Confusion sometimes arises in much of the fuel cell literature due to an unclear definition and interpretation of capillary pressure between the liquid and the gaseous phases in the system. In order to eliminate confusion from this work, a brief description of how capillary pressure is defined in this work will precede any further discussion of capillary pressure as it pertains to transport in a two-phase system.

In a porous matrix filled with a gas/liquid mixture, there is a pressure difference between the gas and liquid due to the surface properties of the porous matrix. As previously discussed, one phase is the wetting phase, while the other phase is said to be the non-wetting phase. Figure 2.1 illustrates the wetting/non-wetting phenomena. The wetting phase is the phase which tends to wet the pore walls and thus takes on a concave shape at the interface. Conversely, the non-wetting phase takes on a convex shape at the interface. The interaction between the solid surface and the two phases draws the wetting phase up the walls of the pore thus exerting a force on the non-wetting phase and leading to a pressure difference across the two phase boundary where the non-wetting phase is at a pressure greater than the wetting phase. The pressure difference across this interface is commonly called the “capillary pressure”. The convention in textbooks [19] is to define capillary pressure to be the difference between non-wetting phase pressure and the wetting phase pressure. This difference in pressure between the fluids is most evident when the fluids are in static equilibrium. Figure 2.1 is a good illustration of how the wetting characteristics of a pore can induce a hydrostatic head, where the non-wetting

fluid is at a higher pressure than the wetting fluid. In this illustration, the hydrophilic capillary tube is wetted by water and the hydrophobic capillary tube is wetted by air.

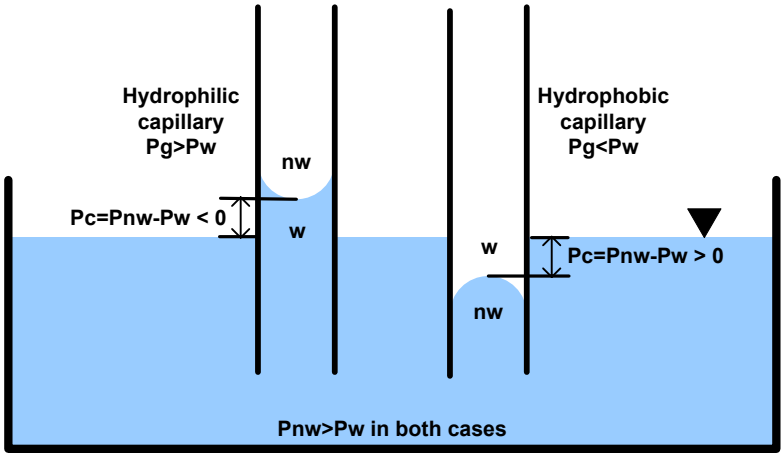

Figure 2.1 – Hydrostatic equilibrium in hydrophobic and hydrophilic capillaries.

Although an illustration of capillary pressure at a fluid-fluid-solid interface which is in static equilibrium is useful for basic understanding, it is less useful in a system where the interface is moving, i.e. there is flow through the pores. Consider the point in time at which the two capillaries in Figure 2.1 were first inserted into the bath of water. At that point, the water moved upward to displace air in the hydrophilic capillary, and air moved downward to displace water in the hydrophobic capillary. The flow stopped in each capillary when the surface tension force pulling the wetting fluid along the capillary wall was equilibrated by the difference in hydrostatic head between the two fluids at the interface. At equilibrium, there is no flow and the water pressure in the hydrophobic capillary is greater than the air pressure in the hydrophobic capillary ($P_{nw}>P_w$, therefore $P_c>0$) by the difference in hydrostatic head between the inside and outside of the capillary.

A different scenario arises if pores similar to those depicted in Figure 2.1 are arranged horizontally yielding negligible gravitational effects. In individual solid wall pores of constant diameter under a negligible gravitational influence, the capillary pressure can be calculated by the Young-Laplace equation [19, 21]:

$$P_c = P_{nw} - P_w = \frac{4\sigma}{d}\cos\theta \tag{2.7}$$

Many of these variables have already been defined with the exception of σ which is the surface tension between the fluid phases, d is the pore diameter, and θ is the contact angle measured from the interior of the wetting phase. Measurement of the contact angle from the interior of the wetting phase always yields a positive value for the *cos* θ term in the capillary pressure expression. Many porous media have mixed (or fractional) wettability, which essentially means that the contact angle can vary from region to region within the porous medium. In such systems, it is more useful to define capillary pressure as the pressure difference between two specific species, rather than the generic definition of the pressure difference between wetting and non-wetting phases. As an example, the capillary pressure in a water-gas system will be described as:

$$P_c = P_g - P_{LW} = \frac{4\sigma}{d}\cos\theta \tag{2.8}$$

In the water-gas system the contact angle is typically measured from the interior of the liquid phase since it is commonly the phase of greater interest (e.g., water droplets on a solid surface). The consequences of the capillary pressure as defined in Eq. (2.8) will be discussed in the context of the pores of differing wettability as displayed in Figure 2.2.

When the contact angles displayed in Figure 2.2 are applied to Eq. (2.8) it can be seen that the capillary pressure can be negative, positive, or zero, depending on the wettability of the pore. For example, the fluid interface in the hydrophobic pore exhibits a liquid water (*LW*) pressure greater than the gas (*g*) pressure (i.e., pressure in excess of the gas pressure must be applied to liquid water to displace gas from a hydrophobic pore). In the case of the hydrophilic pore, the gas pressure must exceed the water pressure to displace the water. The third case represents a pore in which water and gas wet equally well. Therefore, the *LW*-*g* interface in the pore of neutral wettability exhibits no capillary pressure.

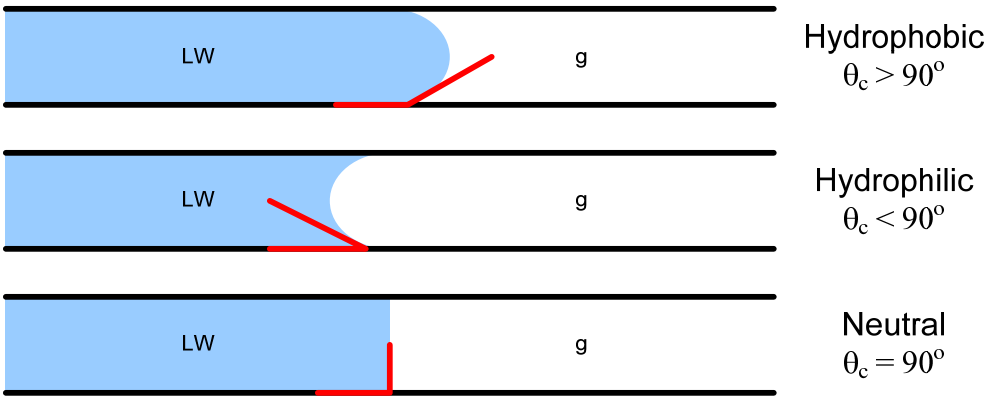

Figure 2.2 – Horizontal pores of differing wettability.

The Hagen-Poiseuille relationship is often used to calculate the velocity profile of steady single phase flows in circular cylinders [22] where:

$$v(r) = \frac{-\Delta P}{4\mu L} R^2 \left[1 - \left(\frac{r}{R} \right)^2 \right] \tag{2.9}$$

Here *v(r)* is the velocity at a given radial location within the cylinder, *ΔP* is the pressure difference along the length of the cylinder, *L* is the length of the cylinder (or the length of fluid contact), *R* is the radius of the cylinder, and μ is the viscosity of the fluid moving through the cylinder. This equation can be applied to laminar flows through cylindrical pores where one fluid (e.g., water) is displacing another fluid (e.g., air) if the *ΔP* term is defined as:

$$-\Delta P = P_c = \frac{2\sigma \cos\theta}{r} \quad \textit{(for horizontal flows)} \tag{2.10}$$

or

$$-\Delta P = P_c - \rho g L = \frac{2\sigma \cos\theta}{r} - \rho g L \quad \textit{(for vertical flows)} \tag{2.11}$$

Substitution of the capillary pressure definitions into the Hagen-Poiseuille equation provides a simple method of modeling the capillary pressure through a pore of known radius at a given mean flow rate. The opposite approach can be taken where the uptake of a given fluid in a porous material can be measured dynamically to solve for the effective pore diameter of the given pore [21]. This method is suitable for individual straight-walled cylindrical pores, and even bundles of cylindrical pores, but does not supply a sufficient description of a porous network of interconnected pores of varying size and shape [21].

A network of interconnected pores of varying size, shape, and wettability adds significant complexity to the modeling of velocity and pressure profiles through the porous matrix. Consider a porous matrix of fractional wettability (e.g., varying degrees of contact angle with the solid phase, $80°<\theta_c<130°$)[†] initially filled with air. The hydrophilic portions of this matrix ($\theta_c<90°$) can be filled with water at pressures slightly below the air pressure ($P_c = P_g - P_{LW}$, therefore $P_c > 0$) in the porous matrix due to the favorable capillary forces pulling water into the matrix. The hydrophobic portions of this matrix ($\theta_c>90°$) are filled with liquid water only if the water pressure is in excess of the air pressure resulting in a negative capillary pressure. The size, shape, and wettability of the pores will govern which portions of the media become more saturated with liquid water. Based on the described sample system of fractional wettability the paths within the porous matrix will become saturated in the following sequence as the applied liquid pressure increases:

I. Paths which exhibit $\theta_c<90°$ and small effective diameter
II. Paths which exhibit $\theta_c<90°$ and large effective diameter, and/or paths which exhibit $\theta_c>90°$ and large effective diameter
III. Paths which exhibit $\theta_c>90°$ and small effective diameter

[†] The range ($80°<\theta_c<130°$) was chosen because it is a range similar to that defined by the minimally hydrophilic carbon fibers in GDL materials and the super-hydrophobic nature of rough PTFE surfaces.

Figure 2.3 illustrates the described phenomena in a porous matrix where Type I, Type II, and Type III refer to the sequence of pore types in the above list.

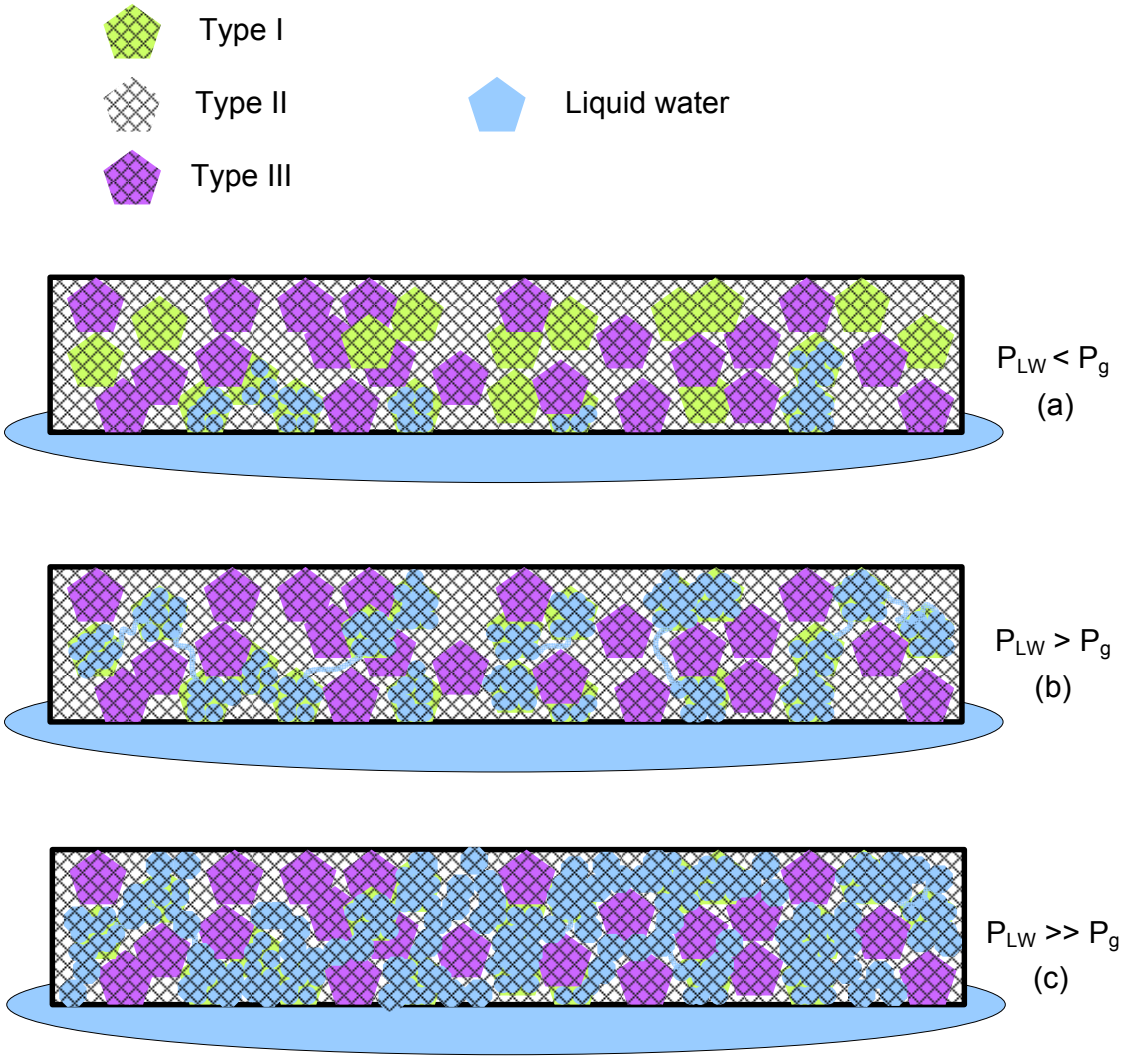

Figure 2.3 – Saturation in a porous matrix of fractional wettability as a function of capillary pressure.

It can be seen here that as the capillary pressure becomes more negative (as P_{LW} increases if P_g is held constant) the porous matrix becomes more saturated with liquid water. When the porous material is initially exposed to liquid water, some water is drawn

into the matrix via capillary forces in the hydrophilic regions of small diameter that have access to the water (a). As water pressure is increased, flow proceeds through some of the hydrophobic sections of sufficiently large effective radii to create flow paths to additional regions of the porous matrix (b). A further increase in water pressure results in nearly all of the hydrophilic regions, and most of the hydrophobic regions of sufficiently large effective radii being filled with water (c). If this process were to continue, nearly the entire porous matrix would eventually be filled with the exception of pores which are not in hydraulic communication with the bulk (S = 1). The relationship between capillary pressure and saturation is presented graphically in Figure 2.4.

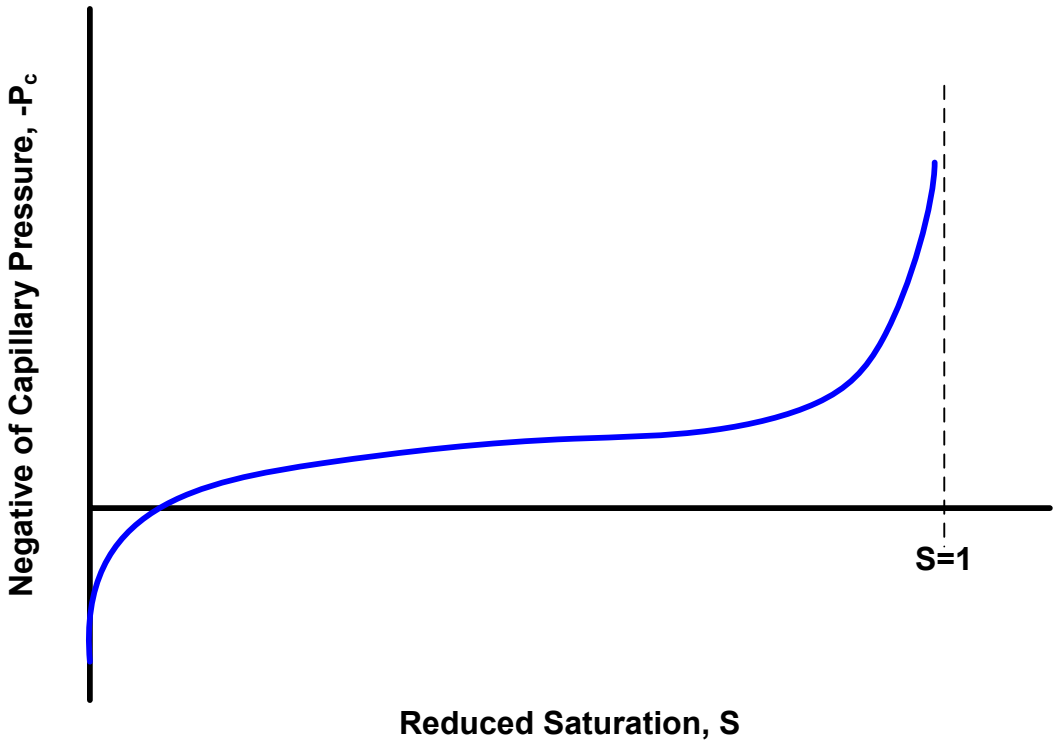

Figure 2.4 – Theoretical P_c – S curve for system described in Figure 2.3.

When the system presented in Figure 2.3 is considered further, it is evident that there is a relationship between saturation and capillary pressure. Although this relationship is illustrated on the entire bulk of the porous matrix it stands to reason that the same principles can be applied at a local level. When the P_c-S relationship is applied

at the local level it implies that the capillary pressure in regions of high gas phase fraction (1-*S*) is greater than the capillary pressure in regions of low gas phase fraction. Similarly, the implication is that the capillary pressure in regions of high liquid phase saturation (*S*) is more negative than it is in regions of lower liquid phase saturation. Much like a single-phase flow in a cylindrical pore flowing from high pressure to low pressure, the gas phase in partially saturated media flows from regions of high capillary pressure to regions of lower capillary pressure, and the liquid phase flows from regions of more negative capillary pressure to regions of less negative capillary pressure[‡]. Extending this thought to saturation shows that each phase wants to move from regions of high saturation (of its own phase) to regions of lower saturation. Therefore, if a proper P_c-S relationship can be applied, then flows in two-phase porous systems can be modeled in a manner that relies on the saturation gradient to be the driving force for the flow.

Using a saturation gradient to model two-phase flow is quite common in textbooks and the PEMFC literature. Assuming laminar flow, Darcy's Law can be modified to accommodate flows driven by saturation gradients. The process of adapting Darcy's Law for two-phase flow begins with defining momentum equations in the Darcean form for each phase individually as presented in Eq. (2.12) and (2.13).

$$u_{LW} = -\frac{\kappa_{LW}}{\mu_{LW}} \frac{dP_{LW}}{dx} \tag{2.12}$$

$$u_g = -\frac{\kappa_g}{\mu_g} \frac{dP_g}{dx} \tag{2.13}$$

Here, the variable u is the velocity in the x direction, κ is the effective permeability of the medium to the fluid of interest, μ is the dynamic viscosity of the fluid, P is the pressure of the fluid, and the subscripts LW and g indicate the liquid water phase and the

[‡] This distinction is due to the choice of using a positive gas phase pressure and a negative liquid phase pressure in the definition of capillary pressure. The end result is the same for both phases: a given phase flows in the direction of its own saturation gradient.

gas phase respectively. Recalling the definition of capillary pressure used previously ($P_c = P_g - P_{LW}$)[§] a substitution can be made where:

$$\frac{dP_c}{dx} = \frac{dP_g}{dx} - \frac{dP_{LW}}{dx} \tag{2.14}$$

Algebraic manipulation of Eq. (2.14) yields an expression that can be substituted into the single-phase momentum equation for liquid water, where:

$$\frac{dP_{LW}}{dx} = \frac{dP_g}{dx} - \frac{dP_c}{dx} \tag{2.15}$$

Substitution of Eq. (2.15) into Eq. (2.12) yields:

$$u_{LW} = -\frac{\kappa_{LW}}{\mu_{LW}}\frac{dP_g}{dx} + \frac{\kappa_{LW}}{\mu_{LW}}\frac{dP_c}{dx} \tag{2.16}$$

The gas pressure gradient in Eq. (2.16) is the term that ties the two momentum equations (gas and liquid) together. The momentum equation for the gas phase can remain in its previously stated form (Eq. (2.13)) to achieve the coupling.

It can be seen in Eq. (2.16) that capillary pressure gradient is now the driving force for the second term on the liquid water momentum equation. However, in a two-phase system it is often more beneficial to keep track of how much liquid water is in a porous matrix than it is to track the pressure of the water. The benefit of saturation tracking is that saturation has a significant impact on gaseous diffusion and therefore the necessary coupling between the liquid water saturation and the gaseous diffusion (to be

[§] This could also be defined as the difference between the liquid water pressure and the gas pressure. There is no particular preference of this definition for media of fractional wettability since the wetting and non-wetting phase can change from location to location. It is, however, very important to stay consistent with the definition of capillary pressure.

discussed in detail later) is more easily achieved when the liquid water momentum equation is built around a saturation gradient instead of a capillary pressure gradient.

Figure 2.4 illustrated a theoretical P_c-S curve. The P_c-S relationship is very valuable now since it is preferred to track saturation through a porous matrix rather than capillary pressure. Taking the derivative of the P_c-S relationship and combining it with a saturation gradient term yields the following momentum equation for liquid water in a two-phase flow porous matrix system:

$$u_{LW} = -\frac{\kappa_{LW}}{\mu_{LW}}\frac{dP_g}{dx} + \frac{\kappa_{LW}}{\mu_{LW}}\frac{dP_c}{dS}\frac{dS}{dx} \tag{2.17}$$

Now, for a system of known P_c-S characteristics and flow field, a saturation field can be calculated throughout a porous matrix. This type of treatment is quite popular in the PEMFC literature and will be discussed further in Section 2.3.

The effective permeability, κ, in each momentum equation is important in two-phase flow systems. The convention ([19, 21]) is to describe the effective permeability of each phase as the product of the *absolute permeability*, K (units of L^2), of the medium, and the *relative permeability*, $k_{r,phase}$ (unitless) of the phase of interest:

$$\kappa_{LW} = Kk_{r,LW} \tag{2.18}$$

$$\kappa_g = Kk_{r,g} \tag{2.19}$$

The relative permeability is highly dependent on saturation and thus must be defined as a function of saturation. Dullien points out that Darcy's Law is only valid for multiphase flow as long as the relative permeabilities at a fixed saturation are independent of pressure gradients. In addition, Dullien [19](pg. 255) cites many references that indicate that this constraint is typically satisfied.

Many transport processes in porous media are heavily dependent on the pore blockage in the media due to saturation. Although this section has focused more on how saturation affects transport due to pressure (or saturation) gradients, saturation also

affects other transport processes. The following section will discuss how saturation, along with other material properties, can effect the diffusion of gaseous species in a porous matrix.

2.2 GASEOUS SPECIES TRANSPORT IN GAS DIFFUSION MEDIA

The gaseous species which are present in the cathode GDL of PEMFCs are typically oxygen, nitrogen, and water vapor, whereas the gaseous species present in the anode GDL are hydrogen and water vapor. When modeling the transport of gaseous species, the more complicated electrode is the cathode. The increased difficulty of cathode gas transport modeling is due to having more gaseous species present, and the production of water at the cathode electrode.

There are two predominant methods by which gaseous diffusion is modeled - binary diffusion using Fick's Law, and multi-component diffusion using the Maxwell-Stefan equations. Both methods of diffusion modeling will be discussed in Section 2.2.1. Additionally, any method of diffusion modeling requires that a value or expression be defined for the ability of a gas to diffuse into each of the other gases in the system. This parameter is commonly referred to as the binary diffusivity when Fick's Law is used, and is referred to as a multicomponent diffusivity when the Maxwell-Stefan equations are used. In a porous media such as the GDL, the values for the diffusivity of each gas must be modified to correct for the effect of the porous structure. The diffusivity of a gas is typically modified by some combination of tortuosity, porosity, permeability, and liquid water saturation. The modifications used in the PEMFC modeling literature will be the topic of Section 2.2.2.

2.2.1 Background

A description of the molecular diffusive flux within a dilute gaseous mixture was first developed by Adolf Fick in 1855. Similar to Fourier's Law pertaining to heat conduction, and Ohm's law pertaining to electron conduction, Fick found that the molar

flux of a species within a gaseous mixture had a linear relationship with the given species concentration gradient. Much like the other laws on which Fick based his theory, a parameter which depended on the nature of the material or substance in which the transfer was taking place was required. Thus, the result of Fick's experimentation is now commonly referred to as Fick's First Law as seen in Eq. (2.20).

$$j_\alpha = -D_{\alpha\beta}\frac{dc_\alpha}{dx} \tag{2.20}$$

In Fick's Law j_α refers to the molecular diffusive flux per unit area of component α, c_α refers to the concentration of component α, and $D_{\alpha\beta}$ refers to the diffusivity of component α in the primary component of the mixture, component β, and x refers to the directional distance of the concentration difference. In general, Fick's Law was developed for dilute binary gas mixtures [23], however it has also been applied to others systems.

As with any transport equation the constant which precedes the gradient is quite important. A variety of methods exist for calculating binary diffusivities, many of them based on the kinetic theory of gases. Other equations which are typically much simpler and have their roots in empirical data also offer sufficiently accurate results for determining binary diffusivities. One such empirical equation was developed by Fuller, Schettler, and Giddings, and can be seen in Eq. (2.21) [24].

$$D_{\alpha\beta} = \frac{10^{-3}T^{1.75}\left(\frac{1}{M_\alpha}+\frac{1}{M_\beta}\right)^{1/2}}{P\left[\left(\sum v\right)_\alpha^{1/3}+\left(\sum v\right)_\beta^{1/3}\right]^2} \tag{2.21}$$

In the above equation $D_{\alpha\beta}$ is the binary diffusivity in units of (cm^2/s), M is the molar mass of the species, T is the temperature of the mixture in units of (K), and P is the pressure of the mixture in units of (atm). The v term is called the diffusion volume and is defined for some simple molecules in Table 2.1.

Table 2.1 – Diffusion volume for common molecules [24].

Simple Molecule	Diffusion Volume (v)
H_2	7.07
N_2	17.9
O_2	16.6
H_2O	12.7

In a binary system the movement of species α is proportional to the negative of the concentration gradient of species α. In multicomponent diffusion other types of species movement may be observed such as: *reverse diffusion* where a species moves against its own concentration gradient; *osmotic diffusion* where a species diffuses even though its concentration gradient is zero, and; *diffusion barrier* where a species does not diffuse even though it has a non-zero concentration gradient. Additionally, the flux of a species in a multicomponent system does not necessarily relate linearly with the concentration gradient of that species [22]. The Maxwell-Stefan equations are a more comprehensive relationship for diffusion in multicomponent flows having both bulk and diffusive fluxes. The Maxwell-Stefan equation is valid for any number of species and allows for interaction among the species rather than assuming each species only interacts with the primary substance in the mixture. The common form of the Maxwell-Stefan equations is [22]:

$$\nabla x_\alpha = -\sum_{\beta=1}^{N} \frac{x_\alpha x_\beta}{\tilde{D}_{\alpha\beta}} \left(\boldsymbol{v}_\alpha - \boldsymbol{v}_\beta \right) \qquad \alpha=1,2,3,...,N \tag{2.22}$$

where x_α is the mole fraction of species α, x_β is the mole fraction of species β where β refers to one of the N components in the gaseous system, $\tilde{D}_{\alpha\beta}$ is the Maxwell-Stefan diffusivity, $\boldsymbol{v}_\beta$ refers to the velocity vector of component β, and $\boldsymbol{v}_\alpha$ is the velocity vector of component α. The Maxwell-Stefan diffusivity, $\tilde{D}_{\alpha\beta}$, is important to use in systems of gases at high density. For low-density gaseous mixtures $\tilde{D}_{\alpha\beta} \cong D_{\alpha\beta}$, and therefore the

binary diffusivity calculated from Eq. (2.21) may be used in the Maxwell-Stefan equations [25].

In gaseous systems of nearly uniform temperature and pressure Eq. (2.22) has been shown to be accurate. Additional driving forces must be accounted for in systems of non-uniform temperature and pressure. For these types of gaseous systems a more complicated diffusive expression must be applied, typically, the *generalized Fick equations* are utilized. For a more detailed discussion of these equations the reader is referred to Bird et al. [22] and Faghri et al. [25].

The use of gaseous diffusion equations is prominent in PEMFC modeling due to the multicomponent gaseous mixtures in the electrodes and gas flow channels. PEMFC electrodes are typically at nearly uniform temperature and pressure and therefore binary diffusivities can be used in the transport equations. Diffusion through the GDL must also account for the porous matrix which interferes and impedes diffusion due to the solid phase. Any governing equation for gaseous diffusion, whether it is the Fick's Law or the Maxwell-Stefan equations, always requires the definition of a diffusivity term among the different gases in the multicomponent gaseous system. For models of partially saturated porous media the gas diffusivities are typically corrected to account for the saturated portions of the porous media (saturated portions reduce the pore volume due to liquid blockage), and for the porosity of the media which again reduces the available volume for diffusion due to the structure of the media. Additionally, a correction for the tortuosity of the diffusion path is also sometimes included in the porosity correction term. Therefore the relationship commonly assumed in PEMFC literature takes the form:

$$D_{\alpha\beta}^{eff} = D_{\alpha\beta} f(\varepsilon, \tau) g(S) \tag{2.23}$$

where $D_{\alpha\beta}^{eff}$ is the *effective* binary diffusivity (or multicomponent diffusivity for systems of nearly uniform temperature and pressure) of species α into species β, $D_{\alpha\beta}$ is the binary mass diffusivity of species α into species β, S is the reduced saturation which was previously defined in Section 2.1, ε is the porosity of the porous media which is included to account for the solid phase impeding diffusion of the gaseous phase and is defined as:

$$\varepsilon = \frac{open\ volume\ of\ porous\ matrix}{total\ volume\ of\ porous\ matrix}$$

Finally, the tortuosity of the diffusion path (τ) accounts for the additional distance of molecular travel due to curvature of the pores and is defined as:

$$\tau = \frac{actual\ distance\ of\ molecular\ diffusion}{apparent\ distance\ of\ molecular\ diffusion}$$

2.2.2 Modeling of gaseous transport in fuel cell gas diffusion media

A solid phase within a gaseous system always impacts the ability of gases to freely diffuse within the mixture. It is obviously necessary to correct gaseous diffusion coefficients for liquid saturation in porous media since the liquid phase blocks diffusive paths within the porous matrix. Much like liquid saturation, the solid phase of the porous matrix can impede diffusion due to its presence. For gaseous diffusion in unsaturated porous media it is common to correct diffusion coefficients for the solid phase of the matrix in one of two ways: 1) mathematically correct diffusivity based solely on an easily measurable parameter such as porosity (ε) and allow this singular correction to account for the volumetric diffusion impedance of the solid phase, and the tortuous impedance of the path the molecules much follow to travel around the solid phase; or 2) correct the diffusivity using two or more terms (often ε and τ) which often involves allowing one of the terms to be tuned to achieve experimental agreement (usually τ since it is difficult to measure). A brief introduction to these two methods will be presented prior to reviewing the diffusivity correction relationships used in the PEMFC literature.

Cunningham et al. [26] discuss diffusivity corrections for porous media and present some relationships which rely solely on porosity to correct the diffusion coefficient for unsaturated media. The system of interest was an isobaric, isothermal gaseous mixture in a porous medium represented by spheres of varying diameters with no external forces acting upon the system. Two different relationships originally proposed

by Neale and Nader, along with a more well known relationship proposed by Bruggeman for the same system, are presented by Cunningham et al. The two relationships proposed by Neale and Nader are:

$$f(\varepsilon) = \frac{2\varepsilon}{(3-\varepsilon)} \tag{2.24}$$

and

$$f(\varepsilon) = \frac{\varepsilon(1+\varepsilon)}{2} \tag{2.25}$$

The diffusivity correction proposed by Bruggeman and presented by Cunningham et al. is:

$$f(\varepsilon) = \varepsilon^{3/2} \tag{2.26}$$

The alternative method of directly accounting for porosity and tortuosity is discussed briefly by Cussler [23]. Cussler notes two diffusion phenomena when presenting the effective diffusivity through porous media. First, Cussler argues that diffusion effectively takes place over a longer distance in a porous matrix than in does in a homogeneous material because the pores are not straight. Second, Cussler attributes a diffusional impedance to the solid phase because it is impermeable and therefore diffusion takes place through a smaller cross-section than it would in a homogeneous field. The diffusivity correction proposed by Cussler is presented in Eq. (2.27).

$$f(\varepsilon) = \frac{\varepsilon}{\tau} \tag{2.27}$$

Additionally, Cussler suggests that the tortuosity typically ranges between two and six, and averages about three. Cussler also claims to have measured tortuosities as large as

ten. Such large values of tortuosity are difficult to justifiy on geometrical arguments alone, thus suggesting that the interaction with the solid phase is more complex than suggested by Eq. (2.27). Cussler also mentions that the tortuosity found for diffusion may vary drastically from the tortuosity found for fluid flow. This again indicates a more complex relationship than is presented.

When comparing the relationships described by Cunningham et al. [26] and Cussler [23], it is clear that any number of relationships could be described to characterize the effects of the solid phase on gaseous diffusion in a porous matrix. Figure 2.5 shows a graphical comparison of the diffusion corrections presented in Eq. (2.25) - (2.27).

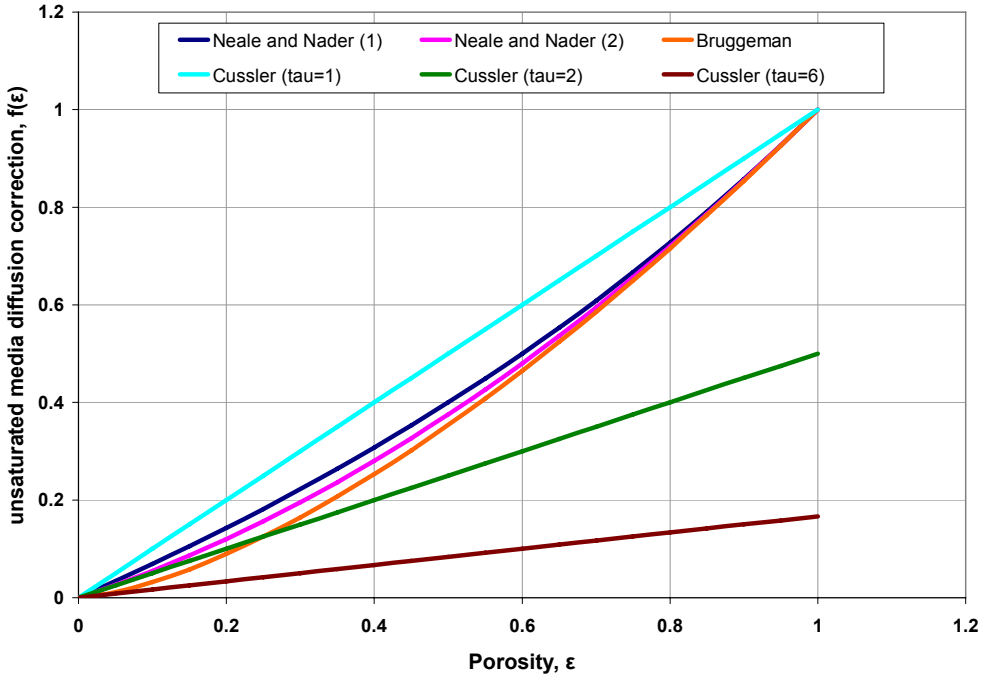

Figure 2.5 – Comparison of unsaturated porous media diffusivity corrections.

It can be seen in Figure 2.5 that there is a drastic difference in the value of $f(\varepsilon)$ when comparing the corrections from Cunningham and the corrections from Cussler using the suggested range of tortuosity, $2< \tau <6$. In order to achieve better agreement between the two schools of thought a value of tortuosity closer to unity must be applied to the correction suggested by Cussler. Figure 2.5 is a good example of the variation in

the porous media literature. Inevitably, this variation has also been transferred into the PEMFC literature. Nearly all diffusivity corrections used in the PEMFC literature are used without justification. The correction is commonly stated in equation form and the focus is quickly shifted to the model results. A variety of works from the PEMFC literature which correct for diffusivity will now be discussed.

One of the only works in the PEMFC literature that discusses a variety of potential diffusivity corrections was authored by Nam et al. in 2003 [10]. Nam et al. suggest a variety of possible forms for the functional relationships for ε and S to correct the mass diffusivity. The effective medium theory has been used to estimate a porosity correction term for spherically packed particles according to:

$$f(\varepsilon) = \varepsilon^{1.5} \tag{2.28}$$

This is the aforementioned Bruggeman correction for porous media.

Additionally Nam et al. reference the work of Mezedur et al. dealing with particle based porous media in catalytic converters. The media in the work of Mezedur et al. consisted of sintered spherical particles with various pore size distributions. In order to model this microstructure the following functional porosity correction was assumed:

$$f(\varepsilon) = [1-(1-\varepsilon)^{0.46}] \tag{2.29}$$

Nam et al. also make reference to work done by Tomadakis et al. who suggest the use of a percolation type correlation for randomly oriented fibrous porous media where:

$$f(\varepsilon) = \varepsilon\left(\frac{\varepsilon-\varepsilon_p}{1-\varepsilon_p}\right)^{\alpha} \tag{2.30}$$

In this correlation ε_p represents the percolation threshold which was found to be 0.11 for porous media composed of two-dimensional, long overlapping random fiber layers.

Additionally, α represents an empirical constant and is found to 0.521 for in-plane diffusion, and 0.785 for through-plane diffusion for the aforementioned porous geometry.

Nam et al. only suggest one functional correlation for the saturation correction which is intended to account for the water saturation reducing the available pathways for gaseous flow, thus creating a more tortuous path for gas diffusion. The function used to approximate the effect of the added diffusion tortuosity is:

$$g(S) = (1-S)^m \tag{2.31}$$

where m is an empirical constant. If the pore structure does not change with saturation and the effective medium theory prediction is assumed then m takes on a value of 1.5. It is also common for m to be determined empirically which was done by Mezedur et al. who determined m to be 0.71 for their catalytic converter model.

Nam et al. produced their own numerical calculations for both diffusion correction correlations. The numerical determination performed by Nam et al. was based on multiple simulations of randomly oriented fibrous mats which are stacked to form a fibrous network of pores. Based on the numerical results for a variety of random orientations Nam et al. chose the following relationship for the porosity correction correlation:

$$f(\varepsilon) = \varepsilon\left(\frac{\varepsilon - 0.11}{1-0.11}\right)^{0.785} \tag{2.32}$$

which is simply the relationship proposed by Tomadakis et al. where $\varepsilon_p = 0.11$, and $\alpha = 0.785$. Additionally, Nam et al. chose to utilize the following correlation for the saturation correction of mass diffusivity:

$$g(S) = (1-S)^2 \tag{2.33}$$

Therefore, Nam et al. chose the following expression for effective mass diffusivity of a species:

$$D_{\alpha\beta}^{eff} = D_{\alpha\beta}\varepsilon\left(\frac{\varepsilon - 0.11}{1 - 0.11}\right)^{0.785}(1-S)^2 \tag{2.34}$$

A full PEMFC model developed by Natarajan et al. in 2001 [16] considered multi-component diffusion in the GDL. As is common among PEMFC models, the diffusivities of the gaseous species in the PEMFC GDL were adjusted to correct for the influence of the porous material. Natarajan et al. argue that the absolute porosity of the material, ε, should be corrected by excluding the pore volume occupied by liquid water prior to applying any correction based on material porosity. Therefore, Natarjan et al. defined a gas porosity, ε_g, which accounts for the volume of pores filled with liquid water as follows:

$$\varepsilon_g = \varepsilon(1-S) \tag{2.35}$$

Following the porosity correction, the Bruggeman correction was applied to the gas porosity rather than the absolute GDL porosity. Therefore, when the overall correction is broken into the functional forms outlined previously, the diffusivity corrections used by Natarajan et al. are as follows:

$$f(\varepsilon) = \varepsilon^{1.5} \tag{2.36}$$

$$g(S) = (1-S)^{1.5} \tag{2.37}$$

Natarajan et al. [16] claim that this correction accounts for the tortuous path of diffusion through the porous structure, and also accounts for the possibility of pore blockage due to liquid water saturation. The complete form of the binary diffusivity correction used by Natarajan et al. is displayed in Eq. (2.38).

$$D_{\alpha\beta}^{eff} = D_{\alpha\beta}\left[\varepsilon(1-S)\right]^{1.5} \tag{2.38}$$

Work published by Lin et al. in 2006 [15] investigated the correction used to modify the diffusion coefficient to be used in the porous and partially saturated structure of the GDL in PEMFCs. Lin et al. chose to use the same correction used by Natarajan et al. which is effectively the well known Bruggeman correction applied to an adjusted GDL porosity due to liquid water saturation. This type of correction can be seen in the preceding discussion of Natarajan et al.'s [16] work. Like many other publications on the PEMFC literature, no justification for the relationships used to modify transport coefficients was given.

A multiphase model in the GDL of PEMFCs was recently developed by Senn et al. [13]. In the model developed by Senn et al. the standard form of providing a porosity correction, and a saturation correction for the diffusion of gaseous species within the GDL was again followed. Senn et al. chose to apply the Bruggeman correction to account for the effects of porosity on mass diffusion by defining:

$$f(\varepsilon) = \varepsilon^{1.5} \tag{2.39}$$

Additionally, Senn et al. chose to estimate the effects of saturation using a quadratic relationship defined as:

$$g(S) = (1 - S)^2 \tag{2.40}$$

Pasaogullari et al. [12, 27] use the same correction used by Natarajan et al. [16] where the Bruggeman correction is applied to the saturation modified porosity as it was in Eq. (2.38).

In another work published by U. Pasaogullari and C.Y. Wang [11], a similar saturation modified porosity relationship is used, but rather than using the standard 1.5 in the exponent for the Bruggeman correction, they choose to use the tortuosity of the GDL, τ, in the exponent. The value used for tortuosity in the gaseous transport model is not included in the publication so it is unknown how much the definition used in this case differs from the work of others.

In 2004, Siegel et al. [17] developed a two-phase model in which the gaseous transport in a PEMFC was modeled. In this work, Siegel et al. chose to modify the diffusivity of gaseous species by including the effects of two GDL material properties, porosity and tortuosity, as well as a modification for liquid water saturation. The resulting relationship for the effective diffusivity of a species can be seen in Eq. (2.41).

$$D_{\alpha\beta}^{eff} = D_{\alpha\beta}\frac{\varepsilon}{\tau}(1-S) \tag{2.41}$$

It can be seen that Siegel et al. chose the following functional forms for their correction functions:

$$f(\varepsilon,\tau) = \frac{\varepsilon}{\tau} \tag{2.42}$$

$$g(S) = (1-S) \tag{2.43}$$

In this case the first modifier is now a function of both porosity and tortuosity, and the second modifier function is simply a linear adjustment with liquid saturation.

There are many relationships used in the existing literature to modify the diffusion coefficients for species diffusing through the porous and partially saturated structure of the GDL in PEMFCs. Table 2.2 summarizes the details of the relationships used in the previously discussed articles in order to adjust the diffusivity of gaseous species in PEMFC models.

Table 2.2 – Summary of diffusivity correction terms.

Reference	*f(ε)*	*g(S)*
Nam et al. 2003 [10]	$\varepsilon\left(\frac{\varepsilon-0.11}{1-0.11}\right)^{0.785}$	$(1-S)^2$
Natarajan et al. 2001 [16]	$\varepsilon^{1.5}$	$(1-S)^{1.5}$
Lin et al. 2006 [15]	$\varepsilon^{1.5}$	$(1-S)^{1.5}$
Senn et al. 2005 [13]	$\varepsilon^{1.5}$	$(1-S)^2$
Pasaogullari et al. 2004, 2005 [12, 27]	$\varepsilon^{1.5}$	$(1-S)^{1.5}$
Pasaogullari et al. 2004 [11]	ε^{τ}	$(1-S)^{\tau}$
Siegel et al. 2004 [17]	$\frac{\varepsilon}{\tau}$	$(1-S)$

2.3 LIQUID WATER TRANSPORT IN THE GAS DIFFUSION LAYER

As previously discussed water vapor is present in the cathode oxidant feed of PEMFCs and is also present as product water due to the electrochemical reaction at the cathode. Invariably, conditions within the cathode such as relative humidity and temperature change, leading to evaporation or condensation of water within the cathode GDL. Many attempts have been made to model evaporation, condensation, and transport of liquid water within the GDL of PEMFCs. The modeling of evaporation and condensation, or the exchange of water between a liquid and a gaseous phase, will be discussed in Section 2.4. This section will deal with the manner in which the movement of liquid water is modeled within the porous GDL of PEMFCs.

There are a few commonalities among nearly all models of liquid water transport in the GDL:

1. The GDL is assumed to be entirely hydrophobic or entirely hydrophilic
2. Liquid water transport is assumed to obey Darcy's Law (or a similar form) where the gradient of capillary pressure is the driving force
3. The capillary pressure is calculated based on an assumed relationship between local capillary pressure and local liquid water saturation of the porous media
4. The permeability coefficient in Darcy's law is assumed to be a function of liquid water saturation

Each of these assumptions is a potential source of inaccuracy in the models which deal with water transport in the GDL of PEMFCs and will be addressed in the following sections.

2.3.1 Background

The modeling of liquid water transport in the GDL of PEMFCs is typically done in one of three ways. The first common method is to separate the conservation equations for the liquid phase from those for the gaseous phase with only source and sink terms linking them together to account for mass exchange among phases when a two phase approach is taken [10, 13-17]. This method is sometimes referred to as the Multi-Fluid Model (MFM) [25]. The second method of liquid water modeling is to lump the mass and momentum of all phases and species into multicomponent mixture conservation equations during the solution process, and subsequently use what is termed the *relative mobility* of each phase to extract the flux of each phase from the solution to the multicomponent conservation equations [12, 18, 27, 28]. This method is commonly referred to as the multiphase mixture model (MMM or M^2 model) [25] and was developed by Wang and Cheng in 1996 [29, 30]. The third approach is to assume that no

liquid water exists in the GDL and that all water is transported through the GDL in the vapor phase [31]. The first two methods will be explained in further detail in Section 2.4.

Regardless of which method is used, whether the liquid water has its own conservation equations or if the liquid water fluxes are calculated after the solution process, a mass flux equation for liquid water is necessary. A convenient form of the momentum equation for liquid water in porous media was presented in Eq. (2.17) and is repeated here as Eq. (2.44) for reasons of clarity.

$$u_{LW} = -\frac{\kappa_{LW}}{\mu_{LW}}\frac{dP_g}{dx} + \frac{\kappa_{LW}}{\mu_{LW}}\frac{dP_c}{dS}\frac{dS}{dx} \tag{2.44}$$

It can be seen from Eq. (2.44) that a constitutive relationship must be established to relate capillary pressure and saturation for this equation to be useful. The determination of the constitutive capillary pressure-saturation relationship in GDL water transport modeling is typically done in one of two ways. The first method is to assume that a relationship established for other types of media and fluids will hold true. The second method is to adjust this relationship until the onset of limiting current predicted by the model closely approximates experimental polarization data. Both methods neglect the physics of the situation and are quite likely to provide inadequate descriptions of the physical characteristics of the system. Improper physical characterization is satisfactory if the purpose of a model is to replicate experimental results, but is unacceptable if the purpose is to predict experimental performance from GDL characteristics.

Significant effort has been applied to the determination of P_c-S in other fields of science, particularly oil recovery. The pioneering work relating capillary pressure to saturation was published in 1941 by M.C. Leverett [20]. Leverett defined what is called a reduced capillary function in the form of:

$$J(S) = \frac{\sqrt{K/\varepsilon}}{\sigma \cos\theta_c} P_c \tag{2.45}$$

where *J(S)* was named the *Leverett J-function* by Rose and Bruce in 1949 [32]. Brown [33] expanded upon Leverett's research by investigating the applicability of the Leverett J-function to a variety of porous cores. Brown found that although the J-function was suitable for characterization of a certain core within the same rock formation, it was not of general applicability. Therefore, if a J-function is used to define the curvature of a P_c-S curve it must be experimentally determined for the specific porous medium of interest.

Although the J-function is only applicable to a specific media, many researchers have used Leverett's data from his air-water system in unconsolidated sand and applied it to other types of media. Udell [34] developed a heat transfer model for multiphase systems in which he applied a polynomial fitted to the imbibition branch of Leverett's P_c-S data. The polynomial form of the Leverett J-function for unconsolidated sand proposed by Udell has found popularity in the PEMFC literature in spite of the fact that it is not related to the actual media that are used in PEMFCs. The Leverett J-function proposed by Udell is:

$$J(S) = \left[1.417(1-S) - 2.120(1-S)^2 + 1.263(1-S)^3\right] \tag{2.46}$$

It is important to note that S here refers to the reduced saturation of the wetting phase. Application of the J(S) polynomial proposed by Udell into the form proposed by Leverett yields a capillary pressure function of:

$$P_c(S) = \frac{\sigma \cos\theta_c}{\sqrt{K/\varepsilon}}\left[1.417(1-S) - 2.120(1-S)^2 + 1.263(1-S)^3\right] \tag{2.47}$$

The following section will detail many of the P_c-S relationships used in the PEMFC literature. Most of the reviewed works use something similar to the polynomial form of the J-function proposed by Udell, while others chose to define their own P_c-S relationships.

2.3.2 Relationship between capillary pressure and saturation

Numerous PEMFC models exist in the literature and many of them include some form of liquid water transport in the GDL of PEMFCs. Each of the models that include liquid transport also includes a special relationship between capillary pressure and saturation. Some include this relationship in derivative form, while others prefer to include it in an explicit form to be differentiated in the modeling software. In this section, capillary pressure is presented as a function of saturation, $P_c = P_c(S)$, although both this form and its derivative are presented and compared for various proposed models at the conclusion of this section.

Natarajan et al. [16] at the University of Kansas developed a two-phase PEMFC model which includes the transport of liquid water through all materials in the PEMFC. Natarajan et al. chose to adjust their $P_c(S)$ relationship until it led to model prediction of polarization behavior that matched experimental results. In terms of selecting solution adjustment parameters for a mathematical model this is a good approach since the $P_c(S)$ relationship can take on an infinite number of values and curvatures, whereas other commonly used solution adjustment parameters have a restricted range of physical meaning (e.g. $0 \le \varepsilon \le 1$). Although allowing the $P_c(S)$ relationship to be adjusted to achieve the desired output is convenient from a mathematical standpoint, it is lacking from a physical standpoint. Nonetheless, the $P_c(S)$ relationship developed by Natarajan et al. allows them to achieve good agreement between their model results and experimental data, and their $P_c(S)$ relationship has been adopted in models elsewhere. The relationship used by Natarajan et al. is actually a first order differential equation as seen in Eq. (2.48), but is displayed in its $P_c = P_c(S)$ form in Eq. (2.49).

$$\frac{dP_c}{dS} = -0.0006401\rho g\left[e^{[-3.7(S-0.494)]} + e^{[3.7(S-0.494)]}\right] \ (Pa) \tag{2.48}$$

$$P_c = 0.000173\rho g\left[e^{[-3.7(S-0.494)]} - e^{[3.7(S-0.494)]} + 21\right] \ (Pa) \tag{2.49}$$

Lin et al. [15] recently published a paper modeling PEMFC species transport which included two-phase flow in the GDL. In Lin et al.'s work they chose to use a linear $P_c(S)$ relationship which yielded good agreement between model and experimental polarization data. The linear $P_c(S)$ relationship is very similar in magnitude to the relationship used by Natarajan et al. The similarity is likely because both works originated at the University of Kansas. The $P_c(S)$ relationship used by Lin et al. can be seen in Eq. (2.50) below.

$$P_c = -22.95S \ (Pa) \tag{2.50}$$

Senn et al. [13] presented a work which focused on the non-isothermal two-phase flow in the GDL of PEMFCs. In the work of Senn et al., the commonly used Leverett J-function [20] in the form proposed by Udell [34] was used to define the curvature of the $P_c(S)$ relationship, while the magnitude of the $P_c(S)$ relationship was determined using a common collection of terms which includes, porosity (ε), permeability (K), surface tension (σ), and contact angle (θ_c). The combination of the magnitude expression and the curvature expression yields the following $P_c(S)$ relationship.

$$P_c = \frac{\sigma \cos\theta_c}{\sqrt{K/\varepsilon}}[1.417S - 2.120S^2 + 1.263S^3] \ (Pa) \tag{2.51}$$

It is important to note here that Senn et al. assumes a hydrophobic GDL which means that water is considered to be non-wetting. It is for this reason that Senn et al. uses S as the independent variable in J-function rather than (1-S) as it was presented in Eq. (2.47). Additionally, based on Senn's assumption that the pores in the GDL were slightly hydrophobic, a contact angle of θ_c = 100° was used. Other parameters in the $P_c(S)$ relationship were defined as follows: surface tension of water, σ = 0.0645 N/m; absolute permeability of the GDL, $K = 2.55\text{x}10^{-13}$ m^2; porosity of the GDL, $\varepsilon = 0.5$.

In 2004 Pasaogullari et al. [12] published a paper which focused on liquid water transport in the GDL of PEMFCs. Pasaogullari et al. allowed for the GDL to be either entirely hydrophobic or hydrophilic. The allowance of the model to function for both

types of diffusion media required a slight modification to the definition of the Leverett J-function. The same basic form used by Senn et al. for the $P_c(S)$ relationship was used by Pasaogullari et al., with the exception that the Leverett J-function could change based on the wetting characteristics of the GDL. The equation used by Pasaogullari et al. for the $P_c(S)$ relationship was:

$$P_c = \frac{\sigma \cos(\theta_c)}{\left(K/\varepsilon\right)^{1/2}} J(S) \ (Pa) \tag{2.52}$$

where $J(S)$ is defined as:

$$J(S) = \begin{cases} 1.417S - 2.120S^2 + 1.263S^3 & for\ \theta_c \geq 90^o \\ 1.417(1-S) - 2.120(1-S)^2 + 1.263(1-S)^3 & for\ \theta_c < 90^o \end{cases} \tag{2.53}$$

Although Pasaogullari et al. allowed for the wetting characteristics to be changed from hydrophobic to hydrophilic they chose a base case scenario which they believed to be representative of a PEMFC. Their base case included the following definitions of parameters: contact angle, θ_c = 110°; surface tension of water, σ = 0.0625 N/m; absolute permeability of the GDL, $K = 6.875 \times 10^{-13}$ m^2; porosity of the GDL, ε = 0.5.

Nam et al. [10] at the University of Michigan developed a one dimensional model that characterizes the flow of liquid water through a GDL, first without a microporous layer (MPL), and second with a MPL. The purpose of Nam's work was to establish the usefulness of the MPL with respect to liquid water transport and saturation within the MPL/GDL combination. The aspect of Nam's model which will be discussed here is the relationship used between capillary pressure and saturation. Nam begins by referencing the commonly used Leverett J-function which defines the curvature of the $P_c(S)$ relationship. Although Nam et al. discuss the Leverett J-function, they instead choose to use a linear approximation of that function at low levels of saturation in the first part of the analysis where no MPL is present. The relationship used by Nam is:

$$P_c = 30,321S \ (Pa) \tag{2.54}$$

Additionally, in the second portion of Nam's work where a macroporous GDL is combined with a microporous layer a different relationship is used in each layer. Equation (2.55) was used to relate pressure to saturation in the macroporous structure, and Eq. (2.56) was used in the microporous layer.

$$P_c = 10,000S \ (Pa) \tag{2.55}$$

$$P_c = 20,000S \ (Pa) \tag{2.56}$$

The choice to alter the capillary pressure saturation relationship in the macroporous structure between the two different analyses (Eqs. (2.54) and (2.55)) is not explained by Nam et al.

In order to summarize the variety of relationships used for the $P_c(S)$ function a graphical representation is implemented in Figure 2.6. It can be seen that the relationships in the existing literature span many orders of magnitude. This great variation further strengthens the argument that these relationships are not grounded in the physical properties of the material, but are instead used out of convenience or as a means to adjust model results.

Referring back to the momentum equation presented in Eq. (2.44) it can be seen that the first derivative of capillary pressure with saturation is what truly drives the flow in porous media. Although it is interesting to see from Figure 2.6 that the magnitude of capillary pressure varies greatly within the literature it is more important to compare the derivative form of capillary pressure with saturation since that is the actual driving force in the momentum equation. This comparison is done graphically in Figure 2.7.

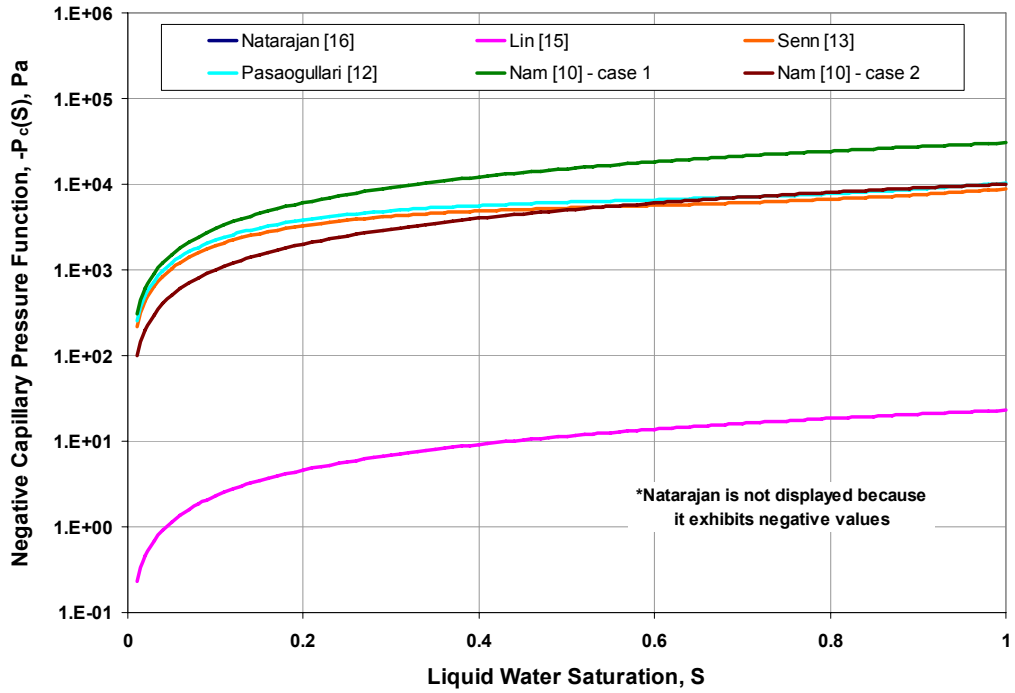

Figure 2.6 – Comparison of capillary pressure functions.

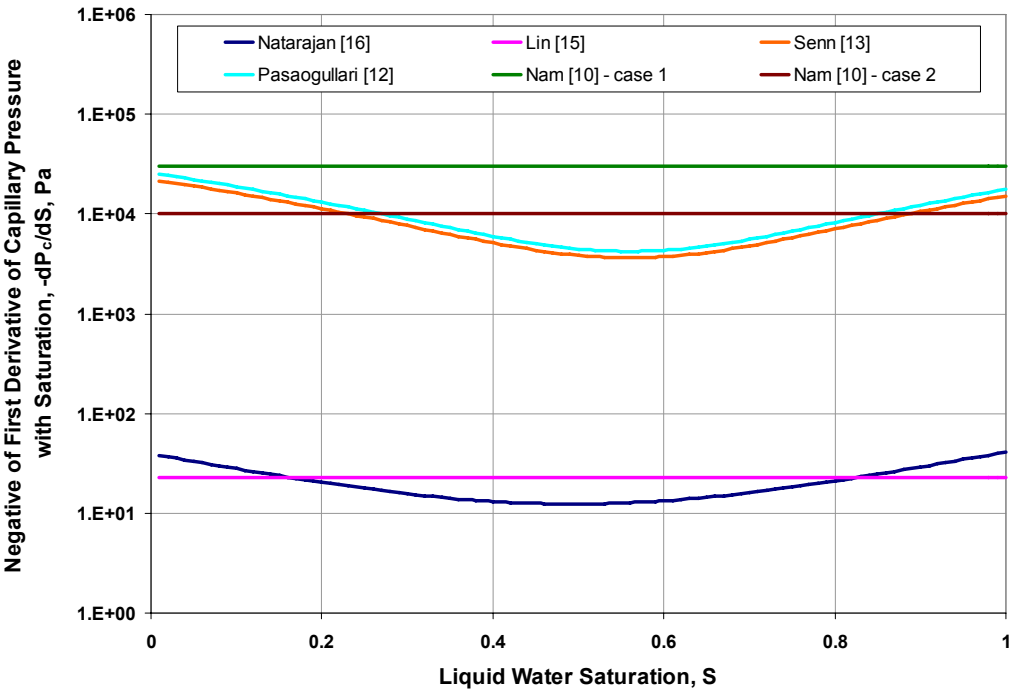

Figure 2.7 - Comparison of capillary pressure-saturation gradient functions.

It can again be seen that there are two trains of thought in the PEMFC literature pertaining to liquid water transport. Many models implement something similar to the Leverett J-function proposed by Udell [34], hoping that the GDL behaves similarly to sand. Conversely, some models utilize capillary pressure-saturation gradients which are tailored to fit experimental PEMFC data.

The momentum equation presented in Eq. (2.44) also relies on an effective permeability for liquid water. Much like capillary pressure, the relative permeability exhibits a dependence on saturation. This will be the topic of the next section.

2.3.3 Liquid water relative permeability function

In two phase porous systems it is necessary to account for the effect that many different variables (e.g., structure of porous matrix, wettability of solid phase, fluid properties, pore blockage) can have on the flow of each phase. When a Darcean approach for transport is used this is usually achieved through the definition of the capillary pressure-saturation relationship and by modifying the permeability term in Darcy's Law as previously discussed in Section 2.1.1. Equations (2.18) and (2.19) displayed the effective permeability for use in the momentum equations for each phase in terms of the liquid water and gaseous phases present in the GDL of PEMFCs. A more general representation of this is shown in Eq. (2.57) where the subscript *i* can refer to any phase of interest. As previously discussed the effective permeability is typically taken to be the product of the absolute permeability of the porous media, and the relative phase permeability for the media as seen in Eq. (2.57),

$$\kappa_i = K k_{r,i} \tag{2.57}$$

where κ_i is the effective phase permeability, K is the absolute Darcy permeability (units of L^2) of the media, and $k_{r,i}$ is the dimensionless relative permeability modifier for the media.

One of the most complete works on fluid transport in porous media is a text by M. Kaviany [21]. Throughout Kaviany's text he refers to the wetting phase as the liquid phase, and the non-wetting phase as the gaseous phase. As previously discussed, the GDL of PEMFCs often exhibits both hydrophilic and hydrophobic pores. Therefore, Kaviany's notation will be modified here to wetting and non-wetting, rather than liquid and gas. Kaviany starts by defining the functionality of the relative phase permeability term as follows:

$$k_{r,i} = k_{r,i}\left(\textit{matrix structures, } S, \sigma, \theta_c, \frac{\rho_w}{\rho_{nw}}, \textit{ history} \right) \tag{2.58}$$

Therefore it is noted that the relative permeability of the medium to fluid *i* depends on the structure of the porous media, the saturation of the media (*S*), the surface tension of fluid *i* (σ), the contact angle of fluid *i* with the solid phase (θ_c), the density (ρ) ratio of the wetting (*w*) and non-wetting (*nw*) fluids, and the history of flow through the media. For a more thorough discussion of the effect of each of these parameters see Kaviany's text [21].

Typically when a parameter depends on so many variables it is simplified to a more manageable expression which captures the most dominant interactions. It has become common practice in porous media literature to assume the relative permeability is a function of saturation only[21]. Therefore:

$$k_{r,w} = k_{r,w}(S) \tag{2.59}$$

and

$$k_{r,nw} = k_{r,nw}(S) \tag{2.60}$$

Over the years numerous empirical correlations for relative permeability have been developed. Kaviany provides a summary of many of these correlations for different

systems, some of which are shown in Table 2.3. Many of these correlations do not distinguish between total saturation *(s)*, and reduced saturation *(S)*. Additionally, Kaviany sticks to the convention in the porous media community of using the term saturation (total or reduced) to refer to the *wetting phase* saturation, whereas the fuel cell literature typically breaks with this convention and uses the term saturation to refer to the *liquid phase* saturation regardless of the wetting characteristics.

Table 2.3 – Relative permeability in various porous systems*.

Porous system	Fluids	$k_{r,w}$	$k_{r,nw}$
Sandstones and Limestones	oil water	S^4	$(1-S)^2(1-S^2)$
Nonconsolidated sand, well sorted	- -	S^3	$(1-S)^3$
Nonconsolidated sand, poorly sorted	- -	$S^{3.5}$	$(1-S)^2(1-S^{1.5})$
Connected sandstone, limestone, and rocks	- -	S^4	$(1-S)^2(1-S^2)$
Sandstone	oil water	S^3	$1-1.11S$
Glass spheres	water water vapor	S^3	$1.2984-1.9832S+0.7432S^2$
Soil	water gas	-	$(1-s_{ir,w}-s_{ir,nw}-s)^{1/2}\left\{(1-s^{1/m})^m-\left[1-(1-s_{ir,w}-s_{ir,nw})^{1/m}\right]^m\right\}^2$

**S is reduced saturation of the wetting phase, s is total saturation, s_{ir} is irreducible saturation*

Prior to discussing specific PEMFC literature a few common variations should be noted. Ideally, two mechanisms of liquid water movement would be captured by a Darcy like momentum equation for liquid water: shear, which accounts for the air velocity dragging the water in the direction of air flow, and capillary forces which drive the water from regions of high saturations to regions of low saturation [14]. The first is often ignored because it is assumed that the gaseous phase does not exhibit a pressure gradient

through the GDL, and therefore is represented as a stagnant bulk with only diffusion moving some species relative to others [10, 13, 15]. For those who assume a constant gas phase pressure, there is no need for a relative permeability of the gaseous phase since there is no pressure gradient to drive bulk gas flow. For those who do consider bulk gas flow, a momentum equation is necessary for the gas phase and therefore a relative permeability must be defined for the gas phase. Additionally, the value used for absolute permeability varies greatly in the PEMFC literature. The values used in the reviewed literature will be presented in this section with the intent of showing the need for reconciliation and validation prior to model development.

Berning et al. [14] chose to use separate momentum equations for the liquid and the gaseous phases within the GDL to include the effects of drag among the phases. They used a simple approach in which the effective permeability for each phase was the product of the absolute permeability of a dry GDL and a relative permeability for each phase that varied linearly with the saturation of the phase of interest. This representation seems to assume that the only effect saturation has is that it reduces permeability via reduction in open pore diameter. This is more easily represented in Eq's. (2.61) and (2.62). Also displayed is Eq. (2.63), which reflects the absolute permeability of the dry media used by Berning et al.

$$K_{r,LW} = S \tag{2.61}$$

$$K_{r,g} = (1 - S) \tag{2.62}$$

$$K_{abs} = 10^{-18}\ \mathrm{m}^2 \tag{2.63}$$

Lin et al. [15] also used a relative permeability in their liquid water momentum equation. Similar to Berning et al. [14], a liquid water relative permeability of $K_{r,LW} = S$ was chosen but no justification was provided. Although the saturation dependence was the same as Berning's [14] work, Lin chose a different absolute permeability of

$K_{abs} = 1.1 \times 10^{-13}$ m^2. Again, no explanation was given for the chosen value of absolute permeability of the GDL in the model developed by Lin et al.

It is not uncommon in the PEMFC modeling literature to assign values to material properties such as relative permeability and absolute permeability without explanation. Numerous models have used the relative permeability relationship for well sorted non-consolidated sand presented in Table 2.3 where $K_{r,w} = S^3$ [10-13, 18, 27, 28]. It is important to notice that Table 2.3 presents the relationship in a form relating the relative permeability of the wetting phase to the saturation of the wetting phase. Nearly all PEMFC modeling papers assume that water is the non-wetting phase, but also present saturation in terms of liquid water saturation rather than wetting phase saturation. Therefore, the relationship for well sorted non-consolidated sand from Table 2.3 can be directly translated to $k_{r,LW} = S^3$ in the PEMFC literature. It is unclear why so many published models have chosen the relationship for a matrix of sand when diffusion media is actually a fibrous media, but nonetheless it has become the predominant relationship used for relative permeability in the PEMFC literature. In addition, most of the models which do not assume a constant gas phase pressure use the companion relationship for well sorted non-consolidated sand where $k_{r,g} = (1-S)^3$.

Although a significant number of PEMFC models use the same expressions for relative phase permeability it is interesting to compare the values used for absolute permeability of the GDL. Nam et al. and Senn et al. [10, 13] used a value of $K = 2.55 \times 10^{-13}$ m^2 and did not provide a reference for this value. The work of Pasaogullari uses three different values for the absolute permeability of the GDL: $K = 6.875 \times 10^{-13}$ m^2 [12], $K = 5.0 \times 10^{-13}$ m^2 [11], and $K = 8.69 \times 10^{-12}$ m^2 [27]. Finally, a value for absolute permeability of $K = 1.0 \times 10^{-11}$ m^2 was used by Wang et al. [28]. The basis (if any) for these values of absolute GDL permeability is given in Table 2.4.

An interesting approach is taken by Natarajan et al. [16] in defining the absolute permeability of the GDL. Rather than using an absolute permeability that is typically measured using air at low to moderate velocities, they choose to define the absolute permeability as an absolute liquid water permeability. The text by Kaviany [21] stipulates

that the absolute permeability be the permeability of the media which would be used in a single phase flow through the porous media. In theory, this value should be the same regardless of the fluid within the Darcean flow regime. If the single phase flow of liquid water does exhibit a different absolute permeability than the single phase flow of gas in PEMFC GDLs then this could be the source of the wide array of absolute permeability's used in the literature. The liquid phase absolute permeability reported and used by Natarajan et al. is $K_{LW} = 7.3 \times 10^{-13}$ m^2. Natarjan et al. also use an unconventional definition for the relative permeability of liquid water. A definition of $k_{r,LW} = (S + 0.01)$ is used, likely to avoid computational difficulty if saturation takes on a value of zero.

To summarize the large number of references discussed in this section, a comparison of the assumptions regarding permeability is provided in Table 2.4. It can be seen that the absolute permeability of the GDL spans seven orders of magnitude in the PEMFC modeling literature. Only two of the referenced works use numbers measured with ex-situ experimentation [16, 27]. Another point of interest is that all of the referenced literature uses either a linear relationship or a cubic relationship between the relative permeability of liquid water and liquid water saturation. Therefore, the values of the compared relative permeability functions should be very similar as $S \rightarrow 1$ or as $S \rightarrow 0$, but will vary greatly for intermediate values of saturation which is the most important region in PEMFC.

Table 2.4 - Summary of permeability's used in PEMFC literature.

Reference	$K(m^2)$		$k_{r,LW}$		$k_{r,g}$	
	value	*basis of use*	*value*	*basis of use*	*value*	*basis of use*
Berning et al. 2003 [14]	$1x10^{-18}$	undocumented assumption	S	reference own previous work	$(1-S)$	reference own previous work
Lin et al. 2006 [15]	$1.1x10^{-13}$	adjusted to fit experimental data	S	undocumented assumption	NA	no gas pressure gradient
Nam et al. 2003 [10]	$2.55x10^{-13}$	undocumented assumption	S^3	reference Kaviany text [21]	NA	no gas pressure gradient
Natarajan et al. 2001 [16]	$7.3x10^{-13}$	reference own previous work	$(S+0.01)$	undocumented assumption	NA	no gas pressure gradient
Senn et al. 2005 [13]	$2.55x10^{-13}$	referenced work of Nam [10]	S^3	referenced work of Nam [10]	NA	no gas pressure gradient
Pasaogullari et al. 2004 [12]	$6.875x10^{-13}$	undocumented assumption	S^3	reference own previous work	$(1-S)^3$	reference own previous work
Pasaogullari et al. 2004 [11]	$5.0x10^{-13}$	undocumented assumption	S^3	undocumented assumption	$(1-S)^3$	undocumented assumption
Pasaogullari et al. 2005 [27]	$8.69x10^{-12}$	experimental (Toray TGPH-120)	S^3	undocumented assumption	$(1-S)^3$	undocumented assumption
Wang et al. 2001 [28]	$1x10^{-11}$	undocumented assumption	S^3	reference own previous work	$(1-S)^3$	reference own previous work

**S refers to reduced liquid water saturation*

2.3.4 Combined effect of liquid water transport relationships

The focus of Section 2.3 has been identifying the variables and constitutive equations which are commonly used in the literature to express the momentum equation for liquid water within the GDL of PEMFCs. Significant variation has been seen in nearly all aspects of liquid water modeling. The capillary pressure functions used in the literature spanned nearly six orders of magnitude and ranged from linear relationships to cubic relationships. The relative permeability of liquid water varied from being linear with liquid water saturation, to being cubic with saturation. Finally, even the absolute permeability of the GDL which is an easily measured material property was assigned values spanning seven orders of magnitude. Each of these variables or constitutive relationships has been discussed as a discrete component, but this evaluation does not present a complete picture since liquid transport is affected by the combination of these factors. Therefore, this section addresses the combined effect of all of the variables and constitutive relationships which are used to govern liquid water flow in the GDL of PEMFCs.

The combined effect of the components of interest in the liquid water momentum equation can be reflected by a group of common variables. Consider the momentum equation presented as Eq. (2.64) where the gas pressure gradient has been neglected.

$$u_{LW} = \frac{Kk_{r,LW}}{\mu}\frac{dP_c}{dS}\frac{dS}{dx} \tag{2.64}$$

The terms preceding the saturation gradient will collectively be termed the liquid water transport coefficient, where in equation form:

$$Liquid\ Water\ Transport\ Coefficient = c_{LWT} = -\frac{Kk_{r,LW}}{\mu}\frac{dP_c}{dS} \tag{2.65}$$

Figure 2.8 provides a graphical comparison of the liquid water transport coefficients used in many of the recent PEMFC two-phase modeling publications.

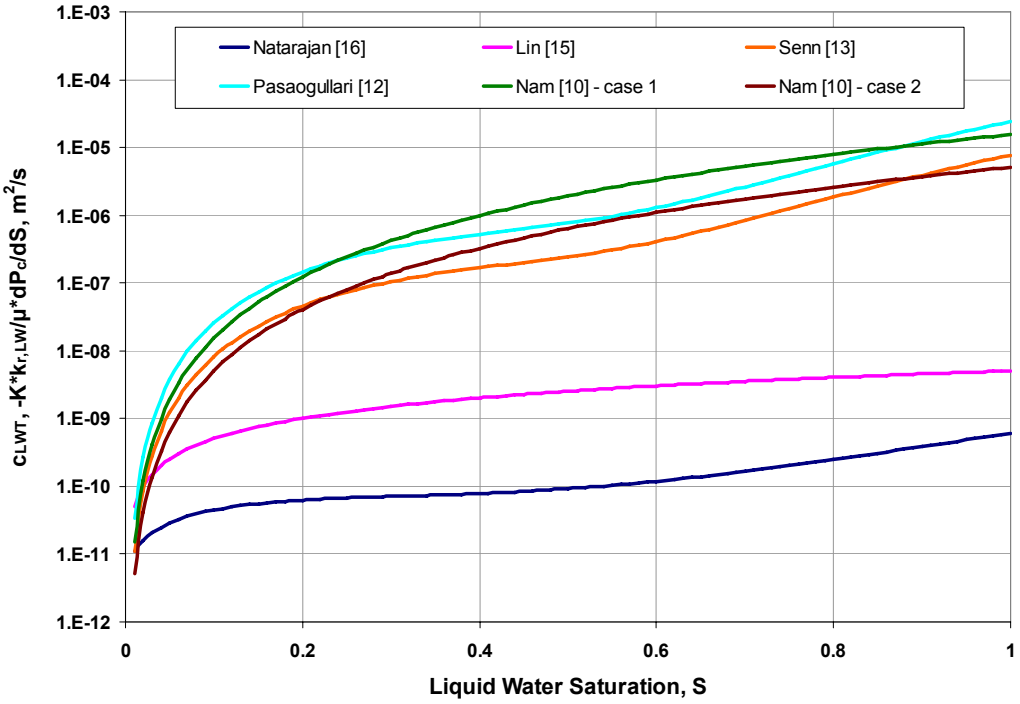

Figure 2.8 – Comparison of liquid water transport coefficient.

Although additional parameters have been incorporated in Figure 2.8 the general shape and trends are similar to the graphical comparisons for the dP_c/dS driving functions plotted in Figure 2.7. It can again be seen that many of the models attempt to characterize the flow of liquid water in the GDL of PEMFCs based on relationships developed for other porous materials such as sand, while others choose to adjust the liquid water flow characteristics to aid in the fitting of experimental data. Each methodology has its own merits but both lack the ability to truly characterize the important characteristics of the GDL since the assumed relationships have never been shown to be applicable to PEMFC GDLs.

The presence and transport of liquid water in the GDL of PEMFCs inevitably leads to the possibility of evaporation and condensation in such a system. Care must be taken to account for this or else the momentum equations for each phase are rendered useless if significant phase change is ignored. Implementation of phase change in the GDL is the topic of the following section.

2.4 TWO PHASE TREATMENT OF WATER

In the GDL of PEMFCs, water can be present in a gaseous phase and in a liquid phase. The preceding sections have discussed methods for modeling the transport of each phase, yet have not discussed the methods for determining the quantity of each phase, or the exchange of mass between the phases. Appropriate modeling of the phase quantities and mass exchange is vital to achieving accurate numerical results for PEMFC performance due to the drastic impact liquid water can have on performance.

Ideally, all of the water within the GDL of a PEMFC would remain as vapor to eliminate the possibility of electrode flooding. This is possible when operating at low current since water production varies linearly with current. At higher currents or with changes in temperature, the gas within the GDL will generally become saturated and water will condense, thus filling available pore volume and reducing the available paths for oxidant diffusion. When condensed water is present it becomes vital to model the transport of the liquid water out of the GDL.

Different techniques exist to model two-phase flow in porous media. Of the two predominant methods in the PEMFC literature, one technique applies momentum conservation to the entire two-phase mixture (M^2 model), while the other technique (MFM) applies momentum conservation to each phase individually. These two methods will be discussed in the following section as a precursor to the discussion of the transfer of mass between the phases. The techniques for quantifying the exchange of mass among phases for each method will be the topic of the remainder of this section.

2.4.1 Background

In a two-phase system, one of two methods can be employed to account for the liquid and gaseous phases moving in the system. The first common method is to use the previously mentioned multicomponent mixture model (MMM or M^2 model). The M^2 method uses a single conservation equation for the flow of the entire two-phase mixture with the interaction of phases captured by advective correction factors which modify velocity according to the phase of interest. These advective correction factors also depend on the definition of the mobility of each phase which is a function of viscosity and relative permeability. Finally, an equilibrium condition must be present to define the relative volumes of each phase prior to fully solving the mixture equations and establishing the individual velocities of each phase.

The second method of two-phase modeling involves tracking each phase individually. In its purest form the multi-fluid modeling (MFM) method would include momentum conservation equations for both the liquid and the gas phases. A common simplification to this method is the application of the unsaturated flow theory (UFT) assumption [25, 27]. The UFT assumption simply assumes that the pressure gradients in the gas phase are extremely small relative to the liquid phase and can therefore be neglected. The advantage of assuming a constant gas phase pressure is the elimination of the momentum equation for the gaseous phase, and simplification of the liquid phase momentum equation. The obvious disadvantage is that assuming a constant gas phase pressure could be a source of error in a model since a gas pressure gradient of zero is

unlikely in a partially saturated porous matrix, especially if all three dimensions are considered. One of the consequences of such an assumption on PEMFC operation would be the elimination of oxygen transport via convection which could represent itself by under-predicting oxygen concentration at the cathode catalyst layer. Another consequence would be that the rate of liquid transport may be over-predicted since the elimination of the gas pressure gradient neglects the drag of the gas phase on the liquid phase.

Regardless of whether the UFT assumption should be used, it commonly is used. Perhaps the most significant reason for the UFT assumption is to reduce computation time and power requirements during the solution process since it eliminates a momentum conservation equation.

There are many comparisons that can be made between the MFM and M^2 techniques such as the number of governing equations required, and the computation time required to solve the system of equations. Such comparisons are beyond the scope of this work and the reader is referred to the text by Faghri (p. 301) [25].

Another comparison which can be made between the MFM and M^2 techniques is the computational results. Pasaogullari et al. [27] investigate the difference in computational results between the M^2 approach and the MFM approach when UFT is applied. The model presented by Pasaogullari et al. claims that the pressure drop in the gas phase through the thickness of the GDL is approximately 30 Pa. Additionally it is claimed that the gas flow counter to the liquid water flow enhances transport of oxygen via convection and improves performance due to a greater oxygen concentration at the catalyst layer. This effect is considered to be most important at high current densities since oxygen concentration is crucial in this region of operation in PEMFCs.

2.4.2 Modeling of two-phase flow

Several published works use the M^2 model in which a single momentum conservation equation is written for a two phase system and then the individual phase velocities are determined based on results from the single momentum equation and

advective correction factors for each phase [11, 12, 18, 27, 28]. These advective correction terms are coupled together by an equilibrium condition which defines the relative volume of each phase within the control volume of interest. The key to phase change within this type of model is definition of the equilibrium condition. It is convenient for the equilibrium variable to be liquid water saturation in the GDL. The equilibrium condition for all PEMFC modeling literature which uses the M^2 model is as follows:

$$S = \frac{C^{H_2O} - C_g^{H_2O}}{C_{LW} - C_g^{H_2O}} \tag{2.66}$$

where S is the local liquid water saturation, C^{H_2O} is the local concentration of total water, $C_g^{H_2O}$ is the local concentration of water vapor (assumed to be saturated), and C_{LW} is the actual physical concentration of liquid water defined as the quotient of the density of liquid water and the molecular weight of water. It is noteworthy that this type of formulation does not allow for rate limited exchange among the phases and assumes local thermodynamic equilibrium among the phases. Application of this limitation provides a clearer representation of Eq. (2.66) presented as Eq. (2.67).

$$S = \frac{concentration\ of\ liquid\ in\ given\ control\ volume}{physical\ concentration\ of\ liquid\ water} \tag{2.67}$$

Additionally, the M^2 formulation requires many more relationships to define the properties of the two phase mixture based upon the properties of the individual phases (e.g., mixture density, and mixture viscosity). The complexities of multi-component mixture modeling in PEMFCs can be seen in the previously referenced publications and will not be discussed in great detail herein.

While the M^2 model approach is not uncommon, the predominant method of two phase modeling in the PEMFC literature is to track the phases individually while applying rate equations to govern the exchange between phases. Models which apply this

method of phase tracking depend on volumetric source and/or sink terms to be included in the conservation equations to account for mass exchange among phases. Some models of this type utilize the UFT assumption of zero gas pressure gradient [10, 13, 15, 16], while others do not [14, 17]. Additionally, some models assume that phase exchange only occurs in one direction (i.e. condensation occurs, but evaporation does not) [10, 13], while others allow for bi-directional exchange of mass [14-17]. Another factor that can significantly impact phase change is whether the GDL domain is considered to be isothermal. This is important due to the significant dependence of water saturation pressure on temperature. Some of the PEMFC models choose to make the isothermal assumption [15, 16], while others do not [10, 13, 14, 17].

In 2003 Nam et al. [10] published a paper which focused exclusively on the one dimensional transport of both water vapor and liquid water within the GDL of a PEMFC. Nam et al. begins by assuming a constant gas phase pressure, thus simplifying the system of equations. Additionally, Nam et al. assumes that all water is produced in the vapor phase and will condense in a rate-limited fashion when the partial pressure of the water vapor is at or above the saturation pressure of water. The preference for rate limited (non-equilibrium) condensation of water is due to Nam's belief that the water vapor would only condense on an area of imperfection in the hydrophobic treatment of the GDL, or only where liquid water was already present within the porous structure. Evaporation is neglected in Nam's model because it is assumed that the cell is operating at high current density and therefore high levels of saturation in the GDL, thus resulting in a saturated gas mixture within the cathode GDL. The condensation equation used by Nam et al. is displayed in Eq. (2.68).

$$VS_{LW} = \gamma M_{H_2O} \frac{p_{g,H_2O} - p^{sat}_{H_2O}(T)}{R_u T} \tag{2.68}$$

In the condensation rate equation used by Nam et al. VS_{LW} is the volumetric source term for liquid water in the mass conservation equation (dimensions are M/L^3/t), γ is the condensation rate constant (1/t), M_{H_2O} is the molar mass of water, p_{g,H_2O} is the local

partial pressure of the water vapor in the gas phase, $p_{H_2O}^{sat}(T)$ is the saturation pressure of water at the local temperature, R_u is the universal gas constant, and T is the local absolute temperature. It is clear here that the driving force for condensation is the difference between the partial pressure of water vapor and the local water saturation pressure. Additionally, Nam et al. define the condensation rate constant as:

$$\gamma = 0.9\frac{A_{lg}}{V} \tag{2.69}$$

where A_{lg} is the interfacial area of liquid and gas, and V is the volume of interest (the gas filled volume). In the rate constant relationship the coefficient of 0.9 was determined using kinetic theory and the fractional term (A_{lg}/V) was left variable to investigate its effect. Nam et al. argue that greater interfacial area results in very high condensation rates because this would indicate that the existing liquid water is spread as a thin film. Therefore, as the quotient of interfacial area and unit volume increases, the condensation approaches thermodynamic equilibrium. In the base case scenario Nam et al. chose A_{lg}/V =1000 m^2/m^3, which results in a condensation rate constant less than what is required for equilibrium.

Work done by Siegel et al. [17] assumes the product water is produced in the vapor phase, but has an active source/sink term to control evaporation and condensation over the entire domain. Rather than assume a rate limited phase change process (as was done by Nam et al.), Siegel et al. assume equilibrium between liquid and vapor phases but impose restrictions to insure that evaporation and condensation take place under the appropriate conditions. These restrictions are incorporated into the source/sink term used by Siegel which is presented in Eq. (2.70).

$$VS_{LV} = \psi_{LV}\gamma S - \gamma(1-S)(1-\psi_{LV}) \tag{2.70}$$

In Eq. (2.70), VS_{LV} is the volumetric source for the formation of water vapor from liquid water, and also the volumetric sink for the opposite phase change direction. The first term

on the right side reflects evaporation which can occur if liquid water is present (S>0) and if the gas is not saturated as indicated by the switch functions ψ_{LV} which takes on a value of unity if relative humidity is less than 98% and a value of zero for all other conditions[**]. The second term on the right reflects condensation which can occur if vapor is present (S<1) and if the gas is saturated (ψ_{LV} = 0). The coefficient for mass transfer among phases, γ (M/L^3/t), was adjusted to be sufficiently large to achieve equilibrium. Siegel et al. used a similar technique to allow the product water to switch into a dissolved phase within the polymer electrolyte. The main focus of this section is the GDL in which there is no dissolved phase so no further discussion will be provided.

In two different publications from the University of Kansas, Natarajan et al. [16] and Lin et al. [15], present isothermal models which include phase change effects in the GDL of PEMFCs. These models assume that the product water is liquid and allow for evaporation anywhere the partial pressure of the water vapor in the gas phase is less than the saturation pressure. Additionally, condensation is allowed if the partial pressure of the water vapor in the gas phase is greater than the saturation pressure. The driving force used to drive the phase change is a combination of saturation and the difference between the water vapor pressure and the saturation pressure. Eq. (2.71) shows the full source/sink expression used.

$$VS_{LV} = \left[\frac{k_e \varepsilon_0 S \rho_w}{M_w}\left(p_g^{sat} - p_g^{wv}\right)\right]\psi - \left[k_c \varepsilon_0 (1-S) x_w \left(p_g^{wv} - p_g^{sat}\right)\right](1-\psi) \qquad (2.71)$$

Here the first term governs evaporation, the second term governs condensation, and the switch function, ψ, turns the appropriate term on or off. All symbols are the same as used by Siegel et al., where the newly introduced terms are defined as follows: k_e is the evaporation rate constant, k_c is the condensation rate constant, ε_0 is the total porosity of the GDL, ρ_w is the density of liquid water, M_w is the molar mass of water, and x_w is the

[**] Siegel et al. chose to use a switch function that uses a hyperbolic tangent function rather than a step function to soften the numerical consequences of a step function.

mole fraction of water vapor in the local gas mixture. The rate constants were given fixed values and it was not clear if these values resulted in a rate limited scenario or if they were sufficiently large to achieve equilibrium. The switch function used is only capable of taking on two values, either -1 or 1, where the negative value turns on the evaporation term and turns off the condensation term, while the positive value does the opposite. Additionally, inclusion of the liquid saturation in the first term stops evaporation if there is no liquid water, while inclusion of the gas fraction (1-*S*) precludes condensation if the pore is already flooded. The switch function used by Natarajan et al. and Lin et al. is displayed in Eq. (2.72).

$$\psi = \frac{1 + \frac{\left| p_g^{sat} - p_g^w \right|}{\left(p_g^{sat} - p_g^w \right)}}{2} \tag{2.72}$$

Work published by Senn et al. presented a non-isothermal GDL model that ignores evaporation due to the assumption that product water is in the vapor phase and only condenses when the local gas phase is saturated. Similar to Nam et al., Senn et al. assume that condensation occurs in a rate limited fashion. Rather than using the difference in water vapor pressure and saturation pressure at the local conditions as the driving force as Nam et al. did, they instead assume that the condensation in the GDL occurs according to a classical condensation scenario. The condensation rate equation used is based on a relationship derived for a condensable vapor flowing under steady state conditions through a stagnant film of non-condensable gas where it then condenses on a cold flat plate [22]. This type of condensation occurs at a rate that is logarithmically related to the molar concentration of water in the gas Eq. (2.73).

$$VS_{VL} = c\gamma \ln\left(\frac{1 - x_{H_2O}^{sat}}{1 - x_{H_2O}} \right) \tag{2.73}$$

In the condensation equation used by Senn et al., c is the total molar concentration of the gaseous mixture, where $c = 35.1\ {}^{mol}/_{m^3}$, x refers to the mole fraction, and γ is the condensation rate constant and is prescribed a value of $\gamma = 900\ {}^{1}/_{s}$.

Two of the four works discussed assumed that phase change only occurred via condensation and that evaporation was negligible [10, 13]. Both of these works chose to use a rate limited form of condensation rather than allowing for equilibrium between the phases. It is reasonably simple to implement rate limited phase change when it is assumed that the GDL is always partially saturated with liquid water as was done by Senn et al. [13] and Nam et al. [10]. However, it is more difficult to include non-equilibrium effects when the possibility of a totally dry, or a totally saturated GDL are not neglected.

Allowing for evaporation and condensation requires a switch function to set the local relative humidity condition which is the threshold around which each type of phase change can occur. Additionally, one of the two modes of phase change is impossible at each extreme of local GDL saturation, i.e., if the GDL is totally saturated no condensation can occur (because there is no vapor), and if the GDL is totally dry no evaporation can occur (because there is no liquid). Natarajan et al. [16] and Lin et al. [15] chose to account for this latter effect by including an S term in their evaporation rate equation, and a (1-S) term in their condensation rate equation. The inclusion of these terms essentially turns off evaporation if S=0 and turns off condensation if S=1. Although it is essential to account for the possibility of S=0 or S=1, the inclusion of saturation as a multiplier in the rate equations implies a linear relationship between saturation and rate of phase change that may or may not be physically justified. For example, if the interfacial area varies linearly with saturation (liquid exists as a thin film) and all phase change occurs at this interface, then the rate constant could be interpreted as the area specific rate of phase change with multiplication by S accounting for the variation in area. On the other hand, this argument would clearly be less applicable for condensation which could occur on an unwetted surface and also less applicable when the liquid exists in a three dimensional volume in which surface area is not linearly related to saturation. An alternate approach is to recognize the relatively high surface area within a porous matrix and assume that the large area over which phase change can occur leads to kinetics which

approach equilibrium behavior. In this approach, adopted by Siegel, the magnitude of the rate constants for phase change are no longer important as long as the rates are sufficiently large to achieve equilibrium. If the rate constants used are sufficiently large for equilibrium then the *S* and (1-*S*) terms can be included in the evaporation and condensation terms respectively, without affecting the equilibrium condition except in the limit as S approaches 1 or 0.

2.5 POROUS MEDIA CHARACTERIZATION

The characterization of constitutive relationships for water transport in gas diffusion media of PEMFCs has been very limited. The previous sections have outlined many of the commonly assumed constitutive relationships which are used to model water transport, both liquid and vapor, in the GDL. In the existing PEMFC literature, very few attempts have been made to characterize the actual transport properties of GDL material. The characterization which has been published along with works from other fields of science will be discussed in this section. Variations of some of the methods discussed here are utilized in this work for PEMFC GDL characterization and will be described in more detail in Chapter 3.

2.5.1 Porosimetry

Porosimetry is a method by which the porosity of a material as well as the volume of pores filled at a given capillary pressure can be determined. Two methods of porosimetry will be discussed here: intrusion porosimetry, and contact porosimetry. Prior to discussion of the porosimetry techniques a simple method for determining total porosity will also be described.

Mathias et al. [35] describe a simple method for determination of total porosity of PEMFC gas diffusion materials. If the thickness and mass of a GDL sample are known, along with the density of the different solid phases within the sample (e.g., 75% carbon fiber, 25% PTFE) then a simple calculation can be performed to determine the pore

volume within the porous structure. First, a volume of the solid phase is calculated based on the material properties according to Eq. (2.74).

$$V_{solid} = \frac{m_{solid}}{(\%PTFE)\rho_{PTFE} + (1-\%PTFE)\rho_{carbon}} \tag{2.74}$$

In Eq. (2.74) V_{solid} is the volume of the solid phase within the porous structure, m_{solid} is the mass of the solid phase, ρ is the mass density of the given solid material, and *%PTFE* is the mass fraction of PTFE in the GDL material. Following the determination of the volume of the solid phase, porosity is calculated using Eq. (2.75).

$$\varepsilon_o = \frac{1-V_{solid}}{At_o} \tag{2.75}$$

In Eq. (2.75) A is the area of the GDL specimen, t_o is the uncompressed thickness, and ε_o is the porosity of the uncompressed GDL specimen. Reliable results for total porosity with this method are questionable due to the difficulty of determining an appropriate material thickness on which to base the calculation.

Intrusion porosimetry is a method where a non-wetting fluid is pressurized incrementally in order to displace a wetting fluid (or a vacuum) in a porous matrix. The most common liquid used for such experiments is mercury because it is a non-wetting fluid regardless of the porous substrate due to its extremely high surface tension. It is common in mercury intrusion porosimetry (MIP) to apply the Young-Laplace equation [36] to relate the capillary pressure to a pore diameter based on the surface tension of the non-wetting fluid and the contact angle within the pores according to:

$$d_{pore} = \frac{4\sigma_{Hg-air}\cos\theta_{Hg-air}}{P_{c,Hg-air}} \tag{2.76}$$

In the Young-Laplace equation d_{pore} is the calculated pore diameter, $\sigma_{Hg\text{-}air}$ is the surface tension of the mercury-air interface, $\theta_{Hg\text{-}air}$ is the contact angle at the mercury-air

interface, and $P_{c,Hg\text{-}air}$ is the capillary pressure across a mercury-air interface. When MIP is performed in a vacuum $P_{c,Hg\text{-}air}$ is simply the pressure of the intruded mercury. The Young-Laplace equation is based on an assumption of straight cylindrical pores with constant contact angle. It is therefore only applicable in porous systems that are representative of such a geometry. Mathias et al. [35] notes that the problem with the application of MIP and the Young-Laplace equation to GDL materials is that such materials are an interconnected porous network with a vast array of pore types (e.g., through pores, or closed pores) rather than a discrete system of cylindrical pores. Oftentimes, pore volume is plotted versus pore diameter for MIP experiments even for materials comprised of non-discrete cylindrical pores. Although the pore diameters calculated via the Young-Laplace equation are of qualitative interest, they are in no way quantitatively accurate. Nonetheless, many researchers still prefer to present porosimetry data for materials exhibiting an interconnected porous network in terms of pore diameters.

Intrusion porosimetry has also been performed using fluids other than mercury. Work done by Jena et al. [37] used water as the intrusion fluid for PEMFC GDLs. Jena et al. argue that the water will spontaneously fill hydrophilic pores and the water intrusion process will only yield results for the hydrophobic pores within the GDL structure. The results presented by Jena et al. indicate that some fuel cell GDL materials exhibit pore distributions in which 25-50% of the pore volume is composed of hydrophobic pores [37, 38].

Mercury is an ideal fluid for intrusion porosimetry because it is known to be non-wetting on all types of surface and because intrusion can be performed in a vacuum since the vapor pressure of mercury is very nearly 0 psia. Unfortunately, problems arise when trying to perform porosimetry in a vacuum with fluids other than mercury as was done by Jena et al. [37], with water as the intrusion fluid. When water is used as the intrusion fluid, the sample chamber is never truly evacuated due to the fairly high vapor pressure of water at ambient temperature. Therefore, the evaporation of water can cause gas to be trapped as intrusion occurs from all sides of the media and result in pockets of water vapor within the media until pressure exceeds the saturation pressure. This makes it impossible to determine the capillary pressure behavior at low pressures. Additionally,

the potential for evaporation of water makes it difficult for reliable intrusion volumes to be measured. Furthermore, the reliance of the Young-Laplace equation on the contact angle inside the pores can be troublesome when fluids other than the highly non-wetting mercury are used. For materials of fractional wettability, such as gas diffusion materials, the contact angle is rarely, if ever, constant. Mathias et al. [35] report sessile drop contact angles of water on Toray carbon paper GDLs with varying levels of bulk PTFE treatment of: 135° (0% PTFE), 156° (9% PTFE), and 164° (23% PTFE). Obviously, reporting pore diameters for water intrusion porosimetry experiments is even less meaningful than diameters reported for mercury intrusion porosimetry since water will exhibit a vast range of contact angles throughout the media.

Another method of intrusion porosimetry that relies on the displacement of gas during liquid water imbibition has recently been reported by Nguyen et al. [39, 40]. A schematic of the experimental method is presented in Figure 2.9.

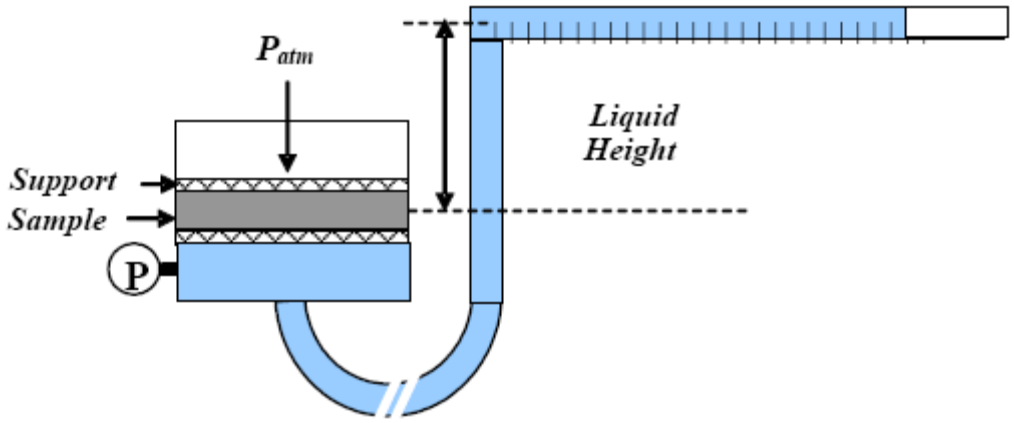

Figure 2.9 – Experimental apparatus developed by Nguyen et al. [40].

The water pressure can be changed by changing the height of the water reservoir, while the transducer connected to the liquid chamber on the underside of the sample holder monitors the pressure. Additionally, the volume of water imbibition is monitored via the graduations on the fluid reservoir. Early results using this method suggested that a sample of Sigracet® 10BA GDL exhibited hydrophobic behavior and reached a saturation of approximately 35% when the liquid pressure was 1000 Pa greater than the air pressure

[39]. However, later results suggest that the same material may exhibit positive and negative capillary pressures with subsequent imbibition and drainage [40]. Further work by Nguyen et al. presents the capillary behavior for a catalyst layer where saturation was measured via neutron radiography [41].

Fairweather et al. [42] recently proposed another intrusion porosimetry technique developed for thin porous materials. This method utilizes stepwise intrusion of liquid water from a syringe pump into a three layer sample comprised of a hydrophilic ceramic, the GDL specimen, and a hydrophobic membrane. The purpose of the hydrophilic ceramic layer on the underside of the GDL is to distribute water over the entire face of the GDL. The purpose of the hydrophobic upper layer is to discourage the flow-through of the liquid water, yet still allow for the displacement of the gas within the porous structure of the GDL. Results presented in a later work by Fairweather [43] suggest that Toray 090 carbon paper exhibits a hydrophilic pore volume of approximately 25% during liquid intrusion. The implications of the hydrophilic ceramic on the underside of the GDL specimen are unclear. It seems as though it may be difficult to distinguish between the filling of the ceramic layer and the filling of the GDL.

Contact porosimetry is a method by which a porous specimen is sandwiched between two calibrated porous plates of known P_c-S characteristics, followed by injection of a wetting fluid into the sandwiched system. The theory of this technique follows the logic that all three materials (2 calibration plates of known capillary behavior and the specimen of interest) will reach capillary pressure equilibrium over a long period of time, at which time the capillary pressure in all three samples will be equal. Following equilibration of capillary pressure the mass of one of the calibrated plates can be measured yielding the saturation of the calibrated specimen. Since the calibrated plate has a known P_c-S relationship the capillary pressure within the calibrated material can be known. Additionally, the mass of the second calibrated plate can be measured in order to assure that equilibrium has been reached throughout the sandwich. Finally, the mass of the specimen of interest can be measured to arrive at its level of saturation. Knowing the saturation of the specimen of interest, and the saturation of the calibrated plates (and therefore the capillary pressure within the calibrated plates) the assumption of capillary pressure equilibrium can be applied to get a single point on the P_c-S curve for the

specimen of interest [44]. A limitation of this method is that the experiment is limited to wetting fluids being used as the working fluid because it relies on wicking action through the sandwiched system to achieve capillary equilibrium.

Contact porosimetry has been applied by Gostick et al. [36] to PEMFC GDL materials. Gostick et al. used a totally wetting low surface tension fluid (octane) to characterize the behavior of all pore types within the GDL. Gostick et al. used Eq. (2.77) to compare MIP results to the contact porosimetry results using octane and good agreement was verified.

$$P_{c,Hg-air} = \frac{\sigma_{Hg-air}\cos\theta_{Hg-air}}{\sigma_{octane-air}\cos\theta_{octane-air}} P_{c,octane\text{-}air} \tag{2.77}$$

It is appropriate to use Eq. (2.77) if the working fluids are either totally wetting ($\theta = 0°$) or totally non-wetting ($\theta = 180°$) because these are the only types of fluids for which the actual contact angle can be known in a fractionally wetting system. For example, Eq. (2.77) should not be applied to water because the contact angle of water within GDL materials can vary from location to location.

In addition, Gostick et al. used water as the saturating fluid to measure the hydrophilic pore behavior in GDL materials. It is impossible to measure the hydrophobic pore behavior with water because water will not wick through the hydrophobic pores to allow capillary pressure equilibrium throughout the contact porosimetry sandwich to be achieved. The results of Gostick's hydrophilic pore study showed that greater than 50% of pore volumes were water wetted. Knowing the P_c-S curve for the hydrophilic regions of the GDL is useful but it is equally important to understand the P_c-S characteristics in the hydrophobic regions. The hydrophobic P_c-S curve for GDLs cannot be directly measured using contact porosimetry due to the requirement that the working fluid be a wetting fluid.

A substantial amount of work has been presented by Kumbur et al. [45-47] using the methods presented by Gostick et al [36]. Kumbur considered the effect of the hydrophobic polymer content [45], the effect of compression [46], and the effect of temperature [47], on the capillary function of GDL material. All of the GDL materials

considered by Kumbur et al. included the addition of a microporous layer (MPL), making it difficult to draw parallels between their work and the work of others. The implications of using a dual layer specimen (macroporous and microporous layers) in a single experimental process are unclear. Nonetheless, Kumbur found that saturation between 2-25% was achieved at an equivalent water-air capillary pressure of 10,000 Pa depending on the PTFE content in the macroporous substrate (SGL 24 series). In contrast, other works focusing on macroporous carbon paper substrates (no MPL is present) suggest that substantially greater saturation is achieved at such large values of water-air capillary pressure [39, 43]. This apparent discrepancy is likely due to the improper assumption of a uniform contact angle to convert pressure data collected using octane as the working fluid to an "equivalent" pressure for water. Another potential reason for this discrepancy could be that the methods employed simply yield different results because they are not truly measuring the same material characteristic.

2.5.2 Permeability

As previously discussed a variety of permeabilities are commonly used in the PEMFC modeling literature. The absolute permeability (K) is a material property that characterizes the resistance of a material to single phase flow. The relative permeability of a given phase characterizes the change in flow resistance of the porous medium due to partial saturation of the material in a two phase flow system. Existing methods of absolute and relative permeability characterization will be discussed in this section.

The absolute permeability of a porous material is a fairly simple material property to measure. Forcing a known volumetric flow rate of a fluid of known viscosity through a porous material and measuring the associated pressure difference across the material is a simple method of obtaining data required to calculate the absolute permeability of the medium of interest. Algebraic manipulation of Darcy's Law into the form presented in Eq. (2.78) yields the absolute permeability of the medium through which flow occurs.

$$K = \frac{\mu}{A}\frac{\dot{V}}{\Delta P}\Delta x \tag{2.78}$$

The variables in Eq. (2.78) are defined as follows: K is the absolute permeability of the medium, μ is the dynamic viscosity of the fluid being forced through the medium, A is the cross-sectional area through which flow occurs, $\dot{V}$ is the volumetric flow rate of the fluid, ΔP is the pressure drop in the fluid across the porous medium, and Δx is the thickness of the porous medium over which the pressure drop is measured. This procedure has been used many times in the literature [35, 48]. It is important to note here that Darcy's Law only accounts for viscous flow and that the relationship presented in Eq. (2.78) is not valid at high Reynold's numbers where inertial effects become substantial. Fortunately, the flows within the GDLs of PEMFCs are quite likely laminar.

Measurement of relative permeabilities for various phases as a function of saturation through porous media is a much more difficult process. Reliable procedures for relative permeability characterization in PEMFC GDLs have yet to be established in the literature. However, two phase flow in soils and rock formations is an important aspect of oil, natural gas, and water recovery. Due to the importance of such natural resources, significant effort has been placed on characterizing two phase flow properties in such media. Two popular methods exist in the hydrology literature for determining relative phase permeabilities. The first is a steady flow experiment, and the second is an unsteady-state or dynamic flow experiment. Both have been reviewed by Dullien [19] and will be discussed below.

In the steady flow method of relative permeability determination, two phases are injected simultaneously at a fixed ratio into a sample core. Over time the core will become partially saturated with each phase until a steady state is reached. Steady state can be determined by confirming that the downstream flows of each phase are equal to the inflows of each phase, or more simply by confirming that the pressure drop across the core has reached a constant value. Dullien notes that attainment of steady state may take anywhere from 2-40 hours depending on the sediment sample [19]. Upon achievement of steady state the saturation of the core can be determined gravimetrically, via x-ray absorption, or by electrical resistivity measurement. Knowing the saturation of the liquid

phase and the volumetric flow rate of the liquid and gaseous phase, the relative permeability of each phase at the equilibrium state of saturation can be determined according to Eq. (2.79) and (2.80) .

$$k_{r,LW} = -\frac{\mu_{LW}}{AK}\frac{\dot{V}_{LW}}{dP/dx} \tag{2.79}$$

$$k_{r,g} = -\frac{\mu_g}{AK}\frac{\dot{V}_g}{dP/dx} = \frac{\mu_g \dot{V}_g}{\mu_{LW}\dot{V}_{LW}} k_{r,LW} \tag{2.80}$$

Many different test methods exist for this type of experiment with the most significant differences being the method in which end effects are minimized and the manner in which the two fluids are introduced into the core. The most popular test method is referred to as the Penn State method. This method relies on a large pressure drop through the core to minimize end effects [19]. The Penn State test apparatus is the most widely used for sedimentary cores and is depicted in Figure 2.10.

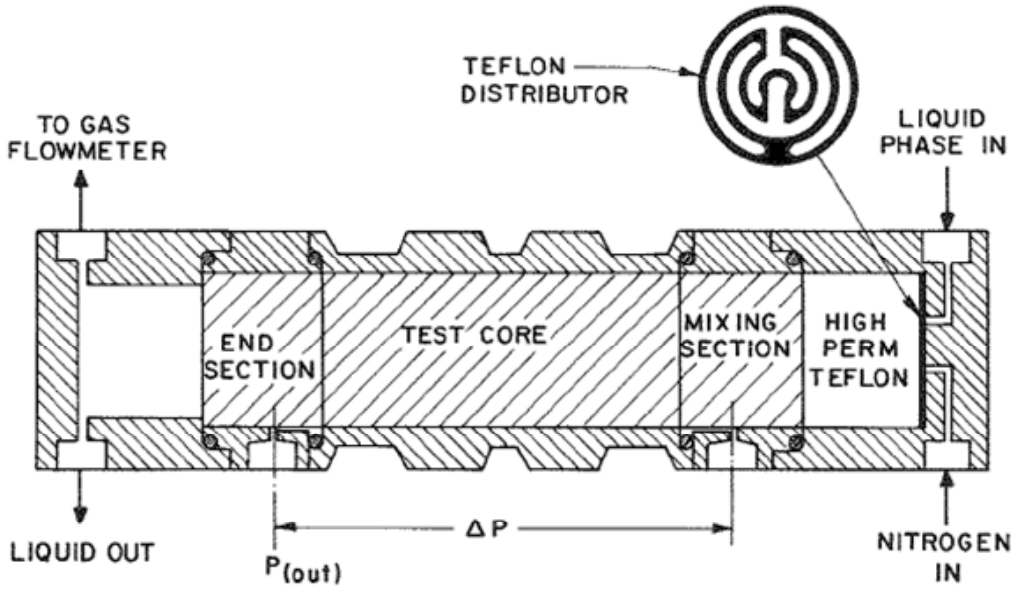

Figure 2.10 - Penn State steady flow relative permeability apparatus [19].

Dynamic determination of relative permeability involves pumping phase A through a porous medium that is saturated with phase B in order to displace phase B from the sample. This procedure allows for the ratio of the relative permeability of phase A to the relative permeability of phase B to be calculated based on the ratio of each phase in the downstream mixture. The method of calculating the relative permeability ratio is complex and will not be detailed herein because its applicability to GDL characterization is minimal. The reason that this method is not particularly viable for GDL characterization is that it only yields a relative permeability ratio. In order to know the actual relative permeability of each phase, the relative permeability of one of the phases must be known independent of the dynamic flow experiment [49]. The reader is referred to the text by Dullien [19] for a more complete description.

Scheideggar [50] analyzed the merits of a variety of relative permeability experimental methods in 1974 and presented his summary in tabular form (Table 2.5).

Table 2.5 - Comparison of relative permeability techniques by Scheidegger [50].

Method	Reliability of results	Speed, Hours per sample	Simplicity of operation	Remarks
Penn State	Excellent	8	Complicated	Uses three core sections
Hassler	Excellent	40	Very complicated	Requires pressure gauges of very low displacement volume
Single sample dynamic	Questionable for short samples	6	Simple	For short samples the relative permeability to wetting phase is too high
Stationary liquid	Questionable at low gas saturations	4	Simple	Applicable only to measurement of relative permeability to gas
Gas drive	Good	2	Very Simple	Can be operated with minimum amount of training and requires a minimum amount of equipment
Hafford	Excellent	7	Simple	Preferable to dispersed feed
Dispersed feed	Excellent	7	Simple	-

Nguyen et al. [40] used a greatly simplified dynamic method to determine the relative permeability of the gaseous phase in PEMFC GDL materials. In this method the GDL was initially saturated with liquid water and the gas flow rate was set constant until a constant pressure drop was achieved. Once a steady pressure drop was achieved the mass of the sample was measured to determine the remaining water saturation in the GDL. The experimental apparatus is depicted in Figure 2.11, and the experimental results for SGL Sigracet® 10BA carbon paper are displayed in Figure 2.12.

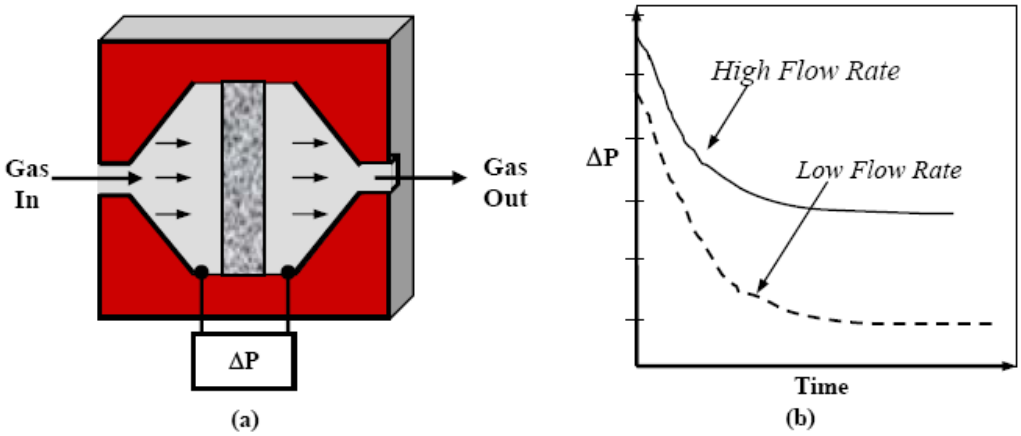

Figure 2.11 - Gas phase relative permeability apparatus used by Nguyen [40].

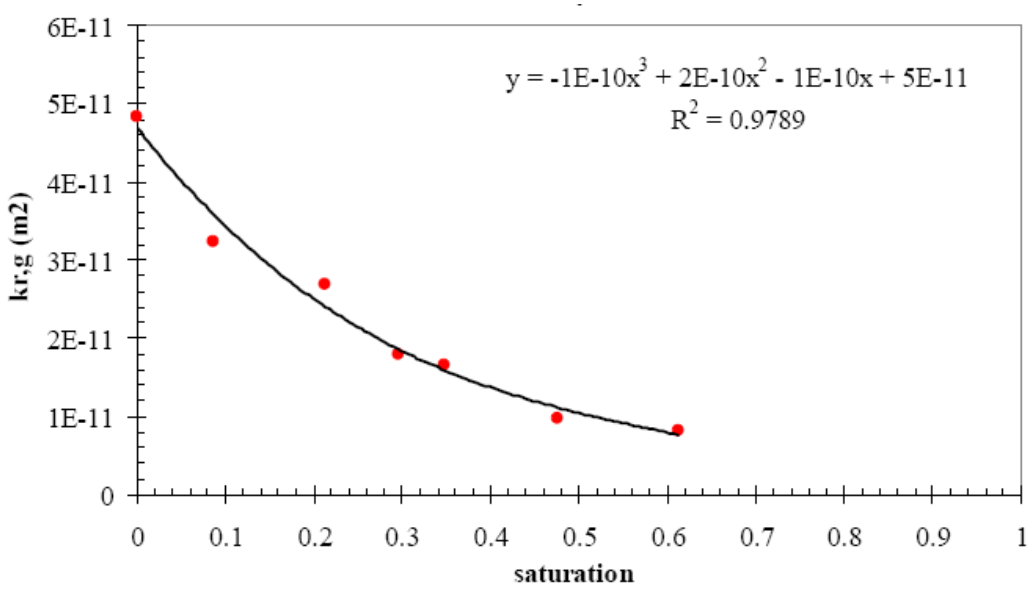

Figure 2.12 – Effective gas permeability ($Kk_{r,g}$) results by Nguyen for SGL Sigracet® 10BA.

Nguyen's experiment is interesting but only provides information regarding the gaseous phase. As previously discussed, the pressure gradient in the gas phase is minimal and is typically assumed to be zero in the modeling literature by application of the UFT assumption. Unfortunately, the dynamic method employed by Nguyen et al. does not have the benefit of being able to directly calculate the relative permeability of the liquid phase from the gas phase via Eq. (2.80) because simultaneous flow is not utilized (i.e., the flow rate of liquid is zero). Nonetheless, this is the only known experimental measurement of relative permeability in the PEMFC literature. Nguyen et al. suggest that a similar method would be possible for liquid phase relative permeability if the GDL were initially saturated with air and water was used as the displacing fluid. No results were reported for liquid water relative permeability.

2.6 CONTRIBUTIONS OF THIS WORK TO GDL WATER TRANSPORT MODELING

Much of the modeling work that exists in the PEMFC literature focuses on trying to develop general performance trends with varying material properties (e.g., porosity or permeability) or operating conditions (e.g., flow rate or humidity) by accounting for a vast array of physics. Although conservation equations are well established and implemented, there is little validation or care for the constitutive relationships used to govern the various transport phenomena. In this work, more value is placed on establishing constitutive relationships that more truly characterize the physics of the situation, and subsequently relating these relationships to PEMFC performance in an analytical framework.

This work focuses primarily on the transport of liquid water in the gas diffusion layer of PEMFCs. Development of novel test methods for determination of the important constitutive equations discussed throughout this chapter will be the most significant contribution to the PEMFC community. Specifically, this work addresses the determination of the P_c-S relationship, and the relative permeabilities of both phases (liquid and gas), for macroporous GDL materials (carbon cloths and carbon papers). Experimental methods for the determination of the constitutive equations governing

liquid water flow in the GDL is a starting point for more thorough evaluation of the effects that the physical properties of the GDL can have on water transport.

Following the development of experiments, a variety of PEMFC GDL materials are evaluated. The evaluation of a representative group of GDL materials provides insight into the effects of GDL characteristics including structure (e.g., carbon paper or carbon cloth), PTFE loading, and compression.

Constitutive relations determined by the new experimental techniques are compared to previously applied relations. In addition, a simple one-dimensional GDL model is presented to show the effect of the constitutive relations. This model will present GDL water transport results for the most popular constitutive relationships currently used in the PEMFC literature, and for the newly developed constitutive relationships.

Ideally the constitutive relationships established in this work will enhance the ability of PEMFC models to be used as design tools. To address this goal, a 2-D GDL model that includes the electrochemical behavior of a PEMFC is presented. The inclusion of the PEMFC electrochemistry is for the purpose of predicting polarization performance for a cell utilizing a particular GDL material. To confirm the effectiveness of the 2-D model the predicted polarization behavior is compared to experimental data.

In summary, this work will investigate the effects that constitutive relationships governing fluid flow in the GDL have on the ability to numerically model such flows. Some of the investigated physical characteristics and developed constitutive equations may prove to vary significantly from previously assumed properties and equations, while others may not. The success of this work will be determined by the ability to confirm existing relationships or establish new relationships, where the overriding goal is to improve the understanding of liquid water transport in the GDL of PEMFCs.

3 EXPERIMENTAL PROCEDURES

The two-phase one-dimensional momentum equation for liquid water transport in the GDL discussed previously (Eq. (2.17)), contains both porous media characteristics and fluid properties. An expanded form of Eq. (2.17) is presented here as Eq. (3.1) to aid the discussion.

$$u_{LW} = -\frac{Kk_{r,LW}}{\mu_{LW}}\frac{dP_g}{dx} + \frac{Kk_{r,LW}}{\mu_{LW}}\frac{dP_c}{dS}\frac{dS}{dx} = \frac{Kk_{r,LW}}{\mu_{LW}}\left(\frac{dP_c}{dS}\frac{dS}{dx} - \frac{dP_g}{dx}\right) \tag{3.1}$$

This work will make some assumptions about the transport properties within the GDL of PEMFCs:

1. For a particular fluid (e.g. water), capillary pressure-saturation relationships are uniform characteristics of the porous media and can therefore be measured for a representative sample and applied locally within the media.
2. Absolute permeability is a characteristic of the porous media and does not change within the laminar flow regime for single phase flow regardless of the fluid.
3. The relative permeability of phases in a multi-phase flow system depends on the fluids within the system and the characteristics of the porous media (including geometry, surface wettability, etc.) through which flow occurs, thus making it a function of fluid properties, the porous media characteristics, and saturation.
4. The saturation adjusted Bruggeman correction for binary gas diffusivities holds true for PEMFC GDL materials.

Based on the aforementioned assumptions, a series of experiments have been developed to quantify the porous media characteristics of the GDL and values for the relative permeability of the liquid and vapor phases flowing through the GDL. For the porous media, a novel method for the determination of the relationship between capillary pressure and saturation in PEMFC GDL materials will be described. It is expected that this relationship will vary significantly depending on the wetting characteristics of the

GDL. To complete the porous media characterization, experiments will be described to measure the absolute permeability of GDL materials. Additionally, the relative permeability of each fluid phase in the GDL media will be established as a function of the level of saturation of the media.

Based on the stated assumptions, the results from the outlined experiments will provide sufficient information to completely characterize fluid transport in the GDL of PEMFCs. Such thorough characterization makes it possible to develop a comprehensive model of fluid transport in the GDL which accounts for bulk flow of the gaseous mixture (this is particularly important in 3-D), bulk flow of liquid water, phase change, and diffusive transport. A PEMFC model utilizing GDL flow characteristics and material properties grounded in experimental results has not yet been developed.

3.1 TOTAL POROSITY OF GDL MATERIALS

Prior to determination of any flow properties of GDL materials, it is useful to have some fundamental information about the structure of the GDL. For this reason, the total porosity of the GDL will be established prior to any other experimentation. Two methods for measuring total porosity will be utilized: the solid phase density method similar to the method proposed by Mathias et al. [35], and a buoyancy method described in this work.

The procedure for determining the uncompressed total porosity by utilization of the solid phase densities is as follows:

1. A die is used to cut a GDL sample of known area (A).
2. The uncompressed thickness (t_o) of the GDL is measured using a flat-faced thickness gage (Mitutoyo® ID-H0530E) mounted on an anvil under a minimal applied load (load will be recorded).
3. Thermal gravimetric analysis (TA Instruments® Q500 TGA) is performed on a small GDL sample (separate from the sample cut in step 1) to determine the relative proportions of solid phases in the GDL.

4. Material property specifications (e.g., carbon fiber density (ρ_{carbon}), and PTFE density (ρ_{PTFE})) are used to determine the volume of the solid phase of the GDL via Eq. (3.2).

$$V_{solid} = \frac{m_{solid}}{(\%PTFE)\rho_{PTFE} + (1-\%PTFE)\rho_{carbon}} \tag{3.2}$$

5. The mass (m_{solid}) of the GDL sample of known area is measured (Mettler Toledo® AB135-S/FACT) and Eq. (3.3) is applied to determine uncompressed porosity (ε_o).

$$\varepsilon_o = \frac{1-V_{solid}}{At_o} \tag{3.3}$$

This method yields the porosity for an uncompressed GDL. In addition, since this method does not rely on any filling of pores or flow through pores, it results in a porosity which includes through pores, dead-ended pores, and enclosed voids within the media.

A value for the porosity of a compressed GDL (ε) can be determined via Eq. (3.4) if the compressed thickness (t) is known.

$$\varepsilon = \varepsilon_o \frac{t}{t_o} \tag{3.4}$$

The buoyancy method of porosity determination allows for the solid phase volume to be determined directly, rather than relying on the density of each phase obtained from material data sheets. The advantage of this method is that it eliminates the measurement of enclosed voids within the media and only accounts for the through pores, and dead-ended pores. Determination of uncompressed porosity by utilization of the buoyancy method will be performed on GDL samples according to the following procedure:

1. The weight of the dry die-cut GDL sample is measured using an analytical balance (Mettler Toledo® AB135-S/FACT).
2. The uncompressed thickness (t_o) of the GDL is measured using a flat-faced thickness gage (Mitutoyo® ID-H0530E) mounted on an anvil under minimal applied load.
3. The GDL sample is suspended from the underside hook of the analytical balance and immersed in a low surface tension, low viscosity, totally wetting fluid (e.g., n-pentane or perfluorohexane); and the weight is recorded.
4. Equation (3.5) is used to determine the volume of the solid phase.

$$V_{solid} = \frac{W_{solid} - W_{solid\ immersed\ in\ pentane}}{\rho_{pentane} g} \tag{3.5}$$

5. Equation's (3.3) and (3.4) will be applied to determine uncompressed porosity and compressed porosity, respectively.

Equation (3.5) is derived from Archimedes' principle, which states that the buoyant force exerted on a body is equal to the product of the volume of displaced fluid, the density of that displaced fluid, and the local gravitational acceleration. Recognizing that the volume of displaced fluid is equal to the volume of the solid phase for a totally immersed sample, results in Eq. (3.5).

It is necessary to determine the total porosity of a GDL prior to characterization of flow properties because most flow properties are dependent on saturation, and the calculation of saturation depends on total porosity as discussed in Chapter 2. With the porosity known, the saturation can be determined as the volume of water contained in the GDL divided by the available pore volume.

3.2 CAPILLARY PRESSURE-SATURATION RELATIONSHIPS IN GDL MATERIALS

Chapter 2 outlined the pros and cons of intrusion porosimetry techniques. Many of these techniques rely on the use of a totally wetting or a totally non-wetting fluid for intrusion. Due to the unreliability of characterizing capillary pressure in an interconnected porous system using a totally non-wetting or a totally wetting working fluid, and converting the results to "equivalent" capillary pressures for a water-air system, a new method was developed. In typical intrusion porosimetry techniques it is common to initially evacuate the specimen and subsequently increase the pressure of the working fluid incrementally. This approach makes it impossible to characterize the system at liquid pressures that are lower than the gas pressure (i.e., at positive capillary pressures in a water-air system where capillary pressure is defined as: $P_c = P_g - P_{LW}$), which would be of interest in hydrophilic regions of the porous media. Also, with the initially evacuated approach, the intrusion fluid must have a low vapor pressure at typical test temperatures. An alternative approach, contact porosimetry, can only characterize pores with wetting characteristics similar to the calibrated porous plates used to determine capillary pressure and capillary equilibrium. Further, contact porosimetry requires a working fluid that wets the specimen of interest because the method relies on wicking through the calibrated plate/specimen/calibrated plate sandwich.

The new method of porosimetry presented in this work is similar to the method used by Fairweather et al. [42, 43] in that liquid water can be used as the working fluid. The new method does not apply pressure and measure fluid uptake (i.e., intrusion porosimetry), nor does it rely on the wetting characteristics of a calibrated medium (i.e., contact porosimetry). The method of *gas displacement porosimetry* (GDP) instead uses a constant flow device to force liquid water at a very slow rate into a sample initially filled with fully humidified air (similar to the gas phase in the GDL).

Since the porous media sample is not initially evacuated it is important to only intrude the working fluid from one face of the sample so as to not trap the gas phase within the pores. In addition, when the working fluid is only pressurized from one side of the media it is imperative that it not be permitted to flow through the largest pores and fill void space above the sample rather than filling the smaller pores in the media. Such a

situation would only be capable of characterizing the P_c-S characteristics of the largest pores in the porous media. In this work a novel method of sample preparation is established which facilitates intrusion from only one face of the GDL, and enables the gas phase to be displaced during intrusion while preventing the liquid phase from exiting from the opposite face. Figure 3.1 is a graphical depiction of the sample developed for gas displacement porosimetry.

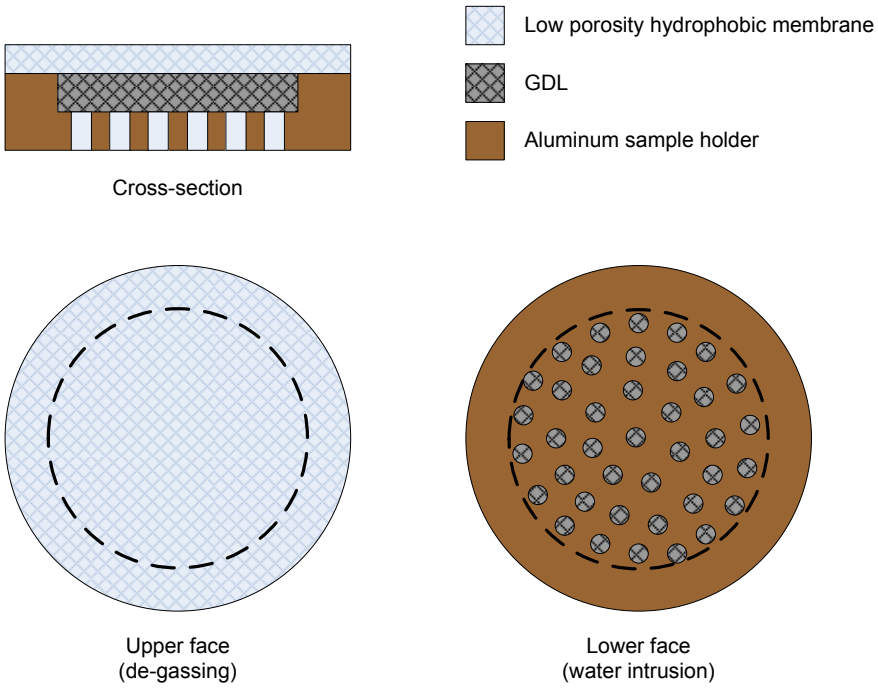

Figure 3.1 - Gas displacement porosimetry test specimen.

The low porosity hydrophobic membrane (LPHM) is a PTFE membrane with small pore sizes commonly used for de-gassing of liquids. The principle behind the use of the LPHM is that capillary pressures of magnitudes in excess of what would be experienced in an operating PEMFC are required to force liquid water through the LPHM. Therefore, all portions of the GDL through which liquid water would flow in an operating PEMFC will be filled before liquid water is forced through the LPHM. This procedure may not yield a complete P_c-S curve for specimens that require very high

pressure to fill some regions, but more importantly, it does yield a precise characterization of the applicable regions on the P_c-S curve for operating PEMFCs.

The sample holder is an aluminum disc with a cavity of known depth machined into the top surface. Holes penetrate the bottom of the sample holder to allow water to be injected from the underside of the GDL sample, while the LPHM is bonded to the top perimeter of the sample holder to allow gas to escape while confining the liquid within the GDL specimen. The cavity in the sample holder can be machined to different depths and will allow characterization of the P_c-S curve for GDL materials at varying levels of GDL compression. This is important in conventional PEMFC stacks since some areas of the GDL are under the GFC (minimally compressed) while others are under the shoulder (or land) area of the bipolar plate (significantly compressed). The cavity depth of the sample holder is machined accordingly. To ensure that the LPHM does not delaminate from the GDL or LPHM, the sample holder/GDL/LPHM assembly will be adhered together in a hot press operation near the melting point of PTFE (320°C). It is important that the LPHM does not delaminate because this would allow water to fill void space between the GDL and the LPHM.

A custom designed and manufactured GDP fixture was developed. Figure 3.2 displays the GDP test apparatus in the assembled view as well as a cross-section view, showing how the GDL multilayer specimen fits inside the experimental apparatus. The test protocol for the GDP experiment is as follows:

1. The specimen is placed in the GDP fixture, the sintered stainless steel disc is placed on top of specimen (to avoid specimen buckling), and the retainer ring is sufficiently tightened to ensure no water can pass between the o-ring and the sample holder.
2. The threaded cap is placed on top of the base but not fully tightened.
3. Valve V1 is closed, and valve V2 is open to allow humidified air (100% RH) to fill the chamber and exit under the loose cap.
4. Valve V1 is open and the cap is fully tightened to equilibrate the test chamber filled with saturated air to atmospheric pressure.

5. Approximately 1 mL of water is injected from the syringe pump to fill most of the void volume under the specimen.
6. Valve V2 is closed and the syringe pump (KD Scientific® Model 200) is started at a constant flow rate of 10 microliters per minute.
7. The difference in pressure between the intruding water and the humid air in the upper chamber is sensed by pressure transducer G1 (Omega® PX-2300-5DI) and is continuously recorded until the high pressure limit of the transducer is reached.

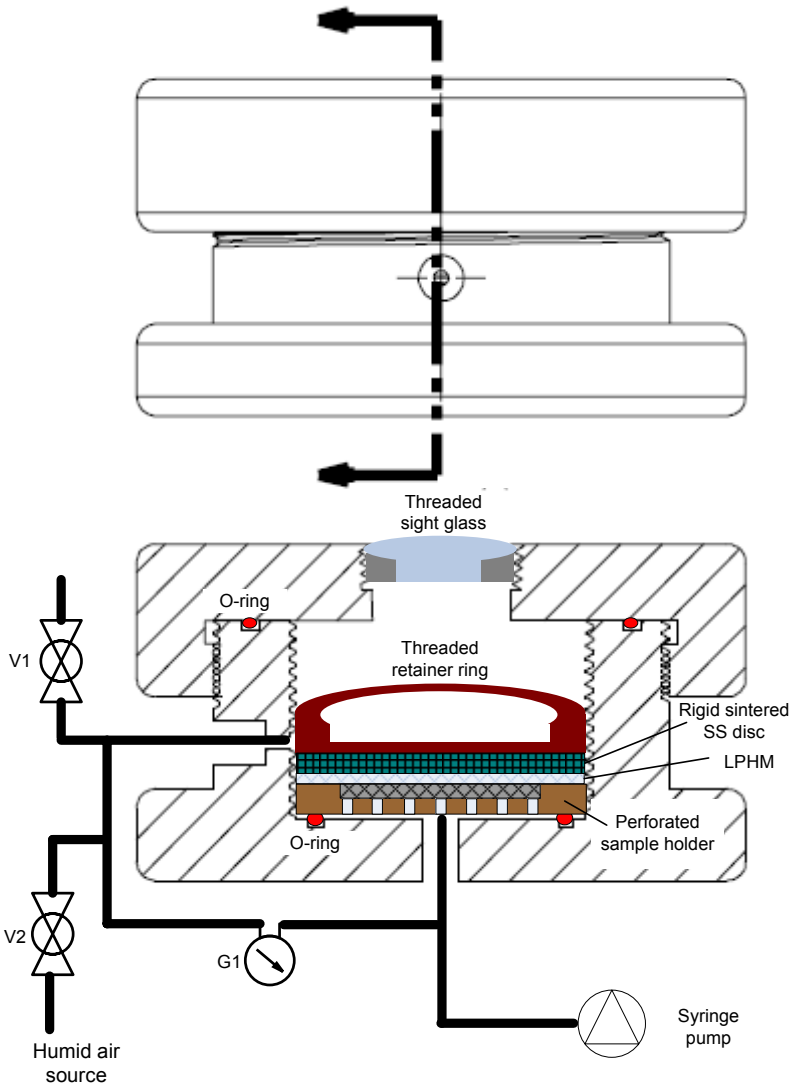

Figure 3.2 - Gas displacement porosimetry (GDP) experimental apparatus.

After completion of step 6, the following response is expected to be observed by differential pressure transducer G1:

- G1 will indicate a pressure of slightly greater than zero because the pressure required for flow will be slightly greater than the internal gas phase pressure.
- G1 will continue to indicate a pressure slightly greater than zero until the void space below the test specimen is totally filled with liquid water.
- Upon complete filling of the void space, G1 will indicate a pressure slightly less than zero IF the specimen has hydrophilic regions within its structure.
- G1 will show increasing differential pressure until the experiment is aborted due to reaching the upper limit of the transducer, or until the pressure limit of the LPHM is reached.

Following completion of the test procedure, the differential pressure data prior to the beginning of sample intrusion will be eliminated. Additionally, the time data associated with the differential pressure data will be zeroed at the point in time just prior to the beginning of water intrusion. The fluid uptake of the specimen will be calculated by multiplying the known flow rate of the syringe pump with the corrected time. The quotient of fluid uptake with the total porosity will be calculated to determine the saturation of the GDL specimen. The results obtained from the gas displacement porosimetry experiment could be somewhat different from the theoretical results presented previously in Figure 2.4. For example, if the porous media of interest has pores that are very difficult to intrude, then the pressure required for infiltration may exceed the pressure limit of the LPHM (scenario depicted in Figure 3.3). However, a complete P_c-S curve can be measured for materials that can be fully saturated at pressure substantially lower than the breakthrough pressure of the LPHM. It is expected that complete P_c-S curves will be able to be obtained for macroporous GDL materials.

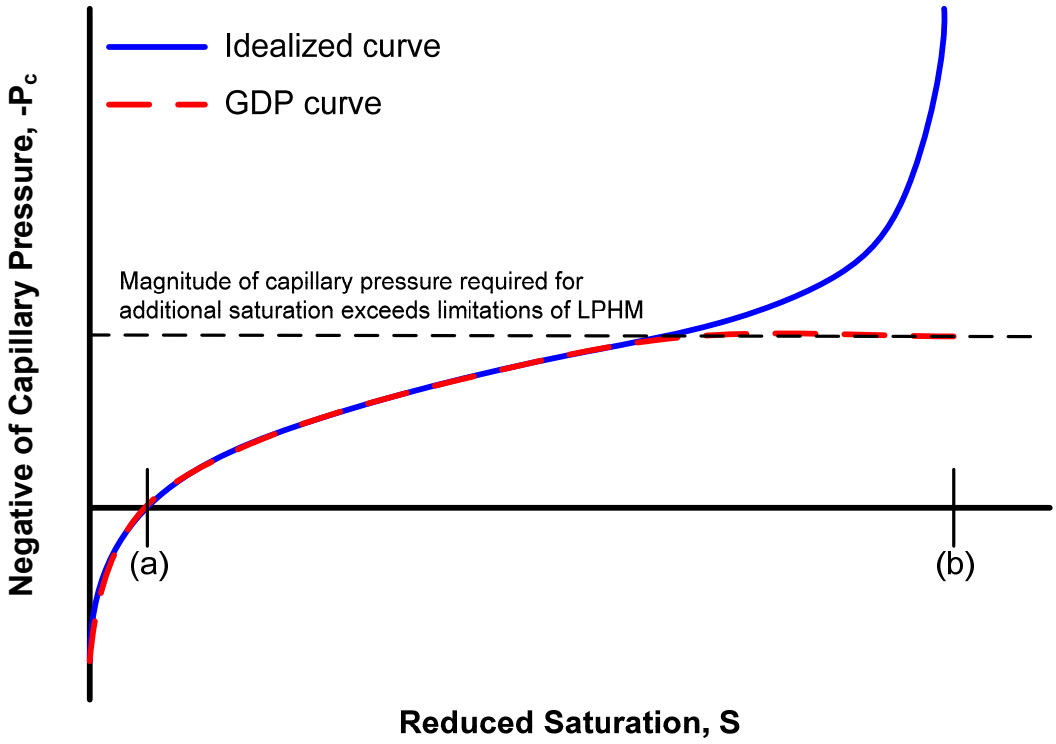

Figure 3.3 – Comparison of idealized P_c-S curve and the curve measured via GDP method for materials that require high pressure to achieve full saturation.

As described in Chapter 2, it has been suggested that some regions of GDL materials are hydrophilic in nature. Whether this is the case or not for GDL materials, an advantage of the GDP method over other porosimetry methods is its ability to measure both hydrophilic and hydrophobic regions of porous media in a single experiment. It can be seen in the hypothetical capillary pressure curve presented in Figure 3.3 that the capillary pressure becomes positive at point (a), and that the porous media is fully saturated at point (b). These two points on the GDP P_c-S curve can be used to determine hydrophilic porosity and hydrophobic porosity according to Eq. (3.6) and (3.7).

$$\varepsilon_{philic} = S_a \varepsilon \tag{3.6}$$

$$\varepsilon_{phobic} = \left(1 - S_a\right)\varepsilon = \varepsilon - \varepsilon_{philic} \tag{3.7}$$

This information could prove to be vital in determining a relationship between the different types of porosity and the curvature and/or magnitude of the P_c-S curve for not only GDL materials, but more generally for any porous media of mixed wettability.

3.3 PERMEABILITY OF GDL MATERIALS

One of the keys to accurate modeling of two phase flow in the GDL is a suitable determination of the porous media characteristics and fluid properties used in the Darcy like momentum equation for each phase. This section will detail procedures for permeability measurements in a variety of GDL materials. First, methods for establishing relative phase permeability's ($k_{r,g}$ and $k_{r,LW}$) for two-phase flow will be discussed. The relative permeability of each phase in the liquid water-humid air system will be measured as a function of saturation, and will be vital for accurate modeling using Darcean momentum equations for each phase. Second, the material property of absolute permeability (K) as defined by single phase flow at low Reynold's numbers will be established.

3.3.1 Relative permeability of individual phases

As previously discussed, the relative permeability of phases is a function of both the porous media characteristics and the fluid properties. Since there is interaction between the porous media characteristics and the fluid properties, as well as interaction between the two fluids, two-phase flow is required for proper characterization of relative permeability. The interaction between the fluids complicates the experiment and therefore significant care must be taken to ensure the fluids are properly mixed and flow is allowed to reach a steady state.

A variation of the Penn State method of relative permeability determination in sedimentary cores (Figure 2.10) is developed and implemented in this work for determination of the relative permeability of GDL materials. The newly developed

method of relative permeability determination will be referred to as the VT-k_r experimental method for the remainder of this work to aid in discussion. The VT-k_r experimental apparatus is displayed in Figure 3.4.

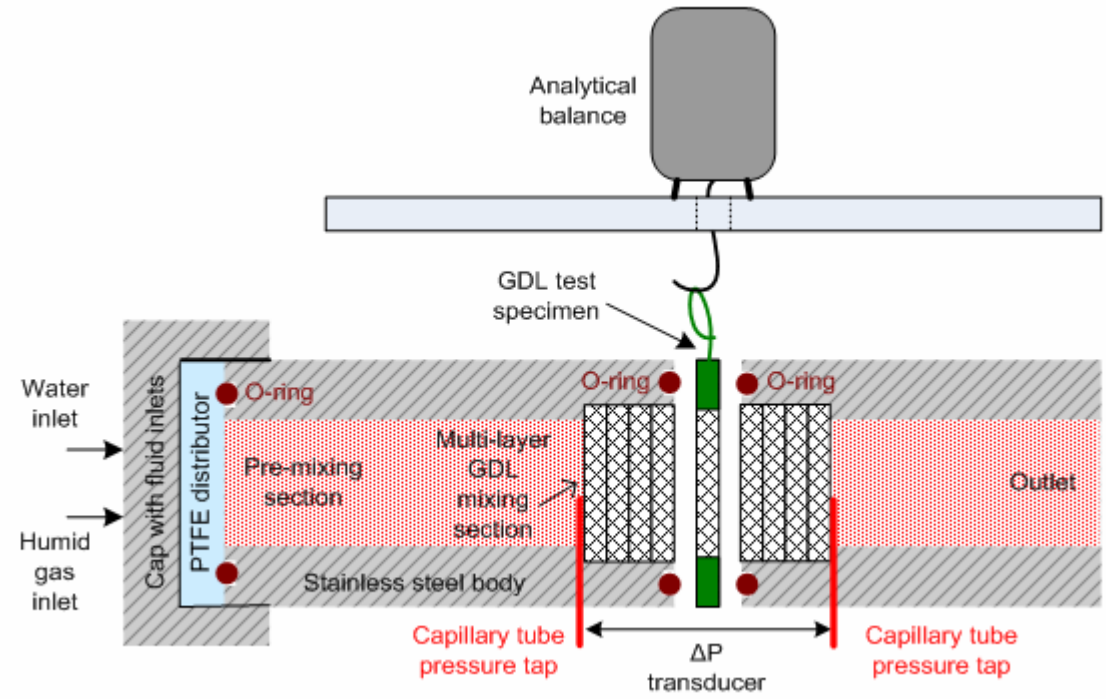

Figure 3.4 - VT-k_r experimental apparatus for determination of relative phase permeability.

Prior to outlining the experimental procedure, some of the highlights of VT-k_r method will be detailed. The water flow rate is controlled using a syringe pump, and the gas flow rate is controlled using a mass flow controller. The PTFE distributor is shaped similarly to the PTFE distributor in the Penn State method. The distributor ensures that water is introduced evenly over the upstream face of the pre-mixing section. The pre-mixing section is hydrophilic and meant to sufficiently distribute the liquid water throughout the gas phase by effectively reducing the size of liquid agglomerates, and to ensure that a uniform liquid flux enters the upstream side of the GDL mixing section. The pre-mixing section was composed of a tightly rolled hydrophilic cloth. Prior to the two-phase mixture entering the actual GDL test specimen, it passes through a layered section of identical GDL material. The GDL mixing section is necessary to reduce end effects.

End effects, such as a saturation gradient through the thickness of the GDL, could significantly impact the accuracy of the gravimetric determination of saturation. The downstream GDL layers also reduce end effects which would otherwise be influential near the downstream face of the GDL test specimen. The sum of the number of layers used in the GDL mixing sections and the sample specimen itself (sum = n) varies depending on the desired level of compression of the material being tested. Small diameter, yet rigid, capillary tubes (OD: 0.0625") were inserted through the wall of the test chamber and sealed so that the pressure differential across the layers could be measured and recorded.

The VT-k_r apparatus, like others [19, 50], relies on the assumption that the gas phase pressure differential, and liquid phase pressure differential, are equal across the specimen's thickness. Application of this assumption and Darcy's Law result in the following equations for calculating the relative permeability of each phase:

$$k_{r,LW} = \frac{\mu_{LW}}{K\Delta P}\frac{tn}{A}\dot{V}_{LW} \tag{3.8}$$

$$k_{r,g} = \frac{\mu_g}{K\Delta P}\frac{tn}{A}\dot{V}_g \tag{3.9}$$

where t is the thickness of a single GDL layer and n is the sum of the GDL layers between the pressure taps.

The test specimen in the VT-k_r procedure is represented in a cross-sectional view in Figure 3.4 and in the frontal view in Figure 3.5. The GDL specimen is prepared in the following manner:

1. Two pieces of thermoplastic film (Dyneon® THV-220G) are cut into a ring shape and placed on the top and bottom of the GDL specimen.
2. The thermoplastic/GDL/thermoplastic sandwich is pressed under light load at 130°C to fill the porous regions around the perimeter of the GDL, and leaving an unfilled region in the center of the GDL specimen.

3. A thin PTFE monofilament is adhered to the edge of the GDL specimen so it can be suspended from the underside hook of an analytical balance.

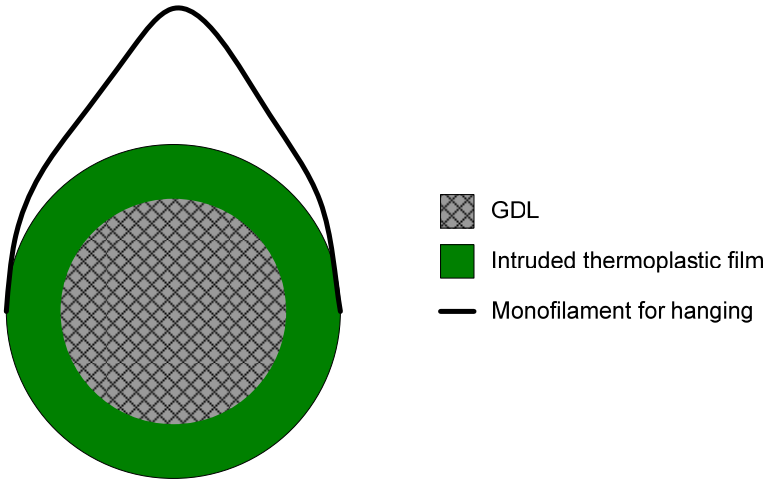

Figure 3.5 - VT-k_r GDL test specimen.

The GDL mixing layers are prepared by cutting appropriately sized discs of GDL from the same sheet stock used for the central GDL specimen. The appropriate number of layers are bonded together around the perimeter and placed in the recess of the upstream and downstream pipe. To avoid the GDL mixing layers from falling out of the pipe recess when the apparatus is opened, a small diameter monofilament is placed over the surface and pushed under the o-ring on the face of the pipe.

Following the fabrication of the VT-k_r GDL test specimen, and inserting the GDL mixing layers in the experimental apparatus, the relative permeability experiment proceeds in the following manner:

1. The mass (m_{dry}), open area (A), and thickness (t) of the GDL specimen is measured.
2. The GDL test specimen is inserted into the VT-k_r fixture and the two sides of the fixture are forced together to ensure a seal at the o-ring/specimen interface on both side of the GDL specimen.
3. Saturated air is delivered at a constant rate.

4. The flow of liquid water is started at a low rate and the pressure differential is monitored over time until steady-state has been achieved. The pressure differential is recorded.
5. The flow is stopped and the two sides of the fixture are separated. The mass of the partially saturated GDL specimen ($m_{partial\text{-}S}$) is measured and recorded.
6. The liquid water saturation (S) is calculated using Eq. (3.10).

$$S = \frac{1}{\varepsilon A t}\left(\frac{m_{partial-S} - m_{dry}}{\rho_{LW}}\right) \tag{3.10}$$

7. The relative permeability of liquid ($k_{r,LW}$) and gas ($k_{r,g}$) phases is calculated via Eq. (3.8) and (3.9), respectively.
8. The fixture is closed, flow is resumed, and the flow rate of liquid water is increased. The pressure differential is monitored until steady-state is reached.
9. Steps 5-8 are repeated until four different points on the k_r-S curve have been measured.

The preceding experimental procedure provides data for the relation between relative permeability and saturation in the various GDL specimens. An appropriate curve fit will be used to arrive at a single relative permeability function for each GDL specimen. A representative plot of the liquid water relative permeability is shown in Figure 3.6.

A balance is required concerning the fluid flow rates for the VT-k_r experiment. Flow rates that are large enough to cause a stable and measurable pressure drop across the media are essential. However, application of Darcy's law is only valid if inertial effects are negligible. Dullien [19] states that steady-flow relative permeability measurements are independent of flow rate within the reasonable range described. Fortunately, this range is expected to be very broad due to the small length scale in GDL materials.

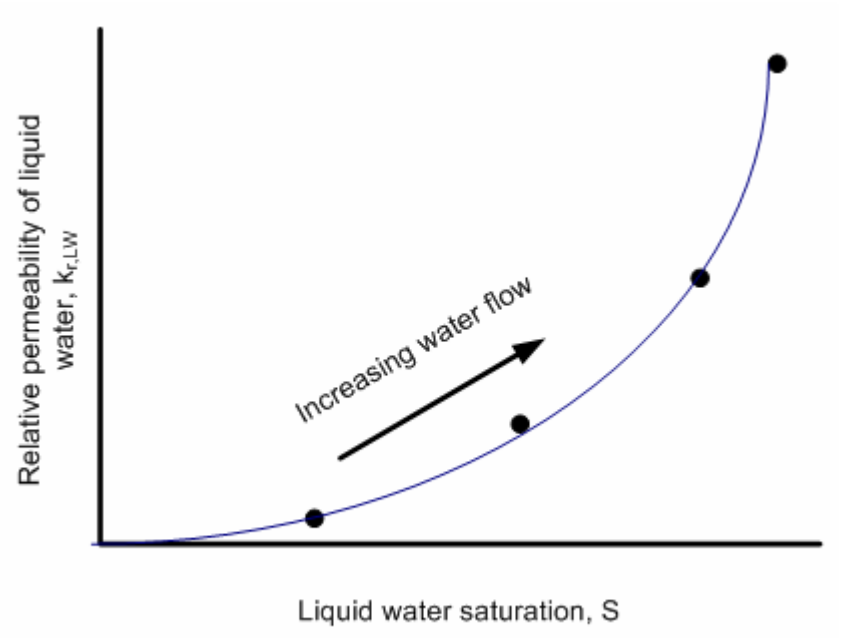

Figure 3.6 - Representative plot of liquid water relative permeability.

3.3.2 Absolute permeability

The measurement of absolute permeability is a straightforward application of Darcy's Law for single phase flow. The absolute permeability can be calculated for a known pressure differential across a material at a given volumetric flow rate by using Eq. (3.11) (repeated here from Chapter 2).

$$K = \frac{\mu}{A}\frac{\dot{V}}{\Delta P}\Delta x \qquad (3.11)$$

The linear relationship between flow rate and pressure implied by this equation becomes invalid at higher flow rates as the flow transitions to a turbulent regime (see Figure 3.7). Quantifying whether a flow is laminar or turbulent in porous media is difficult because the pore sizes are unknown and therefore the Reynold's number inside individual pores is unknown. The linear region is assumed to be the laminar region, and the absolute permeability calculation is based on the data in this region.

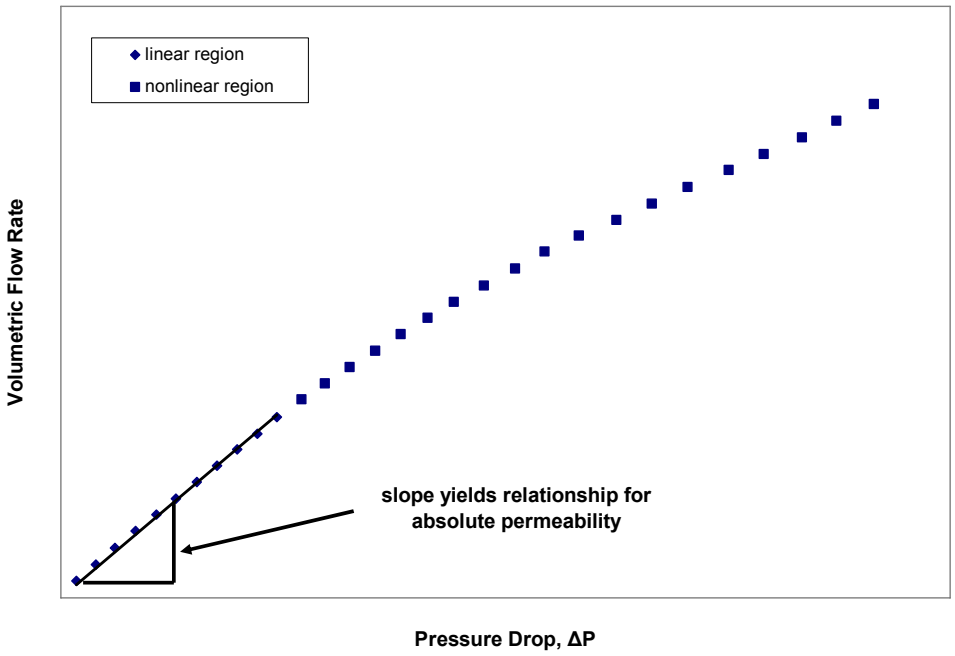

Figure 3.7 - Characteristic absolute permeability data over a range of flow rates.

The VT-k_r test apparatus is also used to measure absolute permeability. This apparatus allows for absolute permeability measurements to be performed on samples exhibiting varying levels of compression, similar to the relative permeability measurements. When performing absolute permeability experiments using the VT-k_r apparatus the following changes are made:

1. The premixing sections are removed.
2. No liquid is forced through the specimen.
3. Dry gas is used rather than humid gas.

As seen in Eq. (3.8) and (3.9), relative permeability is a function of absolute permeability. Therefore, an accurate determination of absolute permeability is vital to the accuracy of relative permeability functions.

3.4 FUEL CELL PERFORMANCE FOR TWO DIMENSIONAL MODEL VALIDATION

The previous sections dealt with the determination of both material and flow properties, and relationships for GDL materials. These properties will be used in the development of finite element (FE) models of the GDL and of an operating PEMFC. The adequacy of the property data and the finite element model will be assessed by comparing predicted cell performance to measured cell performance. This section discusses the methods and equipment employed for fabrication and testing PEMFCs that will be used to validate the numerical results of the PEMFC FE model.

3.4.1 Fabrication of test cells

Test cells were constructed using catalyzed membranes (also commonly referred to as membrane electrode assemblies (MEAs)) obtained from Ion-Power Inc., and carbon based GDL materials obtained from BASF Fuel Cell Inc. The MEAs were loaded with Platinum catalyst at a level of 0.3 mg/cm^2. Two different carbon based GDL materials were used, a cloth material (BASF B1/A) and a paper material (Toray TGPH-090). Nearly incompressible PTFE coated fiberglass gaskets that are approximately 65% of the uncompressed GDL thickness were used as frames around the GDL to control the compressed thickness of the GDL. Following construction of the catalyzed membrane/GDL/gasket sandwich, the assembly was installed inside of a PEMFC test apparatus manufactured by Fuel Cell Technologies Inc. Figure 3.8 depicts the apparatus and assembly method.

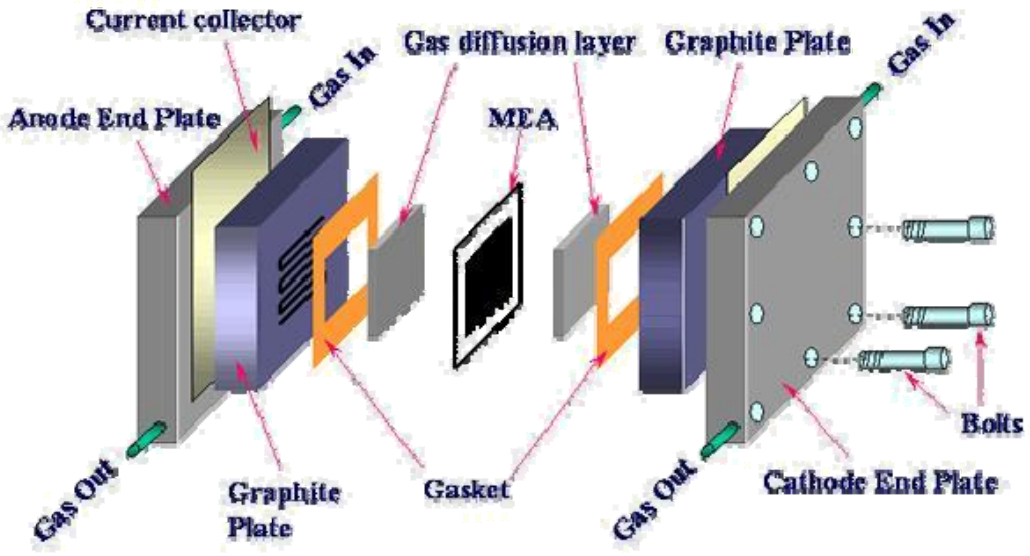

Figure 3.8 - Assembly of validation PEMFC in test apparatus.

The GDLs characterized via the methods discussed in previous sections, and used to construct the validation cells were treated with PTFE to achieve a prescribed level of PTFE content in the bulk structure (0, 10, 20, and 30% by mass). These values for PTFE content were chosen because typical PTFE loadings in GDLs can range anywhere from 0-40%, with the optimal loading usually falling in the range of 10-20% [35, 48, 51-53]. PTFE content in the GDL is determined according to Eq. (3.12).

$$\%PTFE = \frac{m_{treated} - m_{untreated}}{m_{treated}} \times 100 \qquad (3.12)$$

The materials were purchased from BASF Fuel Cell with the desired bulk PTFE treatments already applied.

The test assembly depicted in Figure 3.8 includes a graphite flow field that emulates the 2-D geometry used in the FE model. A single channel, 1 mm wide and 1 mm deep, was arranged in a serpentine configuration with a total length of 322 mm. The cell was operated at high stoichiometric ratios to ensure a nearly uniform oxygen concentration along the entire length of the channel. Previous modeling work has shown that such operation yields nearly uniform current generation along the length of the channel [17] thus making a 2-D representation of the geometry reasonable for the model.

3.4.2 Test conditions and control

The test station used to characterize the performance of the validation PEMFC is manufactured by Fuel Cell Technologies Inc. The station utilizes mass flow controllers and dewpoint humidifiers for both the anode and cathode channel. In addition, the cell temperature and humidifier temperatures are controlled with PID controllers. Electronic back-pressure controllers regulate the downstream pressure of the reactant gasses. An electronic load is used to control the load in the PEMFC circuit and can maintain a given voltage, current, or power in the circuit. The station is connected to a computer and all control parameters can be set, monitored, and recorded using LabVIEW®. Figure 3.9 shows an electrical and plumbing schematic of the test station.

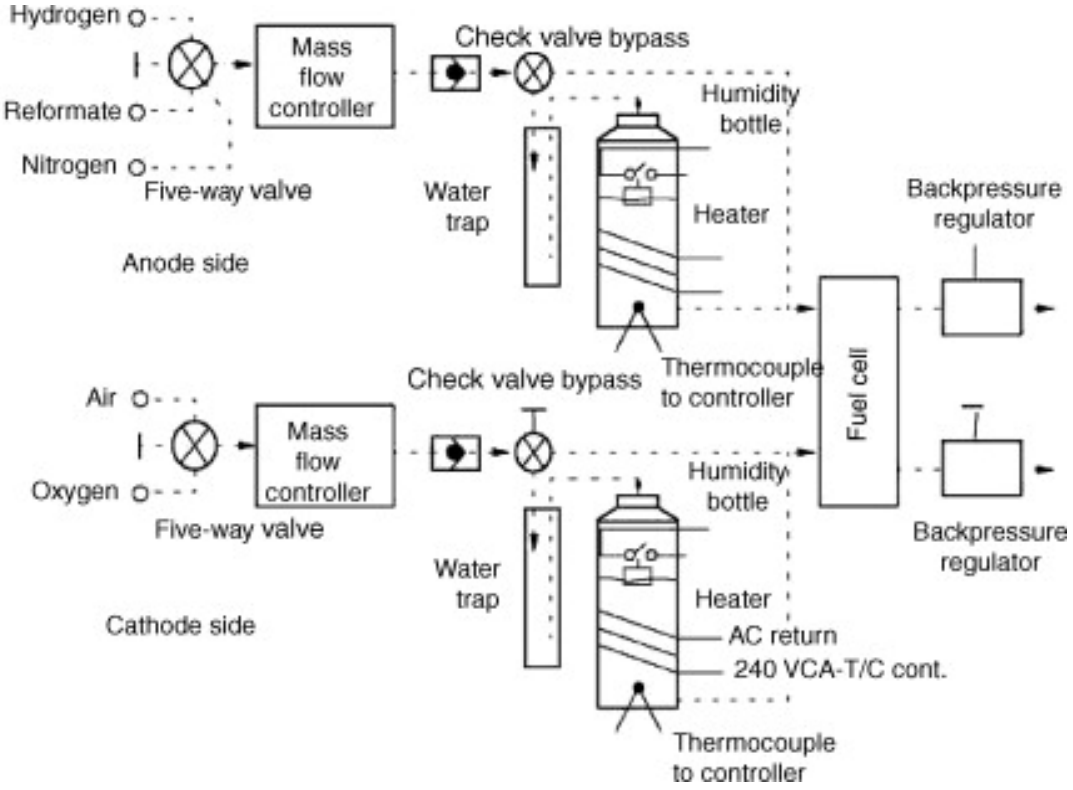

Figure 3.9 - Schematic of PEMFC test station.

Experiments were performed at varying conditions to validate the FE model. The cell temperature was maintained at 80°C for all experiments. The anode gas stream was maintained at a flow rate of 225 sccm of dry H_2 (~6x stoichiometric at 1 A/cm^2) and was humidified to a relative humidity of 100%. The flow rate of the cathode gas was maintained at 550 sccm of dry air (~6x stoichiometric at 1 A/cm^2), yet two relative humidity's were investigated (75% and 95%). Additionally, the anode and cathode gas were both maintained at a back-pressure of 0 psig. The variance in the humidity typically has a significant impact on cell performance due to the change in the concentration of O_2 in the cathode gas, as well as impacting evaporation and condensation within the GDL. Experimental results will be compared to the 2-D FE model results in Chapter 5.

3.5 SUMMARY OF EXPERIMENTAL PROCEDURES

Two types of GDL materials will be investigated: carbon paper and carbon cloth. Additionally, the effect of bulk PTFE treatment on the characteristics of the two different types of GDL media will be explored. The effect of thickness will also be investigated by performing experiments on specimens which are representative of the thickness observed under the shoulder (or land) area of a bipolar plate, and of the thickness observed under the GFC. Although the regions representative of regions under the gas channel are mildly compressed (90-95% of as-received thickness) they will be referred to as uncompressed (u) throughout the remainder of this work to avoid confusion. The specimens representative of GDL regions under the shoulder of the bipolar plate (65-70% of as-received thickness) will be referred to as compressed (c). The combination of the investigated substrate types, bulk treatments, and compression, results in a total of sixteen possible specimens for experimentation, not including the as-received materials. The labeling scheme for the sixteen specimens is shown in Table 3.1.

Table 3.1 - Identification of GDL specimens*.

Substrate		GDL Compression: *under channel - uncompressed (u)*	GDL Compression: *under shoulder - compressed (c)*
	Carbon Cloth	C-0u	C-0c
		C-10u	C-10c
		C-20u	C-20c
		C-30u	C-30c
	Carbon Paper	P-0u	P-0c
		P-20u	P-20c
		P-20u	P-20c
		P-30u	P-30c

* bulk PTFE % indicated by number in specimen name (i.e., 0, 10, 20, 30 %)

Porosity plays a vital role in gas diffusion and in the determination of saturation and will be determined via the gravimetric and buoyancy porosity methods for all 8 as-received materials (completely uncompressed). A PTFE content study using the method of gas displacement porosimetry was performed for all eight nominally uncompressed materials (nominally 90-95% of the as-received thickness), while a compression study (65-70% of as-received thickness) was performed on the cloth and paper specimens with 20% PTFE only. Absolute permeability and relative permeability measurements were performed for the materials loaded with 0 and 20% PTFE content for the nominally uncompressed materials, namely C-0u, C-20u, P-0u, and P-20u. Additionally, the absolute and relative permeability of the compressed materials loaded with 20% PTFE were investigated. Table 3.2 summarizes the experimental matrix.

Table 3.2 – Experimental matrix.

Experiment		
Porosity (gravimetric and buoyant)	*Gas Displacement Porosimetry (GDP)*	*Absolute and relative permeability*
C-0 (as received)	C-0u	C-0u
C-10 (as received)	C-10u	-
C-20 (as received)	C-20u, C-20c	C-20u, C-20c
C-30 (as received)	C-30u	-
P-0 (as received)	P-0u	P-0u
P-10 (as received)	P-10u	-
P-20 (as received)	P-20u, P-20c	P-20u, P-20c
P-30 (as received)	P-30u	-

The data from these experiments is crucial to the development of a comprehensive model of fluid transport in PEMFC GDL materials. The relationships derived from the experimental data, as well as their implementation in 1-D and 2-D finite element GDL models are presented in Chapter 5.

4 MATHEMATICAL MODELS

This chapter presents the modeling efforts that are used to assess the impact of the GDL characteristics determined by the experimental methods outlined in the previous chapter. First, a one-dimensional model of a PEMFC GDL is developed to assess the impact of typical GDL transport equations (discussed in Chapter 2) on water flow and gas diffusion in the GDL. In addition, the constitutive relations developed in this work (via the experiments discussed in Chapter 3) will be implemented in the 1-D model to assess the significance of the experimentally determined transport relations. Second, a two-dimensional representation of a PEMFC will be modeled to investigate the transport of liquid and gas, and the power production of a PEMFC, when the compression of the GDL under the shoulder of the gas flow channel (GFC) is included in the model domain.

4.1 ONE-DIMENSIONAL COMPARATIVE GDL MODEL

The purpose of this model is to compare the experimentally determined GDL water transport characteristics (e.g., the curvature of capillary pressure with saturation, the absolute permeability of the GDL, and the relative permeability of liquid water in the GDL) to some of the assumed characteristics in the modeling literature. The emphasis will be to assess the impact that the liquid water transport coefficient terms (dPc/dS, $k_{r,LW}$, and K) have on liquid water transport and gaseous diffusion through a 1-D representation of the GDL. To qualitatively investigate the impact of the liquid water transport coefficient terms on liquid water transport, reduced saturation (S), and liquid water transport coefficient, will be plotted versus position through the thickness of the GDL. In addition, the product of the diffusivity correction terms ($f(\varepsilon)g(S)$) will also be plotted versus position through the GDL thickness to qualitatively assess the impact of liquid water transport coefficient on gaseous transport.

The comparisons made with this model will be done using a standard set of modeling equations (described in Section 4.2.2), where the only relationships that will be changed for the purpose of comparison are the derivative of the capillary pressure-

saturation function, the absolute permeability of the GDL, and the relative permeability of liquid water. These GDL characteristics will take on one of three forms: 1) the experimentally determined form in this work; 2) the assumed form presented by Pasaogullari et al. [12]; or 3) the assumed from presented by Lin et al. [15] The resulting comparison will represent three trains of thought respectively: 1) GDL characteristics should be grounded in experiments performed on actual GDL materials; 2) it is appropriate to assume GDL characteristics based on experiments performed using other porous media (e.g., packed sand – Leverett); or 3) it is appropriate to determine GDL characteristics by matching mathematical modeling results and secondary experimental results (e.g., polarization curves).

The impact of the three approaches for describing GDL transport will be assessed by predicting the GDL saturation and the diffusivity correction using each approach for specific sets of GDL boundary conditions. The assumptions, geometry, conservation equations, boundary conditions, and constitutive equations used in the development of the 1-D comparative model are presented in this section. The results of the comparisons will be presented in Chapter 5.

4.1.1 Model assumptions

Since the main purpose of the 1-D comparative model is to compare the effect of liquid water transport coefficient on water transport, a variety of simplifying assumptions are incorporated. The assumptions are outlined in bullet form below:

- The fuel cell is operating at steady-state.
- A one-dimensional analysis is sufficient to compare the effects of liquid water constitutive relationships.
- There is no temperature gradient through the GDL, i.e., the model is isothermal.
- There is no gas phase pressure gradient through the GDL due to bulk flow, i.e., the UFT assumption is utilized and the gas phase is isobaric.
- The concentration of oxygen at the GDL/GFC interface is known.

- The flux of water into the GDL can be appropriately characterized by summing the water produced via the electrochemical reaction and the net amount of water transported across the membrane by application of a constant *net effective* electro-osmotic drag coefficient, α_{EOD}.
- The liquid water and water vapor phases are not in equilibrium and mass is exchanged between the phases in a rate limited fashion according to a known rate constant.
- The reduced saturation at the GDL/GFC interface is known.

The application of the preceding assumptions results in the requirement of only three conservation equations: two for species conservation in the cathode gas mixture (n-1 gaseous components), and one for combined mass and momentum conservation equation in the liquid water phase. The details of these equations and the geometry in which they will be utilized are described in the following subsections.

4.1.2 One-dimensional model geometry

The one-dimensional comparative model geometry consists of only a 1-D representation of the GDL thickness as displayed in Figure 4.1. Based on the previously stated assumptions, three governing equations will be needed in the single domain (cathode GDL) model. In addition, each second order governing equation requires a boundary condition at each boundary, B1 and B2. Section 4.1.3 will describe the governing equations while Section 4.1.4 will provide the details of the boundary conditions.

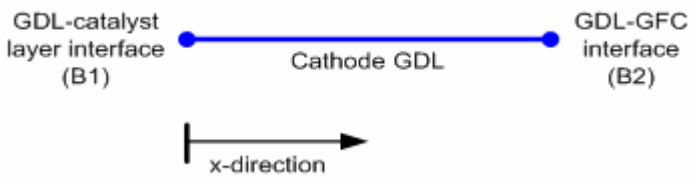

Figure 4.1 - Geometry used for the 1-D comparative FE model.

4.1.3 Conservation equations

A steady-state mass balance for each gas species that includes convection and diffusion takes the form [22, 54]:

$$\nabla \bullet \left[\rho_g \omega_\alpha \boldsymbol{u} - \rho_g \omega_\alpha \sum_{\beta=1}^{n} \mathbb{D}_{\alpha\beta} \nabla y_\beta \right] = VS_\alpha^{net} \tag{4.1}$$

In Eq. (4.1) ρ_g is the local gas mixture density, ω_α is the local mass fraction of the α species, $\boldsymbol{u}$ is the bulk gas mixture velocity, $\mathbb{D}_{\alpha\beta}$ is the local multicomponent Fick diffusivity between species α and β, y_β is the local mole fraction of the β species, and VS_α^{net} is the net volumetric *source* of the α species. Here, the local interaction between multiple gaseous components is embedded in the multicomponent Fick diffusivity, $\mathbb{D}_{\alpha\beta}$. The multicomponent Fick diffusivity relates the local mass fraction of each species and the Maxwell-Stefan diffusivity ($\tilde{D}_{\alpha\beta}$, discussed in Chapter 2) to capture the interaction among species. The manner in which this is achieved will be detailed in the section pertaining to constitutive relations.

Two distinct equations in the form of Eq. (4.1) will be used to model the transport of oxygen and water vapor in the GDL, while the third species distribution (nitrogen) will be solved via the fact displayed in Eq. (4.2), that the mass fractions of all species must sum to unity.

$$\sum_{\alpha=1}^{n} \omega_\alpha = 1 \tag{4.2}$$

The net volumetric source in Eq. (4.1) must be set to zero for the oxygen and nitrogen species (which do not react in the GDL), yet takes on a non-zero value for the water vapor species to allow for evaporation and condensation. For the sake of simplicity

the term governing phase change will be a combination of an evaporation term and a condensation term, each of which utilize the same rate constant, γ. Equations (4.3)-(4.5) display the complete form of the rate of phase change terms.

$$VS_{cond} = \gamma M_w \frac{p_{wv} - p_{sat}(T)}{R_u T} \times \psi_{cond} \tag{4.3}$$

$$VS_{evap} = \gamma M_w \frac{p_{sat}(T) - p_{wv}}{R_u T} \times \psi_{evap1} \times \psi_{evap2} \tag{4.4}$$

$$VS_{LW}^{net} = VS_{cond} - VS_{evap} \tag{4.5}$$

In Eq. (4.3)- (4.5) M_w is the molar mass of water, R_u is the universal gas constant, p_{wv} is the local partial pressure of water vapor in the gaseous mixture, $p_{sat}(T)$ is the temperature dependent saturation pressure of water, ψ_{cond} is the switch function that turns condensation on or off, ψ_{evap1} is the switch function governing evaporation at nearly saturation conditions, ψ_{evap2} is the switch function governing evaporation at nearly dry conditions, VS_{cond} is the volumetric rate of condensation, VS_{evap} is the volumetric rate of evaporation, and VS_{LW}^{net} is the net volumetric rate of liquid water formation. Applying this formulation to the conservation equation governing water vapor, the following results:

$$\nabla \bullet \left[\rho_g \omega_{wv} \boldsymbol{u} - \rho_g \omega_{wv} \sum_{\beta=1}^{n} \mathbb{D}_{wv-\beta} \nabla y_\beta \right] = -VS_{LW}^{net} \tag{4.6}$$

A minimum of two switch functions must be defined to model non-equilibrium phase change. However, to improve solvability, a dead band was introduced in the phase change switch functions. The introduction of the dead band required that a third switch function be formulated. The switch functions which determine the allowance of condensation (ψ_{cond}) and evaporation (ψ_{evap1}, ψ_{evap2}) are defined as:

$$\psi_{cond} = \begin{cases} 1 & if \ \dfrac{p_{wv}}{p_{sat}(T)} \geq 1.004 \\ 0 & if \ \dfrac{p_{wv}}{p_{sat}(T)} \leq 1.002 \end{cases} \tag{4.7}$$

$$\psi_{evap1} = \begin{cases} 0 & if \ \dfrac{p_{wv}}{p_{sat}(T)} \geq 0.998 \\ 1 & if \ \dfrac{p_{wv}}{p_{sat}(T)} \leq 0.996 \end{cases} \tag{4.8}$$

$$\psi_{evap2} = \begin{cases} 1 & if \ S \geq 0.0003 \\ 0 & if \ S \leq 0.0001 \end{cases} \tag{4.9}$$

There are gaps within the values described by the inequalities in each of the above switch functions. The value of the switch function in these gap regions is defined by a smoothed heaviside function that is approximately linear and greatly improves the solvability of the model.

In words, Eq. (4.7) states that no condensation occurs if the local partial pressure of water is less than 100.2% of the local saturation pressure. Furthermore, the full rate of condensation is not realized until this ratio is equal to 100.4%. Between a ratio of 100.2% and 100.4%, a reduced rate of condensation occurs in a nearly linear fashion. Similar conditions are described by Eq. (4.8), where no evaporation occurs if the local relative humidity is greater than 99.8%, and full speed evaporation does not occur until the relative humidity drops below a value of 99.6%. Based on these phase change criterion, it is clear that a dead band exists in the region defined by $0.998 < {}^{p_{wv}}\!/_{p_{sat}} < 1.002$ where no phase change can occur. Finally, Eq. (4.9) ensures that if the liquid water saturation in the GDL approaches zero, then no evaporation can occur. The reason for not defining this switch function at a value of exactly $S = 0$ is again to improve the solvability of the model.

The second governing equation in the comparative GDL model describes conservation of mass and momentum for the liquid water phase. The governing equation

for liquid water with the appropriate reduced saturation substitution and application of the UFT assumption is presented in Eq. (4.10).

$$\nabla \bullet \left[\rho_{LW} \frac{K k_{r,LW}}{\mu_{LW}} \frac{dP_c}{dS} \nabla S \right] = V S_{LW}^{net} \tag{4.10}$$

Each of the variables in Eq. (4.10) has been sufficiently described in previous Chapters and therefore will not be discussed further. The source term in Eq. (4.10) is simply the net rate of condensation. The source terms in the liquid and vapor equations are equal and opposite thus ensuring that overall mass is conserved even though mass is exchanged between the liquid and vapor phase.

4.1.4 Boundary conditions

Two types of boundary conditions will be used: constant conditions, and flux conditions. Constant conditions have no directionality and are therefore simple to specify. To clarify the directionality of flux conditions they are referenced to the inward normal vector ($-\vec{n}$).

The governing equation for gas diffusion requires two boundary conditions for (n-1) species: O_2, and water vapor (*wv*). For the oxygen species, a constant mass flux condition ($\dot{m}_{O_2}$), proportional to the current density (*j*) will be imposed at the GDL-catalyst layer boundary (B1) (Eq. (4.11)).

$$\dot{m}_{O_2}\Big|_{B1} = -\vec{n} \bullet \left(\rho_g \omega_{O_2} \boldsymbol{u} - \rho_g \omega_{O_2} \sum_{\beta=1}^{n} \mathbb{D}_{O_2-\beta} \nabla y_\beta \right) = -M_{O_2} \frac{j}{4F} \tag{4.11}$$

For the water vapor, a zero flux condition is imposed because all water production is assumed to be in the liquid phase.

At the GDL-GFC interface, boundary B2, the following constant mass fraction boundary condition will be utilized:

$$\omega_{wv}\big|_{B1} = \frac{M_{wv}}{M_g}\frac{p_{sat}(T)}{P_g}RH_{GFC} \tag{4.12}$$

This equation is simply a relationship between the stated relative humidity in the GFC and the mass fraction of water vapor at the GFC/GDL interface. In Eq. (4.12) M_g refers to the molar mass of the gaseous mixture which will be defined later. Similarly, it is assumed that the remaining mass fraction is a mixture of O_2 and N_2 where the ratio of the N_2 mass fraction to the O_2 mass fraction is defined as $r_{N_2:O_2}$.

$$\omega_{O_2}\big|_{B2} = \frac{1-\omega_{wv}\big|_{B2}}{1+r_{N_2:O_2}} \tag{4.13}$$

In Eq. (4.13) the ratio $r_{N_2:O_2}$ cannot be less than the ambient air value of 3.2918 but can exceed the ambient value due to depletion of oxygen in the GFC.

Two boundary conditions are also required for the liquid water momentum conservation equation. At the CL-GDL interface (B1) a flux condition (Eq. (4.14)) is applied that accounts for the production rate of water and the net effect of electro-osmotic drag (EOD) and back diffusion by the inclusion of an effective EOD coefficient (α_{EOD}).

$$\dot{m}_{LW}\big|_{B1} = -\vec{n}\bullet\left(\rho_{LW}\frac{Kk_{r,LW}}{\mu_{LW}}\frac{dP_c}{dS}\nabla S\right) = M_w\frac{j}{2F}\left(1+2\alpha_{EOD}\right) \tag{4.14}$$

The coefficient α_{EOD} is defined as:

$$\alpha_{EOD} = \frac{\text{net flux of } H_2O \text{ through the membrane}}{H^+ \text{ flux through the membrane}} \tag{4.15}$$

At the GDL-GFC interface the saturation value at the boundary is specified. The saturation value at the interface ($S_{GDL/GFC}$) is commonly assumed to be zero although it is

likely that there are water droplets at the interface making the value somewhat greater than zero. To allow for some flexibility in the solution process, the constant saturation boundary condition was actually formulated as a convective boundary condition according to Eq.(4.16).

$$\dot{m}_{LW}\big|_{B2} = \vec{n} \bullet \left(\rho_{LW} \frac{K k_{r,LW}}{\mu_{LW}} \frac{dP_c}{dS} \nabla S \right) = h_m \left(S - S_{GDL/GFC} \right) \tag{4.16}$$

In this formulation, the value of the mass transfer coefficient (h_m) could start small and be increased during the solution process until S was effectively equal to $S_{GDL/GFC}$.

4.1.5 Constitutive equations

A significant number of variables were utilized in the preceding sections which depend on local conditions and therefore need further definition. This section will define the relationships used for M_g, ρ_g, $\boldsymbol{u}$, $\tilde{D}_{\alpha\beta}$, $\mathbb{D}_{\alpha\beta}$, p_{wv}, $p_{sat}(T)$, ρ_{LW}, and μ_{LW}. Other variables that have no dependence on the local physical conditions such as R_u, γ, and K will be defined in Chapter 5 as constants. Furthermore, some constitutive relationships depend on the GDL material being modeled and will therefore be defined in Chapter 5 (e.g., $k_{r,LW}$, and $P_c(S)$) which presents experimental results for the GDL.

The gas phase density varies through the domain as the composition changes. To account for this density variation an effective molar mass of the gas mixture is first calculated according to Eq. (4.17). After calculating the local molar mass of the gaseous mixture the local gas phase density is calculated using Eq. (4.18).

$$M_g = y_{O_2} M_{O_2} + y_{wv} M_{wv} + y_{N_2} M_{N_2} \tag{4.17}$$

$$\rho_g = \frac{P_g M_g}{R_u T} \tag{4.18}$$

In Eq. (4.17) and (4.18) the variables are defined as follows: P_g is the pressure of the gaseous mixture, M_g is the local molar mass of the gaseous mixture, y denotes the local mole fraction of each species, M denotes the molar mass of each species, ρ_g is the local density of the gaseous mixture, R_u is the universal gas constant, and T is the local gas temperature.

The convective term in the species mass balance equations requires that a bulk gas phase velocity be defined if such a bulk velocity exists. When considering the diffusion of water vapor and oxygen through a stagnant film of nitrogen it becomes apparent that there is relative motion between the species. If the bulk velocity were to be defined as zero then the solution of the species balance would suggest a flux of nitrogen through the GDL/CL interface since the mass fraction of nitrogen would be changing as oxygen is consumed at the interface (thus resulting in a nitrogen mass fraction gradient). In actuality, the nitrogen species is non-reactive and therefore remains stagnant. Eq. (4.19) displays the equation for the total (bulk and diffusive) mass flux of the nitrogen species ($\dot{m}_{N_2}$) within the GDL. Setting the nitrogen mass flux to zero and solving for $\boldsymbol{u}$ reveals the proper equation for the bulk velocity of the gaseous mixture (Eq. (4.20)).

$$\dot{m}_{N_2} = \rho_g \omega_{N_2} \boldsymbol{u} - \rho_g \omega_{N_2} \sum_{\beta=1}^{n} \mathbb{D}_{N_2\beta} \nabla y_\beta \tag{4.19}$$

$$\boldsymbol{u} = \frac{1}{\omega_{N_2} \rho_g} \left[\rho_g \omega_{N_2} \sum_{\beta=1}^{n} \mathbb{D}_{N_2\beta} \nabla y_\beta \right] = \frac{-\text{diffusive mass flux of } N_2}{\omega_{N_2} \rho_g} \tag{4.20}$$

The Maxwell-Stefan diffusivity ($\tilde{D}_{\alpha\beta}$) is a difficult parameter to measure but it has been shown that for many systems it is appropriate to estimate it as the binary diffusivity ($D_{\alpha\beta}$) discussed in Chapter 2. The empirical equation for binary diffusivity presented as Eq. (2.21) and the diffusion volumes presented in Table 2.1 will be used in this work to calculate the values of the Maxwell-Stefan diffusivity for each species pair. Chapter 2 also discussed the use of binary diffusivity correction terms that incorporate the porosity and saturation of the porous media through which diffusion occurs. The most

common diffusivity corrections used in the literature (summarized in Table 2.2) are also used in this work to modify the Maxwell-Stefan diffusivities and are summarized in Eq. (4.21)-(4.23).

$$\tilde{D}_{\alpha\beta}^{eff} = \tilde{D}_{\alpha\beta} f(\varepsilon) g(S) \tag{4.21}$$

$$f(\varepsilon) = \varepsilon^{1.5} \tag{4.22}$$

$$g(S) = \left(1 - S\right)^{1.5} \tag{4.23}$$

The multicomponent Fick diffusivity, $\mathbb{D}_{\alpha\beta}$, is determined by forming a Maxwell-Stefan diffusivity ($\tilde{D}_{\alpha\beta}$) matrix and appropriately manipulating the matrix to account for interaction among the species. The universal method of diffusivity matrix manipulation is discussed further in the referenced texts [22, 54], but here only the results for a ternary system are presented. The effective multicomponent Fick diffusivities for a ternary system are defined in Eq. (4.24)-(4.26). Additional terms are calculated via cyclic permutation of the species indices (e.g., 1's become 2's, 2's become 3's, and 3's become 1's).

$$\mathbb{D}_{11} = \frac{\dfrac{\left(\omega_2 + \omega_3\right)^2}{y_1 \tilde{D}_{23}^{eff}} + \dfrac{{\omega_2}^2}{y_2 \tilde{D}_{13}^{eff}} + \dfrac{{\omega_3}^2}{y_3 \tilde{D}_{12}^{eff}}}{\dfrac{y_1}{\tilde{D}_{12}^{eff} \tilde{D}_{13}^{eff}} + \dfrac{y_2}{\tilde{D}_{12}^{eff} \tilde{D}_{23}^{eff}} + \dfrac{y_3}{\tilde{D}_{13}^{eff} \tilde{D}_{23}^{eff}}} \tag{4.24}$$

$$\mathbb{D}_{12} = \frac{\dfrac{\omega_1\left(\omega_2 + \omega_3\right)}{y_1 \tilde{D}_{23}^{eff}} + \dfrac{\omega_2\left(\omega_1 + \omega_3\right)}{y_2 \tilde{D}_{13}^{eff}} + \dfrac{{\omega_3}^2}{y_3 \tilde{D}_{12}^{eff}}}{\dfrac{y_1}{\tilde{D}_{12}^{eff} \tilde{D}_{13}^{eff}} + \dfrac{y_2}{\tilde{D}_{12}^{eff} \tilde{D}_{23}^{eff}} + \dfrac{y_3}{\tilde{D}_{13}^{eff} \tilde{D}_{23}^{eff}}} \tag{4.25}$$

$$\mathbb{D}_{\alpha\beta} = \mathbb{D}_{\beta\alpha} \tag{4.26}$$

The density of liquid water varies slightly with temperature. To add breadth to the modeling capabilities the temperature dependence of the density of liquid water was incorporated over a range of reasonable PEMFC operating temperature. The density variation and corresponding correlation to temperature is displayed in Figure 4.2.

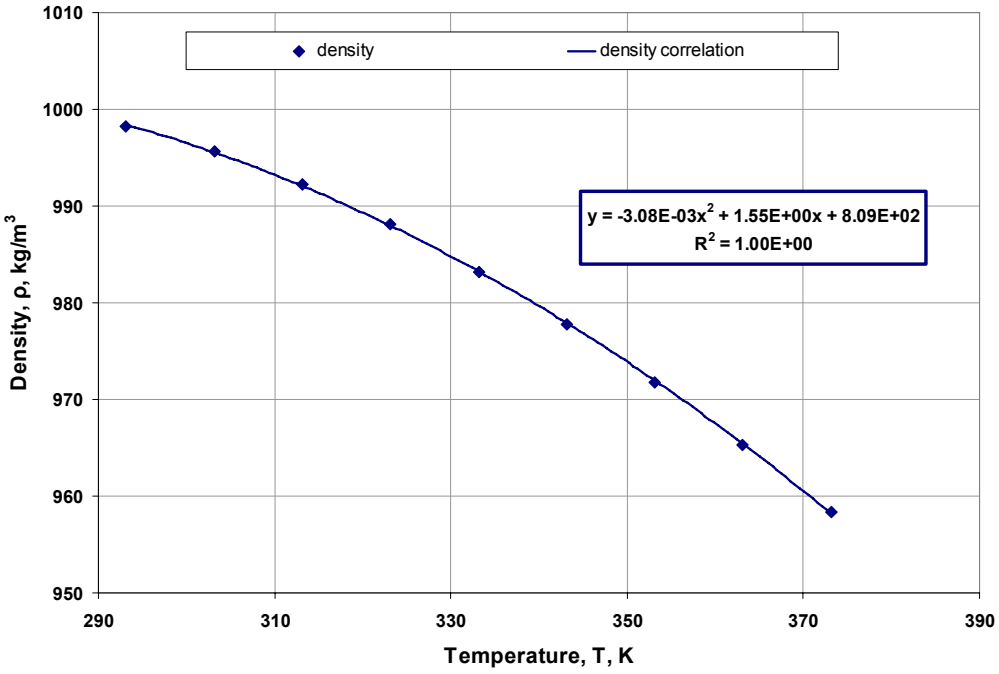

Figure 4.2 – Correlation used for liquid water density, data from [55].

Similar to density, the dynamic viscosity and surface tension of liquid water also vary with temperature. The relationship used in this work to account for the temperature dependence of liquid water viscosity and surface tension can be seen in Figure 4.3.

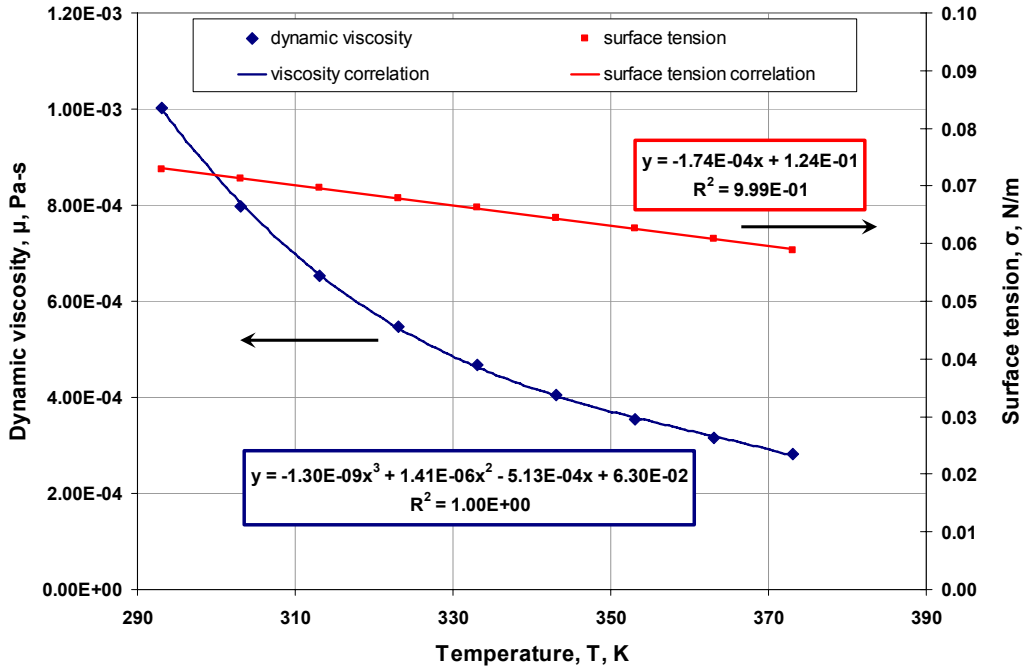

Figure 4.3 - Correlations used for liquid water viscosity and surface tension, data from [55].

4.2 TWO-DIMENSIONAL PEMFC MODEL

The reason for expanding the model to two dimensions is to capture the impact of the GDL compression under the shoulder of the bipolar plate on water transport and gas diffusion. The compressed region is expected to exhibit reduced gas and water permeability, thus causing a significant reduction in current production underneath the bipolar plate shoulder. The intent of the 2-D model is to predict polarization behavior without relying significantly on adjustment or tuning parameters as are common in PEMFC models. This model will focus more on the utilization of experimentally determined constants and transport relations. After the model simulations are performed the results will be compared to experimental polarization data to validate the model. The model inputs and experimental validation will be described in Chapter 5.

The conservation equations and constitutive relations presented in the previous section are also applied to the 2-D model, but there are four major additions. First, an energy conservation equation is implemented to include the impact that condensation and

evaporation can have on the local temperature within the GDL. Second, a charge conservation equation will be added to govern the flow of electrical current through the GDL. Third, a membrane sub-domain is introduced and an ionic charge conservation equation is implemented to capture the ionic losses in the membrane as well as interfacial losses within the cell assembly. Finally, the 2-D model includes an electrochemical relationship at the GDL/CL boundary so that a cell terminal voltage can be assigned and the local current density along the GDL/CL interface can be determined during the solution process. This is in contrast to the 1-D model where a current density is assigned and cell potential is never considered. The addition of an electrochemical boundary condition allows the model to predict polarization behavior, rather than being limited to predictions of field variables (e.g., S, $\dot{m}_{N_2}$, etc.) as was the case with the 1-D model.

4.2.1 Model assumptions

The following assumptions were made in the development of the 2-D PEMFC model:

- The fuel cell is operating at steady-state.
- A two-dimensional analysis is sufficient to model the effects of liquid water constitutive relationships when the PEMFC is operated at high stoichiometric ratios; i.e., down the channel effects can be neglected.
- The temperature in the GFC is constant due to its proximity to the bipolar plates which are held at uniform temperature by the cooling system.
- Thermal effects (e.g., conduction, heat generation due to the electrochemical reaction, and latent cooling due to evaporation) must be incorporated in the GDL model to properly characterize transport within the GDL.
- The concentrations of gaseous species in the GFC are constant and transport from the GDL to the bulk gas in the GFC can be estimated by a constant Sherwood number.

- The net flux of water into the GDL from the cathode catalyst layer in excess of the water produced due to the cathode reaction can be appropriately characterized by a constant *net effective* electro-osmotic drag coefficient (α_{EOD}).
- Water can change phase via evaporation and condensation in a rate limited non-equilibrium manner.

4.2.2 Two-dimensional model geometry

A 2-D cross-sectional view of a PEMFC is depicted in Figure 4.4. The 2-D model will explicitly include the portions of the PEMFC outlined in blue, and implicitly include the portions outlined in the dashed red line. The cathode catalyst layer (outlined in the red dashed line) will be collapsed to an electrochemically active interface where the membrane and cathode GDL mate.

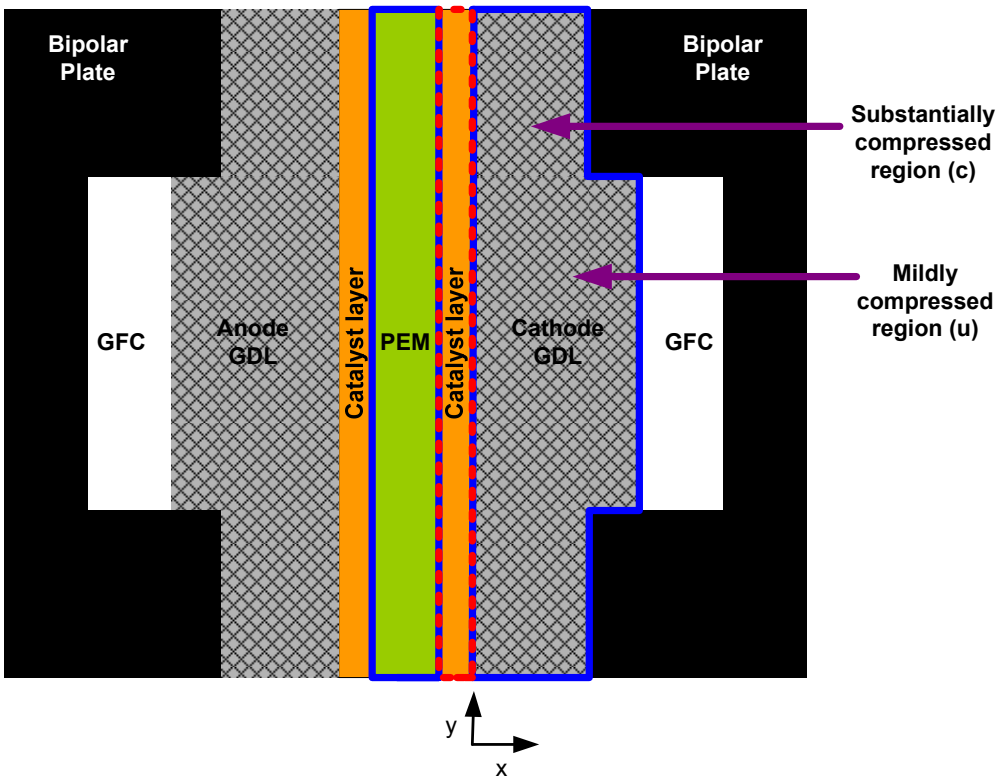

Figure 4.4 – 2-D section of a PEMFC.

Taking into account lines of symmetry, and separating the GDL into two sub-domains (mildly compressed under the channel (essentially uncompressed – "u"), and substantially compressed under the shoulder – "c") to allow for different constitutive equations in each sub-domain, the 2-D model geometry is reduced to that which is depicted in Figure 4.5.

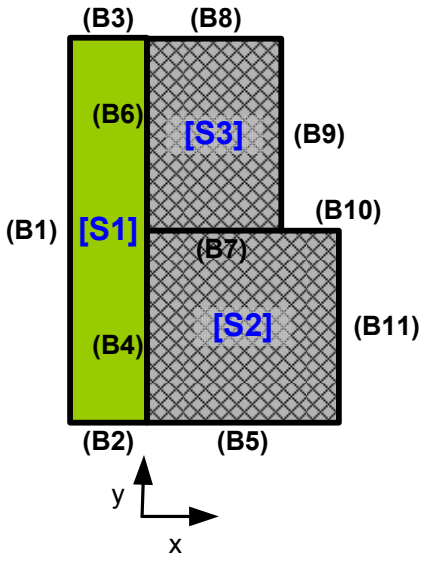

Figure 4.5 – 2-D PEMFC model geometry depicting sub-domains and boundaries.

The relationships derived using the experimental techniques discussed in Chapter 3 will be used to model transport within the GDL. The portions of the PEMFC outlined with the red dashed line in Figure 4.4 will be included implicitly via appropriate boundary equations at boundaries B4 and B6 depicted in Figure 4.5. These boundary conditions will include the effects of water transport through the PEM as well as the electrochemical relationship between local potential and current along the GDL/CL interface.

The equations in Section 4.1 were presented in a multidimensional format to allow for them to be applied in the 2-D model in addition to the 1-D model for which they were presented. The next subsection will present the additional conservation equations used in the 2-D model. In the subsequent sub-section all boundary conditions

will be presented for the 2-D model since the model geometry has changed significantly. The final sub-section will present any additional constitutive equations required for model closure.

4.2.3 Conservation equations

As previously discussed, the conservation equations presented for the 1-D model will also be utilized in the 2-D model. The addition of a thermal energy conservation equation, an electrical charge conservation equation, and an ionic charge conservation equation, will be discussed in this section. Prior to presenting the additional conservation equations it is important to define where each dependent variable will be active within the modeling domain. Figure 4.5 shows three different sub-domains (S1, S2, S3) and not all variables will be active in each sub-domain. Four dependent variables were described in the presentation of the 1-D model, and three additional dependent variables are included in the 2-D formulation. Specifically, the dependent variable for the energy equation is temperature (T), the dependent variable for electrical charge conservation is the electrical potential in the cathode GDL (φ_c), and the dependent variable for ionic charge conservation is the ionic potential in the membrane (φ_i). A description of where each conservation equation is active is presented in Table 4.1.

Table 4.1 – Summary of sub-domain activity for dependent variables.

Sub-domain	Dependent Variable						
	S	ω_{O2}	ω_{wv}	ω_{N2}	T	φ_c	φ_i
1	inactive	inactive	inactive	inactive	inactive	inactive	active
2	active	active	active	active	active	active	inactive
3	active	active	active	active	active	active	inactive

Thermal energy will be governed by conduction and convection through the GDL according to Eq. (4.27).

$$\nabla \bullet \left[-k_{T,eff} \nabla T + \rho_g c_p \boldsymbol{u} T \right] = V S_{th}^{net} \tag{4.27}$$

In Eq. (4.27) $k_{T,eff}$ is the local effective thermal conductivity of the solid/liquid/gas composition in the GDL, T is the local temperature within the GDL (it is assumed that the solid, liquid, and gaseous phase are in thermal equilibrium at any given location), ρ_g is the gas mixture density, c_p is the specific heat of the gas mixture, $\boldsymbol{u}$ is the bulk velocity of the gaseous phase as previously defined to enforce a stagnant nitrogen field, and VS_{th}^{net} is the local volumetric source of thermal energy.

The only source and sink for thermal energy within the GDL are condensation and evaporation, respectively. Therefore, the volumetric source of thermal energy within the GDL will be defined as:

$$VS_{th}^{net} = \Delta h_{fg} VS_{LW}^{net} \tag{4.28}$$

where Δh_{fg} is the enthalpy of vaporization for water, and VS_{LW}^{net} is the net rate of condensation.

Another conservation equation introduced in the 2-D model governs the flow of electrical charge within the GDL. Equation (4.29) presents the charge conservation equation where $\boldsymbol{\sigma}$ is the orthotropic electrical conductivity of the GDL and φ_c is the electrical potential in the cathode GDL. It is important to note that $\boldsymbol{\sigma_c}$ will be different in the compressed region of the GDL than it is under the GFC since the electrical conductivity of GDL materials improves with compression.

$$\nabla \bullet \left[-\boldsymbol{\sigma}_c \nabla \varphi_c \right] = 0 \tag{4.29}$$

The source term in the electrical charge conservation equation is set equal to zero since there is no volumetric source of electrical current generation within the GDL. All current will be introduced via a boundary condition described in the following section.

The final additional conservation equation introduced in the 2-D model governs the flow of ionic charge in the membrane according to Eq. (4.30)

$$\nabla \bullet \left[-\sigma_i \nabla \varphi_i \right] = 0 \tag{4.30}$$

where φ_i is the ionic potential in the membrane and σ_i is the isotropic membrane conductivity.

4.2.4 Boundary conditions

Due to the significant number of boundaries present in the 2-D model (see Figure 4.5), this section will sequentially address the boundary conditions associated with each conservation equation. It is necessary for each conservation equation to be assigned one boundary condition on all boundaries adjacent to the domains in which the conservation equation is active. It is again important to note that flux conditions are referenced to the inward normal vector (- $\vec{n}$).

The boundary conditions for the ionic charge conservation equation (only active in sub-domain S1) are presented in Eq. (4.31) -(4.33).

$$\varphi_i \big|_{B1} = \varphi_{i,A} \tag{4.31}$$

$$\vec{n} \bullet \left[\sigma_i \nabla \varphi_i \right]_{B2,B3} = 0 \tag{4.32}$$

$$-\vec{n} \bullet \left[\sigma_i \nabla \varphi_i \right]_{B4,B6} = -j_e \tag{4.33}$$

The ionic potential defined at B1 is the potential at the anode electrode, $\varphi_{i,A}$. Due to the symmetry at B2 and B3, zero normal flux conditions are assigned at those boundaries. Finally, at boundaries B4 and B6, the ionic current flowing through the membrane toward the catalyst layer is effectively converted to an electrical current, where the electrical current density is designated as j_e.

The water vapor conservation equation is active in sub-domains S2 and S3, and therefore boundary conditions are defined at all boundaries enclosing, and within those

regions. Equations (4.34) – (4.37) define the boundary conditions applicable to the water vapor conservation equation.

$$\dot{m}_{wv}\big|_{B4,B5,B6,B8,B9,B10} = -\vec{n} \bullet \left(\rho_g \omega_{wv} \boldsymbol{u} - \rho_g \omega_{wv} \sum_{\beta=1}^{n} \mathbb{D}_{wv-\beta} \nabla y_\beta \right) = 0 \tag{4.34}$$

$$\dot{m}_{wv}\big|_{B11} = -\vec{n} \bullet \left(\rho_g \omega_{wv} \boldsymbol{u} - \rho_g \omega_{wv} \sum_{\beta=1}^{n} \mathbb{D}_{wv-\beta} \nabla y_\beta \right) = h_D \left(\omega_{wv}\big|_{GFC} - \omega_{wv}\big|_{B11} \right) \tag{4.35}$$

$$\omega_{wv}\big|_{GFC} = \frac{M_w}{M_g} \frac{p_{sat}(T)}{P_g} RH_{GFC} \tag{4.36}$$

$$\vec{n}\big|_{S3} \bullet \dot{m}_{wv}\big|_{B7} = -\vec{n}\big|_{S2} \bullet \dot{m}_{wv}\big|_{B7} \tag{4.37}$$

Conditions of zero mass flux are set at the symmetry boundaries (B5, B8), the boundaries that represent the catalyst layer (B4, B6), and at the boundaries that border the bipolar plate shoulder (B9, B10). The zero flux conditions at the catalyst layer are imposed based on the assumption that the product water is introduced in the liquid phase. At B11 a convective condition is imposed where the water vapor mass fraction in the GFC is defined by Eq. (4.36) and h_D is the diffusive mass transfer coefficient. Finally, at the interior boundary that divides the channel and shoulder regions of the GDL, a continuity condition matches the flux of liquid water in each sub-domain (S2 and S3) at the interface (B7).

The type of boundary conditions for the oxygen species (Eq. (4.38) - (4.42)) are similar to the water vapor species with the exception of a flux into the catalyst layer that is proportional to the local electrical current density (j_e) generated via the electrochemical reaction.

$$\dot{m}_{O_2}\big|_{B4,B6} = -\vec{n} \bullet \left(\rho_g \omega_{O_2} \boldsymbol{u} - \rho_g \omega_{O_2} \sum_{\beta=1}^{n} \mathbb{D}_{O_2-\beta} \nabla y_\beta \right) = -M_{O_2} \frac{j_e}{4F} \tag{4.38}$$

$$\dot{m}_{O_2}\Big|_{B5,B8,B9,B10} = -\vec{n} \bullet \left(\rho_g \omega_{O_2} \boldsymbol{u} - \rho_g \omega_{O_2} \sum_{\beta=1}^{n} \mathbb{D}_{O_2-\beta} \nabla y_\beta \right) = 0 \tag{4.39}$$

$$\dot{m}_{O_2}\Big|_{B11} = -\vec{n} \bullet \left(\rho_g \omega_{O_2} \boldsymbol{u} - \rho_g \omega_{O_2} \sum_{\beta=1}^{n} \mathbb{D}_{O_2-\beta} \nabla y_\beta \right) = h_D \left(\omega_{O_2}\Big|_{GFC} - \omega_{O_2}\Big|_{B11} \right) \tag{4.40}$$

$$\omega_{O_2}\Big|_{GFC} = \frac{1-\omega_{wv}|_{GFC}}{1+r_{N_2:O_2}} \tag{4.41}$$

$$\vec{n}\big|_{S3} \bullet \dot{m}_{O_2}\Big|_{B7} = -\vec{n}\big|_{S2} \bullet \dot{m}_{O_2}\Big|_{B7} \tag{4.42}$$

Each of the variables in the above equations has been described previously with the exception of j_e. In the 1-D model it was inherently assumed that the entire catalyst layer surface produced a uniform local current density since the geometry had been collapsed to a line. Therefore, the local electrical current density produced at the catalyst layer (j_e) was equivalent to the average current density of the fuel cell (j) and the variable j could be used to represent both local and average current density. Unlike the 1-D model, the 2-D model must allow for variations in local current density along the surface of the catalyst layer and therefore must utilize different variables to represent local current density and average current density. The definitions of j and j_e will be covered in the constitutive equations section.

The liquid water conservation equation is inactive in the membrane sub-domain (S1). Additionally, product water is assumed to be introduced in the liquid phase and therefore is represented as a boundary condition associated with the liquid water conservation equation at B4 and B6. Similar to the gaseous species, zero normal flux conditions are imposed at symmetry boundaries and bipolar plate shoulder boundaries for the liquid phase. At the interior boundary (B7) a continuity constraint is assigned, and at the GFC boundary (B11) a convective condition is defined that is used to force a constant

GDL surface saturation, but is defined as a convection term to improve the models solvability. The boundary conditions for the liquid water phase are presented in equation form below.

$$\dot{m}_{LW}\big|_{B4,B6} = -\vec{n} \bullet \left(\rho_{LW} \frac{Kk_{r,LW}}{\mu_{LW}} \frac{dP_c}{dS} \nabla S \right) = M_w \frac{j_e}{2F} \left(1 + 2\alpha_{EOD}\right) \tag{4.43}$$

$$\dot{m}_{LW}\big|_{B5,B8,B9,B10} = -\vec{n} \bullet \left(\rho_{LW} \frac{Kk_{r,LW}}{\mu_{LW}} \frac{dP_c}{dS} \nabla S \right) = 0 \tag{4.44}$$

$$\vec{n}\big|_{S3} \bullet \left(\rho_{LW} \frac{Kk_{r,LW}}{\mu_{LW}} \frac{dP_c}{dS} \nabla S \right)\Bigg|_{B7}^{S3} = -\vec{n}\big|_{S2} \bullet \left(\rho_{LW} \frac{Kk_{r,LW}}{\mu_{LW}} \frac{dP_c}{dS} \nabla S \right)\Bigg|_{B7}^{S2} \tag{4.45}$$

$$\dot{m}_{LW}\big|_{B11} = \vec{n} \bullet \left(\rho_{LW} \frac{Kk_{r,LW}}{\mu_{LW}} \frac{dP_c}{dS} \nabla S \right) = h_m \left(S - S_{GDL/GFC}\right) \tag{4.46}$$

The extended version of the expression describing the mass flux of liquid water was used in the continuity condition at B7 (Eq. (4.45)) because most of the variables that precede the saturation gradient (K, $k_{r,LW}$, and dP_c/dS) exhibit different definitions in S2 and S3.

The electrochemical reaction at the catalyst later is exothermic and therefore heat must be introduced at the representative boundary as described in Eq. (4.47).

$$q\big|_{B4,B6} = -\vec{n} \bullet \left[-k_{T,eff} \nabla T + \rho_g c_p \boldsymbol{u} T \right] = f_{HP} (E_{oc,rev} - E_{cell}) j_e \tag{4.47}$$

In Eq. (4.47), q is the heat flux entering the GDL, f_{HP} is the heat partition factor determining the fraction of the electrochemically generated heat that travels towards the cathode GDL as opposed to traveling towards the anode, $E_{oc,rev}$ is the reversible (open circuit) cell potential, and E_{cell} is the actual terminal potential of the cell.

Furthermore, thermal insulation conditions are imposed at the symmetry boundaries according to Eq. (4.48), and constant temperatures conditions are imposed at

the bipolar plate shoulder (Eq. (4.49)). In Eq. (4.49) T_{cell} is defined as the operating temperature of the PEMFC, which in a PEMFC stack would be controlled by the cooling system.

$$q\big|_{B5,B8} = \vec{n} \bullet \left[-k_{T,eff} \nabla T + \rho_g c_p \boldsymbol{u} T \right] = 0 \tag{4.48}$$

$$T\big|_{B9,B10} = T_{cell} \tag{4.49}$$

Similar to the liquid water condition set at the GFC boundary, a convective term is used to allow flexibility in the solution process. The thermal convection coefficient, h_T, can be appropriately adjusted to achieve a constant surface temperature condition if desired.

$$q\big|_{B11} = \vec{n} \bullet \left[-k_{T,eff} \nabla T + \rho_g c_p \boldsymbol{u} T \right] = h_T \left(T - T_{GFC} \right) \tag{4.50}$$

Finally, the thermal energy conservation equation requires a continuity condition across the interior boundary B7 as shown in Eq. (4.51).

$$\vec{n}\big|_{S3} \bullet \left[-k_{T,eff} \nabla T + \rho_g c_p \boldsymbol{u} T \right]_{B7}^{S3} = -\vec{n}\big|_{S2} \bullet \left[-k_{T,eff} \nabla T + \rho_g c_p \boldsymbol{u} T \right]_{B7}^{S2} \tag{4.51}$$

Here, the local effective thermal conductivity (to be defined in the section on constitutive equations) is a function of the local saturation and porosity, and therefore will vary across the boundary. It is for this reason that the terms in Eq. (4.51) are defined with respect to the sub-domain in which the governing equation is applied.

The boundary conditions applicable to the electrical charge conservation equation are displayed in Eq. (4.52) - (4.55).

$$-\vec{n} \bullet \left[\boldsymbol{\sigma}_c \nabla \varphi_c \right]_{B4,B6} = j_e \tag{4.52}$$

$$-\vec{n} \bullet \left[\boldsymbol{\sigma}_c \nabla \varphi_c\right]_{B5,B8,B10,B11} = 0 \tag{4.53}$$

$$\varphi_c\big|_{B9} = E_{cell} \tag{4.54}$$

$$\vec{n}\big|_{S3} \bullet \left[-\boldsymbol{\sigma}_c \nabla \varphi_c\right]_{B7}^{S3} = -\vec{n}\big|_{S2} \bullet \left[-\boldsymbol{\sigma}_c \nabla \varphi_c\right]_{B7}^{S2} \tag{4.55}$$

In Eq. (4.52) the current flux at boundaries B4 and B6 is set equal to the electrical current generated via the electrochemical reaction (will be defined in next section). Zero flux conditions are described by Eq. (4.53) at the symmetry boundaries and at the GDL/GFC interface. The portion of the GDL that is compressed against the bipolar plate shoulder (B9) is defined as an equipotential surface equal to the terminal potential of the fuel cell. Finally, a current continuity condition is set across interior boundary B7. It is again important to note that the term in front of the gradient (in this case $\boldsymbol{\sigma_c}$) exhibits a different definition in sub-domain S2 and S3.

4.2.5 Constitutive equations

Five new terms have been introduced for the 2-D model in addition to those described in the 1-D model development, including: the effective thermal conductivity in the GDL domain ($k_{T,eff}$), the enthalpy of vaporization of water (Δh_{fg}), the electrical conductivity of the GDL ($\boldsymbol{\sigma_c}$), the effective ionic conductivity of the membrane (σ_i), and the local electrical current density along the GDL/MEA boundary (j_e). Furthermore, the 2-D model will utilize a different set of diffusivity corrections than the 1-D model. This section will describe the equations which govern the aforementioned variables.

The popular Bruggeman correction was used to correct the gas diffusivity in the 1-D model because it is the relationship that was used in the works with which comparisons were made. However, the Bruggeman correction was developed for sand, whereas the relationships presented by Nam et al. [10] were determined numerically for

porous media similar to a carbon fiber paper. Therefore, the 2-D model will utilize the diffusivity corrections suggested by Nam which are presented in Eq. (4.56)-(4.57).

$$f(\varepsilon) = \varepsilon\left(\frac{\varepsilon - 0.11}{1 - 0.11}\right)^{0.785} \tag{4.56}$$

$$g(S) = (1 - S)^2 \tag{4.57}$$

The effective thermal conductivity of the GDL domain is actually a hybrid of the thermal conductivity of the materials which make up that domain. At any given location within the GDL there is a solid phase composed of carbon fiber, a gaseous phase made up of the gas mixture, and a liquid phase made up of liquid water. To develop the equation for the effective thermal conductivity within the GDL domain it is convenient to consider conduction through a plane wall. Allowing each phase to be treated as a proper proportion of the facial area of the wall and allowing heat to flow through each portion of the face in parallel yields Eq. (4.58) which describes the effective thermal conductivity within the GDL domain. It should be noted that the thermal conductivity at any location is considered to be isotropic.

$$k_{T,eff} = (1 - \varepsilon)k_{carb} + \varepsilon S k_{LW} + \varepsilon(1 - S)k_g \tag{4.58}$$

The energy associated with water changing phase from liquid to vapor (Δh_{fg}) appears in many of the governing equations described previously. The magnitude of Δh_{fg} varies with temperature and therefore a functional relationship between the enthalpy of vaporization and temperature must be described. A plot of this relationship along with the linear correlation is displayed in Figure 4.6.

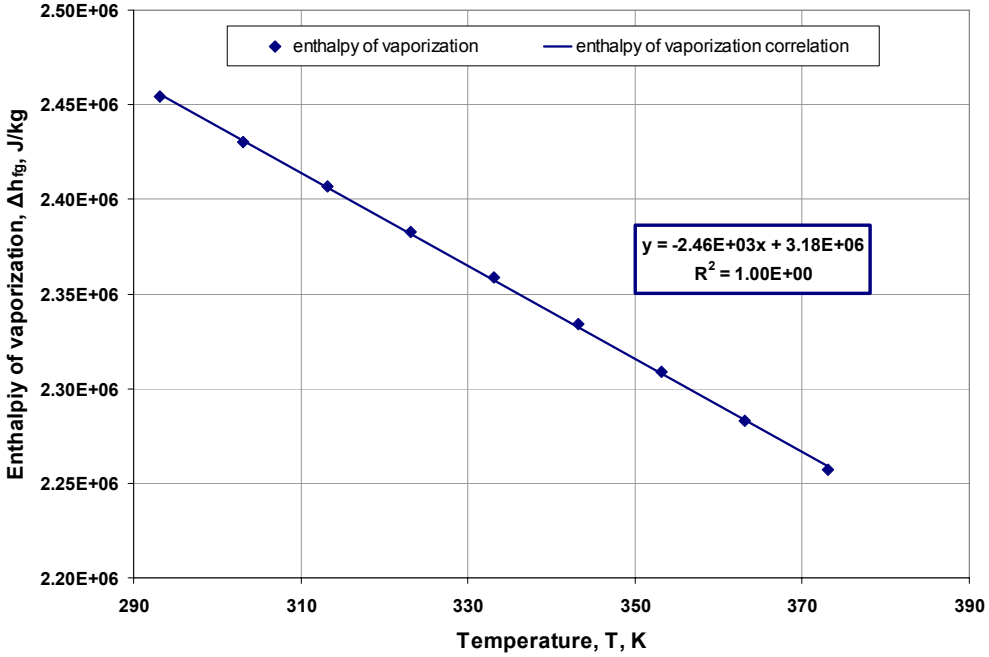

Figure 4.6 – Variation in Δh_{fg} with temperature.

The electrical conductivity of the cathode GDL, σ_c, is actually an orthotropic tensor and accounts for the anisotropy of the GDL. Both the in-plane and through-plane electrical conductivity of the GDL will be considered as defined in Eq. (4.59).

$$\boldsymbol{\sigma}_c = \begin{pmatrix} \sigma_{GDL,x} & 0 \\ 0 & \sigma_{GDL,y} \end{pmatrix} \tag{4.59}$$

It has been shown that in-plane resistance of GDL materials varies minimally under varying degrees of compression, but that through-plane resistance is a strong function of compression [48]. Therefore, the conductivity of the GDL will not only be different under the bipolar plate shoulder than it is under the GFC, it will also vary directionally where $\sigma_{GDL,x}$ refers to the through-plane conductivity, and $\sigma_{GDL,y}$ refers to the in-plane conductivity.

Some elaboration is needed concerning the effective ionic conductivity of the membrane, σ_i. As previously mentioned, the membrane domain is included to account for the membrane resistance as well as all interfacial resistances within the PEMFC

assembly. An equivalent resistance that accounts for all real resistances within a PEMFC can easily be quantified by extracting the high frequency resistance (HFR) from an electrochemical impedance spectrum. Normalizing the measured HFR to the cell area yields an area specific high frequency resistance, HFR', where the units are (Ω-cm^2). It is important to note that the GDL resistance is included explicitly in the model. Therefore, the GDL resistance must be removed from the HFR' measurement prior to implementing the HFR' measurement into an expression for the effective membrane conductivity, σ_i. The area specific resistance of the membrane and interfacial resistances ($ASR_{m,i}$) is defined as:

$$ASR_{m,i} = HFR' - ASR_{2\times GDL} \tag{4.60}$$

where ASR_{2xGDL} is the known value of the combined area specific resistance for the anode and cathode GDLs calculated from a 2D model of the GDL. Finally, the area specific resistance of the membrane and interfaces is converted to an effective membrane conductivity via Eq. (4.61).

$$\sigma_i = \frac{t_{mem}}{ASR_{m,i}} \tag{4.61}$$

The local current density generated along the boundaries representing the interface between the GDL and the CL is not as easily defined as the previously discussed variables. Rather than simply defining j_e with minimal explanation, it is important to provide some background into the development of the constitutive relationships that govern the electrochemical reaction. The remainder of this section is dedicated to developing such relationships.

In the 2-D PEMFC model being developed there are six sources of overpotential. Four of the sources of overpotential are ohmic in nature and are described as follows: the ohmic overpotential associated with the anode GDL ($\eta_{GDL,A}$); the ohmic overpotential of the cathode GDL ($\eta_{GDL,C}$); the ohmic overpotential associated with interfaces within the

cell assembly (η_i); and the ohmic overpotential of the membrane (η_m). The other two sources of overpotential are due to the activation barrier at the electrodes and are defined as: the activation overpotential associated with the anode reaction ($\eta_{act,A}$); and the activation overpotential associated with the cathode reaction ($\eta_{act,C}$). The schematic represented as Figure 4.7 shows the relationship between the open circuit potential (E_{oc}), the terminal potential of the cell (E_{cell}), and the six sources of overpotential.

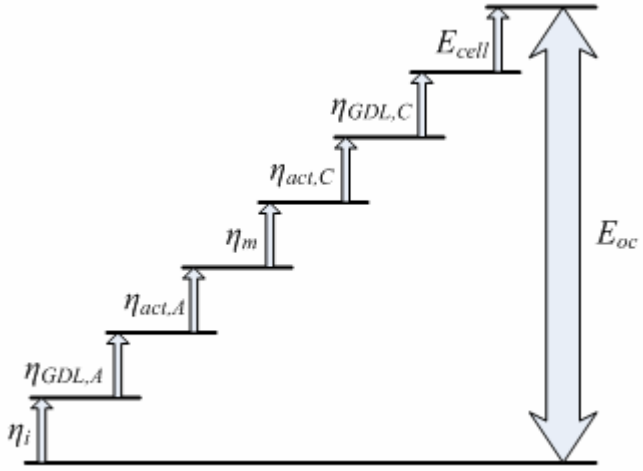

Figure 4.7 – Schematic of overpotentials in a PEMFC.

For hydrogen-air PEMFCs, the activation overpotential associated with the anode is generally negligible due to the minimal activation barrier at the anode. In addition, it will be assumed in this work that the two GDL overpotentials are equal. Application of these assumptions results in the following equation that describes the activation overpotential at the cathode catalyst interface.

$$\eta_{act,C} = E_{oc} - E_{cell} - 2\eta_{GDL} - \eta_{m,i} \tag{4.62}$$

where $\eta_{m,i}$ is the sum of the membrane overpotential (η_m) and interfacial overpotential (η_i).

It is necessary to further define some of the terms in Eq. (4.62). E_{oc} is measured for the cell of interest. The GDL overpotential is essentially the potential drop realized by the current traveling from its source location at the GDL-CL interface, to its collected location at the bipolar plate-GDL interface. This potential drop varies with location and can be defined as:

$$\eta_{GDL}(y) = \varphi_c(y)\big|_{B4,B6} - E_{cell} \tag{4.63}$$

As previously discussed, the ohmic overpotential associated with the membrane and all interfaces is lumped together to calculate an effective conductivity in the membrane. Therefore the combination of the interfacial and membrane is defined as:

$$\eta_{m,i}(y) = \varphi_{i,A} - \varphi_i(y)\big|_{B4,B6} \tag{4.64}$$

where $\varphi_{i,A}$ is the arbitrarily defined value of ionic potential at the equipotential anode surface of the membrane, and $\varphi_i(y)\big|_{B4,B6}$ is the local ionic potential at the cathode catalyst layer which varies with location. The value assigned to $\varphi_{i,A}$ is inconsequential because what is actually important is the potential drop across the membrane, and not the actual value of the ionic potential.

Combining the preceding definitions with Eq. (4.62) yields a convenient expression that will be utilized later.

$$\eta_{act,C}(y) = E_{oc} + E_{cell} - 2\varphi_c(y)\big|_{B4,B6} - \varphi_{i,A} + \varphi_i(y)\big|_{B4,B6} \tag{4.65}$$

In electrochemical devices the relationship between potential and current is typically determined by some form of the Butler-Volmer equation. The Butler-Volmer equation basically states that in an electrochemical reaction the current produced increases exponentially with overpotential. This equation can take on various forms, but the form that we will start with in this work was specifically derived to include both activation and diffusive losses, where the diffusive losses are incorporated via a

concentration ratio. The textbook authored by O-Hayre [56] presents the diffusion and activation limited form of the Butler-Volmer equation as:

$$j_e = j_0^0 \left[\frac{c_R^*}{c_R^{0*}} \exp\left(\frac{\alpha n F}{R_u T} \eta \right) - \frac{c_P^*}{c_P^{0*}} \exp\left(-\frac{(1-\alpha) n F}{R_u T} \eta \right) \right] \tag{4.66}$$

where j_e is the current density at the electrode surface (in this case the GDL/CL boundary), j_0^0 represents the exchange current density measured at the reference reactant and product concentrations (c_R^{0*} and c_P^{0*} respectively), c_R^* and c_P^* represent the surface concentrations of the rate-limiting reactant and product species, α is the transfer coefficient and relates to the symmetry of the reaction (typical range: $0.2 < \alpha < 0.5$) , n is the number of electrons transferred in the electrochemical reaction, F is Faraday's constant, R_u is the universal gas constant, T is the local temperature, and η in this case refers to the cathode activation overpotential ($\eta_{act,C}$).

Simplifications are common when dealing with the Butler-Volmer equation. In particular, if the system of interest operates at relatively large overpotentials (50-100 mV) the backwards reaction is negligible (i.e., the forward reaction dominates) and the second exponential term in the Butler-Volmer equation can be eliminated. Elimination of the second exponential term in Eq. (4.66), substituting the expression displayed in Eq. (4.65) for η, and recognizing that the reactant in this case is oxygen yields an expression for the local current density.

$$j_e(y) = j_0^0 \left[\frac{c_{O_2}(y)}{c_{O_2}^0} \exp\left(\frac{\alpha n F}{R_u T} \left(E_{oc} + E_{cell} - 2\varphi_c(y)\big|_{B4,B6} - \varphi_{i,A} + \varphi_i(y)\big|_{B4,B6} \right) \right) \right] \tag{4.67}$$

Equation (4.67) is defined only along boundaries B4 and B6 since those are the boundaries which represent the catalyst layer surface. In Eq. (4.67) the reactant concentrations refer to the oxygen species where c_{O_2} is defined as:

$$c_{O_2}(y) = \frac{y_{O_2} P_g}{RT} \tag{4.68}$$

along the catalyst later interface. Alternatively, the reference concentration ($c_{O_2}^0$) will be determined based on the concentration of oxygen for which the parameters j_0^0, and α were measured.

4.3 SUMMARY OF MODELING EFFORTS

The primary focus of this work was to develop relationships grounded in experimental results that properly govern the transport of liquid water within the GDL of PEMFCs. By nature, empirical relationships are only useful if they are properly implemented in an analytical setting. This chapter outlined the efforts toward an analytical implementation of the constitutive relationships measured experimentally via the methods described in Chapter 3.

It is the hope of the author that the one-dimensional model will provide insight into the appropriateness of the relationships making up the liquid water transport coefficient that have been used in previous attempts at modeling water transport in PEMFCs. The 1-D parametric study will not only confirm or refute the previously used relationships but it will also provide guidance for future GDL design.

The two-dimensional model is expected to be able to predict polarization behavior for a variety of GDL materials while using experimentally determined water transport characteristics. Although the 2-D model is not comprehensive in that it only addresses the physics within the cathode GDL, it is viewed as a stepping stone toward a comprehensive PEMFC model which can aid in future PEMFC design and performance improvement.

5 RESULTS AND DISCUSSION

This chapter will present the results of the experimental efforts described in Chapter 3, and the analytical efforts described in Chapter 4. The purpose of the experiments described in Chapter 3 was to establish constitutive relations that govern the transport of liquid water in the macroporous GDL of PEMFCs. Such relations are vital to the understanding of liquid water transport but yet, prior to this work, have generally been assumed or adapted from other porous media. Chapter 4 presented a 1-D model developed to compare the influence of the constitutive relations that govern water transport. The experimentally determined constitutive relations from this work and the assumed relations used in other works will be implemented and compared. In addition, Chapter 4 presented a 2-D model that included the effects of GDL compression under the shoulder of a bipolar plate, and the electrochemical relationship necessary to predict polarization behavior. The 2-D model was built to investigate the ability of a model to predict polarization behavior for PEMFCs based on the constitutive relations developed for the different porous GDL media (carbon paper and carbon cloth).

The portions of this chapter dealing with experimental results will first discuss the porosity measurements performed on several gas diffusion layer materials (Section 5.1). Section 5.2 will present and discuss the capillary behavior of these materials, and Section 5.3 will describe the absolute and relative permeability of a subset of the GDL materials investigated. Finally, Section 5.4 will summarize the experimental results. The remainder of Chapter 5 focuses on the analytical efforts described in Chapter 4. In Section 5.5 the results obtained from the 1-D comparative model show the disparity among constitutive equations used in PEMFC modeling. Section 5.6 presents the experimentally determined polarization behavior for two fuel cells utilizing two different representative GDL materials. In the final section, Section 5.7, the 2-D model is used to predict polarization performance based on the properties measured for each representative GDL material.

5.1 POROSITY OF GDL MATERIALS

The results of the buoyancy and gravimetric methods of porosity determination described in Chapter 3 are the focus of this section. Carbon cloth type B-1A (BASF Fuel Cell), and carbon paper (Toray TGPH-090) obtained from BASF Fuel Cell with a variety of specified bulk PTFE treatments (0, 10, 20, and 30% by mass) were tested. The results of the porosity experiments are presented in Table 5.1, where C and P refer to carbon cloth and carbon paper respectively, and the digits following the C or P refer to the weight percent of PTFE treatment specified by the manufacturer.

As described in Chapter 3, the buoyancy method relies on Archimedes principle where the weight of the media is measured in air and also while suspended in a totally wetting fluid (n-pentane). The difference in weight, along with the volume of the sample can be used to determine the porosity. The gravimetric method relies on a determination of the bulk PTFE loading via thermal gravimetric analysis (TGA) followed by application of the actual weight percent of PTFE, and the density of each constituent, to a sample of known total volume to determine the porosity of the sample.

It can be seen in Table 5.1 that the buoyancy method always suggests a greater porosity than the gravimetric method which is the opposite of what was expected. Recall from Chapter 3, that the buoyancy method cannot account for trapped pore space while the gravimetric method can. Thus, the buoyancy method should understate the porosity. However, there is a clear trend suggesting that the methods themselves, and not the materials, are responsible for the differences. The suspension of the materials in n-pentane during the buoyancy measurement could cause a small mass of unconsolidated PTFE and carbon fibers to be rinsed from the pore space of the medium. Such rinsing would reduce the mass of the material, and suggest a greater buoyant force, therefore suggesting a greater pore volume than is truly present. Nonetheless, the porosity values determined via the two methods only vary by a maximum of 4.7% and an average of 2.1%. Therefore, the average of the two values will be used throughout the remainder of this work.

Table 5.1 – Results from porosity experiments.

GDL designation	As-received thickness (t_o)*	Specified PTFE content	PTFE content by TGA	Calculated as-received porosity (ε_o)		
	(μm)	*(wt %)*	*(wt %)*	*gravimetric*	*buoyancy*	*average*
C-0	374	0	0	0.813	0.819	**0.816**
C-10	412	10	9.2	0.810	0.813	**0.812**
C-20	429	20	18.1	0.797	0.799	**0.798**
C-30	419	30	30.5	0.795	0.795	**0.795**
P-0	290	0	0	0.752	0.772	**0.762**
P-10	295	10	8.9	0.720	0.753	**0.737**
P-20	299	20	20.8	0.705	0.734	**0.719**
P-30	280	30	27.0	0.694	0.723	**0.709**

*measured under stress of < 16 kPa

5.2 CAPILLARY PRESSURE-SATURATION RELATIONSHIPS IN GDL MATERIALS

The capillary pressure-saturation behavior for each of the eight materials described in the previous section was measured via the method described in Chapter 3. It was the desire in this work to measure constitutive relations that are applicable to the state of the media in a fuel cell environment. Therefore, a mildly compressed sample of the GDL materials, representative of the region under a bipolar plate gas channel, was used for the study related to PTFE content of the GDL materials. The materials tested under this mildly compressed state carry a "u" after their material designation that states that they are representative of the nominally *uncompressed* material under a channel in a bipolar plate. For example, P-20u is carbon paper with a 20% bulk PTFE treatment that approximates the media under a gas flow channel in a bipolar plate (i.e., the thickness is 89% of the as-received thickness). Alternatively, the effects of increased compression were also investigated with a subset of materials, namely C-20 and P-20. The materials tested under increased compression were representative of the material under the shoulder area of a bipolar plate, and carry a "c" at the end of their material designation to indicate a substantial level of *compression*. Table 5.2 presents the actual percentage of the uncompressed thickness achieved for each material.

Table 5.2 – Fraction of uncompressed thickness for each material tested.

GDL designation	As-received thickness (t_o)	Sample holder cavity depth - uncompressed - "u"		Sample holder cavity depth - compressed - "c"	
	(μm)	*(μm)*	% t_o	*(μm)*	% t_o
C-0	374	381	102%	279	-
C-10	412		92%		-
C-20	429		89%		65%
C-30	419		91%		-
P-0	290	267	92%	191	-
P-10	295		90%		-
P-20	299		89%		64%
P-30	280		95%		-

The porosity results presented in the previous section, along with the level of compression presented above, are critical parameters in the measurement of P_c-S curves when using the method of gas displacement porosimetry (GDP) described in Chapter 3. The uncompressed porosity, coupled with the compressed thickness of the material allow for the calculation of the pore volume of the compressed material. The pore volume of the material being tested is vital to the determination of saturation.

Prior to presenting the complete results for the materials of interest, a brief discussion demonstrating the applicability of the GDP method, addressing the repeatability of the experimental method, and establishing the uncertainties associated with the GDP method is presented.

5.2.1 Proof of concept, measurement uncertainty, and repeatability

The primary advantages of the GDP method compared to other porosimetry methods discussed in Chapter 3 is its ability to use water as its working fluid, and to measure the hydrophilic porosity of porous materials exhibiting mixed or fractional wettability. To investigate the ability of the GDP technique to measure hydrophilic porosity, a low porosity hydrophobic membrane (LPHM), as described in Chapter 3, was bonded to an aluminum washer, and a highly hydrophilic rayon cloth (Bemcot S-2 clean room wiper) was placed underneath the LPHM inside the sample chamber.

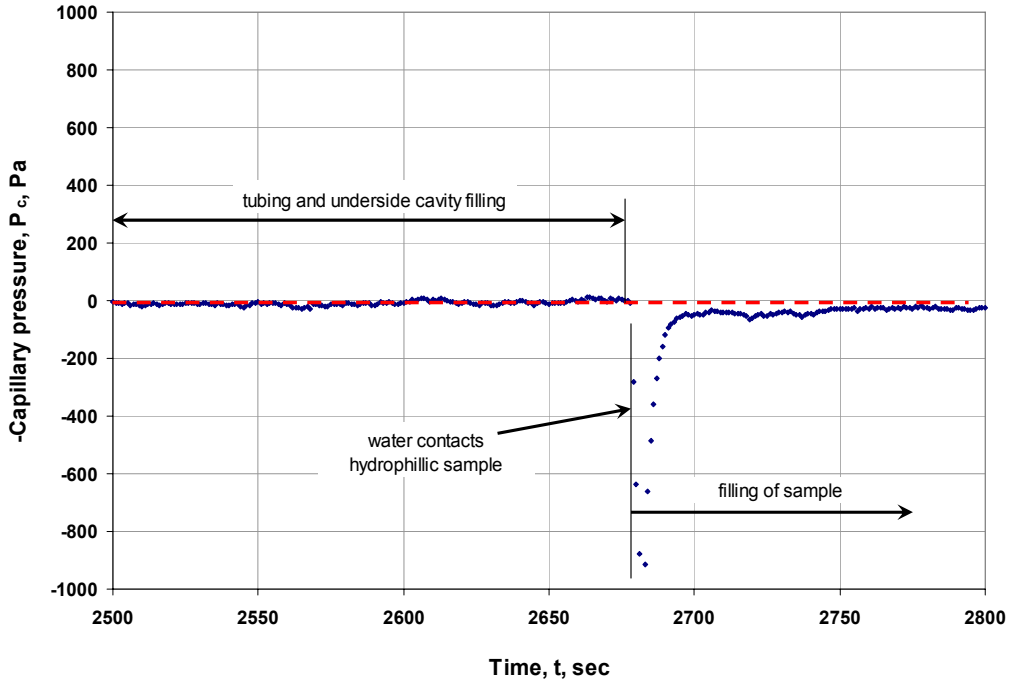

Figure 5.1 – GDP proof of concept for a hydrophilic cloth.

The resulting pressure versus time curve is presented in Figure 5.1. It should be noted that the y-axis of the following plot is the negative of the capillary pressure (so that the GDL behavior is represented primarily by positive numbers) consistent with the convention outlined in Chapter 2.

It can be seen that the water fills the tubing leading to the chamber for approximately 2675 seconds before it comes in contact with the hydrophilic cloth. The moment the water contacts the cloth, a significantly positive capillary pressure (negative on the graph) is measured, representing a vacuum effect in the water filling tube because the syringe pump is not set at a rate sufficient to satisfy the demands of the hydrophilic cloth. Subsequently, the syringe pump rate can sustain the rate of intrusion that the hydrophilic cloth requires and hydrophilic intrusion continues at a minimally positive capillary pressure until the cloth is saturated.

The resolution of the differential pressure transducer (which was selected for the maximum range appropriate to diffusion media) is admittedly not sufficient to reduce the scatter about the zero capillary pressure reference line, but even so, it is sufficient to

illustrate that hydrophilic pores do exhibit a positive capillary pressure in the GDP method.

The measurement error associated with the collection of P_c-S data is evaluated for the pressure measurement and the saturation measurement. The uncertainty of the capillary pressure is based solely on the stated accuracy of the differential pressure transducer. In contrast, saturation is determined via Eq.(5.1), and therefore requires a propagation of error analysis.

$$S = \frac{\Delta V_{pump} - \Delta V_{trans}}{\pi/4 D^2 t \left(\varepsilon_o \, 1/t_o\right)} \tag{5.1}$$

In Eq. (5.1) ΔV_{pump} is the volume discharged from the syringe pump into the sample, ΔV_{trans} is the volume change in the liquid side cavity of the pressure transducer which is a function of pressure, D is the diameter of the GDL sample, t is the compressed thickness of the specimen, ε_o is the uncompressed porosity of the specimen, and t_o is the uncompressed thickness of the specimen.

As can be seen from Eq. (5.1) the following sources of error must be addressed in the propagation of error analysis: the error of the syringe pump volume displacement ($u_{\Delta V_{pump}}$) ; the error of the thickness gage used to measure the uncompressed GDL thickness (u_{t_o}); the machining tolerance of the sample cavity holder depth (u_t); the error associated with the calipers used to measure the sample diameter (u_D); an assumed error for the value of porosity used in the saturation calculation (u_{ε_o}); and finally, the error associated with the volumetric displacement of the diaphragm in the differential pressure transducer ($u_{\Delta V_{trans}}$). The resulting equation describing the propagation of error associated with the calculation of saturation is displayed in Eq. (5.2).

$$u_S = \pm\left[\left(\frac{\partial S}{\partial x_1}u_{x_1}\right)^2 + \ldots + \left(\frac{\partial S}{\partial x_n}u_{x_n}\right)^2\right]^{1/2}$$

$$= \pm\left[\begin{array}{l}\left(\dfrac{1}{\pi/4\, D^2 t\left(\varepsilon_o\, {}^{t}/_{t_o}\right)}u_{\Delta V_{pump}}\right)^2 + \left(\dfrac{1}{\pi/4\, D^2 t\left(\varepsilon_o\, {}^{t}/_{t_o}\right)}u_{\Delta V_{trans}}\right)^2 + \\ \left(2\dfrac{\Delta V_{pump} - \Delta V_{trans}}{\pi/4\, D^3 t\left(\varepsilon_o\, {}^{t}/_{t_o}\right)}u_D\right)^2 + \left(\dfrac{\Delta V_{pump} - \Delta V_{trans}}{\pi/4\, D^2 t\left(\varepsilon_o^{\,2}\, {}^{t}/_{t_o}\right)}u_{\varepsilon_o}\right)^2 + \\ \left(2\dfrac{\Delta V_{pump} - \Delta V_{trans}}{\pi/4\, D^2 t^2\left(\varepsilon_o\, {}^{t}/_{t_o}\right)}u_t\right)^2 + \left(\dfrac{\Delta V_{pump} - \Delta V_{trans}}{\pi/4\, D^2 t^2 \varepsilon_o}u_{t_o}\right)^2\end{array}\right]^{1/2} \qquad (5.2)$$

The cavity volume on the liquid side of the diaphragm style differential pressure transducer increases with increasing water pressure thus requiring that the volume of water entering the cavity be reflected in the calculation of saturation. To account for this volume, the syringe pump output was dead ended into the liquid side of the transducer, while the gas side was left open to the atmosphere. After bleeding the liquid side cavity until all of the air was displaced, the bleed port was closed and the pressure increase as the syringe pump forced additional liquid into the transducer was recorded. This was repeated fourteen times and a 95% confidence interval about the average was calculated (Figure 5.2). The uncertainty of the transducer volume change is the difference between the average curve and the 95% confidence curve. Polynomial curve fits for these two curves are presented in Figure 5.3.

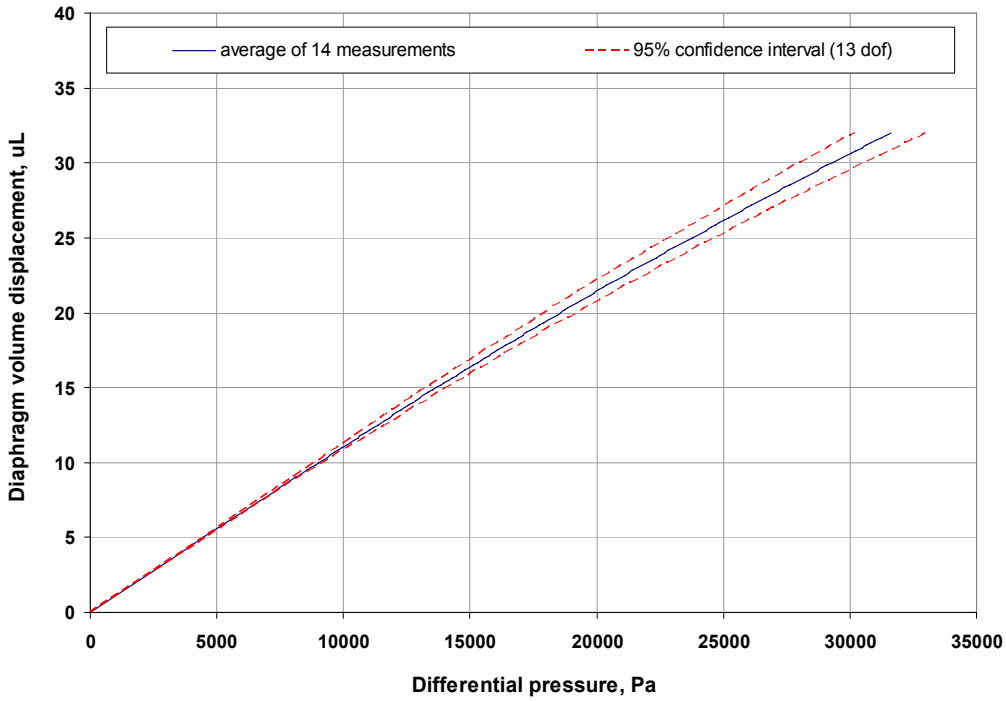

Figure 5.2 – Liquid volume calibration for differential pressure transducer used for P_c-S measurements.

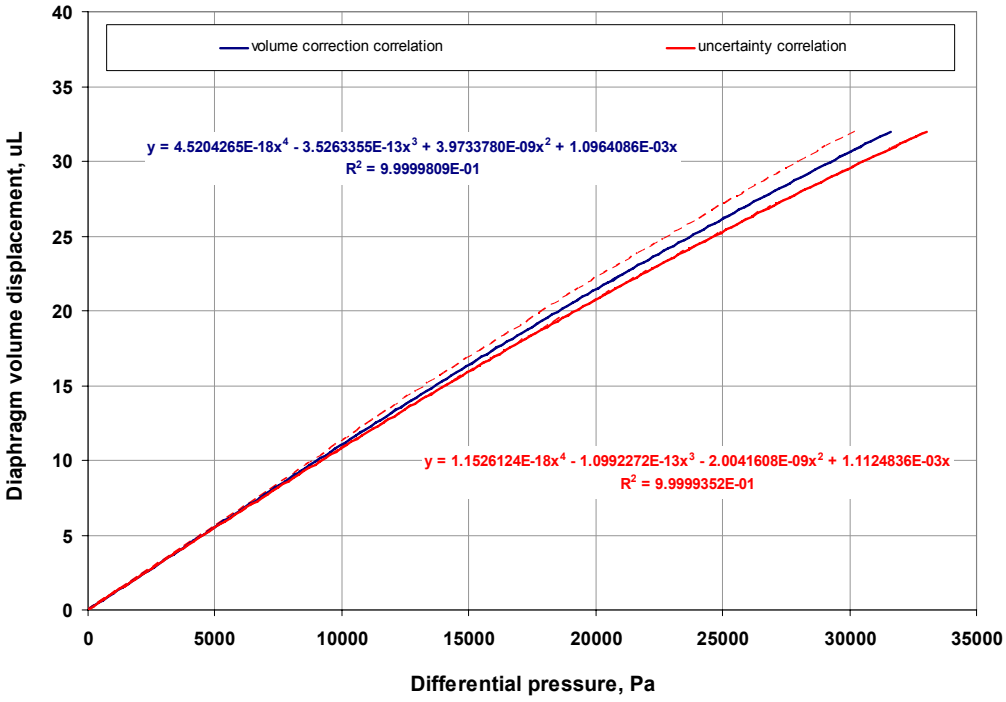

Figure 5.3 – Correlations for average and 95% CI for transducer volume.

Table 5.3 presents the values of each uncertainty used in the propagation of error analysis performed for the GDP experiments. Using these values in Eq. (5.2) yields an uncertainty in saturation of less than 0.02.

Table 5.3 – Uncertainty values for GDP experimental method.

Uncertainty	Units	Value	Notes
$u_{\Delta V_{pump}}$	µL	$0.00065\Delta V_{pump}$	measured
$u_{\Delta V_{trans}}$	µL	fcn of pressure	measured (Fig. 5.4)
u_D	mm	0.01	manufacturer spec.
u_{ε_o}	-	0.015	estimated
u_t	mm	0.0125	machining tolerance
u_{t_o}	mm	0.0005	manufacturer spec.
u_{P_c}	Pa	86.2	manufacturer spec.

The repeatability test included two independent runs of the same material, as well as a third independent run of the same material with the entire GDP apparatus titled 0.5° to assess the impact of out-of-level installation of the sample. The material tested was P-20u, and each sample was cut from a large piece of stock material and prepared in the sample holder independent of one another. The resulting P_c-S curves are presented in Figure 5.4.

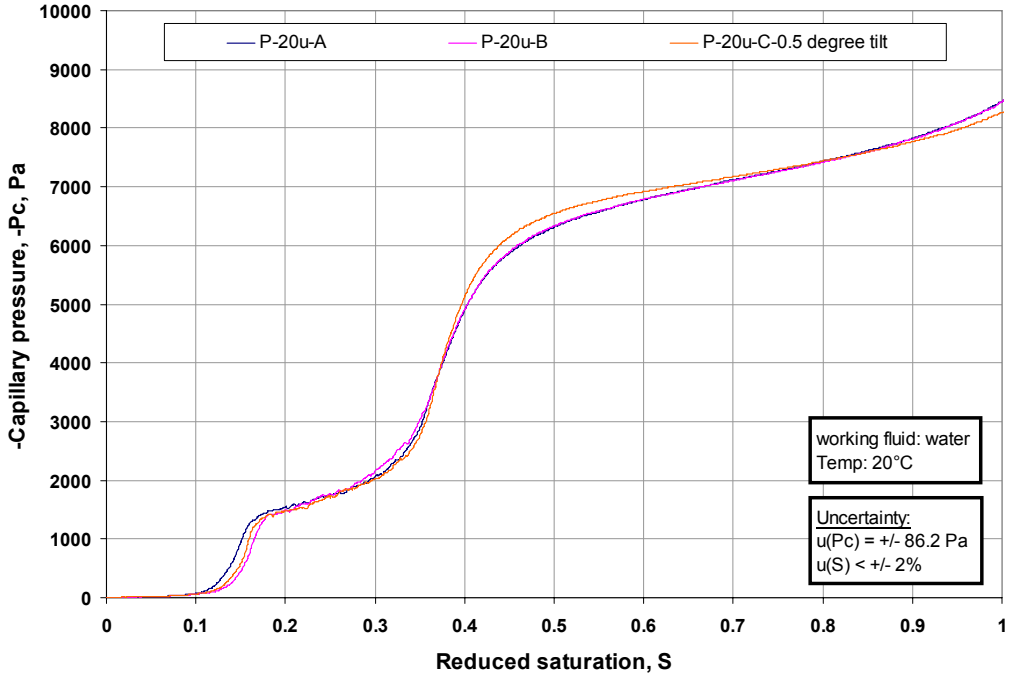

Figure 5.4 – Results of GDP repeatability study performed using P-20u.

Results displayed in Figure 5.4 suggest that the GDP method is remarkably repeatable and that while it is important to install the instrument level, the gravitational effects associated with a slight tilt in the apparatus are relatively small.

After showing that the GDP method is capable of measuring positive capillary pressures, and that the method yields repeatable results, a study of the impact that the hydrophobic PTFE treatment has on the capillary characteristics of the GDL materials was undertaken.

5.2.2 Effect of hydrophobic treatment

To investigate the impact of PTFE treatment on the capillary characteristics of the GDL materials of interest, a study was performed using the nominally uncompressed materials representative of media under the gas flow channel in a PEMFC stack. Figure 5.5 depicts the results obtained for P-0u, P-10u, P-20u, and P-30u.

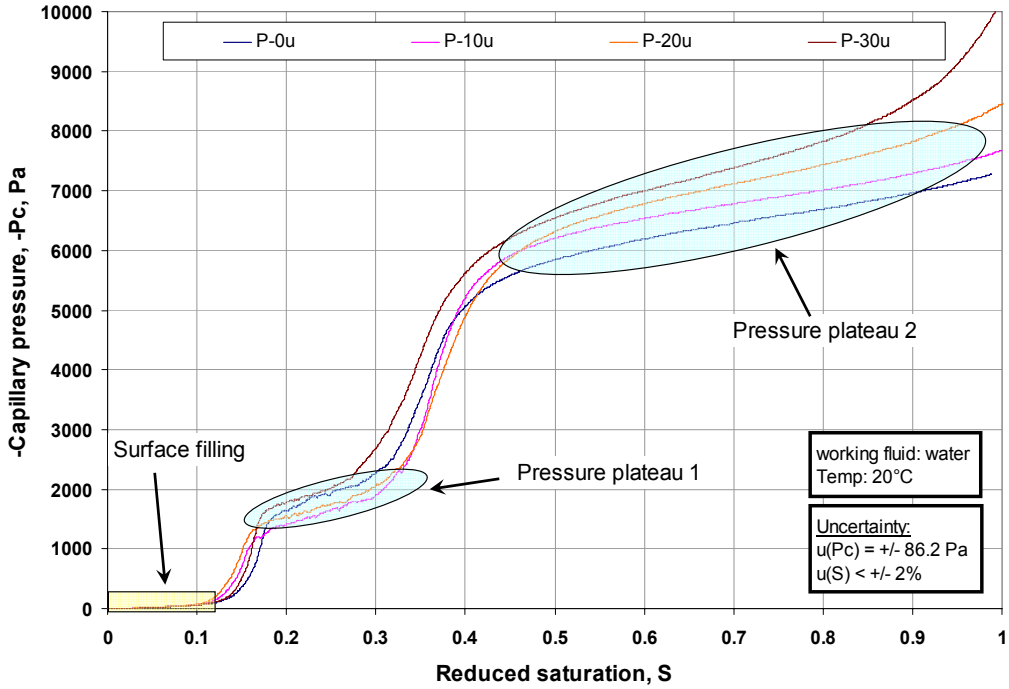

Figure 5.5 – Results of PTFE loading study for carbon paper GDL materials.

The results in Figure 5.5 indicate that when saturation is below 0.45 the curves are very similar in shape and randomly ordered with respect to PTFE content. In addition, none of the carbon paper materials investigated exhibit positive capillary pressures, therefore suggesting that the carbon fiber used in the paper making process is hydrophobic in nature. At saturations in excess of 0.45, a clear trend appears where greater capillary pressure is required for greater saturation according to increased PTFE content. For example, a capillary pressure of approximately 7 kPa is required to reach a saturation of 0.9 for the untreated carbon paper (C-0u), while a capillary pressure of approximately 8.6 kPa is needed to achieve the same saturation in the specimen treated with 30% PTFE.

A microscopy study was also performed to aid in understanding the dual plateau, and the separation at high saturations seen in the capillary pressure curves. Prior to presenting the results of the microscopy study, it is useful to review the manufacturing process for carbon paper based GDL. Mathias et al. [35] cover this process in great detail, and only a summary is provided here. The carbon paper making process is as follows:

1. Chopped carbon fibers undergo a wet-lay process to form a paper-like mat.
2. The mat is impregnated with a high carbon yield resin.
3. The resin in the impregnated mat is cured under heat and pressure in a molding process.
4. The molded impregnated sheet is heat treated in an inert atmosphere to temperatures in excess of 2000°C to graphitize the carbon fibers and carbonize the resin.

Following step 4, further treatment may occur by fuel cell material suppliers to alter the surface energy of the material, i.e., the carbon paper may be treated with hydrophobic polymer or undergo further heat treatment in an oxidizing environment. Figure 5.6 depicts the surface (a,b, and c) and cross-section (d) of the P-0 material in its as-received state.

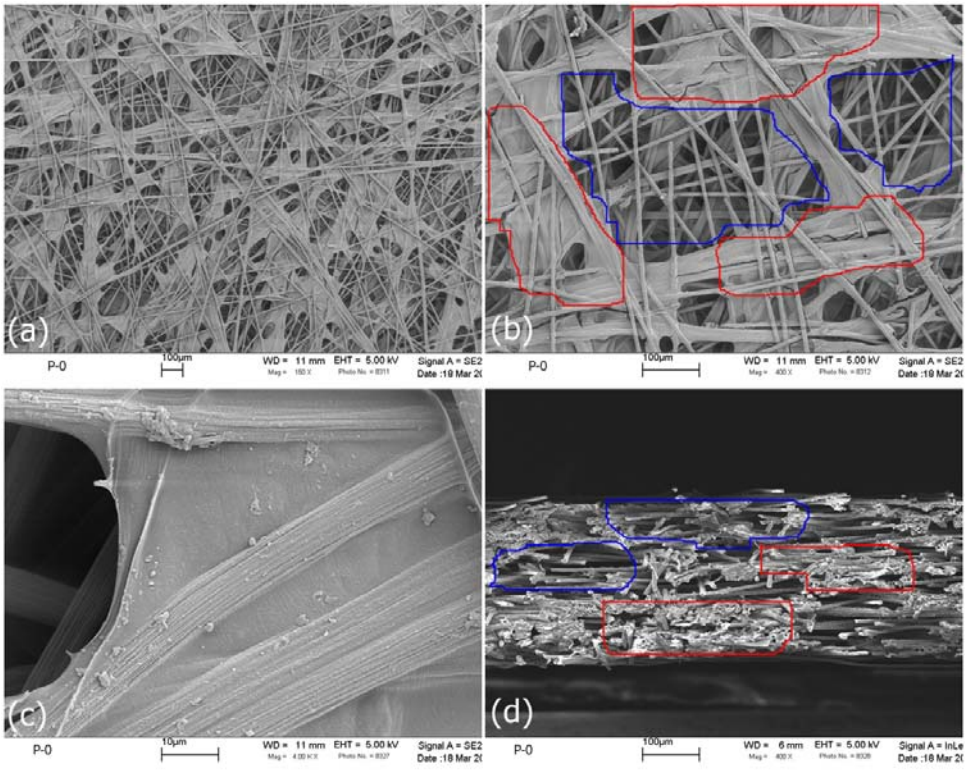

Figure 5.6 – FESEM micrographs of P-0 GDL material.

Figure 5.6(a) and (b) show regions where virtually no resin residual is present (outlined in blue) and regions where the porosity is substantially reduced by resin residual (outlined in red). Figure 5.6(c) depicts the interconnection among fibers achieved by the resin residual. It can again be seen in a cross-section view (d) that there are very distinct regions of low porosity and of high porosity. Clearly, two distinct porous regions exist within carbon paper GDL materials, therefore explaining the presence of two distinct capillary pressure plateaus in Figure 5.5. The low water pressure plateau is where regions with minimal resin residual are being saturated, while the high water pressure plateau represents regions that are substantially filled with resin residual.

Energy Dispersive Spectroscopy (EDS) was performed on additional micrographs to investigate the cause of curve separation with PTFE content at high water pressure, and the lack of a trend at low water pressure. An EDS spectrum focused on a region of resin residual in the P-0 material is depicted in Figure 5.7. The analysis reveals that the resin residual is in fact pure carbon.

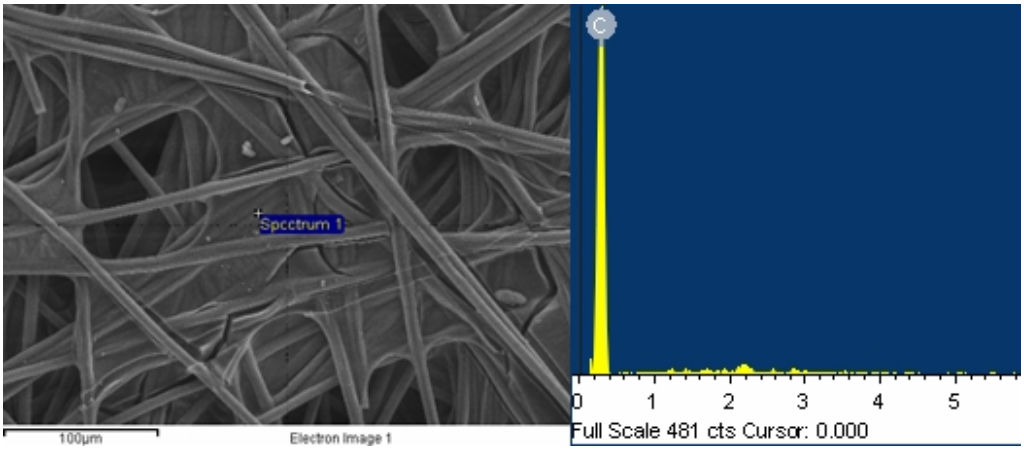

Figure 5.7 – Elemental composition of filled region with P-0 material.

Figure 5.8 displays the elemental analysis on two different regions on the P-30 material. In part (a) of the figure, the elemental composition of a point on one of the carbon fibers within the porous structure reveals that the fiber is 100% carbon and is therefore not coated with PTFE. The EDS spectrum in Figure 5.8(b) reveals a substantial presence of fluorine (~50%) in regions of resin residual suggesting that the PTFE treatment primarily impacts regions in the porous structure where resin residual is present. Knowing that the

PTFE treatment only coats regions of resin residual clearly explains why the capillary pressure curves plateau sequentially with increasing PTFE content when the low porosity regions of the carbon papers are filled. This result also explains why there is no clear trend in the capillary pressure curves at low water pressures, because at low water pressure the high porosity regions being filled in all of the materials (P-0, P-10, P-20, and P-30) are essentially the same (i.e., none of the high porosity regions are coated with PTFE). Therefore, the random nature of the curves in the lower water pressure region is a testament to the variability in the carbon paper making process, and is unrelated to the PTFE post-treatment.

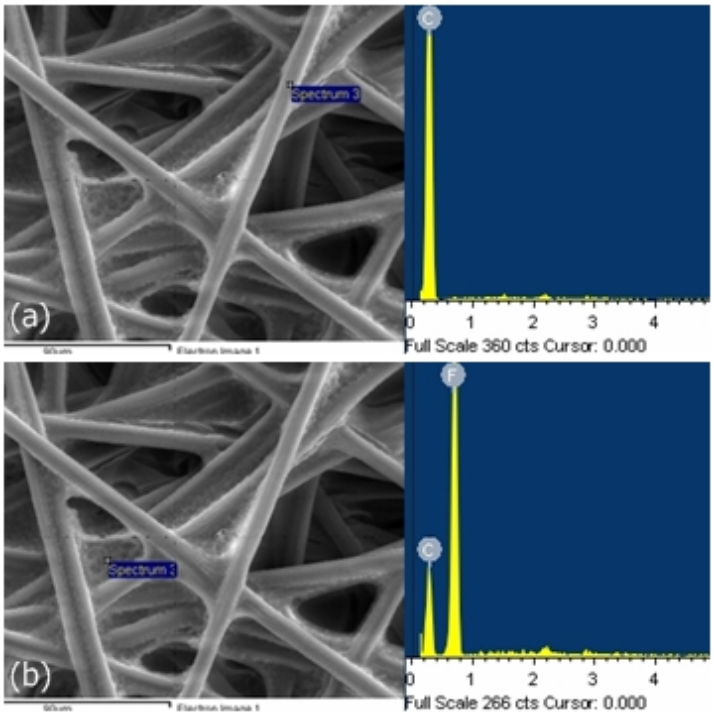

Figure 5.8 – Elemental analysis of the regions within P-30.

The reason that the PTFE only coats the resin residual and not the fibers themselves cannot be fully determined due to a lack of knowledge of the entire processing cycle. However, it is well established that PAN based carbon fibers that have not undergone secondary heat treatments or surface modifications exhibit low surface energies. Additionally, it is not uncommon for PTFE emulsions to be comprised primarily of water. Considering the combined impact of these likelihoods suggests that an

aqueous emulsion would not coat regions of low surface energy (e.g., carbon fibers), but rather coat regions of higher surface energy (e.g., resin residual). Although this hypothesis cannot be proven with the available information, it has been proven that the PTFE treatment primarily coats the regions of resin residual and does not coat the fibers themselves, regardless of the physical reason.

As noted in Chapter 2, it is actually the slope of the capillary pressure function (dP_c/dS) that is important in describing water transport in porous media. The substantial changes in the slope of the P_c-S functions depicted in Figure 5.5 were due to a transition between two fundamentally different pore structures. While introducing PTFE into the porous structure does impact the water pressure required to penetrate one of the two different pore types, it does not fundamentally change the structure of the porous region. Therefore, there is no reason to expect a substantial change in the slope of the P_c-S function with the introduction of PTFE. The presentation of the capillary pressure slopes for carbon paper presented in Figure 5.9 supports the hypothesis that PTFE content should not affect the slope of the capillary pressure function. The slopes of the curves depicted in Figure 5.5 were calculated using a centered difference approximation with $\Delta S \approx 0.02$.

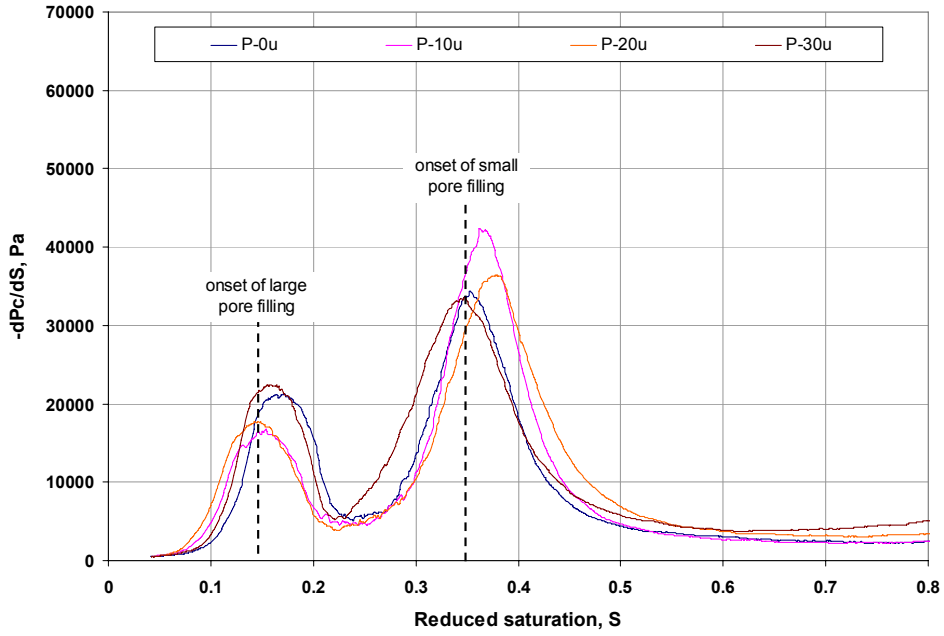

Figure 5.9 – Slope of the capillary function for carbon paper GDL materials.

The magnitude of the curves presented in Figure 5.9 warrant interpretation. Low values of dP_c/dS indicate that only a small increase in water pressure is associated with an incremental increase in saturation, while large values of dP_c/dS are indicative of a substantial increase in pressure with an incremental increase in saturation. For example, a large pressure increment is required to begin filling the regions with small pores (those with substantial resin residual), yet, once those regions begin filling (S~0.35) a low value of dP_c/dS is apparent because they can continue to fill without further increase in pressure. In contrast, it does not require a very large water pressure to fill regions of large pores (those with no resin residual). However, in comparison to the water pressure required to fill surface contours there is a significant difference. Therefore, once the surface contours are saturated (S~0.1), further increase in saturation requires that a new pore type begin to fill, and this is manifested as a significant increase in the magnitude of dP_c/dS. To summarize, low values of dP_c/dS indicate further saturation of a particular pore type, while large values indicate a transition from one pore type to another. Putting this in the context of previous discussions it stands to reason that the derivative of the Leverett function does not exhibit sudden increases or decreases over the full range of saturation since it was derived from unconsolidated sand which would be expected to have similar pore structure throughout.

The dP_c/dS functions depicted in Figure 5.9 show that the curves are very similar but follow no clear trend pertaining to PTFE content. Variability in these curves is therefore attributed to the variability in the paper making process, and not the PTFE post-treatment. Since the results show that dP_c/dS is independent of PTFE content, a single dP_c/dS curve applicable to Toray TGPH-090 carbon paper, regardless of the PTFE loading, can be determined. A piecewise function was necessary to achieve a suitable fit to the collection of dP_c/dS data, where the divisions were taken at $S = 0.18$, and 0.4. The resulting piecewise function is displayed in Figure 5.10. To avoid clutter, the actual data points were removed, but the quality of fit can be seen in the large R^2 values achieved.

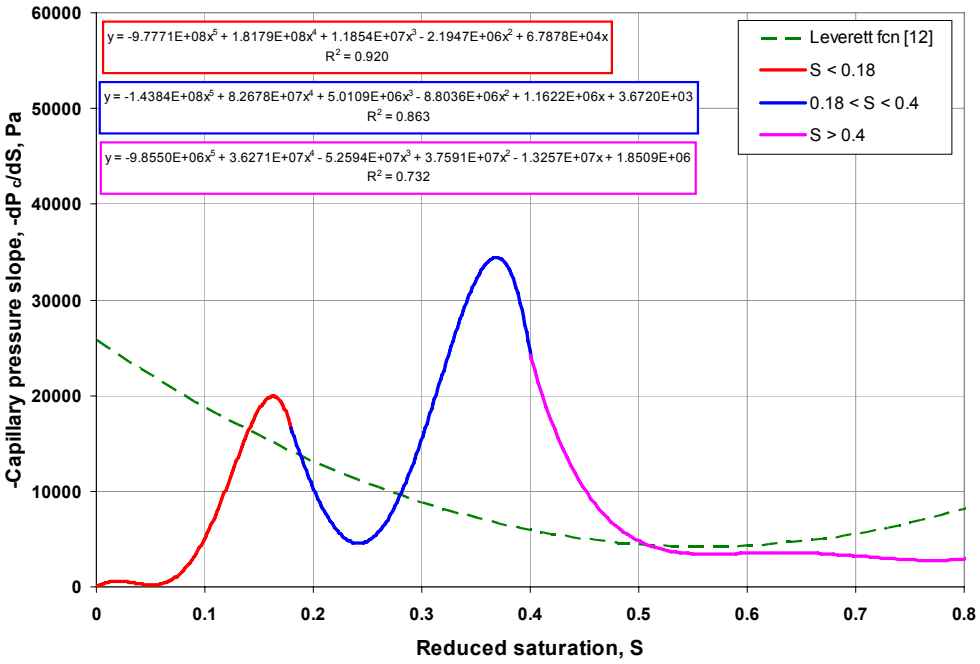

Figure 5.10 – Piecewise function describing the curvature of the capillary function for Toray TGPH-090 carbon paper.

A similar set of experiments were performed for the carbon cloth GDL materials. Prior to presenting the capillary behavior results, a visual description of the cloth materials will be presented. In contrast to the carbon paper materials, the carbon cloth material investigated in this work had no resin impregnation. An FESEM micrograph of the cloth material with no PTFE treatment (C-0) is displayed in Figure 5.11 where it can be seen that carbon fiber tows are comprised of continuous fibers arranged in a plain weave.

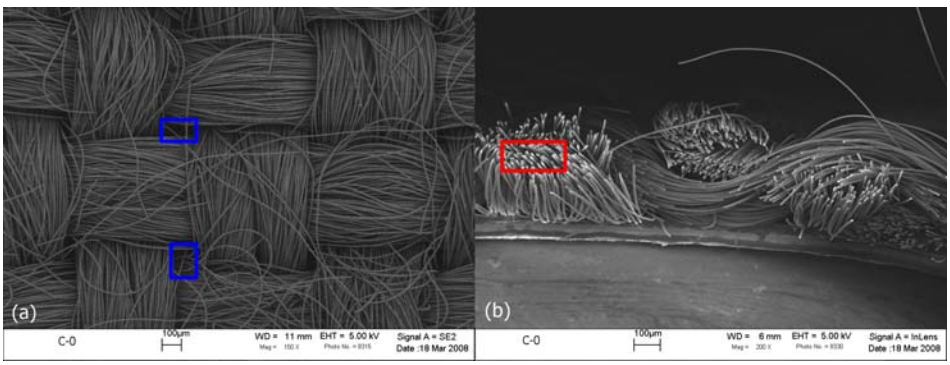

Figure 5.11 – FESEM micrograph of C-0: top surface (a), and cross-section (b).

Similar to the carbon paper materials, Figure 5.11 shows 2 fundamentally different porous regions. The regions outlined in blue are fairly large open regions (~100 μm) with minimal fiber intrusion, while the regions outlined in red are very small openings between fibers within the yarn. The largely open regions in the carbon cloth are approximately the same size as the open regions in the carbon paper. Because the large pores are approximately the same size in both materials, it is expected that the low pressure plateau corresponding to the fairly open regions within the carbon cloth would occur at nearly the same capillary pressure as it did for the carbon paper. The capillary pressure curves measured for the cloth materials with differing PTFE content are presented in Figure 5.12.

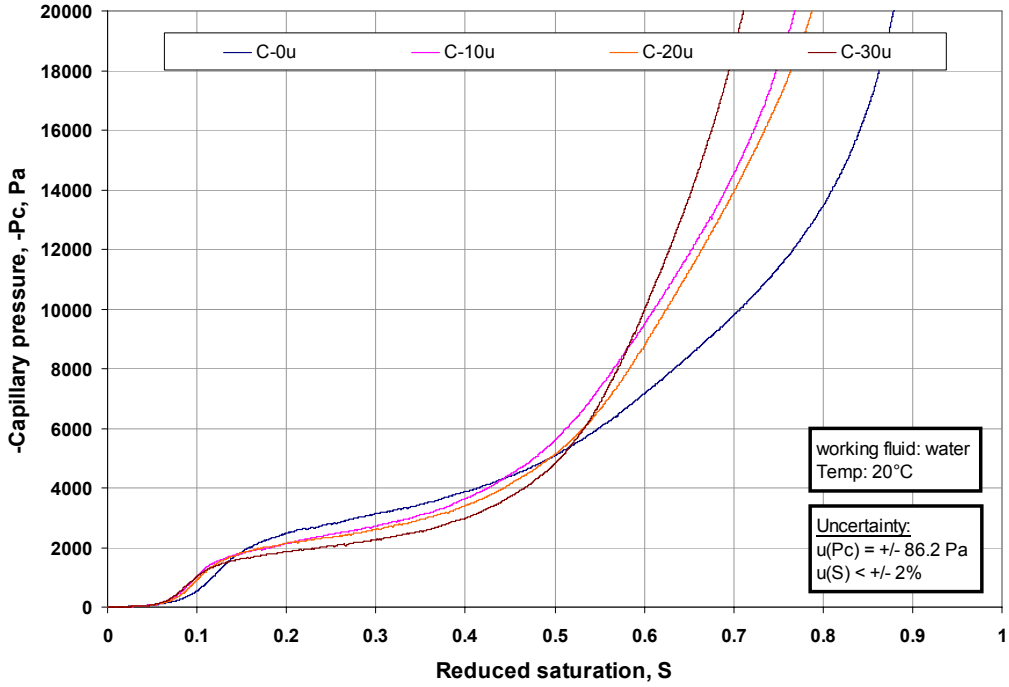

Figure 5.12 – Capillary pressure curves for carbon cloths with varying PTFE content.

As can be seen in Figure 5.12 the low water pressure plateau occurs around 2000 Pa as it did for the carbon paper material. However, the low water pressure plateau for the carbon cloth materials continues on to much greater levels of saturation in comparison to the carbon paper materials. The increased saturation achieved at low water pressure

suggests that the open regions in the weave constitute a greater fraction of the pore volume that the regions free of resin residual do in the carbon paper material.

After the large pores are filled, the water begins to infiltrate the much smaller pore space between fibers within the yarns. The spacing between fibers in the C-0 material (~2-10 μm) is much smaller than even the smallest pores (~10-50 μm) observed for the carbon papers. This suggests that the second pressure plateau should occur at a substantially greater pressure for the carbon cloth materials. Or perhaps, there is no second pressure plateau and the water incrementally fills the pore space between fibers sequentially with size. If there were to be a second pressure plateau, it is not observed in Figure 5.12 because it would occur outside the range of the 5 psid (~30 kPa) transducer, and therefore was not realized during the GDP experiment for the carbon cloth specimens. On the other hand, if the increase in pressure at saturations in excess of 0.4 is due to the water incrementally filling smaller and smaller open regions between fibers then no plateau would be expected. The second hypothesis where there is no second plateau seems more likely since 70-90% of the pore volume is already saturated at a capillary pressure magnitude of 20 kPa.

It is interesting to notice that the slopes of the curves after the first plateau are affected by PTFE content for carbon cloths (unlike the slopes for the carbon papers). The carbon paper results suggested that the slope of the capillary function only changes if a fundamentally different porous region is encountered by the water. For the carbon papers, the slope of the capillary function was similar for all materials at a given saturation level because the addition of PTFE simply coated the solid regions of resin residual without significantly impacting the form of the porous structure. However, since the slope of the capillary curves changes substantially, a fundamental change of the pore structure, and not simply coating of a commonly shared structure, is expected for the cloth materials. Micrographs of P-30 are depicted in Figure 5.13.

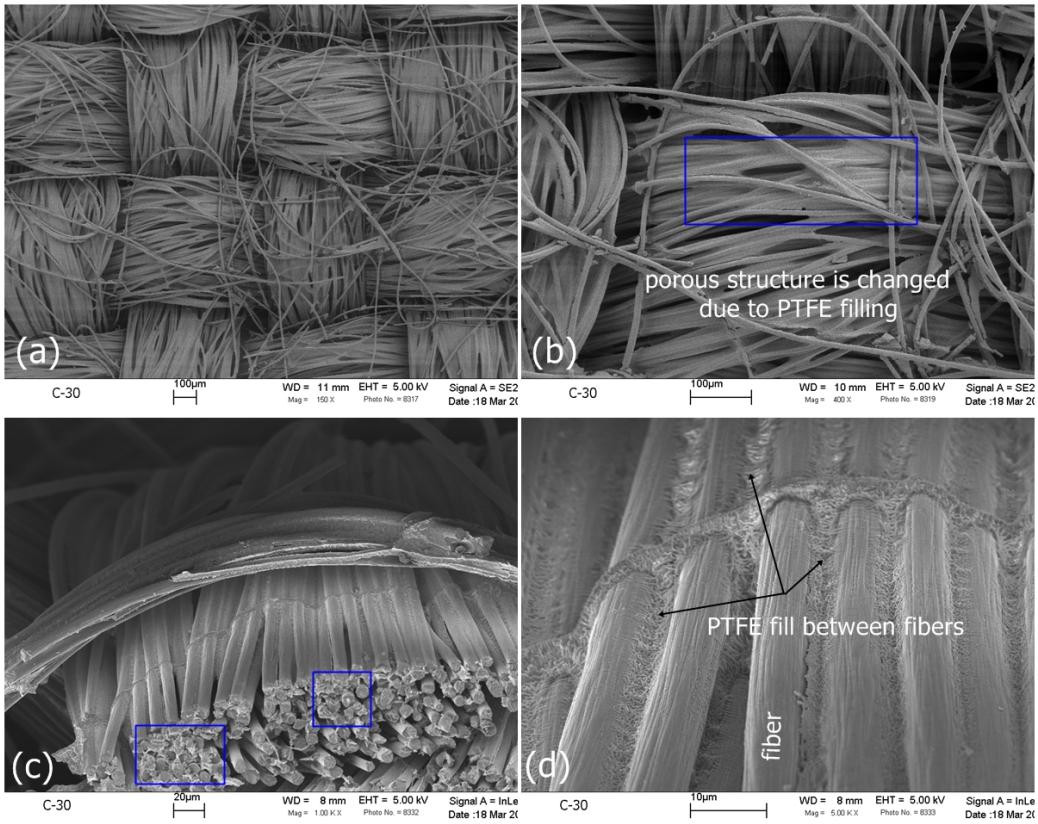

Figure 5.13 – FESEM images of C-30 showing effect of PTFE on pore structure.

Figure 5.13(b) is a higher magnification of the region depicted in (a), and it clearly shows that the PTFE penetrates and coats the individual fibers. Part (d) of the figure shows that the PTFE can actually eliminate porosity between fibers within the yarns and effectively create a new pore structure that has a different shape, size, and wettability than was evident in the C-0 material. Therefore, the conclusions regarding the impact of structure on the slope of the capillary function are supported by the micrographs.

Since the modeling of liquid water transport relies on the slope of the capillary function, it is once again necessary to present the dP_c/dS functions for carbon cloth GDL materials (Figure 5.14).

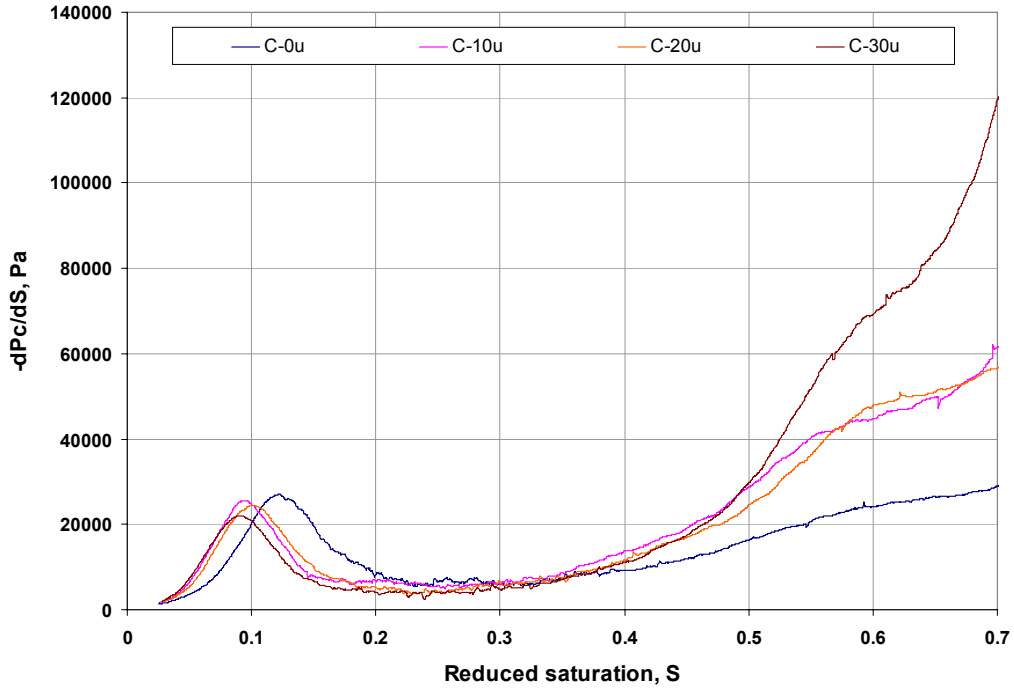

Figure 5.14 – Slope of the capillary pressure functions for carbon cloth with varying PTFE.

A clear shift toward lower saturation in the regions of large pore space between the carbon fiber yarns is evident for all of the materials treated with PTFE. This shift is likely due to a substantially reduced available volume in the regions between yarns because the PTFE coating begins to displace open volume. However, for all of the cloth materials where PTFE has been introduced, the shape and magnitude of the capillary function slope is nearly identical below a saturation of 0.5. Beyond 50% saturation the substantial changes in the porous structure with increasing levels of PTFE becomes increasingly evident.

Other works in the literature have shown that the optimal PTFE content in the macroporous GDL materials commonly used in PEMFCs is between 10-20% by mass, while greater loadings are detrimental to cell performance [51, 52]. Therefore, only the data for C-10 and C-20 will be fitted to form the analytical expression for dP_c/dS to be utilized in water transport models. The derived relationship is shown in Figure 5.15. It can again be seen in Figure 5.15 that the slope of the Leverett function does not appropriately describe the slope of the actual capillary pressure function for carbon cloth GDL materials.

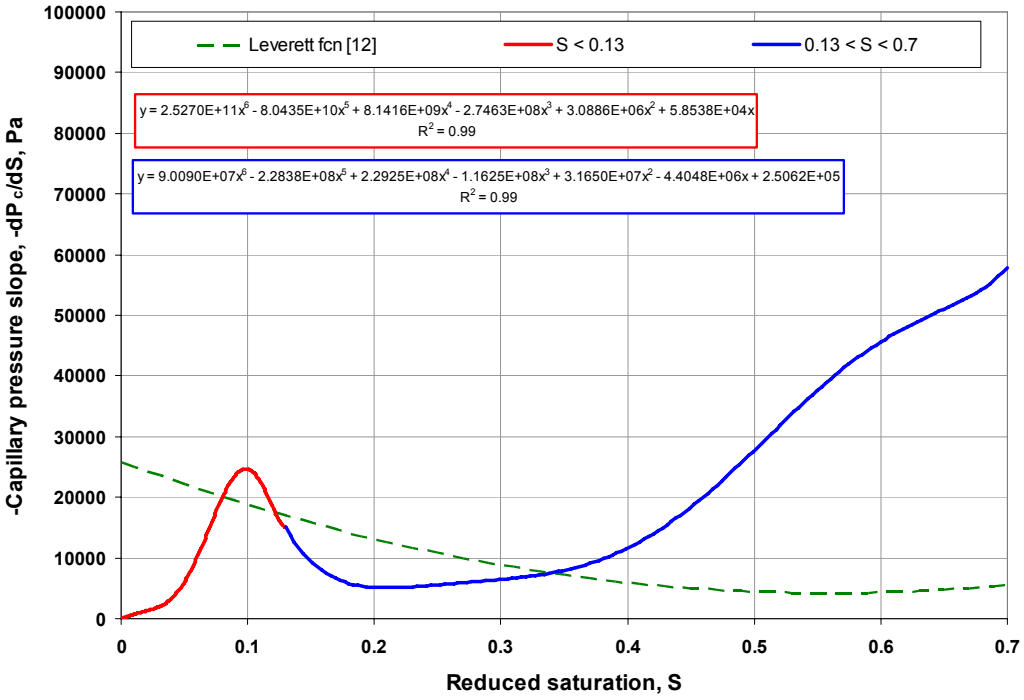

Figure 5.15 – Polynomial fits representing the slope of the capillary pressure function for materials C-10u and C-20u.

5.2.3 Effect of compression

The effect of compression on capillary behavior was investigated for a subset of the GDL materials of interest. More specifically, carbon cloth and carbon paper with 20% PTFE loading compressed at a level similar to what would be expected under the shoulder area of a bipolar plate were investigated. The 20% PTFE loading was chosen because it is suggested in the PEMFC literature that GDL materials with approximately 20% PTFE provide a substantial performance benefit [51, 52].

The resulting P_c-S curves for the nominally uncompressed P-20u and the substantially compressed P-20c materials are compared in Figure 5.16.

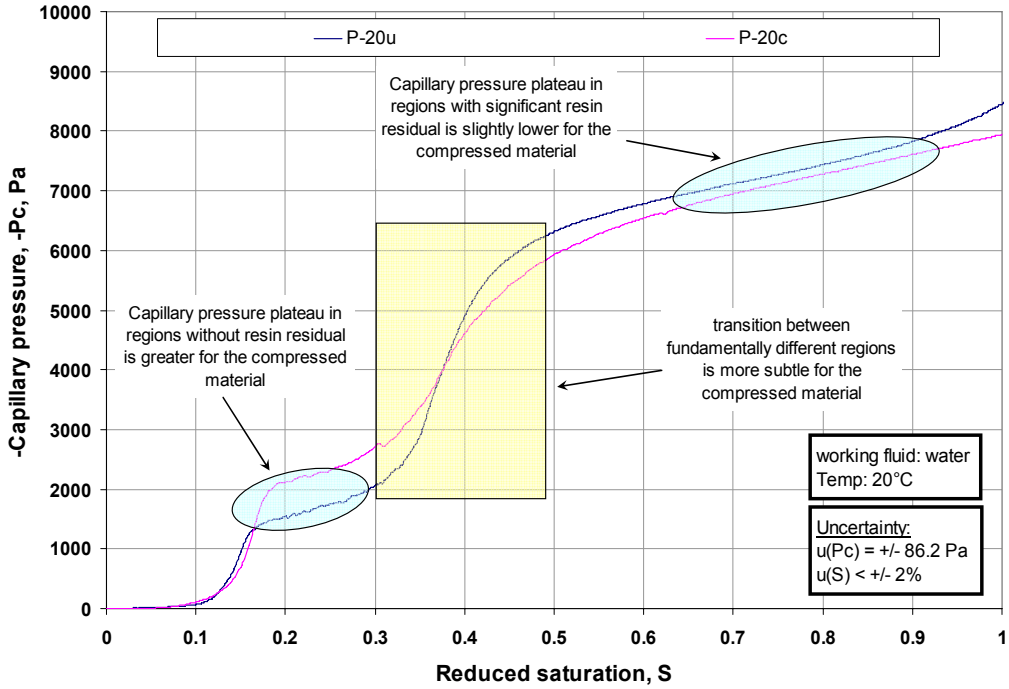

Figure 5.16 – Effect of compression on capillary behavior for the P-20 material.

It can be seen that the water pressure in porous regions with no resin residual is substantially greater for P-20c in comparison to P-20u. Furthermore, the transition from the regions with high porosity (no resin residual) to the regions with low porosity (substantial resin residual) is less pronounced for P-20c. Finally, the residual filled plateau region occurs at a slightly lower water pressure for the P-20c material in comparison to the P-20u material. All three of these observations suggest that the compression has a homogenizing effect of carbon paper. In other words, substantial compression causes the two distinct porous regions to become more similar. A reasonable explanation for such a result is that the more open porous regions are mechanically weaker and are therefore more prone to partially collapsing when under compression. Such collapse would cause a more significant spike in capillary pressure around S = 0.15, and would also smooth the transition that occurs between S = 0.2 and S = 0.4. At saturations in excess of 0.4, similar behavior would be expected between the two samples since the porous regions reinforced by substantial resin residual are less susceptible to collapse. However, the compression may cause damage to the residual filled regions, slightly increasing pore size in those regions (and consequently decreasing pore size in

adjacent regions with minimal resin residual), and lower the plateau pressure as observed. Figure 5.17 presents a FESEM micrograph of a compressed sample of P-20c.

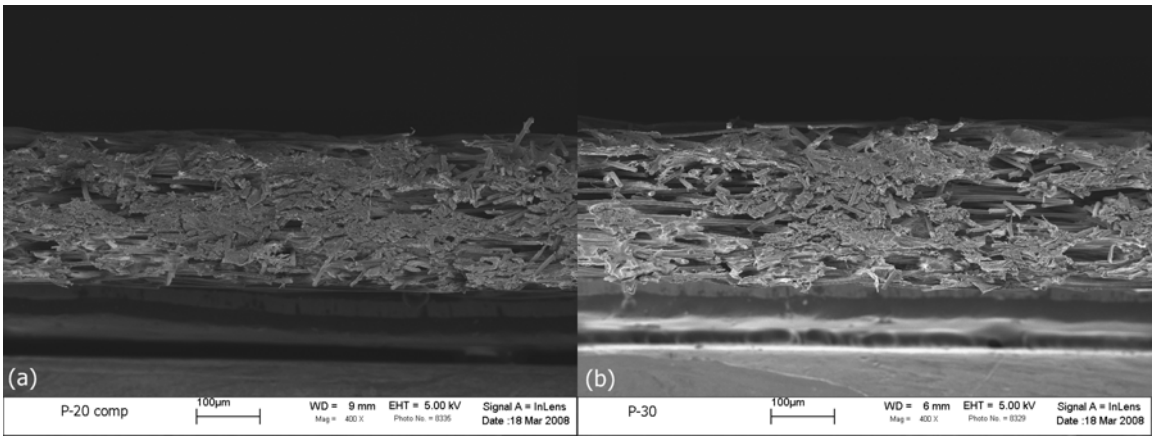

Figure 5.17 – Cross-section of (a) P-20c and (b) P-30u.

Although two distinct regions can still be observed for both materials in Figure 5.17, the cross section view of the compressed P-20 (a) clearly shows a more homogenous porous network than the uncompressed P-30 (b). The homogenizing effect of compression for carbon papers supports the data presented in Figure 5.16.

Due to the two distinct porous regions becoming more similar when the P-20 material is substantially compressed, the slope of the capillary pressure behavior with saturation also changes. It is evident in Figure 5.18 that the two distinct porous regions have become nearly identical in terms of the magnitude of the slope required to fill each porous region. It is interesting to note that the peaks would likely continue to become more similar as increased levels of compression were applied to the P-20 material. Furthermore, if the material was compressed to a point where all regions of significant porosity were crushed, the media would essentially become an unconsolidated bed of solid particles and the slope of the capillary pressure function would approach a nearly constant value. Such behavior is similar to what Leverett [20] found for unconsolidated sand in 1941.

The effect of compression on the capillary behavior for carbon cloth GDL materials was also investigated. The results for C-20c are presented in Figure 5.19 where the capillary function is compared to C-20u.

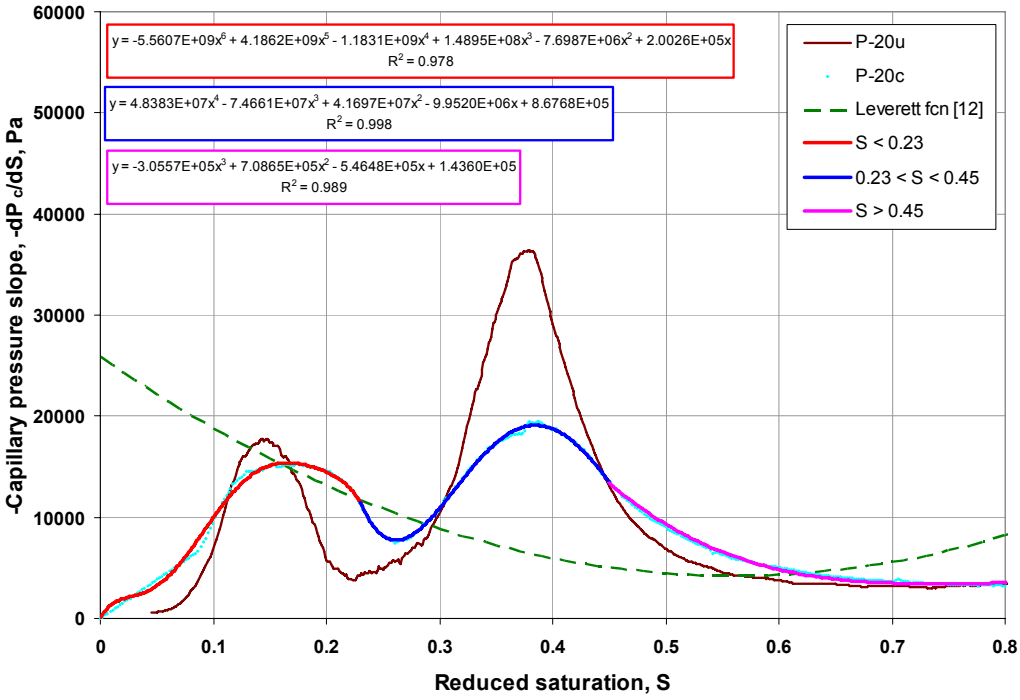

Figure 5.18 – Comparison of dP_c/dS functions for P-20u and P-20c.

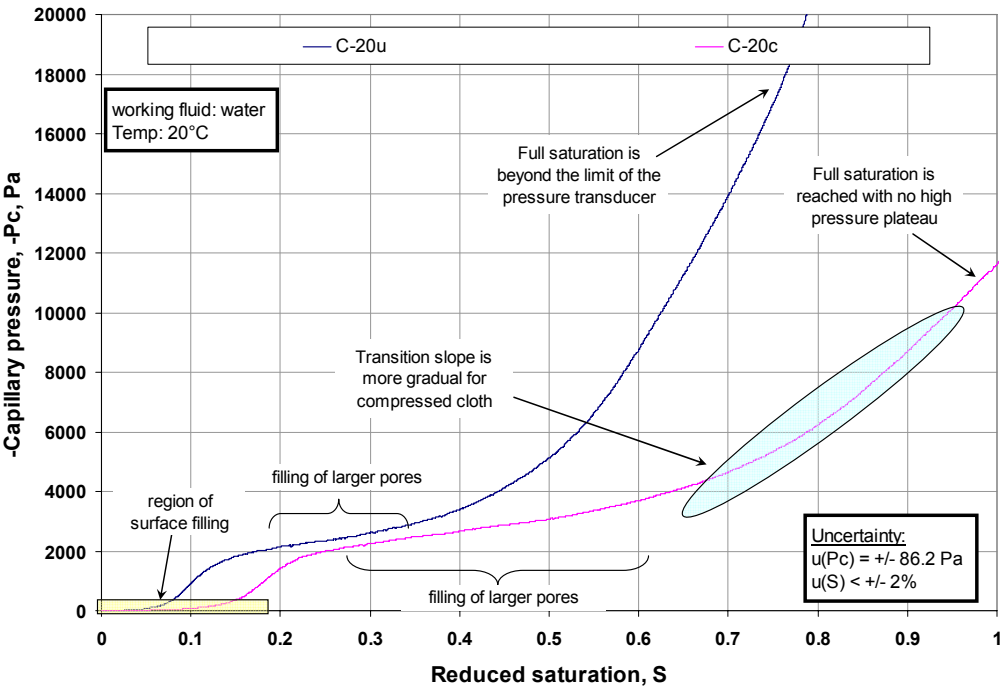

Figure 5.19 – Capillary pressure functions for compressed and uncompressed C-20.

It is evident that compression has a significant impact on the capillary characteristics of carbon cloth. Keeping in mind that saturation is measured as a fraction of total porosity, it is interesting to see that surface filling constitutes a greater fraction of the total porosity for the compressed material that the uncompressed material. This suggests that compression does not decrease surface roughness, but rather that the effect of compression is manifested in the bulk of the structure. It is also interesting to note that compression greatly reduces the increase in pressure after the large pores between yarns are filled. In the compressed material, there is a slower increase in capillary pressure that suggests that all regions are now similar in structure, but require increasingly greater water pressure to fill them. This phenomenon is perhaps due to the compression fracturing the PTFE bond between fibers, and allowing the fiber yarns to be spread into a more homogeneous layer. In this scenario, water would sequentially fill pore space within the fiber bundles according to size. In other words, the pore structure is now nearly homogeneous, yet a distribution in pore size is still apparent within the fiber bundles and therefore the bundles fill over a range of capillary pressure. Unfortunately, micrographs of the compressed state of carbon cloth were not possible due to the fact that the cloth materials rebound from compression unlike the paper materials that tend to remain in a compressed state after the compressive load is removed. Therefore, this theory cannot be verified. However, regardless of the reason for the drastic change in capillary behavior, the change still exists and therefore must be reflected in the description of diffusion media behavior. The analytical expression for the slope of the capillary function for compressed C-20 cloth is presented in Figure 5.20.

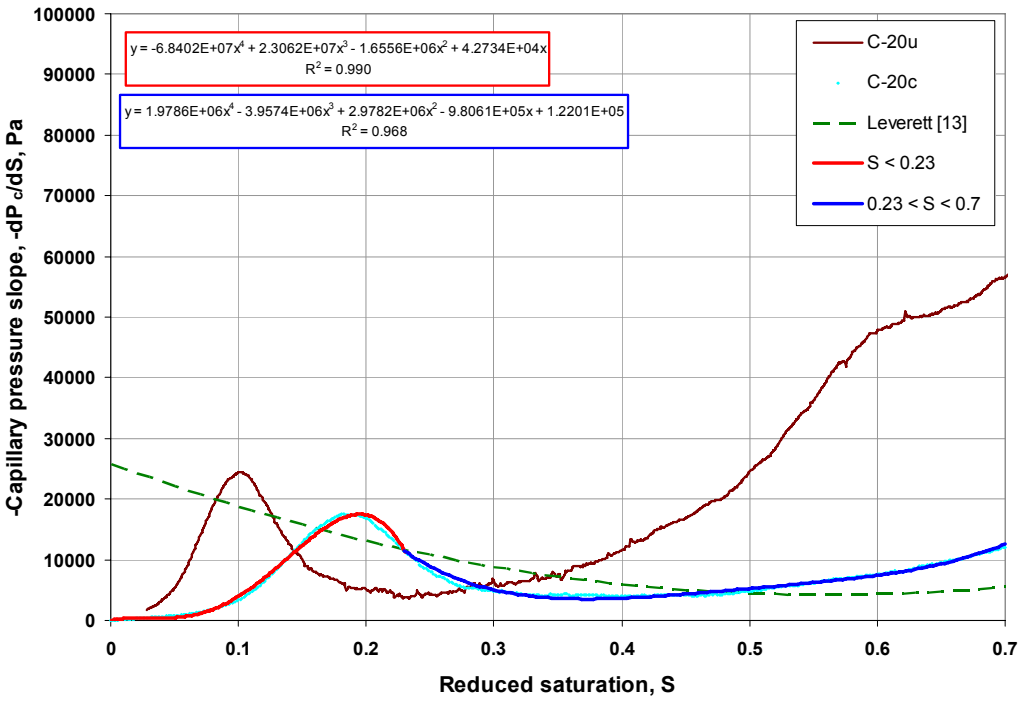

Figure 5.20 – Analytical expressions for the slope of the capillary function for C-20c.

The purpose of developing analytical expressions for the capillary behavior of common GDL materials is so they can be included in mathematical models of PEM fuel cells. It is important to include temperature effects in PEMFC models for several reasons; including the impact that temperature can have on the surface tension of liquid water. The expressions presented thus far will be adapted to include temperature dependence by assuming that capillary pressure varies linearly with surface tension in accordance with Eq. (5.3).

$$P_c\left(S,T\right)=\frac{\sigma(T)}{\sigma(T_{ref})}P_c\left(S\right) \tag{5.3}$$

In Eq. (5.3) T is the temperature of interest, whereas T_{ref} is the reference temperature at which the GDP experiment was performed. Here, the surface tension of water has units of (N/m) and P_c has units of (Pa). In like fashion, the temperature dependent slope of the capillary function takes the form presented in Eq. (5.4).

$$\frac{dP_c}{dS}(S,T) = \frac{\sigma(T)}{\sigma(T_{ref})}\frac{dP_c}{dS}(S) \tag{5.4}$$

The functions presented in this section represent the first time in which the capillary behavior for macroporous PEMFC GDL materials has been quantified experimentally without assuming a uniform contact angle. As described in Chapter 2, assuming a single contact angle for porous materials with varying pore shapes, surface energies, and sizes, is not generally appropriate. The method of gas displacement porosimetry (GDP) was developed in this work to avoid such assumptions.

5.3 PERMEABILITY OF GDL MATERIALS

The absolute and relative permeability assumed for gas diffusion media varies greatly within the existing body of literature. The need for experimentally determined absolute permeability values, and relative permeability functions is addressed in this section. This section will first present the results for a simple determination of absolute permeability. Following the discussion of absolute permeability, the focus will shift to the more complicated measurement of relative permeability of phases in a two-phase flow system. Prior to presenting relative permeability results, a brief discussion addressing the uncertainty and repeatability of the relative permeability results is presented. Finally, relative permeability results which investigate the impact of hydrophobic treatment and compression on both paper and cloth based GDL materials are presented.

Prior to any further discussion, clarity needs to be provided for the terminology in this section. The relative permeability curves presented in this section are exclusively for the liquid phase since it is the most prevalent in the PEMFC literature. When the phrase "relative permeability" is used, the default reference is to the relative permeability of liquid water. One of the advantages of the VT-k_r method is that both fluids are driven through the material simultaneously, experience the same pressure drop through the media, and therefore the relative permeability of the gaseous phase is simply calculated via the following ratio (derived from Eq. (3.8) and (3.9)):

$$\frac{k_{r,g}}{k_{r,LW}} = \frac{\mu_g \dot{V}_g}{\mu_{LW} \dot{V}_{LW}} \tag{5.5}$$

Thus, while only $k_{r,LW}$ is determined, the calculation of $k_{r,g}$ from the results is straightforward.

5.3.1 Absolute permeability

As described in Chapter 3, absolute permeability is a readily measured material property that describes the ability of a single phase flow to move through a porous medium. A volumetric flow rate of 200 sccm of dry nitrogen was used to determine the absolute permeability of the GDL materials being investigated because prior experience [48] has shown that such a flow rate is well within the Darcy flow regime. Six materials were considered for both relative and absolute permeability measurements including: P-0u, P-20u, P-20c, C-0u, C-20u, and C-20c. The absolute permeability results for these materials are presented in Table 5.4.

Table 5.4 – Absolute permeability results.

GDL specimen	Absolute permeability (K) (10^{-12} m^2)
C-0u	33.35 ± 1.61
C-20u	39.59 ± 2.24
C-20c	16.88 ± 0.45
P-0u	4.43 ± 0.13
P-20u	3.71 ± 0.09
P-20c	0.96 ± 0.03

It is evident from Table 5.4 that compression has a significant impact for both carbon cloth and carbon paper. The carbon paper material treated with 20% PTFE exhibits an absolute permeability nearly 20% less than the untreated carbon paper,

therefore suggesting that significant pore blockage does occur during the hydrophobic treatment process for paper based GDL materials. Such blockage would be expected. However, for the cloth materials, the cloth with PTFE (C-20u) exhibits a greater permeability than the untreated cloth (C-0u). There is no obvious explanation for this other than the possibility of variability within the cloth substrate, or variability in the sample preparation. Nevertheless, when the extremes of the errors are considered for the C-0u and C-20u materials, the difference is less than 7%. The fact that the permeability is nearly the same, or perhaps slightly greater for the cloth with a PTFE treatment suggests that the pores in the cloth materials are not as prone to clogging when PTFE is added, in comparison to the paper substrate.

The values of absolute permeability and the uncertainty of these values were determined via Eq. (5.6) and Eq. (5.7) respectively.

$$K = \frac{\mu_g \dot{V}_g}{\pi/4 D^2} \frac{\Delta x}{\Delta P} \tag{5.6}$$

$$u_K = \pm \left[\left(\frac{\partial K}{\partial x_1} u_{x_1} \right)^2 + \ldots + \left(\frac{\partial K}{\partial x_n} u_{x_n} \right)^2 \right]^{1/2}$$

$$= \pm \left[\left(\frac{\mu_g \Delta x}{\pi/4 D^2 \Delta P} u_{\dot{V}_g} \right)^2 + \left(\frac{\mu_g \dot{V}_g}{\pi/4 D^2 \Delta P} u_{\Delta x} \right)^2 + \left(2 \frac{\mu_g \dot{V}_g \Delta x}{\pi/4 D^3 \Delta P} u_D \right)^2 + \left(\frac{\mu_g \dot{V}_g \Delta x}{\pi/4 D^2 \Delta P^2} u_{\Delta P} \right)^2 \right]^{1/2} \tag{5.7}$$

In the above equations, μ_g is the dynamic viscosity of dry nitrogen, $\dot{V}_g$ is the volumetric flow rate of dry nitrogen, K is the absolute permeability of the GDL of interest, Δx is the combined thickness of GDL material between the pressure taps, and ΔP is the differential pressure through the entire thickness of the GDL mixing sections and central sample, and u is the uncertainty associated with each measured variable. The value for each measurement uncertainty is presented in Table 5.5.

Table 5.5 – Values used in error propagation for absolute permeability.

Uncertainty	Units	Value	Notes
$u_{\dot{V}_g}$	sccm	0.04	manufacturer spec.
$u_{\Delta x}$	mm	0.05	machining tolerance
u_D	mm	0.01	manufacturer spec.
$u_{\Delta P}$	Pa	0.6225	manufacturer spec.

5.3.2 Relative permeability – proof of concept, uncertainty, and repeatability

Recalling from Chapter 2, effective permeability (the product of relative and absolute permeability) is a measure of the ease with which each phase travels through a partially saturated medium in a two-phase flow system. The experimental technique developed in Chapter 3 for the determination of the relative permeability of GDL materials, the VT-k_r method, is a method derived from previously developed methods in the oil and water recovery industries. In the VT-k_r method a known volumetric flow of both liquid water and gas is forced through a multi-layered GDL specimen. Equilibrium is reached when the pressure drop across the sample is constant, at which time the saturation of the center sample is determined gravimetrically. The VT-k_r method allows for a variety of flow rate ratios to be applied, each of which yields a different saturation within the GDL specimen. By changing the flow rates, a curve relating relative permeability to saturation can be developed. Such a complicated experiment lends itself to the possibility of significant error and the possibility of not being sufficiently repeatable. This section addresses these concerns.

Similar to the capillary pressure experiments, the uncertainty of the relative permeability measurements is addressed quantitatively while the repeatability is addressed qualitatively. A propagation of error analysis is required for each calculated variable: one for the saturation, and one for the relative permeability of liquid water. The equations used to calculate values for saturation and relative permeability are presented in Eq.(5.8) and Eq.(5.9), respectively.

$$S = \frac{m_{wet} - m_{dry}}{\pi/4 \, D^2 \rho_{LW} t \left(\varepsilon_o \, t/t_o \right)} \tag{5.8}$$

$$k_{r,LW} = \frac{\mu_{LW} \dot{V}_{LW}}{\pi/4 \, D^2 K} \frac{\Delta x}{\Delta P} \tag{5.9}$$

The variables in the relative permeability expression were sufficiently described in the section discussing absolute permeability. The variables in the saturation expression are defined as follows. S is the saturation of the central GDL specimen, m_{wet} is the mass of the partially saturated central GDL, m_{dry} is the dry mass of the central sample, D is the diameter through which flow occurs, ρ_{LW} is the density of liquid water, t is the thickness of a single GDL layer (defined as Δx divided by the number of GDL layers), ε_o is the as-received porosity of the GDL of interest, t_o is the as-received thickness of the GDL of interest.

The propagation of error analysis for the relative permeability expressions was performed in identical fashion to the analysis performed for the GDP experiment. Therefore, the details of the error propagation are not included here. However, the results are reflected in the error bars in the plots presenting the results of the relative permeability experiments. It should be noted that the presented error bars do not include the error associated with the necessary human interaction with the VT-k_r method. The human interaction only impacts the measurement of m_{wet} because it is necessary in this measurement to swab the filled border of the central sample to avoid including the mass of droplets that cling to the border. If a small droplet is not properly removed from the filled border, a substantial error in saturation is introduced that is not included in the uncertainty analysis. For completeness, the uncertainty of each variable is presented in Table 5.6.

Table 5.6 – Values used for relative permeability uncertainty calculations.

Uncertainty	Units	Value	Notes
$u_{m_{wet}}$	mg	0.5	manufacturer spec.
$u_{m_{dry}}$	mg	0.01	manufacturer spec.
u_{D}	mm	0.01	manufacturer spec.
u_{ε_o}	-	0.015	estimated
u_{t_o}	mm	0.0005	manufacturer spec.
$u_{\dot{V}_{LW}}$	µL/min	7	measured
u_{K}	-	see Table 5.4	calculated
$u_{\Delta x}$	mm	0.05	maching tolerance
$u_{\Delta P}$	Pa	17.24 (cloth)	manufacturer spec.
		86.2 (paper)	manufacturer spec.

To assess the repeatability of the VT-k_r method, two experimental trials were run in which two independently prepared samples were tested. Qualitative inspection of the relative permeability curves obtained from the independent trials using the P-20u material show that the relative permeability experiment exhibits a sufficient level of repeatability. The results are displayed in Figure 5.21.

It can be seen in Figure 5.21 that significant agreement is achieved with the exception of one point. The outlying point is attributed to the error associated with the human interaction which requires that the border of the central sample be swabbed to remove water droplets prior to weighing. If a small droplet around the border of the central sample is not absorbed during the swabbing process a false and excessive value for saturation is measured. Now that it has been shown that the VT-k_r procedure is repeatable, the effect of the hydrophobic polymer treatment and the effect of compression will be discussed.

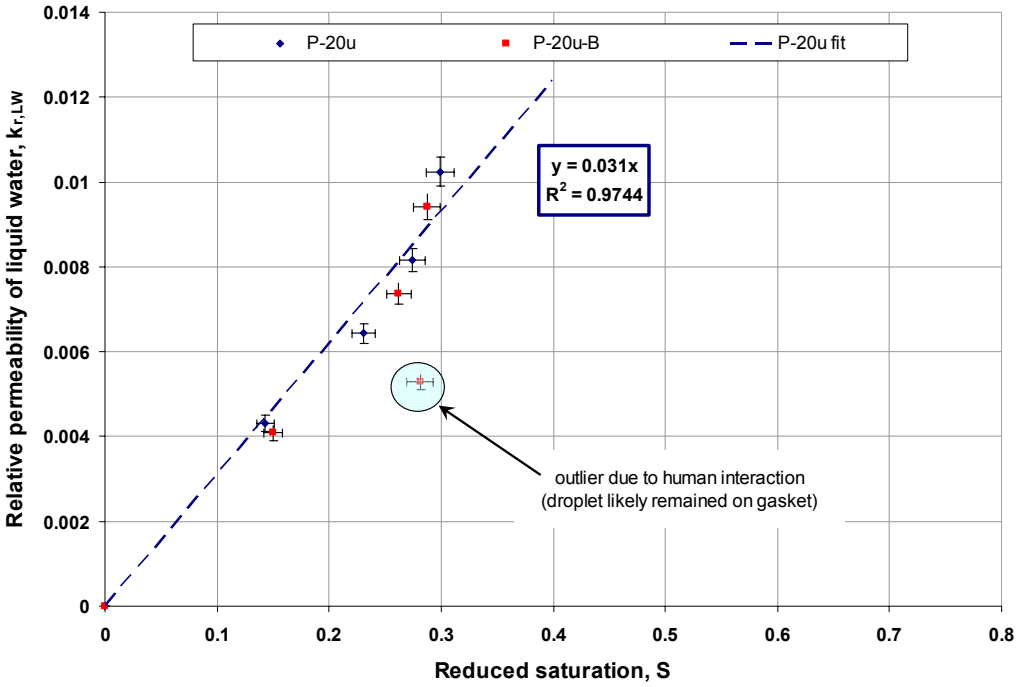

Figure 5.21 – Results of VT-k_r repeatability study using P-20u.

5.3.3 Effect of hydrophobic treatment on relative permeability

As discussed in Chapter 3, the capillary behavior of a porous media is a material property whereas the relative permeability of a porous media is dependent on the characteristics of the material, as well as the properties of the fluids in the two-phase system. When measuring the capillary characteristics using the GDP method, the water has no choice but to fill all open pore volume within the porous media. The GDP results showed that PTFE loading did not have a significant impact on the capillary characteristics of the carbon paper materials. Alternatively, when the fluids are given the freedom to flow through the material as in the VT-k_r experiment, a different result would be expected. Figure 5.22 displays the results obtained for the relative permeability of liquid water for the P-0u and P-20u GDL materials, as well as the cubic function commonly used in PEMFC modeling.

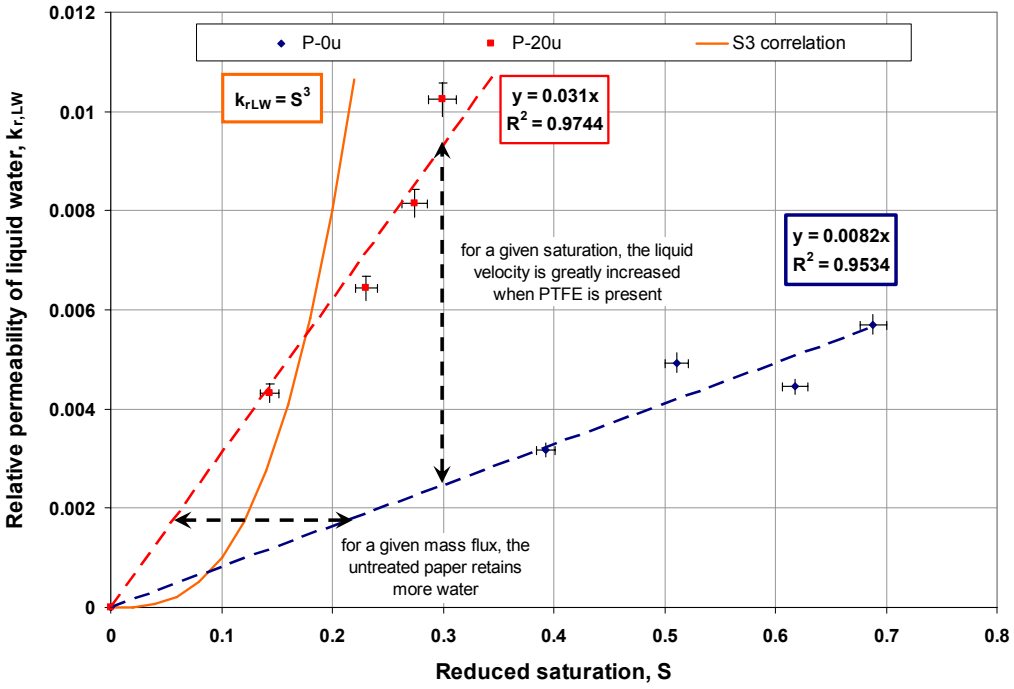

Figure 5.22 – Liquid water relative permeability results for P-0u and P-20u.

It is evident from Figure 5.22 that relative permeability has a significant dependence on PTFE loading for carbon paper materials. Increased PTFE loading causes a distinct increase in the slope of the relative permeability function for carbon paper GDL materials. If a constant saturation is considered, it is evident that the PTFE treated carbon paper will yield a significant increase in liquid water velocity. Looking at the impact of PTFE from another perspective suggests that for a given mass flux of water ($k_{r,LW}$ and dP/dx are held constant) the specimen with no hydrophobic treatment will retain more water than the treated sample.

The relative permeability curves measured for carbon cloth specimens C-0u and C-20u are presented in Figure 5.23. Similar to the carbon paper material, it can again be seen that the addition of hydrophobic polymer to the porous matrix induces a significant increase in the slope of the relative permeability function. The curve displayed for the relative permeability of the C-20u material includes a significantly greater number of data points than other curves. The reason for the increase in data points is that the human interaction caused significant scatter in saturation at such small values of saturation (i.e., the impact of a small droplet on the border of a sample is much more significant at low

values of saturation). Due to the added scatter, three curves were collected. Of the 14 points collected, 2 points exhibited unreasonable variance in saturation and were discarded as outliers.

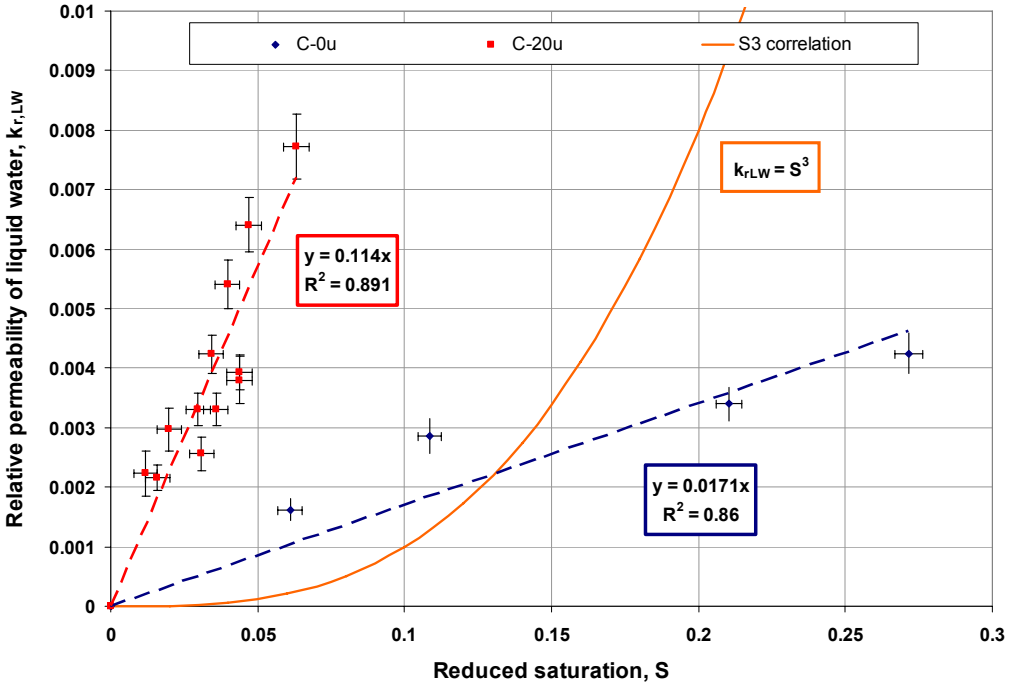

Figure 5.23 – Liquid water relative permeability results for C-0u and C-20u.

The increase in slope with greater PTFE content for both the carbon paper and carbon cloth materials suggests that for a given pressure gradient and saturation, the materials with a hydrophobic treatment will provide substantial improvement in water transport in the form of increased permeability at a given level of saturation. In contrast, the GDP results suggested that PTFE content had a minimal effect on the derivative of capillary pressure with saturation (the driving force for liquid transport). These conclusions quantify for the first time how a hydrophobic treatment actually improves PEMFC performance – the PTFE increases relative permeability without significantly affecting dP_c/dS behavior.

5.3.4 Effect of compression on relative permeability

It is common for GDL materials to be compressed under the shoulder region of a bipolar plate. Therefore, it is important to characterize the liquid water relative permeability for compressed GDL materials in addition to the uncompressed materials already presented. The results for significantly compressed carbon paper loaded with 20% PTFE (P-20c) are depicted in Figure 5.24.

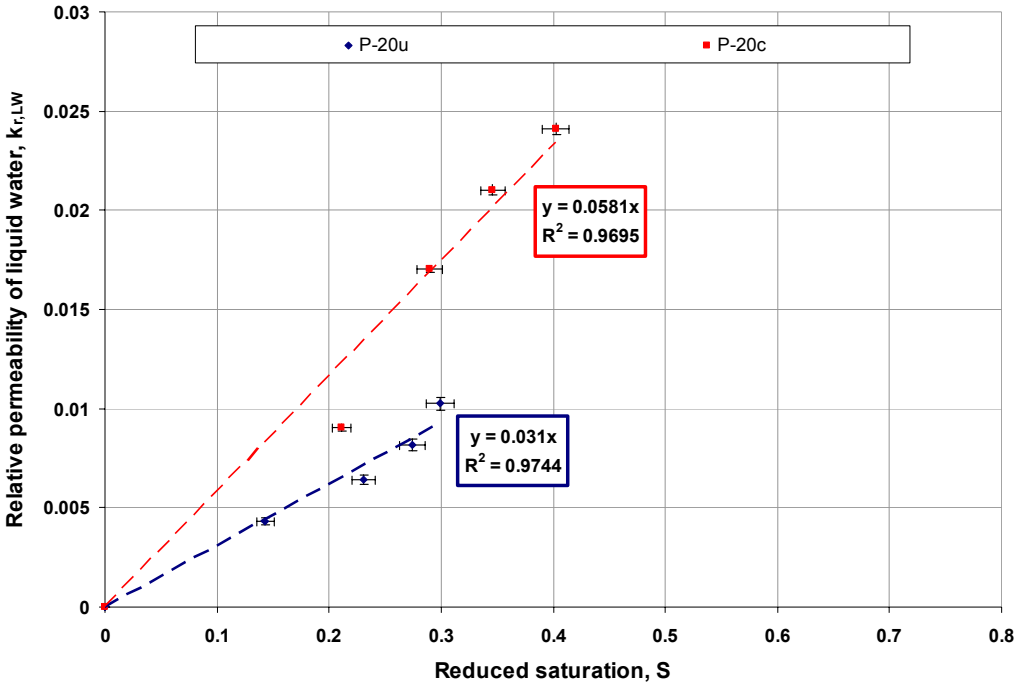

Figure 5.24 – Comparison of relative permeability functions for P-20u and P-20c.

It is evident in Figure 5.24 that compression causes an increase in the slope of the relative permeability function for carbon paper. However, the results for the compressed carbon cloth (Figure 5.25) indicate that the slope of the relative permeability function decreases for the compressed specimen.

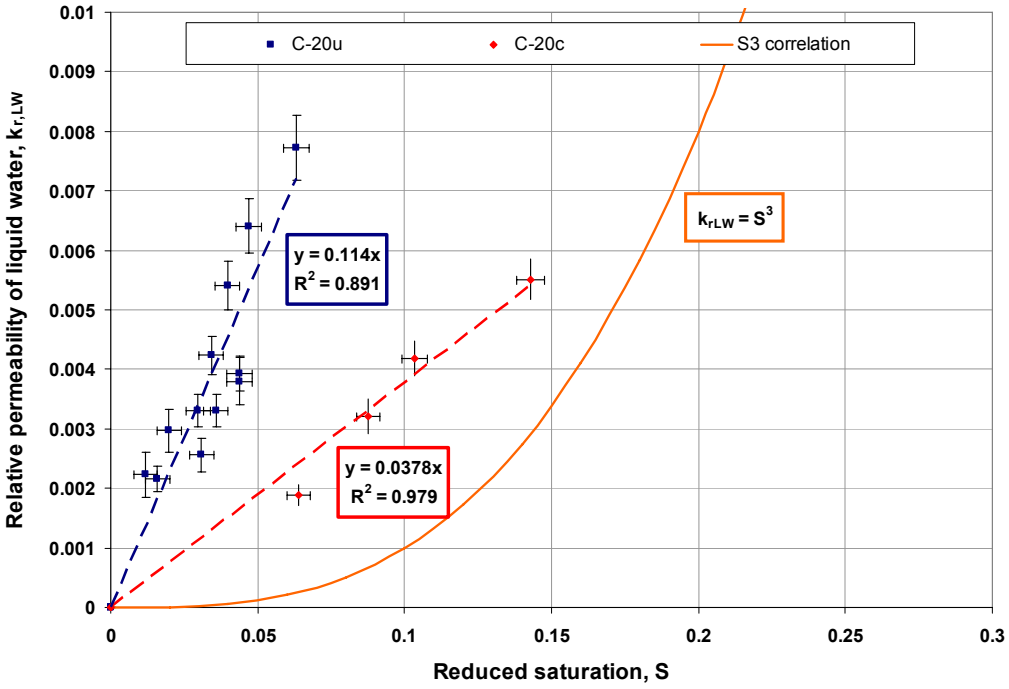

Figure 5.25 - Comparison of relative permeability functions for C-20u and C-20c.

Although the results of the compression study for the carbon cloth and paper suggest a different trend for each material it is important to realize that the relative permeability is simply a modifier to the absolute permeability. In other words, the actual effective permeability of liquid water (κ_{LW}) is the product of the absolute permeability (K) and the relative permeability function ($k_{r,LW}$). Plots of the change in effective permeability with compression for the P-20 and C-20 materials are presented in Figure 5.26 and Figure 5.27 where the absolute permeability was taken from Table 5.4.

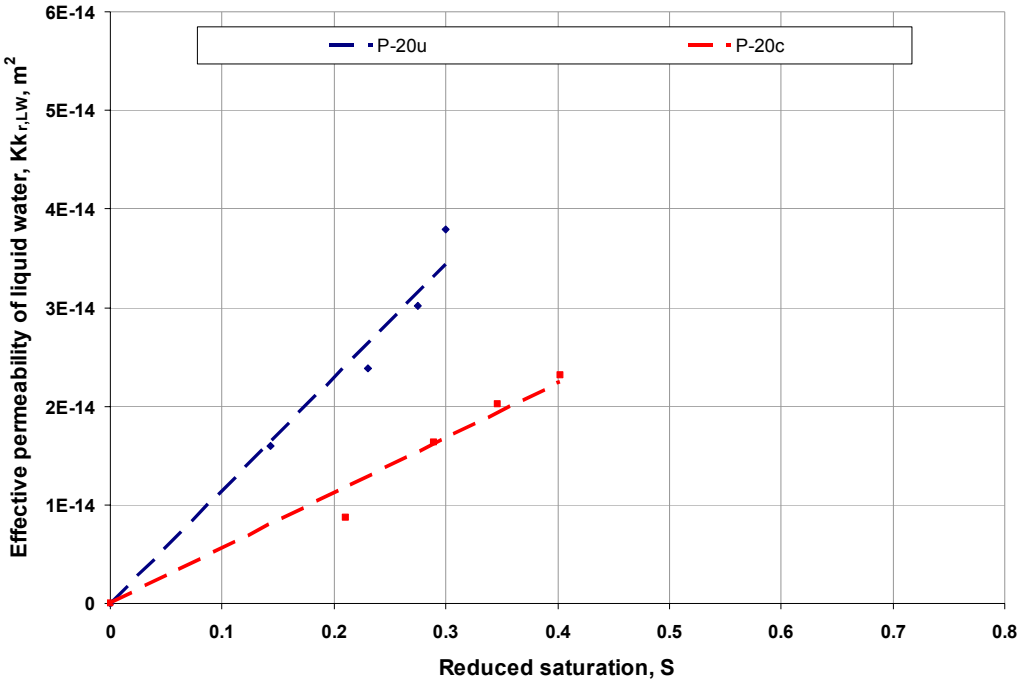

Figure 5.26 – Effective permeability of liquid water through P-20u and P-20c.

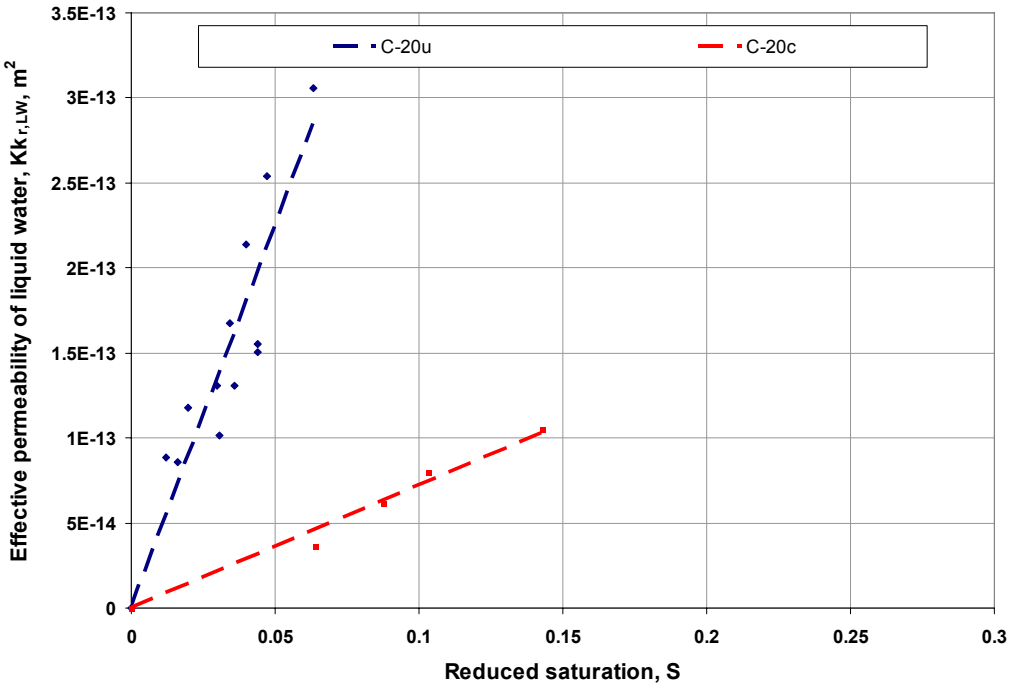

Figure 5.27 – Effective permeability of liquid water through C-20u and C-20c.

It is evident from Figure 5.26 and Figure 5.27 that when effective permeability is compared, the same trend emerges for both material types. Compression clearly causes a substantial reduction in effective permeability, particularly for the cloth material. Relating this discussion back to the previous discussion pertaining to the impact of PTFE content suggests that compression alters flow in a similar way to a reduction in PTFE content. In other words, compression encourages water retention within the GDL and/or reduces liquid velocity.

5.4 SUMMARY OF GDL PROPERTY CHARACTERIZATION

Although it has been commonplace for many years in the fuel cell industry to apply a hydrophobic treatment to GDL materials, the impact of such treatment has never before been directly linked to any particular constitutive relationship. The loading of PTFE is seen to have a mild impact on the absolute permeability for both types of media (paper and cloth). Additionally, for the carbon paper materials, it was evident that hydrophobic polymer content had minimal impact on the capillary pressure function, $P_c(S)$, yet had a strong influence on the relative permeability of the liquid phase. For the carbon cloth materials with intermediate values of PTFE content (10 and 20%) that are commonly recognized as the most beneficial to performance, the capillary pressure functions were found to be nearly identical. However, the relative permeability was again strongly affected by PTFE content for the carbon cloth materials.

The impact of compression on GDL materials manifests itself in many ways. Compression has a significant impact on the absolute permeability for both material types, causing a 57% reduction in the permeability of the carbon cloth, and a 74% reduction in the permeability of carbon paper. Furthermore, it was shown that compression has a homogenizing effect on carbon paper and carbon cloth materials with regard to their capillary behavior which is manifested in the flattening of the dP_c/dS function. The impact that compression has on the *effective permeability* (κ) is essentially the opposite of the impact of PTFE loading. In essence, increased compression encourages water retention within both media types.

5.5 PARAMETRIC STUDY OF LIQUID WATER FLOW USING 1-D GDL MODEL

The intent of the one-dimensional model described in Chapter 4 is to compare the effect on liquid water transport of the constitutive relations and the materials properties that comprise the liquid water transport coefficient. These material properties, dP_c/dS, $k_{r,LW}$, and K, have been compared in previous sections, yet the collective effect of them has yet to be investigated. This section will qualitatively compare the impact of the liquid water transport coefficient terms from two literature sources [12, 15], and the relationships developed for the P-20u material in this work. It is important to note that the two literature sources being referenced were not developed around any particular GDL material. Instead, the GDL properties were assumed and/or adjusted to achieve the desired model output. Therefore, there is no particular reason to believe that the experimentally determined relations and properties for the P-20u material will yield water transport results similar to those produced by using the relations and properties from the literature sources. However, since the commonly assumed relationships are applied to many different types of diffusion media throughout the PEMFC literature it is important to compare them to relationships with experimental grounding.

All governing equations, constitutive relations, and constants with the exception of those included in the liquid water transport coefficient term, and the investigated parameters (gas channel relative humidity and current density) will remain the same for all simulations. For the parametric study the relative humidity will take on two different values (75 and 95%) and the current density will take on three different values (0.5, 1, and 1.5 A/cm^2).

5.5.1 Definition of constants and constitutive relationships

This section details the values of all constants used in the 1-D model, as well as the definitions of the constitutive relations for the three different cases being considered. Table 5.7 displays the constants used in the 1-D model.

Table 5.7 – Definition of constants in 1-D model.

Description	Symbol	Value	Units
molar mass of diatomic oxygen	M_{O2}	0.032	*kg/mol*
molar mass of water vapor	M_{wv}	0.018	*kg/mol*
molar mass of diatomic nitrogen	M_{N2}	0.028	*kg/mol*
mass ratio of N2 to O2 in GFC	$r_{N2:O2}$	3.2917	-
universal gas constant	R_u	8.314	$Pa\text{-}m^3/(mol\text{-}K)$
Faraday's constant	F	96485	$Coul/mol\ e^-$
isobaric gas pressure	P_g	101325	*Pa*
water phase change rate constant	γ	900	s^{-1}
isothermal cell temperature	T	353	*K*
GDL porosity	ε	0.6	-
GDL thickness	t	3.00E-04	*m*
effective EOD coefficient	α_{EOD}	0.5	$mol\ H_2O/mol\ H^+$

The constants in Table 5.7 are fairly self explanatory with the possible exceptions of $r_{N2:O2}$, γ, ε, and α_{EOD}. Recalling from Chapter 4, $r_{N2:O2}$ is the ratio of nitrogen to oxygen in the dry oxygen/nitrogen gas mixture in the gas flow channel. This ratio is assigned a value of 3.2917 which corresponds to ambient air. The water phase change rate constant, γ, represents non-equilibrium phase change, where the value of 900 s^{-1} is based on kinetic theory and borrowed from Nam et al. [10]. Since porosity does not factor into the liquid water transport coefficient, it was held constant for all three constitutive relation sets. A value of 0.6 was chosen because it is similar to the value used by Pasaogullari [12], and Lin [15], which constitute two of the three sets of modeling parameters considered in the

1-D simulations. Finally, the value for α_{EOD} was borrowed from Nam et al. [10] and falls within the reasonable range described by Springer et al. [5].

As previously mentioned, three key transport parameters, the parameters making up the liquid water transport coefficient (c_{LWT}), are varied in the 1-D model. The expressions or values assigned to these parameters are displayed in Table 5.8. The dP_c/dS relationship used for the P-20u model has been adjusted for temperature to comply with the base case condition of $T_{cell} = 80°C$.

Table 5.8 – Liquid water transport coefficient parameters for 1-D model.

Source	$-dP_c/dS$ (Pa)	$k_{r,LW}$ (unitless)	K (10^{-12} m^2)
Lin [15]	22.95	S	0.11
Pasaogullari [12]	$18230\left[1.417-4.24S+3.789S^2\right]$	$S^3+1e\text{-}6$*	0.6875
Sole (P-20c)	$10^6\begin{cases}\left[\begin{matrix}-840.723S^5+156.319S^4+10.193S^3\\-1.887S^2+0.0584S\end{matrix}\right] & S<0.18\\\left[\begin{matrix}-123.687S^5+71.094S^4+4.309S^3\\-7.570S^2+0.999S+0.00316\end{matrix}\right] & 0.18\le S<0.4\\\left[\begin{matrix}-8.474S^5+31.189S^4-45.225S^3\\+32.324S^2-11.340S+1.5916\end{matrix}\right] & S\ge 0.4\end{cases}$	$0.031S$	3.71

*a small shift of $1x10^{-6}$ was introduced to improve numerical stability at small values of S

The base 1-D model described in Chapter 4, along with the constants and constitutive relations described in Table 5.7 and Table 5.8 are the basis for the curves generated in the following sections. In essence, one boundary condition that has a significant impact on evaporation (RH_{gfc}), and one boundary condition that has a significant impact on the introduction of liquid water at the catalyst layer (j), will be varied to qualitatively investigate the impact of the terms comprising the liquid water transport coefficient (c_{LWT}).

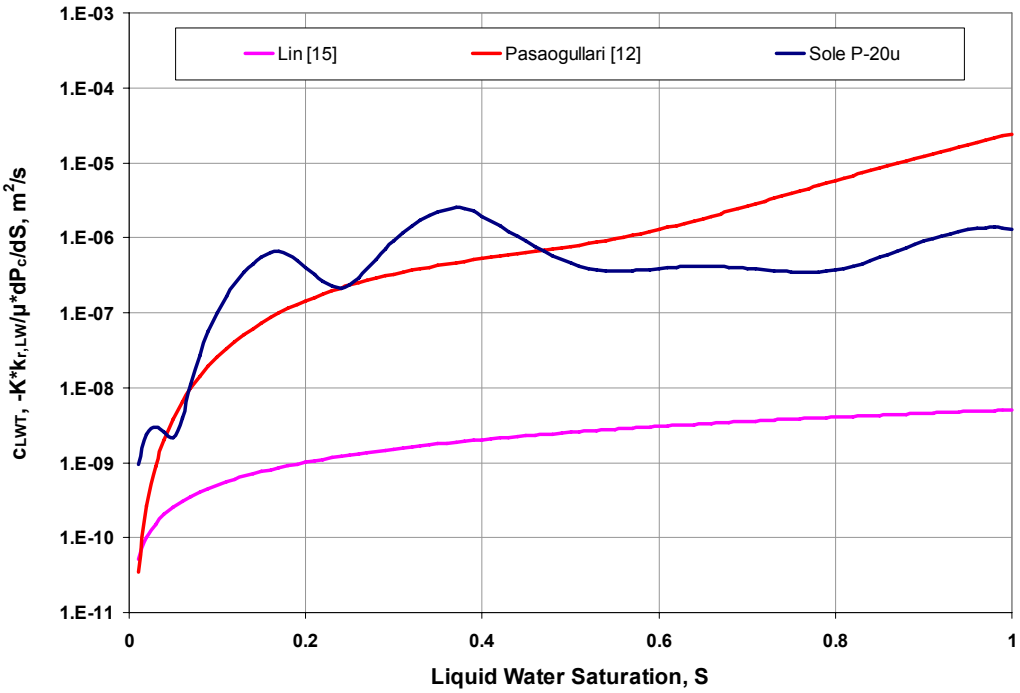

Figure 5.28 – Variation in c_{LWT} with saturation for the works investigated in the 1-D model.

As an initial comparison of the terms comprising c_{LWT}, a plot describing the coefficient of liquid water transport as a function of saturation is provided in Figure 5.28. The curvature of the dP_c/dS function measured in this work is evident in the c_{LWT} function for the P-20u material. It is interesting to note that the magnitude of c_{LWT} is similar (within an order of magnitude for most values of S) for the Sole model and the model presented by Pasaogullari. However, it is evident in Table 5.8, that the means by which the magnitude of c_{LWT} was achieved is drastically different for the two models. For example, the absolute permeability utilized by Pasaogullari is less than 20% of the value measured and used in the Sole model.

5.5.2 Effect of GFC relative humidity and average current density

Incrementing the gas channel relative humidity and the current density will obviously have a substantial impact on the saturation within the GDL. However, the constitutive relations and material properties defined in Table 5.8 govern the momentum

of liquid water and therefore can drastically impact on the saturation profile in the GDL. Figure 5.29 displays the predicted saturation profile for both 75% and 95% gas channel relative humidity for a current density of 0.5 A/cm^2.

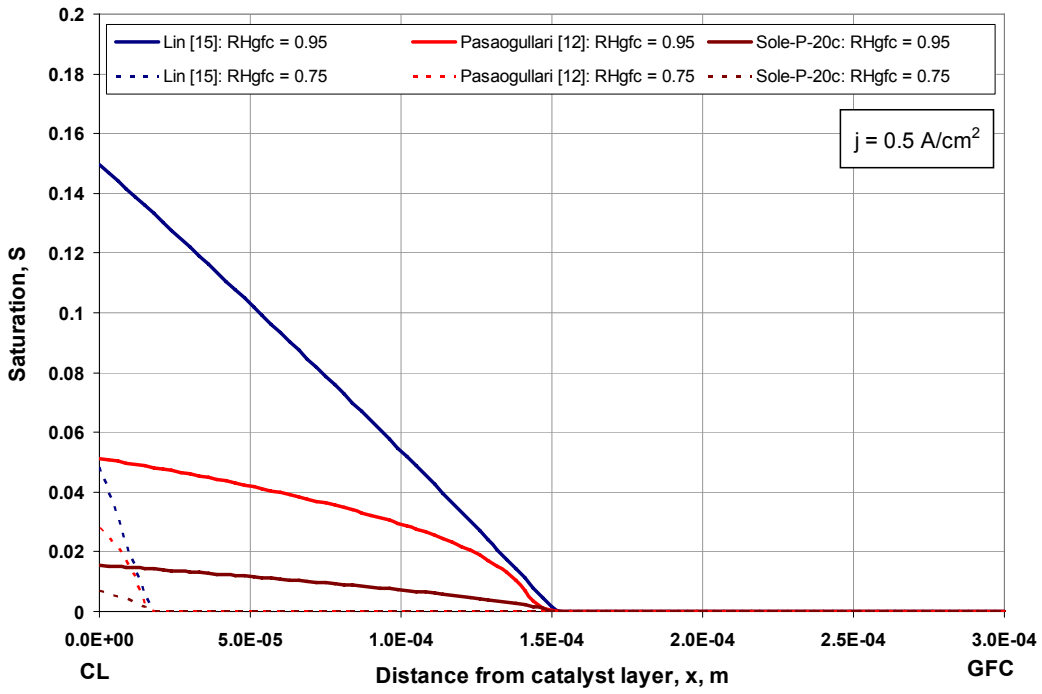

Figure 5.29 – 1-D model saturation profiles for 0.5 A/cm^2 at 95% and 75% RH$_{gfc}$.

It is evident in Figure 5.29 that the GDL becomes dry a very short distance from the catalyst layer when the gas channel relative humidity is only 75%, whereas partial saturation is evident through approximately half of the GDL at 95% for all three models (Pasaogullari, Lin, and Sole). Perhaps more interesting is the disparity in the saturation at the catalyst layer (CL) for each model. At 95% RH, the CL saturation for the model fashioned after the work of Pasaogullari predicts a saturation that is approximately three times the CL saturation predicted for the P-20u relations determined in this work. A more drastic difference is observed for the model fashioned after the work of Lin, where the CL saturation is an order of magnitude larger than it is for the model utilizing the relations determined for P-20u.

When the current density is increased (1 A/cm^2 in Figure 5.30, and 1.5 A/cm^2 in Figure 5.31), similar disparity is observed where the CL saturation predicted for the

expressions by Lin is an order of magnitude larger than the CL saturation predicted for the P-20u material of this work. The CL saturation for the Pasaogullari relations are again approximately three times the values predicted for P-20u for both current densities.

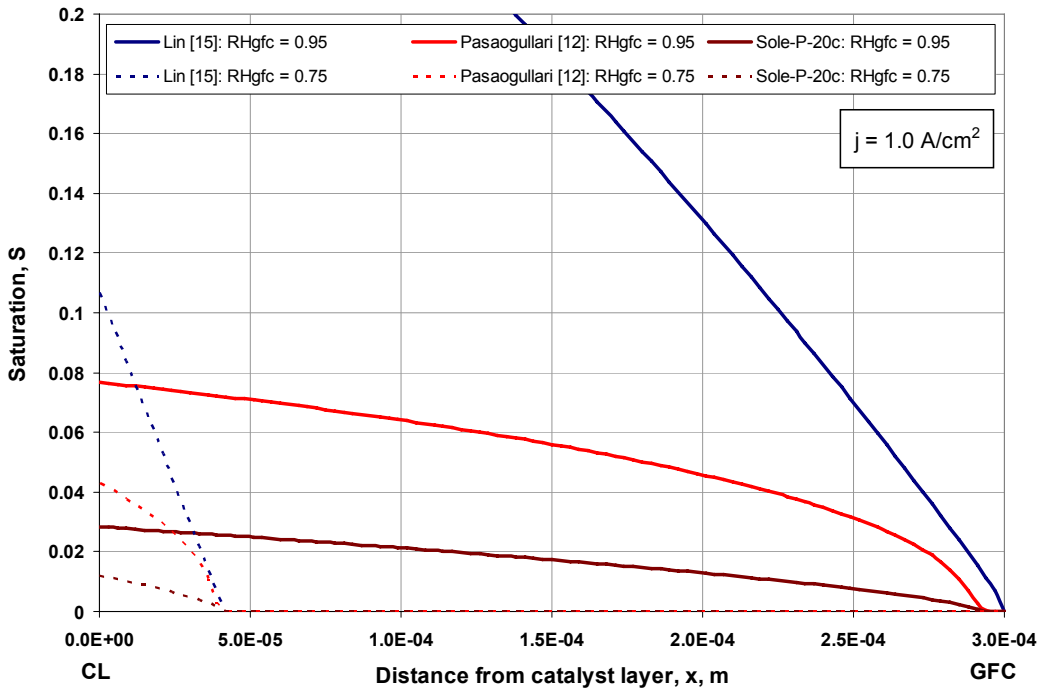

Figure 5.30 - 1-D model saturation profiles for 1.0 A/cm^2 at 95% and 75% RH$_{gfc}$.

The impact of relative humidity is again seen in Figure 5.30 and Figure 5.31. Increased GFC relative humidity increases the distance into the GDL that is wet. Increased current density also increases the wet thickness due to excess product water being available to saturate the gaseous mixture with in the GDL. It can be seen in Figure 5.31 that at high current density and high gas channel humidity, that all three models predict partial saturation throughout the entire GDL domain. However, great disparity in the level of saturation among the three models is still observed.

In order to asses the reason for the disparity in the saturation profiles it is useful to compare the liquid water transport coefficient for each set of model relations. Figure 5.32 displays c_{LWT} for all three sets of constitutive relations at 1 A/cm^2 and both humidity levels.

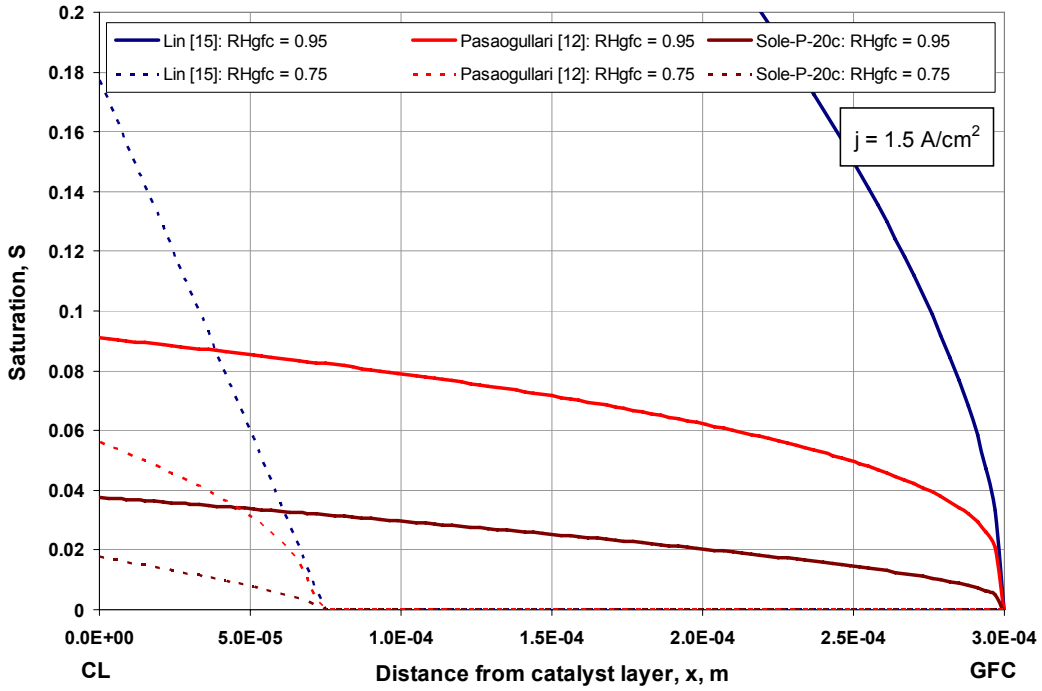

Figure 5.31 - 1-D model saturation profiles for 1.5 A/cm^2 at 95% and 75% RH_{gfc}.

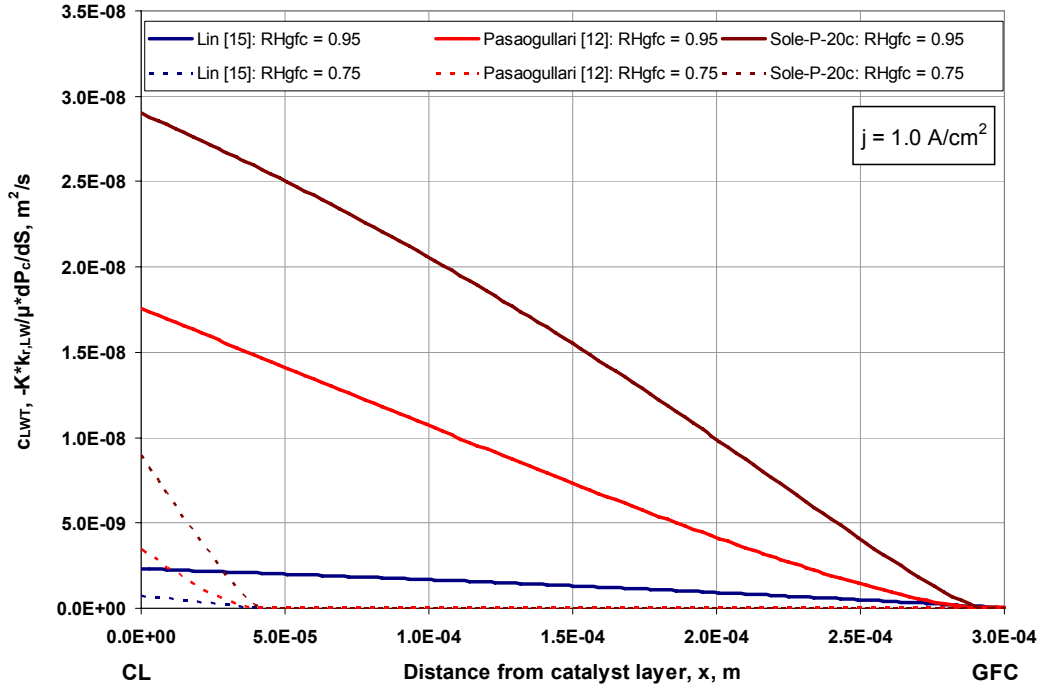

Figure 5.32 - 1-D model liquid water transport coefficient profiles for 1 A/cm^2 at 95% and 75% RH_{gfc}.

In Figure 5.32 it is evident that the small values of saturation in the GDL predicted for the P-20u material are largely due to the significantly larger values of $c_{LWT.}$ A large value of c_{LWT} suggest that liquid water moves quickly through the GDL and accumulation is minimal, therefore explaining the small values of saturation predicted for the P-20u model. At greater current densities, and therefore greater water production, the value of the liquid water transport coefficient is still quite large for the P-20u model (Figure 5.33).

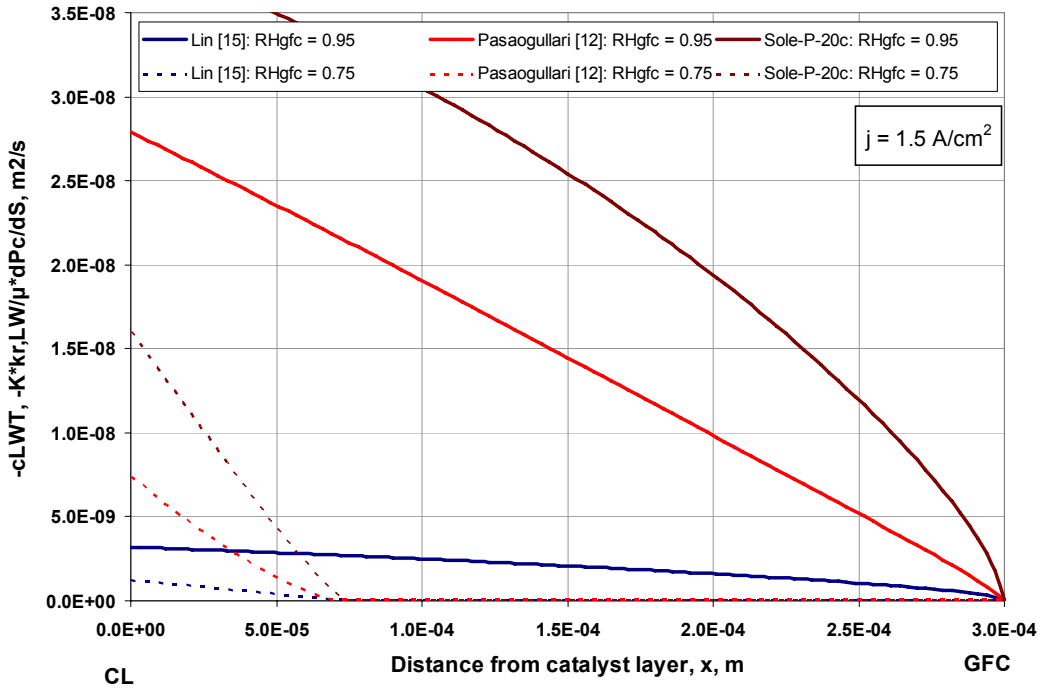

Figure 5.33 – Spatial variation in the liquid water transport coefficient at 1.5 A/cm^2.

The large c_{LWT} values for the P-20u results are primarily attributable to the value measured for absolute permeability (K). The value of K for the P-20u model is 5.4 times greater than the value used by Pasaogullari, and 34 times greater than the values used by Lin. Although, the value of c_{LWT} is substantially larger for the P-20u model than it is for the others, the disparity in c_{LWT} is not directly proportional to the differences in absolute permeability. In fact, when comparing the value of c_{LWT} at the catalyst layer for the 95% RH case, the value for the P-20u materials is approximately 1.6 times greater than the value for the model using the relations described by Pasaogullari, and approximately 11 times greater than the value for the model utilizing the relations described by Lin. This

observation reveals how easily liquid water transport can be manipulated in PEMFC modeling by adjusting the wrong material properties and/or constitutive relations to achieve the desired model output.

Figure 5.34 depicts the diffusivity correction for both humidity levels at a current density of 1 A/cm^2. For the unsaturated regions the diffusivity correction is constant and takes on the value associated with the correction term accounting for the GDL porosity, $f(\varepsilon) = \varepsilon^{1.5}$ (where $\varepsilon = 0.6$ for all cases). In regions of partial saturation, the $g(S)$ term begins to influence the diffusivity of gases. However, for the simulation utilizing the relations described by Pasaogullari and the relations derived in this work for the P-20u material, the low saturations only impact the diffusivity corrections by a maximum of 10%. On the other hand, since the simulation utilizing the relations proposed by Lin predicts substantially greater levels of saturation, a greater limitation on diffusivity follows.

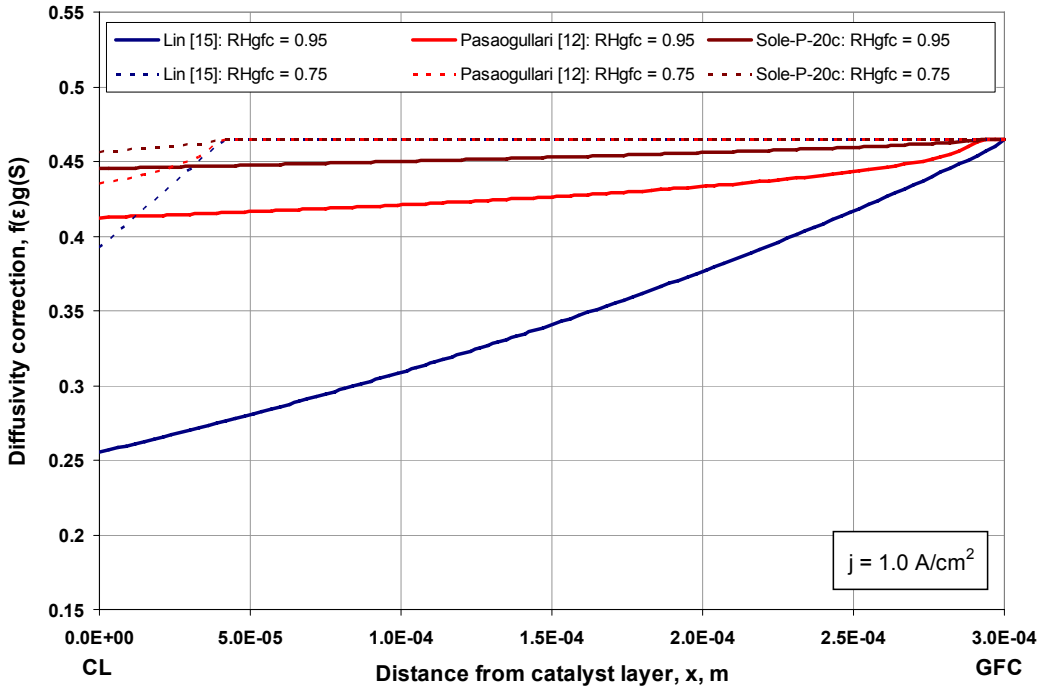

Figure 5.34 – Gas diffusivity correction for 1 A/cm^2 at 95% and 75% RH$_{gfc}$.

The primary purpose of the 1-D model was to investigate the substantial impact that the terms which form the liquid water transport coefficient can have on liquid and gaseous transport. The c_{LWT} (as calculated from K, $k_{r,LW}$, and dP_c/dS) and the resulting saturation field and diffusivity correction are strikingly different among the three models – Lin, Pasaogullari, and Sole. It is important to note that the models developed by Lin and Pasaogullari were not for any particular GDL material. Pasaogullari focused on how parameters such as contact angle impact saturation and made no comparisons to experimental data, and Lin adjusted K until the model output matched experimental polarization behavior. However, the GDL that Lin used in the cell from which the polarization data was collected was not reported. In both cases, the overall model was adjusted to predict the desired trends or polarization behavior. However, for model results to be useful in guiding GDL design, they must be tied to experimentally measurable GDL characteristics.

5.6 EXPERIMENTAL PERFORMANCE OF 2-D VALIDATION CELL

The 2-D cathode GDL model described in Chapter 4 was developed to include the effects of GDL compression, and to predict polarization behavior for an operating PEMFC utilizing representative GDL materials investigated in this work (P-20 and C-20). The 2-D model described in Chapter 4 requires inputs of four operational constants determined via in-situ measurements. These constants include the operational open circuit potential (E_{oc}), the Tafel reaction parameter (αn), the exchange current density measured at reference conditions (j_o^0), and the area specific high frequency resistance that includes all ohmic overpotentials in the cell (*HFR'*). In addition to these four in-situ parameters, polarization curves for the two representative operational PEMFCs are presented. Ultimately, the intent of the model is to predict polarization behavior without any adjustment parameters.

5.6.1 Carbon cloth based GDL performance

At relatively large values of overpotential the Butler-Volmer equation simplifies to the Tafel equation which can be used to calculate some of the parameters required in the Butler-Volmer equation presented in Chapter 4. The Tafel equation as presented by O'Hayre [56] is presented here as Eq. (5.10).

$$\eta_{act} = -\frac{R_u T}{\alpha n F} \ln j_0^0 - \frac{R_u T}{\alpha n F} \ln j = a + b \ln j \tag{5.10}$$

Here it is important to note that the activation overpotential should not include any ohmic losses and therefore must be calculated using an IR-corrected cell potential according to Eq. (5.11).

$$\eta_{act} = \eta_{tot} - \eta_{IR} = \left(E_{oc} - E_{cell}\right) - HFR' \times j \tag{5.11}$$

Here E_{oc} is the operational open circuit potential, *HFR'* is the area specific resistance measured at high-frequency, and j is the average current density measured at E_{cell}.

Making the appropriate modifications and plotting the activation overpotential versus ln(j) (a Tafel plot) allows for easy extraction of the necessary reaction parameters (αn and j_o^0) according to Eq. (5.12)-(5.13):

$$\alpha n = b \frac{F}{R_u T} \tag{5.12}$$

$$j_o^0 = \exp\left[a/b\right] \tag{5.13}$$

where a and b were defined in Eq. (5.10) and can be extracted from a Tafel plot.

The Tafel plot with an appropriate curve fit for the operating PEMFC utilizing the C-20 GDL is depicted in Figure 5.35. From Figure 5.35 it is clear that the Tafel slope (*b*

in Eq. (5.10)) is 0.0234 and the reference exchange current density (as defined in Eq. (5.13)) is 2.391 A/m^2 for the C-20 cell operating at 95% cathode relative humidity and a cell temperature of 80°C.

A Tafel plot was also generated for the cell utilizing the C-20 GDL at a cathode relative humidity of 75%. The resulting curve is presented in Figure 5.36.

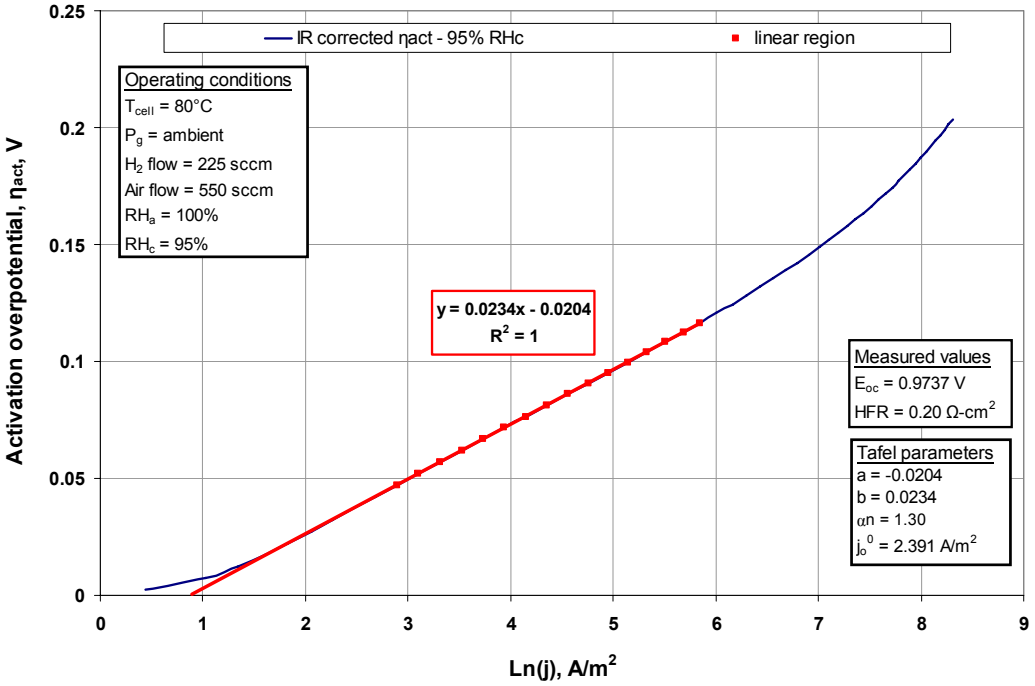

Figure 5.35 – Tafel plot for C-20 cell operating at 95% cathode RH.

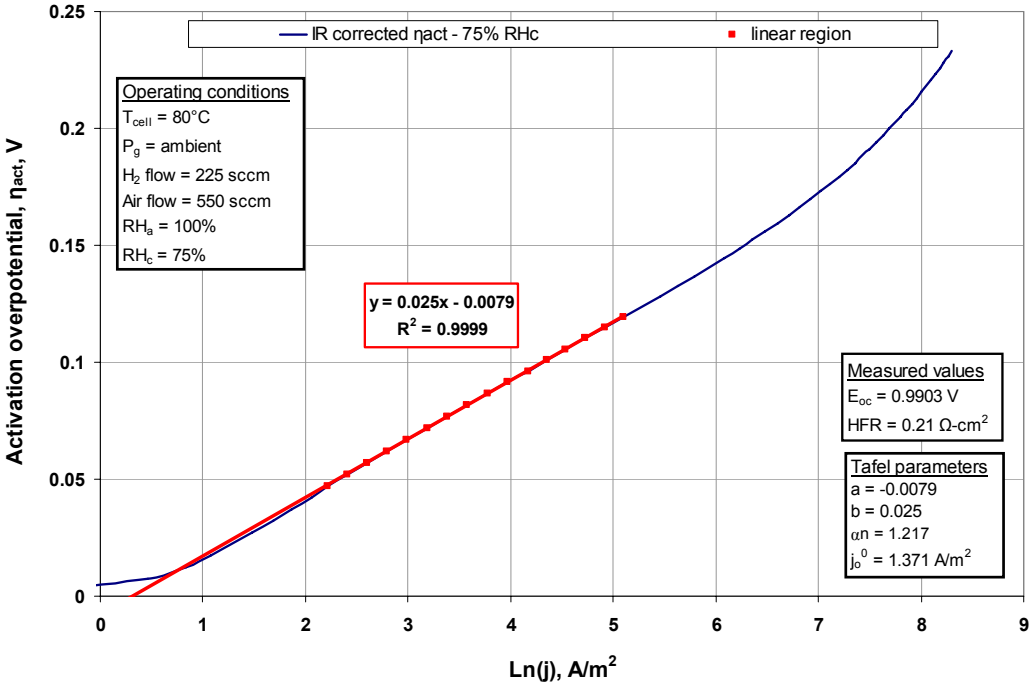

Figure 5.36 – Tafel plot for C-20 cell operating at a cathode RH of 75%.

The ultimate intent of a PEMFC model is to predict polarization behavior at a variety of operating conditions and cell potentials. Therefore, polarization data at the two different cathode relative humidity's being considered was also collected. Figure 5.37 presents the results for the C-20 cell operating at a cathode humidity of 95% and 75%.

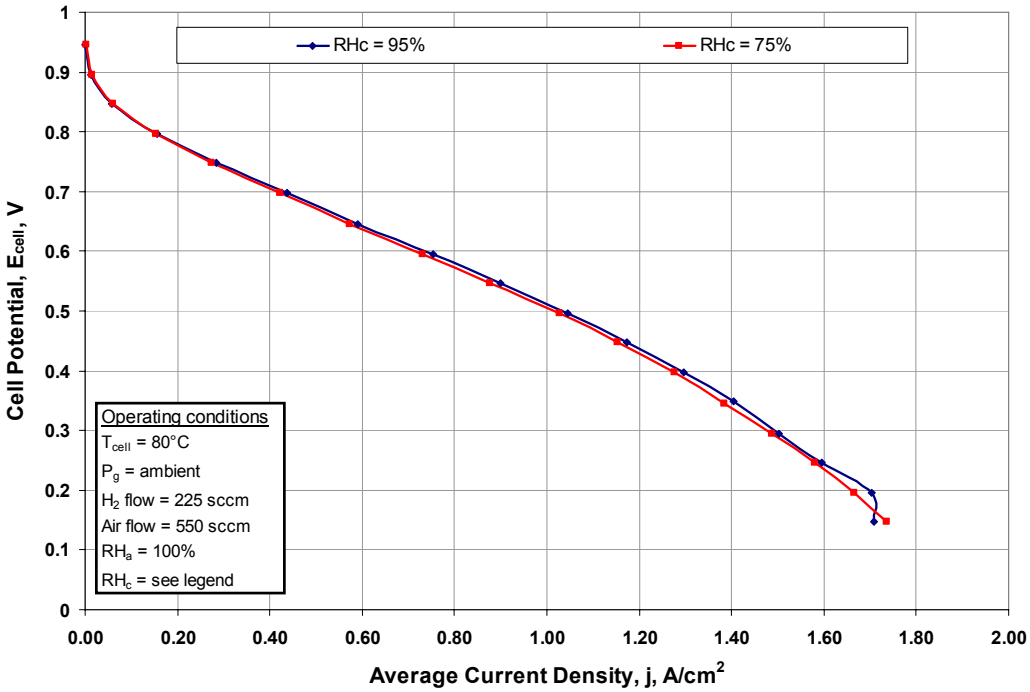

Figure 5.37 – Polarization behavior for the C-20 validation cell at 95% and 75% RH_c.

The performance at the two different cathode humidity levels is nearly identical. This suggests that relative humidity has nearly no impact on the concentration losses in the cell. Such a result may be indicative of little to no change in the diffusive fluxes within the GDL, therefore suggesting that the GDL is minimally saturated for both humidity conditions. The steep slopes exhibited by the relative permeability functions, and the high value of absolute permeability exhibited by the C-20 material support the hypothesis that the water moves through the GDL quickly, therefore minimizing the likelihood of water accumulation (saturation).

5.6.2 Carbon paper based GDL performance

An identical set of experiments were performed on the P-20 validation cell. Figure 5.38 and Figure 5.39 display the Tafel slope data for the P-20 cell operating at a cathode inlet relative humidity of 95% and 75% respectively.

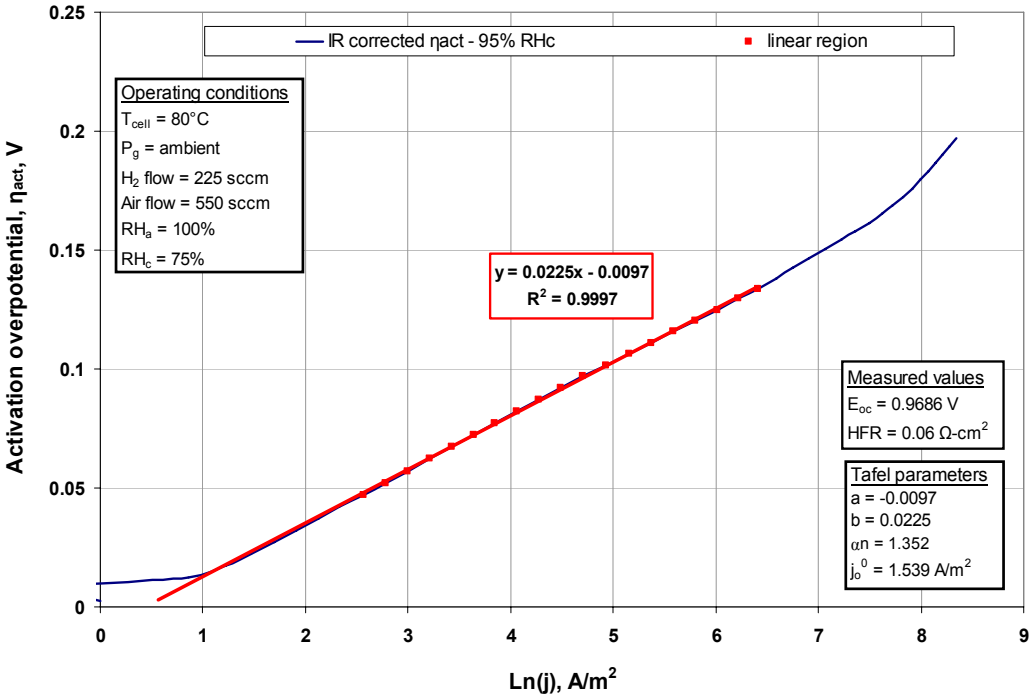

Figure 5.38 – Tafel slope measurement for P-20 cell operating at RH_c = 95%.

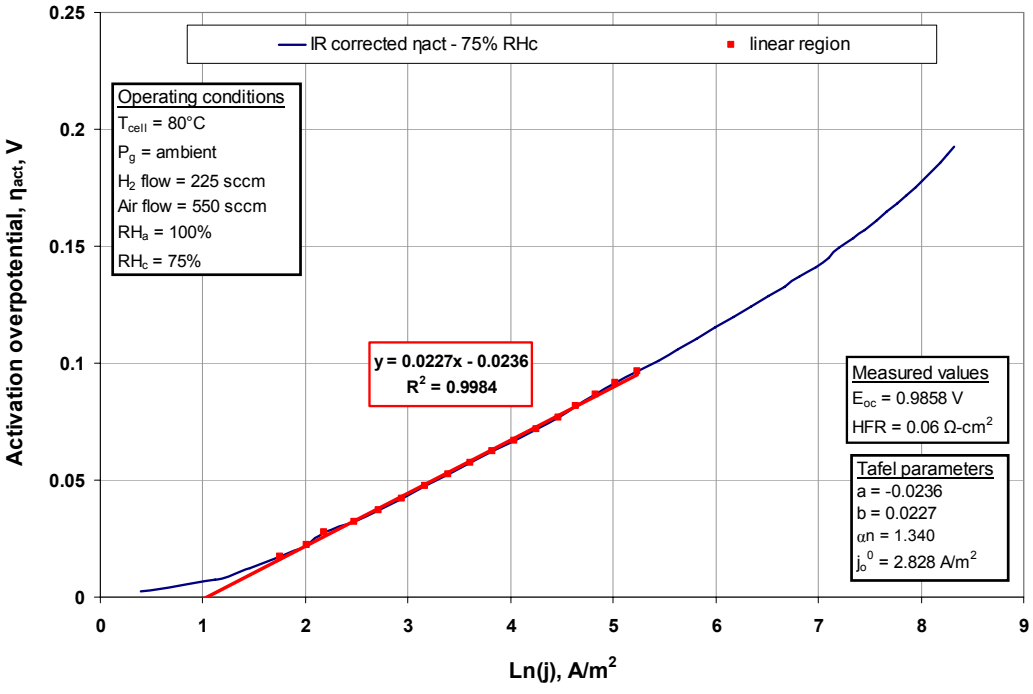

Figure 5.39 - Tafel slope measurement for P-20 cell operating at RH_c = 75%.

The current density of the P-20 cell operating at a cathode relative humidity of 95% exhibited unsteady behavior when a constant cell potential was maintained (Figure 5.40). The unsteady behavior could be due to water droplets impeding flow in the GFC, or due to a thin liquid layer accumulating between the GDL and catalyst layer because of the absence of a microporous layer. In either case, measuring reliable polarization data for a cell exhibiting unsteady current production is impossible. In addition, comparisons to the 2-D model are unrealistic since the steady-state model clearly cannot account for such dynamic behavior. Fortunately, the dynamic behavior was minimized by reducing the cathode humidity. The polarization data for the P-20 cell operating at a cathode relative humidity of 75% is presented in Figure 5.41.

By comparing Figure 5.37 and Figure 5.41, it is evident that the performance of the P-20 cell is substantially greater than the C-20 cell. This is likely due to the significantly lower high frequency resistance as depicted in the Tafel plots.

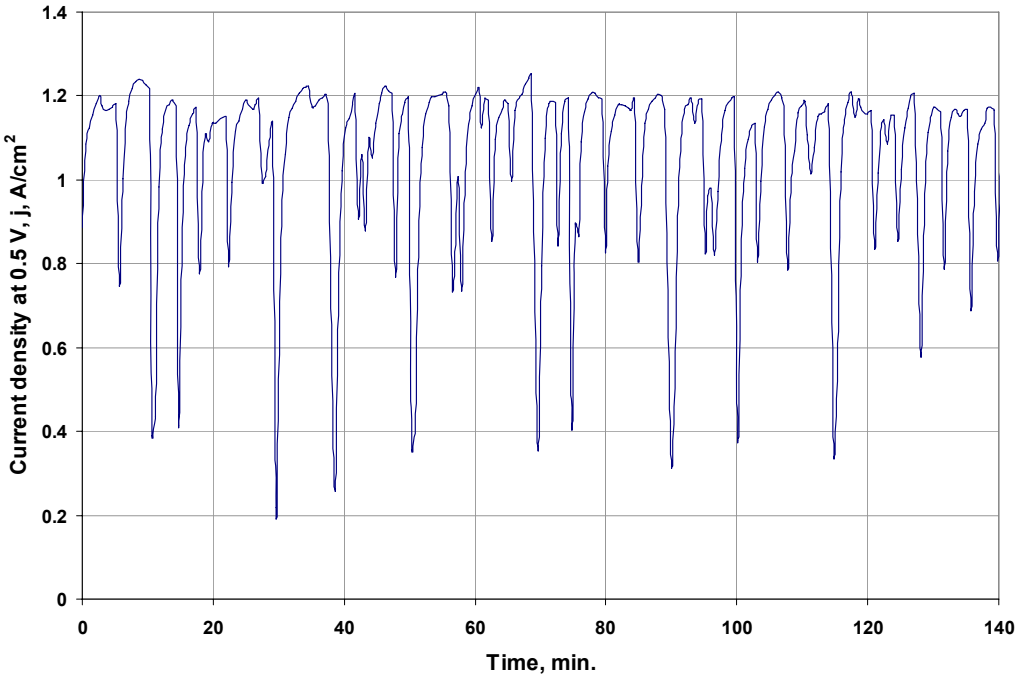

Figure 5.40 – Current output of P-20 cell operating at E_{cell} = 0.5 V and 95% RH_c.

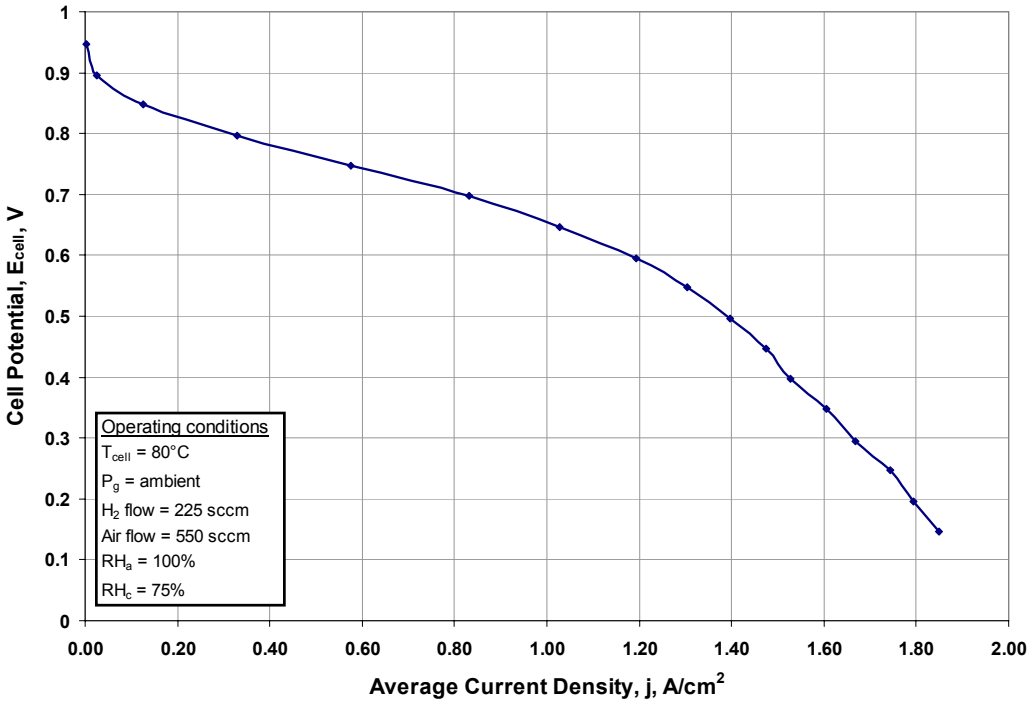

Figure 5.41 – Polarization performance for the P-20 cell operating at RH_c = 75%.

5.6.3 Experimental performance summary

The four key inputs to the 2-D model for each material and relative humidity that were measured in-situ during cell operation are summarized in Table 5.9. In addition, the area specific resistance of the membrane and interfaces ($ASR_{m,i}$), which is simply the measured *HFR'* minus the apparent GDL resistance, is also included.[††] These parameter values will be used in the 2-D model to predict polarization behavior for each GDL and relative humidity under consideration. These inputs, along with the constitutive relations and material properties discussed in the experimental results will be combined in the 2-D model in order to validate its ability to predict performance.

[††] The apparent GDL resistance is determined using a FE model of a dual-layer GDL in which the conductivity is characterized by the orthotropic conductivity tensor described in Chapter 4. In the model, a uniform current is assigned at one GDL/shoulder interface, and a ground condition is assigned on the opposing GDL/shoulder interface. The quotient of the resulting potential drop and given current flux is used to determine the proportion of the HFR that is contributed by the GDLs in the in-situ measurement.

Table 5.9 – Key in-situ parameters for 2-D model input and GDL corrected $ASR_{m,i}$.

GDL material	Cathode relative humidity	E_{oc}	αn	j_0^0	HFR'	$ASR_{m,i}$
		V	-	A/m^2	Ω-cm^2	Ω-cm^2
P-20	0.95	0.9686	1.352	1.539	0.06	0.0488
	0.75	0.9858	1.34	2.828	0.06	0.0488
C-20	0.95	0.9737	1.3	2.39	0.2	0.1561
	0.75	0.9903	1.22	1.37	0.21	0.1661

Although it is unrealistic to predict polarization behavior for the P-20 cell operating at 95% RH_c, the in-situ parameters are included here for completeness. The next section will utilize these parameters to assess the sensitivity of the 2-D model at a particular cell potential.

5.7 2-D MODEL CONSTANTS, CONSTITUTIVE RELATIONS, AND SENSITIVITY

The process of validating the 2-D model is two-fold. First, a base case will be established and the model's sensitivity to a small group of assumed parameter values will be assessed. These assumed parameters are parameters that cannot be readily measured and include: the phase change rate constant (γ), the heat partition factor (f_{HP}), the effective electo-osmotic drag coefficient (α_{EOD}), the GDL/GFC interface saturation (S_{gfc}), and the GFC nitrogen-to-oxygen ratio ($r_{N2:O2}$). If the model can be shown to be relatively insensitive to these values then the practice of assuming them rather than measuring them is better justified. After establishing the models sensitivity to the estimated parameters, an attempt to predict the polarization behavior of the experimental cells utilizing both cloth and paper GDLs (C-20 and P-20 respectively) is presented.

5.7.1 Base case conditions and region specific definitions

To assess the sensitivity of the model to the group of assumed parameters, a base case scenario must first be established. The base case condition is built upon the experimentally determined constitutive relations, material properties, and in-situ cell parameters described in previous section for the C-20 and P-20 validation cells. Additionally, the base case is taken to be at a cell potential of 0.5 V. The collection of base case constants that are independent of GDL region are presented in Table 5.10.

Table 5.10 - Base case constants that are independent of GDL region and material.

Description	Symbol	Value	Units	Basis
molar mass of diatomic oxygen	M_{O2}	0.032	kg/mol	-
molar mass of water vapor	M_{wv}	0.018	kg/mol	-
molar mass of diatomic nitrogen	M_{N2}	0.028	kg/mol	-
universal gas constant	R_u	8.314	Pa-m^3/(mol-K)	-
Faraday's constant	F	96485	Coul/mol e$^-$	-
thermal conductivity of carbon fiber	k_{carb}	6.75	W/m-K	est.
thermal conductivity of gas phase	k_g	0.02	W/m-K	est.
thermal conductivity of liquid water	k_{LW}	0.58	W/m-K	est.
specific heat capacity of gas phase	c_p	1008	J/kg-K	est.
mass transfer convection coefficient	h_m	1000	kg/m^2-s	adj.[1]
heat transfer convection coefficient	h_T	1.13	W/m^2-K	flat plate est.
reversible open circuit potential	$E_{oc,rev}$	1.17	V	calc.
reference anode potential	$\varphi_{i,A}$	0	V	-
isobaric gas pressure	P_g	101325	Pa	exp. cond.
cell temperature	T_{cell}	353	K	exp. cond.
gas channel relative humidity	RH_c	0.95	-	exp. cond.
cell terminal potential	E_{cell}	0.5	V	exp. cond.
heat partition factor	f_{HP}	0.7	-	assumed
effective EOD coefficient	α_{EOD}	0.5	mol H_2O/mol H^+	assumed
water phase change rate constant	γ	900	s^{-1}	assumed
GFC/GDL interface saturation	S_{gfc}	0	-	assumed
ratio of N2 to O2 in GFC	$r_{N2:O2}$	3.2917	-	assumed

[1] - adjusted until a surface saturation of Sgfc is achieved

In addition to the list of model constants presented in Table 5.10, there is another set of constants that depend on the GDL region in the 2-D model. These constants account for the differences in material properties in the nominally uncompressed region under the GFC and the compressed region under the bipolar plate shoulder. The values of the constants that are GDL region dependent are described in Table 5.11.

Table 5.11 – GDL region specific constants for 2-D model input.

		P-20		C-20	
Constant	**Units**	*S1 (u)*	*S2 (c)*	*S1 (u)*	*S2 (c)*
thickness (t_{GDL})	μm	270	190	380	280
porosity (ε)	-	0.649	0.457	0.707	0.521
through-plane conductivity (σ_x)	S/m	59	286	13.6	115
in-plane conductivity (σ_y)	S/m	21800	31000	5350	7300
absolute permeability (K)	10^{-12} m^2	3.71	0.96	37.6	14.9

Another set of model inputs related to the experimentally determined constitutive relations (dP_c/dS *and* $k_{r,LW}$) presented previously in this Chapter are necessary for the 2-D model. Once again, these relations vary with GDL region. The relations presented for dP_c/dS in Table 5.12 were measured at 20°C and were adjusted for thermal dependence according to Eq. (5.4) in the modeling software.

Table 5.12 – Constitutive relations for 2-D model.

		$-dP_c/dS$		$k_{r,LW}$
		Pa		-
P-20	S1 (u)	$10^6 \begin{cases} \begin{bmatrix} -977.71S^5 + 181.79S^4 + 11.854S^3 \\ -2.1947S^2 + 0.06788S \end{bmatrix} \\ \begin{bmatrix} -143.84S^5 + 82.678S^4 + 5.0111S^3 \\ -8.8036S^2 + 1.1622S + 0.00367 \end{bmatrix} \\ \begin{bmatrix} -9.855S^5 + 36.271S^4 - 52.594S^3 \\ +37.591S^2 - 13.257S + 1.851 \end{bmatrix} \end{cases}$	$S < 0.18$ $0.18 \le S < 0.4$ $S \ge 0.4$	$0.031S$
	S2 (c)	$10^6 \begin{cases} \begin{bmatrix} -5560.7S^6 + 4186.2S^5 - 1183.1S^4 \\ +148.95S^3 - 7.699S^2 + 0.2003S \end{bmatrix} \\ \begin{bmatrix} 48.383S^4 - 74.661S^3 + 41.697S^2 \\ -9.952S + 0.8677 \end{bmatrix} \\ \begin{bmatrix} -0.3056S^3 + 0.7087S^2 \\ -0.5465S + 0.1436 \end{bmatrix} \end{cases}$	$S < 0.23$ $0.23 \le S < 0.45$ $S \ge 0.45$	$0.0581S$
C-20	S1 (u)	$10^8 \begin{cases} \begin{bmatrix} 2527S^6 - 804.35S^5 + 81.416S^4 \\ -2.746S^3 + 0.031S^2 + 0.0006S \end{bmatrix} \\ \begin{bmatrix} 0.901S^6 - 2.284S^5 + 2.293S^4 - 1.163S^3 \\ +0.317S^2 - 0.0441S + 0.0025 \end{bmatrix} \end{cases}$	$S < 0.13$ $0.13 \le S < 0.7$	$0.1145S$
	S2 (c)	$10^6 \begin{cases} \begin{bmatrix} -68.402S^4 + 23.062S^3 \\ -1.656S^2 + 0.0427S \end{bmatrix} \\ \begin{bmatrix} 1.979S^4 - 3.957S^3 + 2.978S^2 \\ -0.981S + 0.122 \end{bmatrix} \end{cases}$	$S < 0.23$ $0.23 \le S < 0.7$	$0.03785S$

5.7.2 Sensitivity to unknown parameters

As noted in Table 5.10, five parameters in the 2-D model are estimated without sufficient physical evidence to defend a particular value. Therefore, it is necessary to assess the impact that these unknown constants can have on the models results. The constants of concern, and the low, high, and base case values are presented in Table 5.13.

Table 5.13 - Sensitivity study parameter values.

Parameter	Units	Parameter values		
		low (L)	*base (B)*	*high (H)*
phase change constant (γ)	1/s	90	900	2500
heat partition factor (f_{HP})	-	0.5	0.7	0.9
EOD coefficient (α_{EOD})	mol H_2O/mol H^+	0.25	0.5	0.75
GDL/GFC saturation (S_{gfc})	-	-	0	0.1
N2:O2 ratio in GFC ($r_{N2:O2}$)	kg N_2/kg O_2	-	3.2917	4.08*

*average of inlet and outlet @ 2 A/cm^2 for inlet flow of 550 sccm dry air

To assess the impact of each parameter on the predicted saturation field, the thermal field, and the electrical output, plots of saturation in excess of the GFC/GDL interface saturation, the maximum temperature difference, and the average current density were generated.

Figure 5.42 presents the difference between the maximum GDL saturation and the GDL/GFC interface saturation for the conditions outlined in Table 5.13. It is evident that the base case produces a maximum saturation of approximately 0.018 (GDL/GFC saturation is zero at base case). As speculated from the relative permeability results, water moves quickly through the PTFE treated cloth materials, therefore resulting in a low saturation throughout. Only one of the parameters being considered significantly impacts the maximum saturation difference in the GDL, namely S_{gfc}. When a large value is used for S_{gfc}, the liquid water transport coefficient at the GDL/GFC interface increases substantially and the GDL maintains a constant saturation throughout that is equal to the GFC saturation because of the potential for high liquid velocity at the GDL/GFC interface.

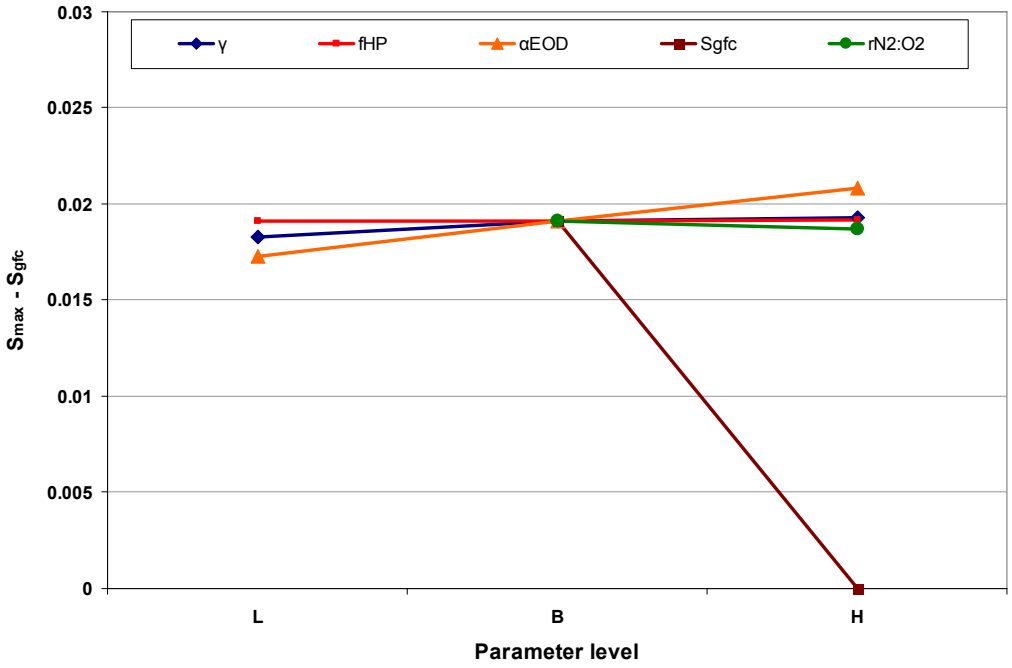

Figure 5.42 – Impact of unknown parameters on GDL saturation for C-20, 95% RH_c model simulation.

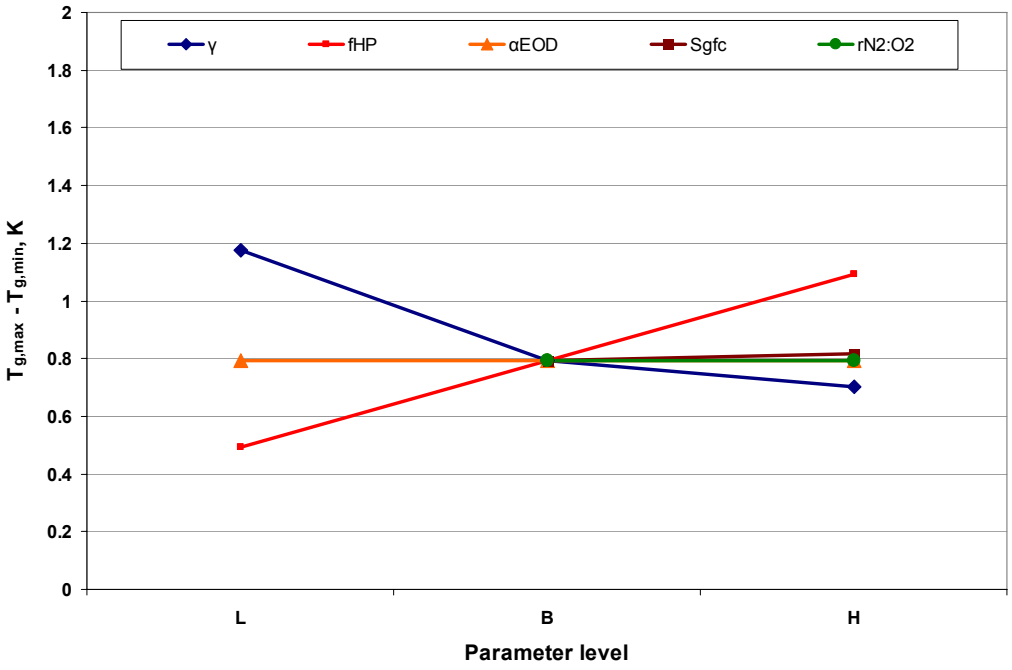

Figure 5.43 – Impact of unknown parameters on the temperature with the GDL for C-20, 95% RH_c model simulation.

The thermal effects of the unknown parameters are described in Figure 5.43. Only two of the parameters of interest have a significant impact on the maximum temperature difference in the GDL. Obviously, the heat partition factor that governs the fraction of electrochemically generated heat that moves toward the cathode rather than the anode plays a significant role in the GDL temperature. Here it is seen that the maximum temperature difference can vary from 0.5 to 1.1°C depending on the value used for f_{HP} (base case suggest a difference of 0.8°C). It is also evident in Figure 5.43 that the phase change rate constant has a moderate impact on the GDL temperature. When the rate of phase change (γ) is reduced the maximum temperature difference in the GDL increases due to a reduction in evaporative cooling. Although the change in the maximum temperature difference can be substantial (~50%) when f_{HP} or γ is varied from the base case, it is unlikely that these changes will have a significant influence on the predicted cell performance.

The most important aspect of the model output is the predicted average current density of the PEMFC. The current density sensitivity study for the C-20 cell is presented in Figure 5.44 where it can be seen that only two of the five parameters have a significant impact on the model output. In this case, the increased saturation at the GFC increases the saturation field throughout the entire GDL and therefore performance is reduced because of the reduction in gas diffusivity. However, the impact is not large enough for concern. The other parameter if importance, $r_{N2:O2}$, also reduces the predicted current density because it effectively reduces the oxygen concentration in the GFC therefore causing a reduction in O_2 flux at the catalyst layer and reducing electrical current generation. The "high" setting for $r_{N2:O2}$ is an extreme case and since the impact on current generation is small (~2.3%) even at the extreme value of $r_{N2:O2}$, the effect of assuming $r_{N2:O2}$ to be the ambient value is acceptable.

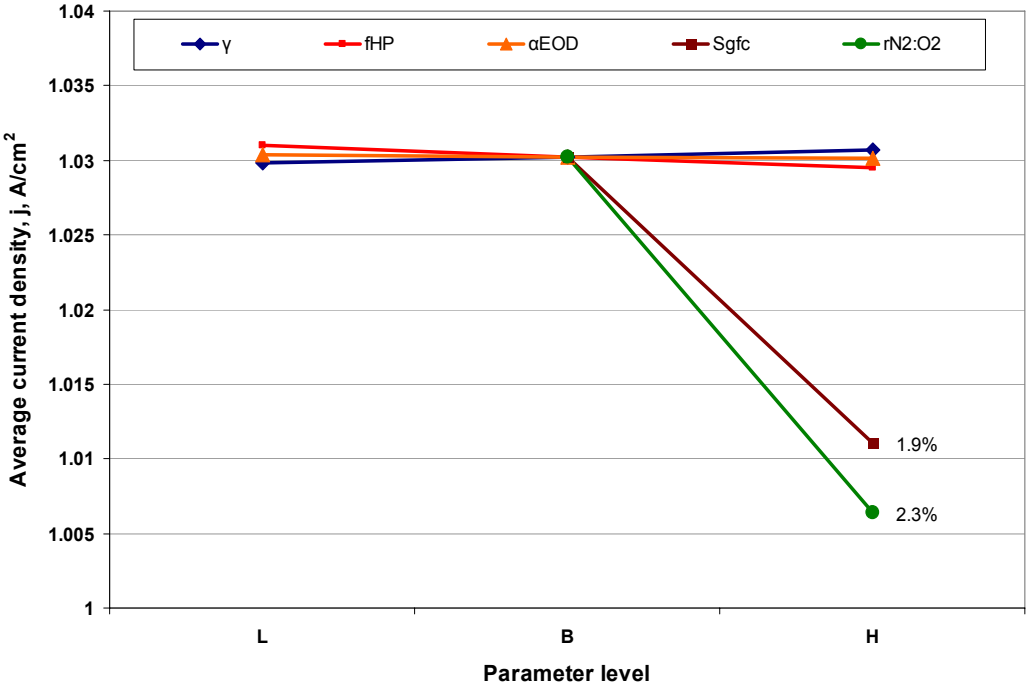

Figure 5.44 – Impact of unknown parameters on average current density for C-20, 95% RH_c model simulation.

A similar sensitivity study was performed for the carbon paper 2-D model. Similar results were observed for the water transport and thermal effects (i.e., parameter sensitivity was negligible). However, when the average current density was compared for all parameter values, the P-20 model exhibited an increased level of sensitivity to the nitrogen-to-oxygen ratio in the GFC. Figure 5.45 suggests that $r_{N2:O2}$ can reduce current production by as much as 8% in the extreme case. Although this is significant, implementation of a more accurate representation of $r_{N2:O2}$ would require an iterative solution process, or a predetermined variation in $r_{N2:O2}$ with average current density. Both of these techniques would add significant complexity to the model and therefore will not be implemented at this time. However, greater consideration will be given to the implementation of a self adjusting $r_{N2:O2}$ later. It should be noted that the sensitivity study performed on the P-20 model was done at the base case condition of RH_c = 95% to be consistent with the C-20 sensitivity study even though polarization data for the P-20 cell was unreliable.

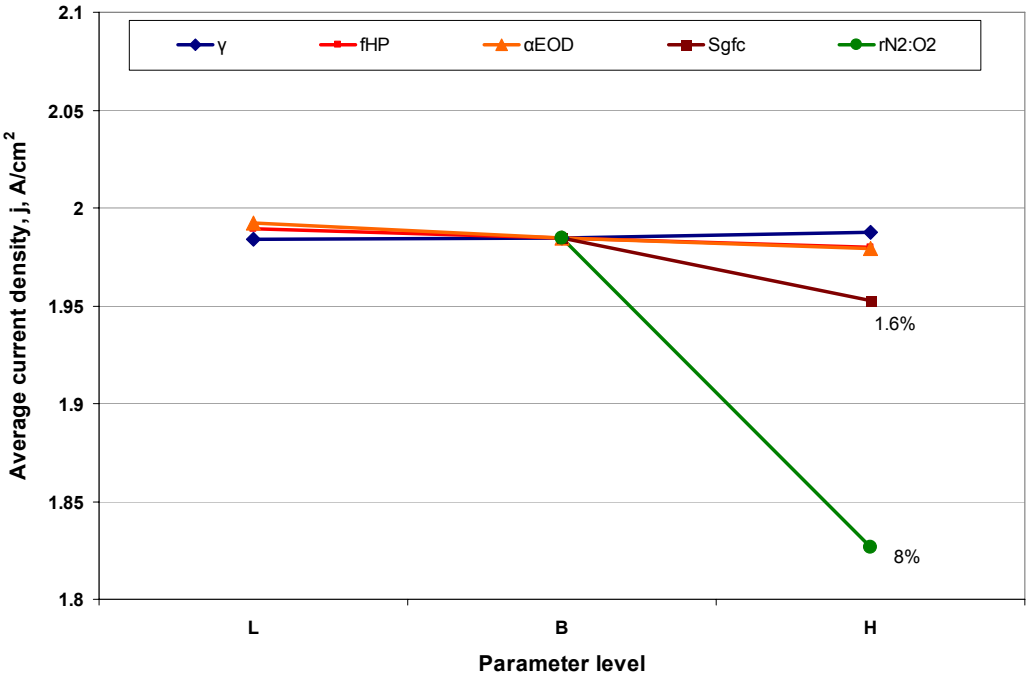

Figure 5.45 – Current density sensitivity to unknown parameters for P-20 cell at 95% RH_c.

5.8 VALIDATION OF THE 2-D PEMFC MODEL

The ultimate goal of the 2-D GDL model is to predict polarization behavior. However, the impact that the GDL has on performance is also of interest. As a means of comparison, a simple algebraic expression that captures the effect of the in-situ determined model inputs is presented. The expression for what will be called the "algebraic model" takes the form:

$$E_{cell} = E_{oc} - \eta_{act} - jASR_{m,i} \tag{5.14}$$

where E_{oc} is the measured open circuit potential, η_{act} is the activation overpotential that was previously defined in Eq.(5.11), and the product $jASR_{m,i}$ account for the ohmic losses associated with the membrane and interfaces. This simple algebraic model provides a good means of comparison for the 2-D finite element model.

5.8.1 Validation using C-20

The 2-D model output, along with the experimental polarization curve and the algebraic model, is presented in Figure 5.46 for the C-20 cell operating at 95% RH_c. Very good agreement is achieved between the 2-D model and the experimental performance, particularly at current densities less than 1.4 A/cm^2. At greater current density, the slight over-prediction (~5%) is likely due to the limitations associated with assuming a constant ratio of nitrogen-to-oxygen in the GFC. As previously discussed, oxygen depletion down the channel would cause an increase in the value of this ratio and decrease the current predicted by the model at a particular potential.

The effect of the GDL is substantial. A clear difference in slope at moderate current between the 2-D FE model and the algebraic model suggests that the GDL resistance is significant. Additionally, at current densities above 1.4 A/cm^2, diffusive limitations are evident in the 2-D model output.

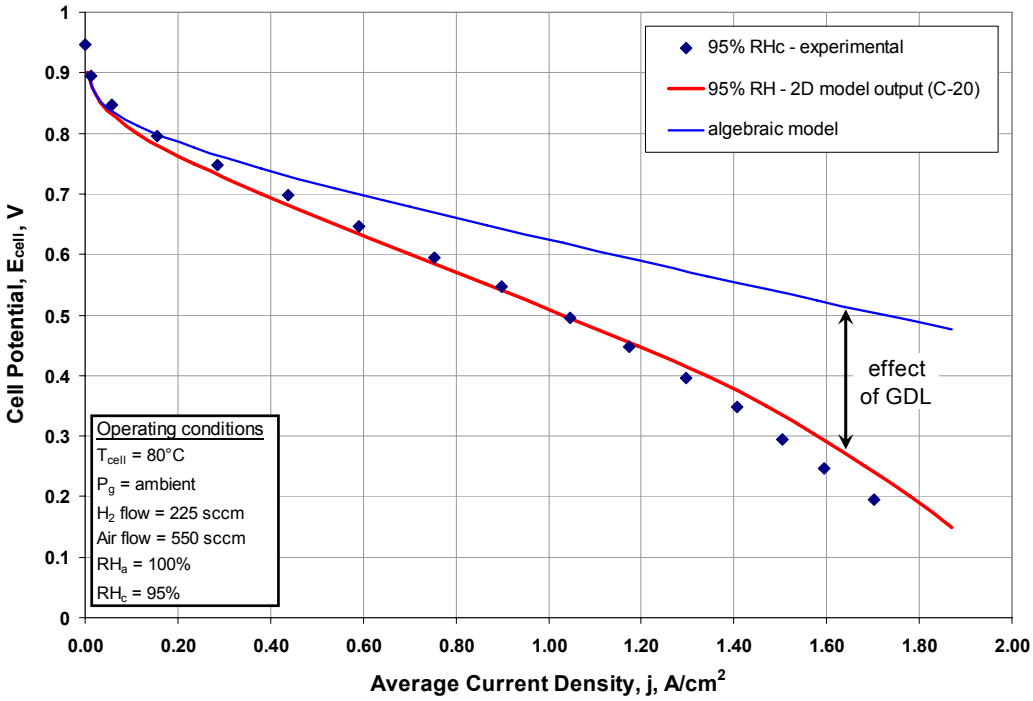

Figure 5.46 – 2-D model validation for the C-20 cell operating at RH_c = 95%.

The modeling results for the C-20 cell operating at 75% RH_c are presented in Figure 5.47. Very similar behavior is predicted by the 2-D model in comparison to the cell operating at 95% RH_c. This result was expected since the experimental C-20 cell exhibited nearly identical performance at both levels of cathode humidity. Once again, slight disagreement at high current density is observed.

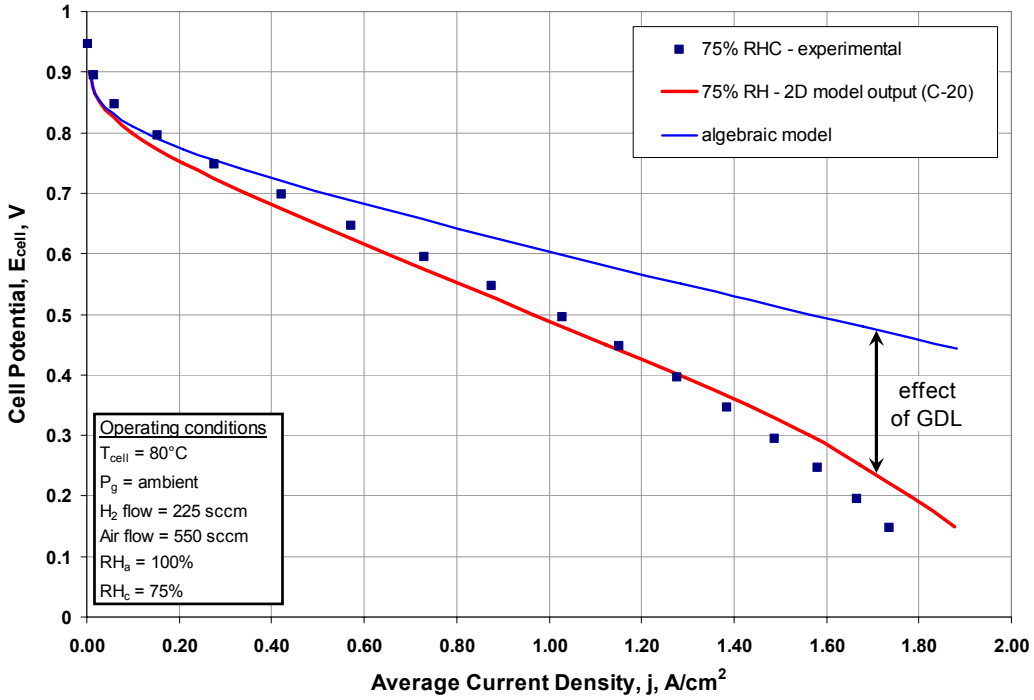

Figure 5.47 - 2-D model validation for the C-20 cell operating at RH_c = 75%.

Considering the intermediate cell potential of 0.5 V, it is interesting to compare the saturation field and the oxygen mole fraction predicted by the 2-D model throughout the GDL. The results for the C-20 simulation at RH_c=95% are presented in Figure 5.48, and the results for RH_c=75% are presented in Figure 5.49.

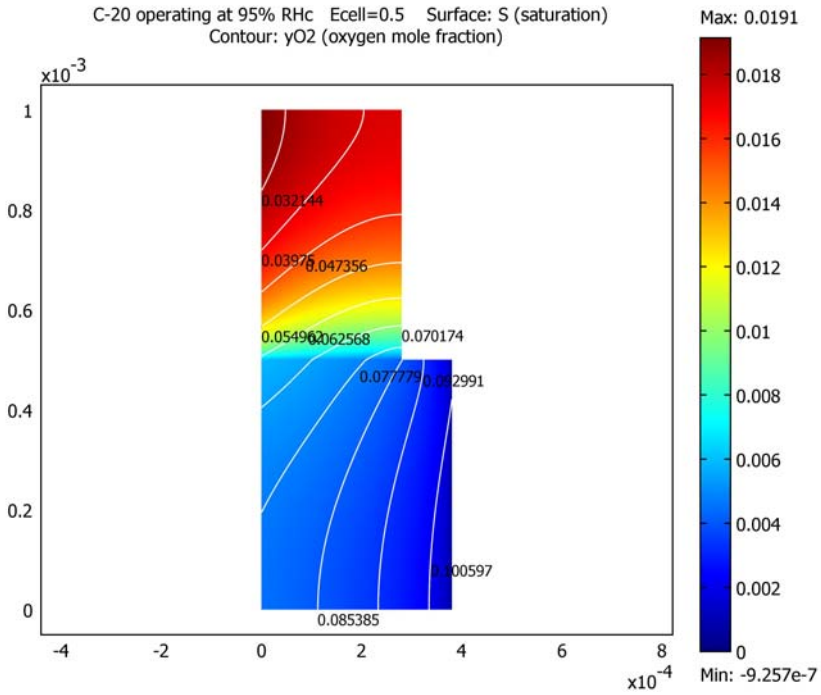

Figure 5.48 – Saturation field and oxygen mole fraction contours predicted for the C-20 cell operating at RH_c = 95% and E_{cell} = 0.5 V.

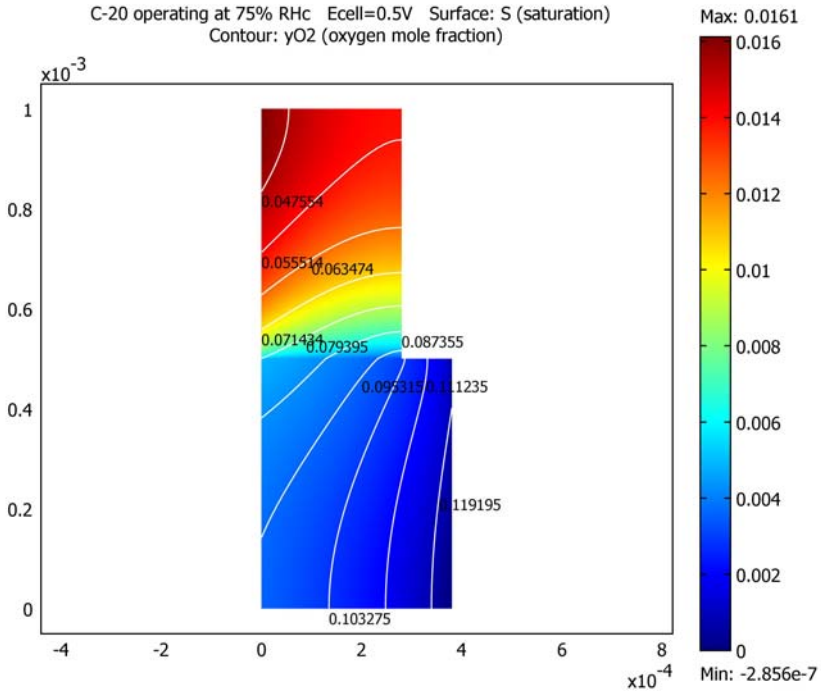

Figure 5.49 - Saturation field and oxygen mole fraction contours predicted for the C-20 cell operating at RH_c = 75% and E_{cell} = 0.5 V.

It is evident in that the saturation under the shoulder is much greater for both humidity levels. This is largely due to the decrease in the slope of the relative permeability function with increased compression measured for the C-20 material. As expected, the saturation is slightly greater in when the cell is operated at greater humidity. Furthermore, the saturation fields suggest that the saturation in the nominally uncompressed region under the GFC is minimal due to the ease with which liquid is transported in the C-20u material.

The oxygen mole fraction contours presented in Figure 5.48 and Figure 5.49 suggest that the mole fraction of oxygen under the shoulder is reduced to approximately 30-40% of the mole fraction near the GFC for both values of GFC relative humidity. Such a reduction in oxygen concentration would be expected to reduce current production under the shoulder. Figure 5.50 presents the current density as a function of position along the catalyst layer at both humidity levels, where current density is plotted on the x-axis to be consistent with the geometry presented in the previous illustrations.

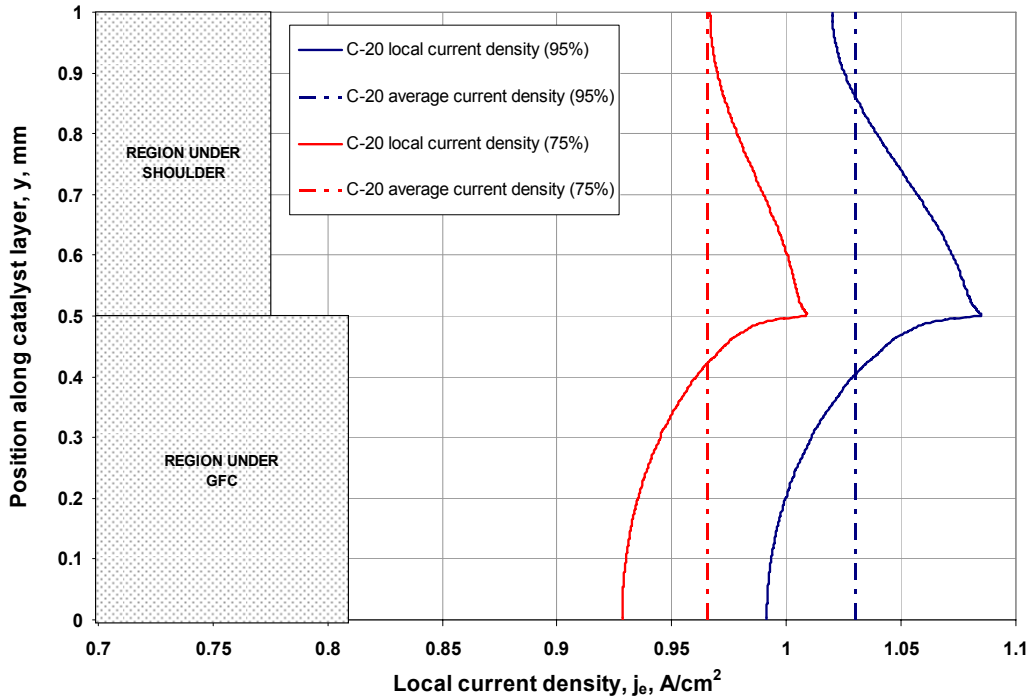

Figure 5.50 – Current density profile along catalyst layer surface for C-20 cell at 0.5 V.

The current density under the shoulder is actually greater than it is under the GFC. This result suggests that the increase in the through-plane conductivity of the GDL under the shoulder actually outweighs the impact of the reduced oxygen concentration in the compressed region. It can be seen in Figure 5.50 that the peak current density occurs at the interface between the two GDL regions. It is at this interface that the combined benefit of high oxygen concentration and high GDL conductivity is maximized. The slightly greater currents predicted for the cell operating at 95% RH_c is likely due to the reduced resistance of the membrane and interfaces. The high humidity condition likely leads to improved membrane hydration, thus reducing its resistance. Finally, the plot of local current density indicates that the current density varies by no more than 10% along the surface of the catalyst layer. This result suggests that the C-20 material exhibits a good balance between liquid transport and gaseous transport.

5.8.2 Validation using P-20

Although good agreement between the model and the experimental data was achieved for the C-20 cell, this was not the case for the P-20 cell. The 2-D model results for the P-20 cell operating at 75% cathode relative humidity are presented in Figure 5.51. As discussed previously, the P-20 cell operating at 95% cathode relative humidity exhibited unsteady behavior and will not be discussed in this section.

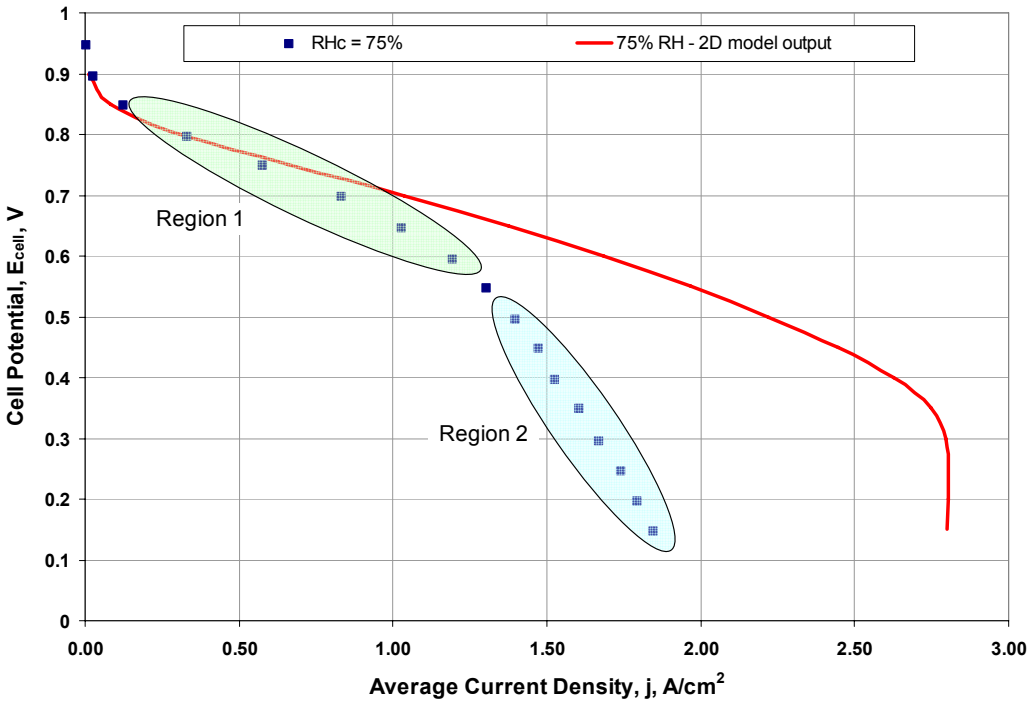

Figure 5.51 – 2-D model results for P-20 cell operating at 75% cathode relative humidity.

For the P-20 cell the predicted current density at a particular cell potential exceeds the experimental results by as much 70%. In Region 1 displayed in Figure 5.51, a clear difference in slope is apparent. This suggests that the method of including the resistance of the interfaces may be insufficient for the P-20 material. One possible reason is that the interfacial resistance under the GFC may be substantially greater than the interfacial resistance under the shoulder. Consequently, the *HFR* measurement used as a model input more closely represents the resistance through a circuit under the shoulder, than it does an average resistance that can be applied uniformly over the entire catalyst layer. This was not a significant issue in the C-20 simulation because the current generated along the catalyst layer surface was nearly uniform. In Region 2, an increase in slope is observed. This is probably due to the impact of a reduced GFC oxygen concentration, which until now has been neglected.

Figure 5.52 displays the predicted saturation field and oxygen mole fraction for the P-20 simulation.

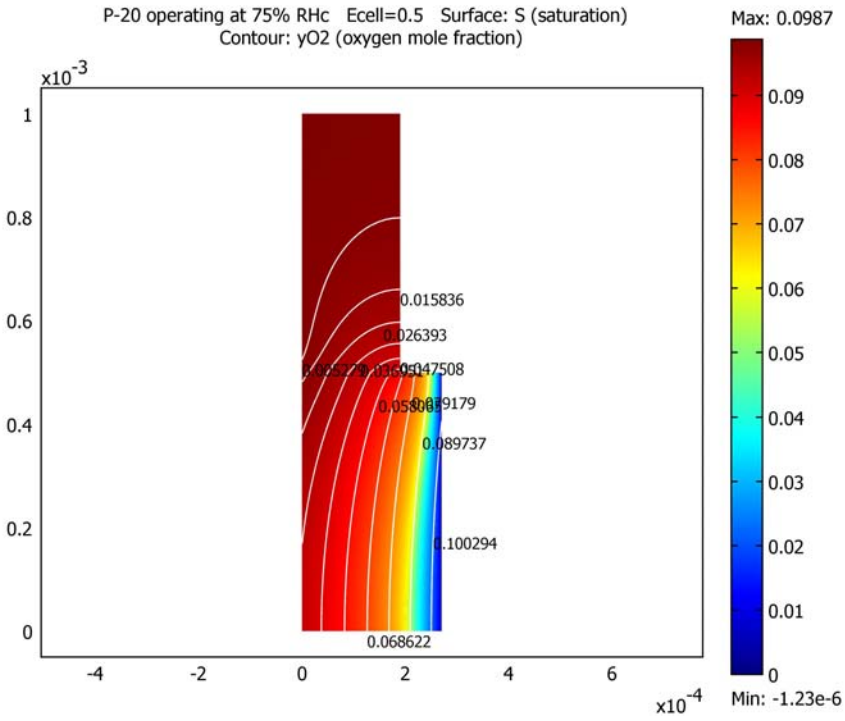

Figure 5.52 – Saturation field and oxygen mole fraction contours for P-20 simulation.

It is evident in Figure 5.52 that the saturation in the paper GDL is much greater than it is in the cloth GDL (Figure 5.49). This is primarily due to the slower liquid transport through the P-20 material when compared to the C-20 material. The significant reduction in oxygen mole fraction in the compressed region is largely due to the substantial reduction in porosity in that region that in turn reduces the effective diffusivity. However, the reduced oxygen concentration under the shoulder it is also likely due to the high rate of oxygen consumption at the catalyst layer under the GFC. To further investigate this possibility a plot of local current density along the surface of the catalyst layer is presented (Figure 5.53).

Similar to the C-20 simulation, the current density profile for P-20 reveals that a peak in current density occurs at a point on the catalyst layer corresponding to the shoulder/GFC edge. At this point the oxygen concentration is still high, and the GDL resistance is low, resulting in an optimal combination for current production. However, the P-20 simulation suggest that the current density at a location centered under the shoulder (y = 1 mm) is nearly zero. The reason for this is threefold: first, the porosity in the compressed region is low and therefore significantly reduces oxygen diffusion;

second, liquid water transport is slow under the shoulder, and causes a reduction in oxygen diffusivity (due to saturation), and encourages evaporation that in turn reduces the oxygen concentration due to an abundance of water vapor; third, the region of catalyst layer under the GFC produces so much current that the concentration gradient available to drive oxygen diffusion under the shoulder is minimized.

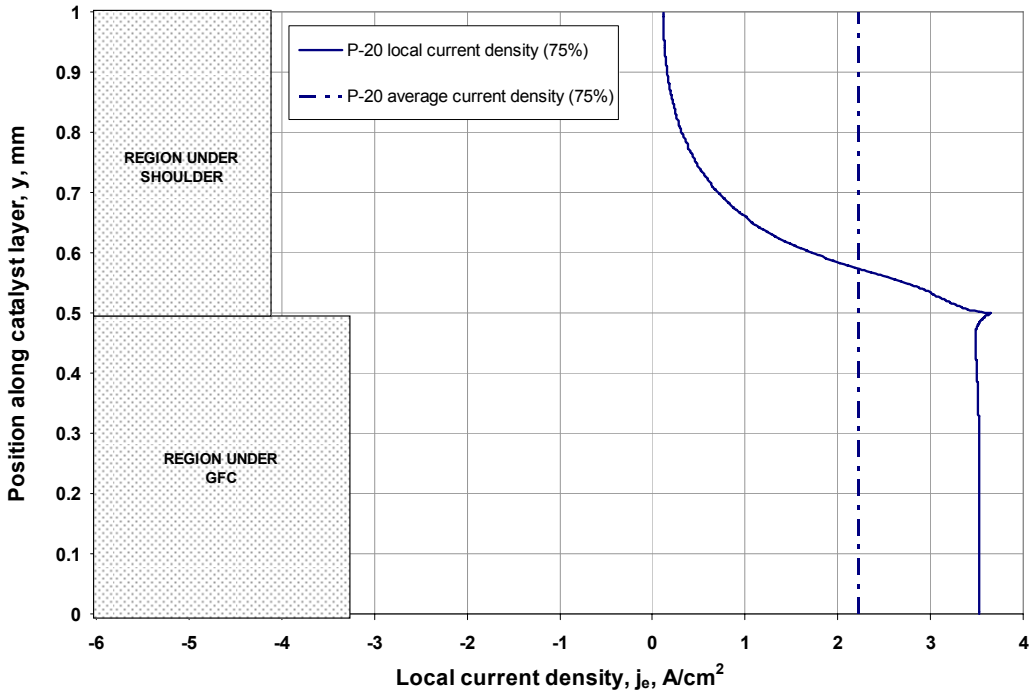

Figure 5.53 – Current density profile along catalyst surface for P-20 simulation at 0.5 V.

As was evident in Figure 5.51, the predicted polarization performance for the P-20 cell did not agree well with the experimental results. Two hypotheses were suggested (higher interfacial resistance under the GFC, and significant oxygen depletion) to potentially explain the disagreement between the P-20 model results and experimental results. These hypotheses will be investigated further in the next section.

5.8.3 Further investigation of P-20 modeling results

The significant variation in current density along the catalyst layer suggested by the model (Figure 5.52) further substantiates the impact that a difference in interfacial resistance under the GFC versus under the shoulder could have on performance. Measuring the contact resistance between the GDL and catalyst layer is quite difficult and has been attempted many times recently [57-59]. In 2007, Nitta et al. [59] used a combined experimental and analytical approach to estimate the contact resistance between the CL and GDL at different levels of GDL compression. The GDL of interest in the work of Nitta was an SGL carbon fiber paper similar to the Toray carbon fiber paper used in this work. It was found by Nitta [59] that the contact resistance between the CL and GDL when the GDL is nominally uncompressed ($t = 0.92t_o$) is between 2.9-40 times greater than it is in a compressed state ($0.80t_o < t < 0.40t_o$). However, this range is reduced when more reasonable levels of GDL compression are considered. For example, the ratio of the nominally uncompressed contact resistance to the compressed contact resistance when $t = 0.65t_o$ is equal to 5.6. More recently in 2008, Nitta et al. [58] applied an AC-impedance approach to the determination of contact resistance between the CL and GDL. The contact resistance found for an SGL carbon fiber paper (t_o = 380 μm) at a compressed thickness of 300 μm was found to be approximately 0.044 Ω-cm^2. In a more substantially compressed state (t = 230 μm) the contact resistance between the CL and GDL was found to be approximately 0.012 Ω-cm^2. The ratio of contact resistance in these two cases is 3.7.

To investigate the hypothesis that the disagreement between experimental and modeling results is attributable to the interfacial resistance under the GFC being greater than the interfacial resistance under the shoulder, a new parameter is defined. The contact resistance factor, f_{cr}, defines the increase in interfacial resistance under the GFC compared to the shoulder. It is assumed that the area specific resistance of the membrane and interfaces ($ASR_{m,i}$) appropriately characterizes the resistance seen by the current produced under the shoulder. To implement f_{cr}, the following is defined:

$$ASR_{m,i}^{GFC} = R_{mem}'' + f_{cr}\left(ASR_{m,i}^{shoulder} - R_{mem}''\right) \tag{5.15}$$

where $ASR_{m,i}^{shoulder}$ is the value used for $ASR_{m,i}$ in the model of the previous section, and will be applied in the membrane region under the shoulder; $R_{mem}^{"}$ is an approximate value for the area specific resistance of the membrane; and $ASR_{m,i}^{GFC}$ will be applied in the membrane region under the GFC. To estimate the area specific resistance of the membrane, a fully saturated state is assumed for Nafion. Utilizing an analytical expression presented by O'Hayre [56] for calculating the conductivity of Nafion® yields a value of $R_{mem}^{"} \cong 0.0245\ \Omega\text{-cm}^2$ (for a water content (λ) of 22 mol H_2O/mol SO^-_3).

To address the impact of reduced oxygen species in the GFC, the average of the inlet and outlet nitrogen-to-oxygen ratios will be calculated at each cell potential. To perform this calculation without developing an iterative solution process, the current density must be known at each potential prior to model implementation. In this case, the current density is known at each potential because experimental data was collected. Turning the polarization curve for the P-20 cell sideways and fitting a polynomial to the data yields an expression for the average current density as a function of cell potential (Figure 5.54).

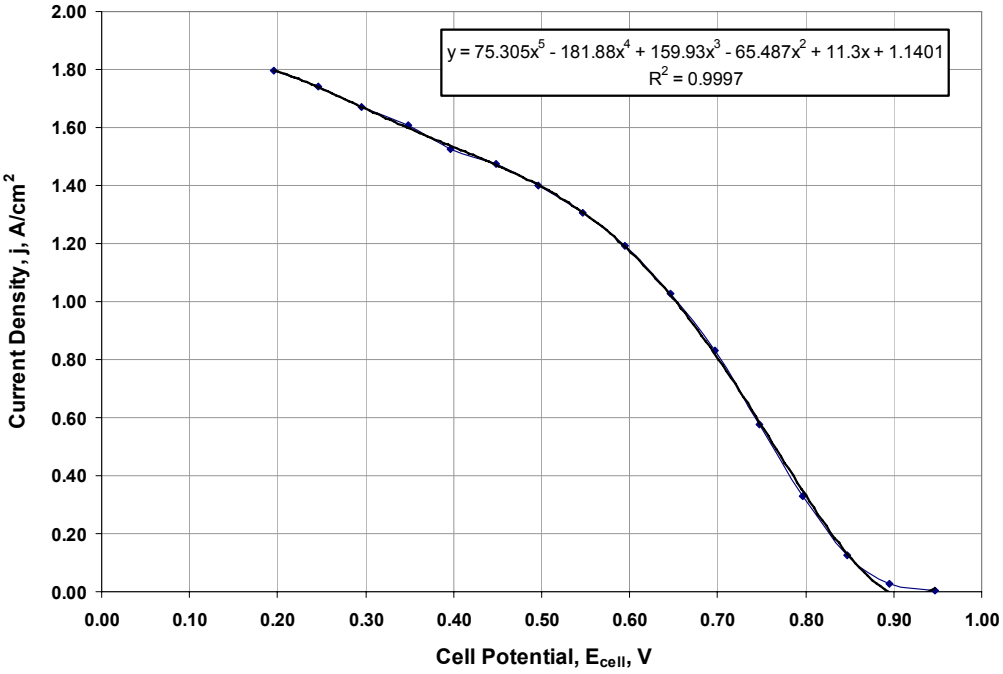

Figure 5.54 – Average current density as a function of cell potential for P-20 cell.

The calculation of the average value of $r_{N2:O2}$ is fairly straightforward and is described sequentially in Eq. (5.16) - (5.19):

$$r_{N2:O2}^{inlet} = \frac{\dot{m}_{N_2}^{inlet}}{\dot{m}_{O_2}^{inlet}} \tag{5.16}$$

$$\dot{m}_{O_2}^{rxn}(kg/s) = M_{O_2}\frac{I}{4F} \tag{5.17}$$

$$r_{N2:O2}^{outlet} = \frac{\dot{m}_{N_2}^{inlet}}{\dot{m}_{O_2}^{inlet} - \dot{m}_{O_2}^{rxn}} \tag{5.18}$$

$$r_{N2:O2}^{avg} = \frac{r_{N2:O2}^{inlet} + r_{N2:O2}^{outlet}}{2} \tag{5.19}$$

where the inlet ratio of nitrogen-to-oxygen ($r_{N2:O2}^{inlet}$) is simply the quotient of the inlet mass flow of nitrogen ($\dot{m}_{N_2}^{inlet}$) and the inlet mass flow of oxygen ($\dot{m}_{O_2}^{inlet}$); the rate of oxygen consumption due to the electrochemical reaction ($\dot{m}_{O_2}^{rxn}$) is proportional to the total current; and the outlet species ratio ($r_{N2:O2}^{outlet}$) is simply the inlet nitrogen flow (no nitrogen is depleted so the inlet flow is equal to the outlet flow), divided by the outlet oxygen flow (inlet – consumption).

The two hypotheses were implemented into the 2-D model in a stepwise fashion. First the increased interfacial resistance was implemented where a value of f_{cr} = 6.4 provides a much better match to the experimental data. However, the deviation from the experimental results was significant at high current densities. Next, the variation in $r_{N2:O2}$ with current density was implemented. The GFC oxygen concentration dependence on current density substantially improved the agreement between the model and experimental data. The results of these model implementations can be seen in Figure 5.55.

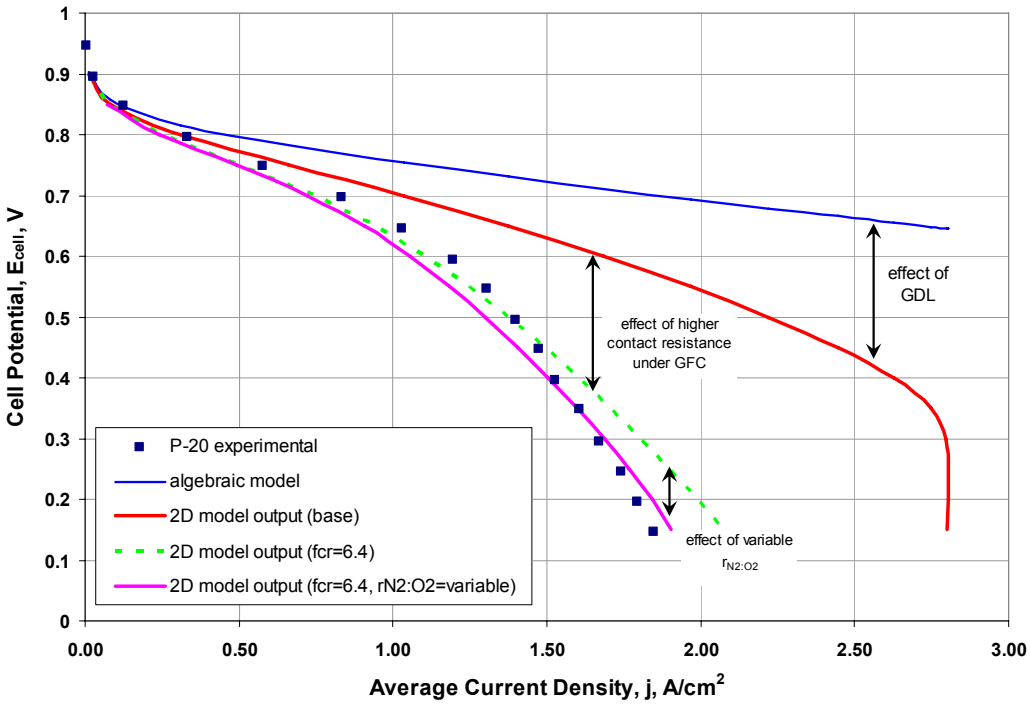

Figure 5.55 – 2-D model output incorporating increased contact resistance under the GFC and reduced oxygen concentration proportional to current.

5.8.4 Summary of 2-D modeling results

The 2-D model results for the C-20 cell exhibited very good agreement with experimental data. The greatest deviation occurred at high current density, and it was shown in the preceding section that the high current density region can be brought into closer agreement by making $r_{N2:O2}$ dependent on current.

The P-20 modeling results did not agree well with the experimental data in the base case. However, agreement was achieved when the interfacial resistance under the GFC was increased, and the oxygen depletion in the GFC was accounted for. The multiplier used to describe the increase in resistance under the GFC cannot be validated at this time. However, this will be a topic of future work. The next and final chapter, Chapter 6, will provide some conclusions regarding the results presented in this work, and will also provide some recommendations for future work.

6 CONCLUSIONS AND RECOMMENDATIONS

This work has presented a wide array of experimental and analytical efforts pertaining to the transport of liquid water in the macroporous GDL region of PEMFCs. This chapter will first detail the key conclusions that can be extracted from this work. Additionally, this chapter will make recommendations concerning the future experimental and analytical work necessary to gain further understanding of liquid water transport in GDL materials. Finally, some closing remarks pertaining to the past, present, and future status of the understanding of liquid water transport in PEMFC materials will be made to conclude this work.

6.1 CONCLUSIONS

This work has produced experimental and analytical tools to aid in the understanding of liquid water transport in GDL materials. Experimental fixtures to characterize essential constitutive relations for water transport modeling were developed, and demonstrated. Furthermore, analytical tools have been developed to assess the impact of water transport relations on gaseous transport and liquid transport through a 1-D representation of a cathode GDL. Finally, a 2-D GDL model that can predict polarization performance and quantify the impact of GDL compression under the bipolar plate shoulder was also developed.

The results of the *gas displacement porosimetry* (GDP) experiments have identified critical water transport relations that quantify the effect of media type, hydrophobic polymer content, and GDL compression. For carbon papers it was shown that PTFE content only affects capillary behavior at high saturation, probably because the PTFE emulsion primarily coats regions with small pores (regions with resin residual). Although the capillary pressure curve was mildly affected, the slope of the curve was not, therefore allowing for the development of a single dP_c/dS function for all mildly compressed Toray TGPH-090 carbon papers regardless of PTFE content. For carbon cloth, PTFE content played a more substantial role at high saturations; however, a single

dP_c/dS function for mildly compressed B1/A carbon cloth with 10-20% PTFE content was established. The impact of compression was similar for both carbon paper and carbon cloth. Compression has a homogenizing effect on the porous regions within both types of media (i.e., larger pores were crushed and/or redistributed). The homogenization of the pore structure caused a flattening of the dP_c/dS function, ultimately approaching the behavior of unconsolidated sand proposed by Leverett.

The results of the *Virginia Tech relative permeability (VT-k_r)* experiments successfully demonstrated that a hydrophobic treatment enhances water transport in the GDL of PEMFCs. For the cloth materials, a 570% increase in the slope of the relative permeability function was measured for the C-20u material in comparison to the C-0u material. For the paper materials a 280% increase in slope was realized for the P-20u material in comparison to the P-0u material. The significance of this is apparent when a constant dP_c/dS, saturation, and saturation gradient are considered: in such a situation, the liquid water velocity increases nearly seven-fold for the cloth material, and four-fold for the paper material, when a 20% PTFE treatment is applied. Compression has the opposite effect of PTFE, where compression causes a reduction in liquid water velocity if all other variables are held constant. However, the primary source of the reduced water permeability with compression is manifested in the reduction in absolute permeability, and not in the relative permeability.

The *one-dimensional comparative model* qualitatively assessed the impact of three different sets of liquid water transport relations that combine to form the liquid water transport coefficient (c_{LWT}). The significant impact that absolute permeability (K), liquid water relative permeability ($k_{r,LW}$), and capillary pressure slope (dP_c/dS) can have on GDL saturation, gas diffusivity, and the liquid water transport coefficient (c_{LWT}) was evident for all current densities and relative humidity's considered. Perhaps the most significant result was the disparity in the magnitude of the predicted saturation when comparing the model grounded in experimentally determined transport relations (this work), and the model where the capillary behavior and permeability were used to adjust polarization data (Lin et al. [15]).

The *2-D cathode GDL model* is one of the few, if not the only, PEMFC model that does not utilize adjustment parameters or functions. It is common practice in the

PEMFC literature to adjust values of parameters (e.g., absolute permeability, or porosity) or to adjust the functional form of constitutive relations (e.g., capillary function slope, or relative permeability) to achieve the desired polarization behavior. The 2-D model presented here goes to great lengths to utilize experimentally determined material properties. The results from the sensitivity study demonstrate that all assumed parameters are relatively inconsequential to the model predictions of current generation. However, more information is needed to resolve the variation in temperature observed with changes in the phase change rate constant and the heat partition factor. Furthermore, the predicted saturation profiles within the GDL domain for the two different media types demonstrate the importance of using experimentally determined water transport relations. The simulation representing a cloth GDL predicts a nearly dry GDL for almost all of the operating conditions investigated, whereas the paper GDL exhibits saturations in excess of 10% for typical PEMFC operating conditions. Finally, it was also demonstrated that the 2-D model could accurately predict polarization behavior for the cloth-based GDL without the use of any adjustment parameters. However, an interfacial resistance adjustment factor was necessary to achieve good agreement for the paper-based GDL.

6.2 RECOMMENDATIONS FOR FUTURE WORK

This work addressed liquid water transport in the GDL from an experimental and analytical perspective. Based on the experience gained during the course of this work recommendations for future work can be made. The proposed future work includes potential improvements to the developed experimental fixtures, future experimentation to further contribute to the understanding of liquid water transport in PEMFCs, and future enhancements to the 2-D analytical model.

The following is a list of recommendations for future work regarding potential improvements to the experimental fixtures presented herein:

- *Enhance the resolution of the GDP experiment at saturations less than 10%.* Based on computational results, this is the critical region of the dP_c/dS function.

Higher resolution pressure measurements at low saturation may reveal water transport characteristics that were not captured in this work.

- *Improve the accuracy of the gravimetric determination of saturation for the* VT-k_r *experiment.* The primary challenge with this experiment was properly swabbing the sample border to remove stray droplets. An improved design for sample preparation that excludes the filled border or an alternative method of saturation determination could improve the reliability of the experimental method.

The potential for future experimentation with the experimental apparatus' developed during this work is substantial. However, the possible experiments that are considered to be most critical to an improved understanding of water transport in PEMFCs are listed below:

- *Determine the* dP_c/dS *functions and* $k_{r,LW}$ *functions for an array of microporous layer (MPL) compositions*. It is common practice for the macroporous cloth or paper GDL structure to be coated with a MPL. It has been speculated that the MPL improves water management but the physical reason for such improvement has never been determined. The source of MPL performance enhancement would likely be revealed through GDP and VT-$k_{r,LW}$ experimentation.
- *Expand upon the investigation of compression effects for GDL materials.* Although the data presented in this work provides valuable insight into the impact of compression on water transport relations, it does not cover a very wide range of compression levels. An expanded investigation may reveal the optimal level of GDL compression with respect to water management within a PEMFC stack.
- *Develop a library of water transport relations for a wide array of GDL materials.* If such a library existed it would enable PEMFC stack designers to select a GDL material that is most suitable for the desired power range and operating conditions of a given system, thereby reducing the demand for balance-of-plant peripherals.

The 2-D model presented in this work is a step in the right direction with regard to the elimination of adjustment parameters; however, the versatility of the model can be improved in the future. Some potential improvements are as follows:

- *Introduce an anode to the model geometry.* Without an anode the model cannot predict water profiles throughout the entire cell, nor can it properly account for the membrane resistance that varies with water content. The introduction of an anode could eliminate the need for the input of an in-situ high frequency resistance measurement.
- *Introduce membrane water transport to the model.* Membrane hydration is critical to cell performance and therefore water transport within the membrane is essential to developing a comprehensive understanding of water transport in PEMFCs.
- *Utilize the $r_{N2:O2}$ parameter to implement a down-the-channel solution procedure.* By treating the 2-D geometry as a small yet finite region of the actual fuel cell and building a "for loop" around the current solution structure, the $r_{N2:O2}$ parameter could be properly adjusted in each region as the solution progresses along the gas flow channel to capture effects of down-the-channel oxygen depletion.

6.3 CLOSING REMARKS

The transport of liquid water has always been recognized as a vital aspect of PEMFC design and performance, which is why such transport is the primary focus of this work. The understanding of water transport has been relatively limited and it has been common in the literature to adjust assumed water transport parameters to match experimental data. The reason for adjusting water transport parameters is twofold: First, until now many of the constitutive relations used to model water transport have never been experimentally measured; and second, liquid water can have such a significant impact on performance that adjusting constitutive relations associated with liquid water transport can drastically impact numerical results.

Ideally, this work has defined approaches leading to the experimental determination of water transport constitutive relations. Although the materials investigated in this work are not exhaustive, the water transport relations developed in this work represent a new direction for fuel cell modeling that leads to a fundamental physical representation of liquid water transport in PEMFCs.

REFERENCES

[1] Lee, W. K., Ho, C. H., Van Zee, J. W., and Murthy, M., 1999, "The Effects of Compression and Gas Diffusion Layers on the Performance of a PEM Fuel Cell," Journal of Power Sources, 84(1), pp. 45-51.

[2] Litster, S., and Mclean, G., 2004, "PEM Fuel Cell Electrodes," Journal of Power Sources, 130(1-2), pp. 61-76.

[3] Wilson, M. S., and Gottesfeld, S., 1992, "Thin-Film Catalyst Layers for Polymer Electrolyte Fuel-Cell Electrodes," Journal of Applied Electrochemistry, 22(1), pp. 1-7.

[4] Larminie, J., and Dicks, A., 2003, *Fuel Cell Systems Explained, 2nd Edition*, John Wiley & Sons.

[5] Springer, T. E., Zawodzinski, T. A., and Gottesfeld, S., 1991, "Polymer Electrolyte Fuel-Cell Model," Journal of the Electrochemical Society, 138(8), pp. 2334-2342.

[6] Zhang, J., Li, J., and Han, Y., 2004, "Superhydrophobic Ptfe Surfaces by Extension," Macromolecular Rapid Communications, 25(11), pp. 1105-1108.

[7] Weber, A. Z., and Newman, J., 2003, "Transport in Polymer-Electrolyte Membranes - I. Physical Model," Journal of the Electrochemical Society, 150(7), pp. A1008-A1015.

[8] Weber, A. Z., and Newman, J., 2004, "Transport in Polymer-Electrolyte Membranes - II. Mathematical Model," Journal of the Electrochemical Society, 151(2), pp. A311-A325.

[9] Weber, A. Z., and Newman, J., 2004, "Transport in Polymer-Electrolyte Membranes - III. Model Validation in a Simple Fuel-Cell Model," Journal of the Electrochemical Society, 151(2), pp. A326-A339.

[10] Nam, J. H., and Kaviany, M., 2003, "Effective Diffusivity and Water-Saturation Distribution in Single- and Two-Layer PEMFC Diffusion Medium," International Journal of Heat and Mass Transfer, 46(24), pp. 4595-4611.

[11] Pasaogullari, U., and Wang, C. Y., 2004, "Two-Phase Transport and the Role of Micro-Porous Layer in Polymer Electrolyte Fuel Cells," Electrochimica Acta, 49(25), pp. 4359-4369.

[12] Pasaogullari, U., and Wang, C. Y., 2004, "Liquid Water Transport in Gas Diffusion Layer of Polymer Electrolyte Fuel Cells," Journal of the Electrochemical Society, 151(3), pp. A399-A406.

[13] Senn, S. M., and Poulikakos, D., 2005, "Multiphase Transport Phenomena in the Diffusion Zone of a PEM Fuel Cell," Journal of Heat Transfer-Transactions of the ASME, 127(11), pp. 1245-1259.

[14] Berning, T., and Djilali, N., 2003, "A 3d, Multiphase, Multicomponent Model of the Cathode and Anode of a PEM Fuel Cell," Journal of the Electrochemical Society, 150(12), pp. A1589-A1598.

[15] Lin, G. Y., and Van Nguyen, T., 2006, "A Two-Dimensional Two-Phase Model of a PEM Fuel Cell," Journal of the Electrochemical Society, 153(2), pp. A372-A382.

[16] Natarajan, D., and Van Nguyen, T., 2001, "A Two-Dimensional, Two-Phase, Multicomponent, Transient Model for the Cathode of a Proton Exchange Membrane Fuel Cell Using Conventional Gas Distributors," Journal of the Electrochemical Society, 148(12), pp. A1324-A1335.

[17] Siegel, N. P., Ellis, M. W., Nelson, D. J., and Von Spakovsky, M. R., 2004, "A Two-Dimensional Computational Model of a PEMFC with Liquid Water Transport," Journal of Power Sources, 128(2), pp. 173-184.

[18] You, L. X., and Liu, H. T., 2002, "A Two-Phase Flow and Transport Model for the Cathode of PEM Fuel Cells," International Journal of Heat and Mass Transfer, 45(11), pp. 2277-2287.

[19] Dullien, F. A. L., 1979, *Porous Media, Fluid Transport and Pore Structure*, Academic Press Inc., London.

[20] Leverett, M. C., 1941, "Capillary Behavior in Porous Solids," Transaction of the AIME, 142, pp. 151-169.

[21] Kaviany, M., 1995, *Principles of Heat Transfer in Porous Media*, *Mechanical Engineering Series*, Springer-Verlag New York, Inc., New York.

[22] Bird, R. B., Stewart, W. E., and Lightfoot, E. N., 2002, *Transport Phenomena, 2nd Ed.*, John Wiley and Sons, Inc., New York.

[23] Cussler, E. L., 1997, *Diffusion, Mass Transfer in Fluid Systems, 2nd Ed.*, Cambridge University Press, Cambridge, UK.

[24] Welty, J. R., Wicks, C. E., Wilson, R. E., and Rorrer, G. L., 2001, *Fundamentals of Momentum, Heat, and Mass Transfer,4th Ed.*, John Wiley and Sons, Inc., New York, NY.

[25] Faghri, A., and Zhang, Y., 2006, *Transport Phenomena in Multiphase Systems*, Elsevier, Academic Press,

[26] Cunningham, R. E., and Williams, R. J. J., 1980, *Diffusion in Gases and Porous Media*, Plenum Press, New York, NY.

[27] Pasaogullari, U., Wang, C. Y., and Chen, K. S., 2005, "Two-Phase Transport in Polymer Electrolyte Fuel Cells with Bilayer Cathode Gas Diffusion Media," Journal of the Electrochemical Society, 152(8), pp. A1574-A1582.

[28] Wang, Z. H., Wang, C. Y., and Chen, K. S., 2001, "Two-Phase Flow and Transport in the Air Cathode of Proton Exchange Membrane Fuel Cells," Journal of Power Sources, 94(1), pp. 40-50.

[29] Wang, C. Y., and Cheng, P., 1996, "A Multiphase Mixture Model for Multiphase, Multicomponent Transport in Capillary Porous Media .1. Model Development," International Journal of Heat and Mass Transfer, 39(17), pp. 3607-3618.

[30] Cheng, P., and Wang, C. Y., 1996, "A Multiphase Mixture Model for Multiphase, Multicomponent Transport in Capillary Porous Media .2. Numerical Simulation of the Transport of Organic Compounds in the Subsurface," International Journal of Heat and Mass Transfer, 39(17), pp. 3619-3632.

[31] Dutta, S., Shimpalee, S., and Van Zee, J. W., 2001, "Numerical Prediction of Mass-Exchange between Cathode and Anode Channels in a PEM Fuel Cell," International Journal of Heat and Mass Transfer, 44(11), pp. 2029-2042.

[32] Rose, W., and Bruce, W. A., 1949, "Evaluation of Capillary Character in Petroleum Reservoir Rock," AIME Petroleum Transactions, 186 pp. 127-142.

[33] Brown, H. W., 1951, "Capillary Pressure Investigation," AIME Petroleum Transactions, 192 pp. 67-74.

[34] Udell, K. S., 1985, "Heat-Transfer in Porous-Media Considering Phase-Change and Capillarity - the Heat Pipe Effect," International Journal of Heat and Mass Transfer, 28(2), pp. 485-495.

[35] Mathias, M., Roth, J., Fleming, J., and Lehnert, W., 2003, Handbook of Fuel Cells: Volume 3 - Fuel Cell Technology and Applications, John Wiley & Sons, Ltd, New York, Chapter 46 - Diffusion Media Materials and Characterisation.

[36] Gostick, J. T., Fowler, M. W., Ioannidis, M. A., Pritzker, M. D., Volfkovich, Y. M., and Sakars, A., 2006, "Capillary Pressure and Hydrophilic Porosity in Gas Diffusion Layers for Polymer Electrolyte Fuel Cells," Journal of Power Sources, 156(2), pp. 375-387.

[37] Jena, A., and Gupta, K., 2005, "Characterization of Pore Structure of Fuel Cell Components Containing Hydophobic and Hydrophilic Pores," 41st Power Sources Conference.

[38] Lee, W.-K., Zee, J. W. V., Jena, A., and Gupta, K., 2004, "Characterization of Permeability Changes and Hydrophobic Nature of GDL, and Correlation with PEMFC Performance," Fuel Cell Seminar.

[39] Ohn, H., Nguyen, T. V., Jacobson, D., Hussey, D., and Arid, M., 2006, "Capillary Pressure Properties of Gas Diffusion Materials Used in PEM Fuel Cells," ECS Transactions, 1(6), pp. 481-489.

[40] Nguyen, T. V., Guangyu, L., Heebong, O., Dan, H., David, J., and Muhammad, A., 2006, "Measurements of Two-Phase Flow Properties of the Porous Media Used in PEM Fuel Cells," ECS Transactions, 3(1), pp. 415-423.

[41] Ye, Q., and Van Nguyen, T., 2007, "Three-Dimensional Simulation of Liquid Water Distribution in a PEMFC with Experimentally Measured Capillary Functions," Journal of the Electrochemical Society, 154(12), pp. B1242-B1251.

[42] Fairweather, J., Cheung, P., Schwartz, D. T., and St-Pierre, J., 2006, "Microfluidic Tools for Assessing the Multiphase Properties of Water in PEMFC Gas Diffusion Electrodes," ECS Transactions, 3(1), pp. 981-987.

[43] Fairweather, J. D., Cheung, P., St-Pierre, J., and Schwartz, D. T., 2007, "A Microfluidic Approach for Measuring Capillary Pressure in PEMFC Gas Diffusion Layers," Electrochemistry Communications, 9(9), pp. 2340-2345.

[44] Volfkovich, Y. M., Bagotzky, V. S., Sosenkin, V. E., and Blinov, I. A., 2001, "The Standard Contact Porosimetry," Colloids and Surfaces a-Physicochemical and Engineering Aspects, 187, pp. 349-365.

[45] Kumbur, E. C., Sharp, K. V., and Mench, M. M., 2007, "Validated Leverett Approach for Multiphase Flow in Pefc Diffusion Media, I. Hydrophobicity Effect," Journal of the Electrochemical Society, 154(12), pp. B1295-B1304.

[46] Kumbur, E. C., Sharp, K. V., and Mench, M. M., 2007, "Validated Leverett Approach for Multiphase Flow in Pefc Diffusion Media, II. Compression Effect," Journal of the Electrochemical Society, 154(12), pp. B1305-B1314.

[47] Kumbur, E. C., Sharp, K. V., and Mench, M. M., 2007, "Validated Leverett Approach for Multiphase Flow in Pefc Diffusion Media - III. Temperature Effect and Unified Approach," Journal of the Electrochemical Society, 154(12), pp. B1315-B1324.

[48] Sole, J. D., 2005, "Investigation of Novel Gas Diffusion Media for Application in PEM Fuel Cell Ribbon Assemblies," M.S. Thesis, Virginia Polytechnic Institute and State University, Blacksburg, VA.

[49] Welge, H. J., 1952, "A Simplified Method for Computing Oil Recovery by Gas or Water Drive," AIME Petroleum Transactions, 195, pp. 91-98.

[50] Scheidegger, A. E., 1974, *The Physics of Flow through Porous Media, 3rd Ed.*, University of Toronto Press, Toronto.

[51] Park, G. G., Sohn, Y. J., Yang, T. H., Yoon, Y. G., Lee, W. Y., and Kim, C. S., 2004, "Effect of Ptfe Contents in the Gas Diffusion Media on the Performance of PEMFC," Journal of Power Sources, 131(1-2), pp. 182-187.

[52] Prasanna, M., Ha, H. Y., Cho, E. A., Hong, S. A., and Oh, I. H., 2004, "Influence of Cathode Gas Diffusion Media on the Performance of the Pemfcs," Journal of Power Sources, 131(1-2), pp. 147-154.

[53] Wang, C., Mao, Z. Q., Xu, J. M., Xie, X. F., and Yang, L. Z., 2005, "Influence of Carbon Paper on Self-Humidifying Performance of PEMFC," Chemical Journal of Chinese Universities-Chinese, 26(1), pp. 125-128.

[54] Comsol, 2005, *Comsol Multiphysics - Chemical Engineering Module, Users Guide*, Burlington, MA.

[55] Munson, B. R., Young, D. F., and Okiishi, T. H., 2006, *Fundamentals of Fluid Mechanics*, John Wiley and Sons, New York, NY.

[56] O'Hayre, R., Cha, S.-W., Colella, W., and Prinz, F. B., 2006, *Fuel Cell Fundamentals*, John Wiley and Sons, Inc., New York, NY.

[57] Makharia, R., Mathias, M. F., and Baker, D. R., 2005, "Measurement of Catalyst Layer Electrolyte Resistance in Pefcs Using Electrochemical Impedance Spectroscopy," Journal of the Electrochemical Society, 152(5), pp. A970-A977.

[58] Nitta, I., Himanen, O., and Mikkola, M., 2008, "Contact Resistance between Gas Diffusion Layer and Catalyst Layer of PEM Fuel Cell," Electrochemistry Communications, 10(1), pp. 47-51.

[59] Nitta, I., Hottinen, T., Himanen, O., and Mikkola, M., 2007, "Inhomogeneous Compression of PEMFC Gas Diffusion Layer Part I. Experimental," Journal of Power Sources, 171(1), pp. 26-36.